A Microstrip based RF Filter for Biosensor Applications

By

Idris Musa

A Thesis submitted in fulfilment of the requirements for the Degree of Doctor of Philosophy

School of Engineering

Newcastle University, United Kingdom

October 2021

A Microstrip based RF Filter for Biosensor Applications

By

Idris Musa

A Thesis submitted in fulfilment of the requirements for the Degree of Doctor of Philosophy

School of Engineering

Newcastle University, United Kingdom

October 2021

Dedication

I dedicate this thesis to my beloved family

Acknowledgement

My sincere acknowledgement goes to the creator of the worlds for giving me the strength, health, intellect, and resources to complete the thesis, without whom this work would not be possible. I sincerely say Alhamdullilah.

I wish to specially thank my sponsor the Petroleum Technology Development Fund (PTDF) for the opportunity and support throughout my research.

I want to also extend my deepest appreciation to my supervisor Dr. John Hedley, for his kind guidance and unending support during the course of my research, his support has been immensely useful. I want to acknowledge my parent for their consistent prayers and wishes during my study, these has been a great source of strength for me. I also want to acknowledge my dearest wife for her love, understanding and unending support throughout this journey. I also wish to acknowledge my children Afrah and Jamal for their understanding with me for the early mornings, late nights, and long weeks, this has also been a source of strength and joy to carry on with my work. May I also acknowledge the support of Dr. Andrew Pike and Dr. Neil Keegan for their support during my time with them, their support was very useful. I wish to thank Julia Spoors also, for her kind support and understanding during my time in the lab.

Let me also that Frank Atkinson for his kind support and understanding during my time working with him. My special thanks also go to everyone in the mechanical engineering workshop for their support. To my colleagues I wish to say a very big thank you for their assistance and understanding during our time together, particularly Fadoo Unom, Hayder Ashelaish, Abdullah Faqihi and Elmira Alimohammadzadeh just to mention a few, I wish you guys all the best in life.

Abstract

There is need in medical diagnostics for accurate, fast, and inexpensive devices, which can be routinely used. In this context, micro-biosensors are considered to provide viable solutions to the problems posed by the current healthcare industry. This is because these biosensing devices offer considerable advantages, such as specificity, small size, faster response, and low cost. Hence, innovative technique is desirable such as microstrip technology, which is a good means of employing planar and miniaturized high frequency filter designs. The advantages of implementing a high frequency filter design using microstrip technology includes low cost, light weight, compact size, planar structure and easy fabrication and integration with other components when deployed as a biosensor. Designing a highly sensitive and selective sensing element of a Biosensor is the aim of this research. To achieve this task a 5^{th} and 7^{th} order Chebyshev type low pass filter possessing a passband ripple of 1dB and a 3^{rd} and 5^{th} order Chebyshev type Bandpass filter possessing a bandwidth of 0.5GHz, a fractional Bandwidth of 20% and a centre frequency of 2.5GHz were designed. A second fabrication run was used to fine tune the device design and test point on the device.

Three sets of microstrip filters were produced, two of these were on a quartz substrate using two distinct materials, one of these materials is the chemically reduced graphene oxide (rGO), produced from the hydrazine reduction of graphene oxide, while the second filter produced on a quartz substrate is the one made from a nano gold film material this was being produced by gold deposition technique on the quartz substrate, the third of the three set is the microstrip filter produced on an FR4, this was made from a laser ablation technique resulting in a laser inscribed graphene (LIG). For the first two cases, mask of the designed geometry was used to precisely implement the filter design on the substrate, while for the LIG microstrip filter, the design was engraved on a Kapton tape using a laser machine. The conductivity of the rGO was observed to have a maximum value of 8.7mS/m, while that of the gold film material is known to be 45.2 $x10^6$ S/m, and the conductivity of the LIG was observed to be 0.28mS/mm. The sensor's RF characteristics was investigated using a vector network analyser (VNA), while ANSYS and Sonnet Lite

simulation tools indicate the potential for rGO material, but very good results were recorded for the gold film material, while the LIG results indicated the need for improved conductivity. The gold 5th order bandpass filter (5BPF) filter showed best repeatability with a frequency of 2.38GHz and standard deviation in the resonant frequency measurements of a single device of +/- 0.19MHz. Its initial functionalisation and then monolayer coverage of the sensor with a layer mouse IgG indicated that the corresponding shift in frequency response occasioned by the presence and volume of the target sample is an indication of the system's selectivity and suitability for deployment for biological sensing application. Plans are currently on the way to test more biological samples with lower concentration levels to verify the filter's sensitivity, selectivity, and wide range applicability as a biosensor sensing element. The future areas to be addressed are to enhance the fabricated material's property and sensor device miniaturisation.

Table of Contents

List of Tables

List of Figures

List of Publication

1. Rapid fabrication approach of Graphene based RF Sensor for Biological Application (SENSORCOMM 2019).

2. Generic Fabrication Technique of Graphene based RF Sensor Towards Biological Application. (IJRTE).

3. Microstrip Approaches for the Implementation of Reduced Graphene Oxide RF LPF Devices for Biosensor Application. (Unpublished work).

Chapter 1. Introduction

1.1 Background and Motivation

Currently, in the health sector, the laboratory diagnostic turnaround in the handling, sensing, testing and the manipulation of fluids to produce accurate end result can be a process that is demanding, time consuming and in most cases expensive in an ever fast, quick result driven and precision demanding society, hence it can be a daunting task. Large impact on the result can be caused by small changes in the process analysis and evaluation. Consequently, there is the need for new technology to develop point-of-application sensors (equipment) used currently for the clinical diagnosis of pregnancy, glucose monitoring, pH sensors and protein binding. This push towards point-of-application testing has opened a new technological research area in the usage of integrated systems where functionality of the sensor is carefully optimized and supported with electronics, fluidics, and separation technology. The maintenance of health is one of the most laudable technological objectives challenging science and technology and diagnosis is an essential prerequisite for treatment and prevention of disease. It is however important to explore ways of achieving quick, cheap, and reliable results from test samples at the point-of-care (POC), hence the need for research in the design of a device that would serve this purpose.

The application of sensor technology has been studied and known to have significant impact in point-of-care applications, especially the biosensor. Related applications of biosensors, such as the maintenance of food safety and environmental monitoring can be aligned with this central objective. The developing world has a desperate need for robust diagnostics that can be deployed in the field by both health care professionals and volunteers, in order to cut down the diagnostic turnaround time, which leads to quick and reliable diagnostic results that aids quick and precise medication so as to cut down on preventable deaths. According to World Health Organization (WHO) Infectious diseases account for around a quarter of worldwide deaths, although they are projected to decline as a percentage of total deaths in the coming decades, as other cause become more prevalent [1]. In developing countries we are faced with diseases of poverty such as

HIV/AIDS and tuberculosis, where the former kills almost 2 million people each year and the latter still affects around a third of the world's population and accounts for an estimated 1.5 million deaths, according to the WHO (2012), although the incidence has been falling globally at a rate of 2.2% in recent years [1]. In addition, there are 2.5 million deaths from diarrheal infections and almost eight hundred thousand (800 000) from malaria. Of the estimated 57 million global deaths in 2008, 36 million (63%) were due to non-communicable diseases [1]. The population of older people aged 60 years and over has increased in recent years, in most countries and regions, and that growth is predicted to increase in the coming decades. Between 2015 and 2030, the number of people in the world aged 60 years or over is projected to increase by 56 per cent, from 901 million to 1.4 billion, and by 2050, the worldwide population of older people is projected to more than double its 2015 size, reaching almost 2.1 billion [2, 3]. This impact of population aging will directly affect the health sector, therefore there is a need for innovative technology to counter or at least minimize this effect. One among this disruptive technology is the investigation and research in the area of POC test and diagnostic technique so as to device a rapid and accurate detection health-care platform[4].

One of the basic aims of developing POC devices is to significantly cut down the diagnostic test result time[5, 6], as well as making medical test devices easy to handle. Developing very sensitive, accurate, reliable, and rapid response biomedical analysis system is the basis for POC testing systems. According to the WHO, the USA already spends 17.9% of its GDP on health care, while the European Union average is closer to 9.5% (UK and Sweden 9.6%) [1]. Technology needs to offer more economic solutions and distributed diagnostics enabled by biosensors and enhanced by consumer products available over-the-counter are a key part of the solution [1]. All this adds up to a prediction of a strong commercial future for biosensor technology. The clear need for sensors in several prospective markets globally continues to drive substantial research in the field of both chemical and biological sensors. This has become more evident, as such soil, air and water contamination monitoring in real time became a necessity following some natural disasters, pandemic, and industrial accidents such as that in Fukushima, Japan 2011, the M 6.3 2011

Christchurch earthquake, in New Zealand, the incessant flooding in the UK and the Covid-19 pandemic.

In environmental monitoring just like in health care, the enduring principle is that, early detection translates into informed interventions that can have lasting value. There is a demand for both high through-puts sensing in traditional laboratory-based sensing instrumentation and of low-cost sensing for field or personal use. Environmental monitoring for the detection of pollutants is becoming increasingly significant to regulatory agencies and the public. This is mainly true for compounds that pose an impending human health risk or risk to the environment. Many of the monitoring requirements of this environmental legislation might easily be accomplished by the applications of biosensor.

The disadvantage high cost and slow turnaround times usually related with the measurement of regulated pollutants, clearly shows a need for, methods for screening and monitoring the environment which are fast, portable, and cost-effective[7]. To meet this need, a variety of field analytical schemes have been introduced, a few of which are now commercially available or in the process of being developed[8]. In addition to what has been said thus far, recently it has been understood that biological systems and processes have become very viable commercially, this has led to the development of sensor technologies that is apt for their sensing, monitoring and control [9]. It is also worthy of note that such sensing devices aptly called biosensors, could greatly change analytical technology in fields such as health care, food safety, defense, drug discovery, veterinary care, agriculture and pollution monitoring and control [10]. Because of their exceptional characteristics, technologies such as biosensors might be exploited to fill specific applications in the environmental monitoring area. Though the potential of the environmental market is very large, there are several technical and commercial obstacles which must be addressed for biosensors or other field of analytical technologies to have a significant impact on environmental monitoring. These obstacles include the large quantity of potential pollutants and the extensive range of their chemical classes, the wide range and complexity of environmental matrices, the diversity of possible co-

contaminants, the wide range of pollutant concentrations, the lack of adequate markets for specific applications, and the all-important regulatory acceptance requirements[8].

1.2 Aim and Objectives

The aim of this work is to design and implement a generic low-cost, sensitive and selective microstrip RF sensing element for biosensor implementation, to be used for real time diagnosis to be incorporated with a point of care diagnostics system. This was done anticipating the high electrical conductivity of Graphene as well as that of a thin film gold material. In order to achieve this aim, the following research objectives were accomplished:

- Design the electrical radio frequency (RF) filter (i.e. the lumped element filter)
- Convert the lumped element RF filter into it microstrip planar equivalent
- Implement the RF microstrip filter using Graphene, Laser-scribed Graphene, reduced graphene oxide (rGO) and Gold.
- Functionalised the fabricated planar RF filter sensor for the intended biological application.
- Compare the sensitivity and selectivity of the Graphene/rGO Planar RF filter sensor with a gold equivalent.

1.3 Hypothesis

The hypothesis of this work is based on the fact that research has shown that Graphene possesses very high electrical conductivity which means rapid electron transfer through it. This speed of electron transfer through it could be exploited to design and implement a sensitive and selective sensing element for biosensor device that can be used in the field of biochemical and biological application for cheap, quick, and reliable diagnostic results. This improved device outcome uses the effect of the interaction between RF field and specific molecules hybridised onto the surface of the sensor as the fundamental principle exploited for the development of this biosensor. This high frequency signal interrogation

of biological cell resulted in the improved designed of a label free RF biosensor with high selectivity and low limit of detection.

1.4 Thesis Outline

The thesis is structured in the following manner: chapter one is based mainly on the introduction of the research work, the justification of the work the scope and the aim and objectives that are to be achieved so as to ensure the completion of the research. Chapter two of this thesis will mainly be on the definition of subject area, summary of relevant previous work, and how this research fits into it. Chapter three of this work will be on system design and mathematical formulation; it will also highlight the several systems being designed as well as their resultant geometry. Device fabrication and implementation will be discussed in chapter four, here the several materials and methods used in the fabrication of the different sets of sensors will be discussed. Chapter five will be about the sensor devices characterisation, this section will highlight how the sensing points on each of the sensor device was determined to ensure high selectivity and sensitivity. The biological testing of the sensor devices, the analyte sensed, and the functionalisation protocol deployed in the biological sensing are well discussed in chapter six. Chapter seven will deal with the conclusion and recommendation of the work done on the RF biosensor. To get a better view of the overall thesis figure 1.1 below shows the diagram of the thesis structure of this work, while figure 1.2 illustrates the biosensor structure to emphasis its make-up.

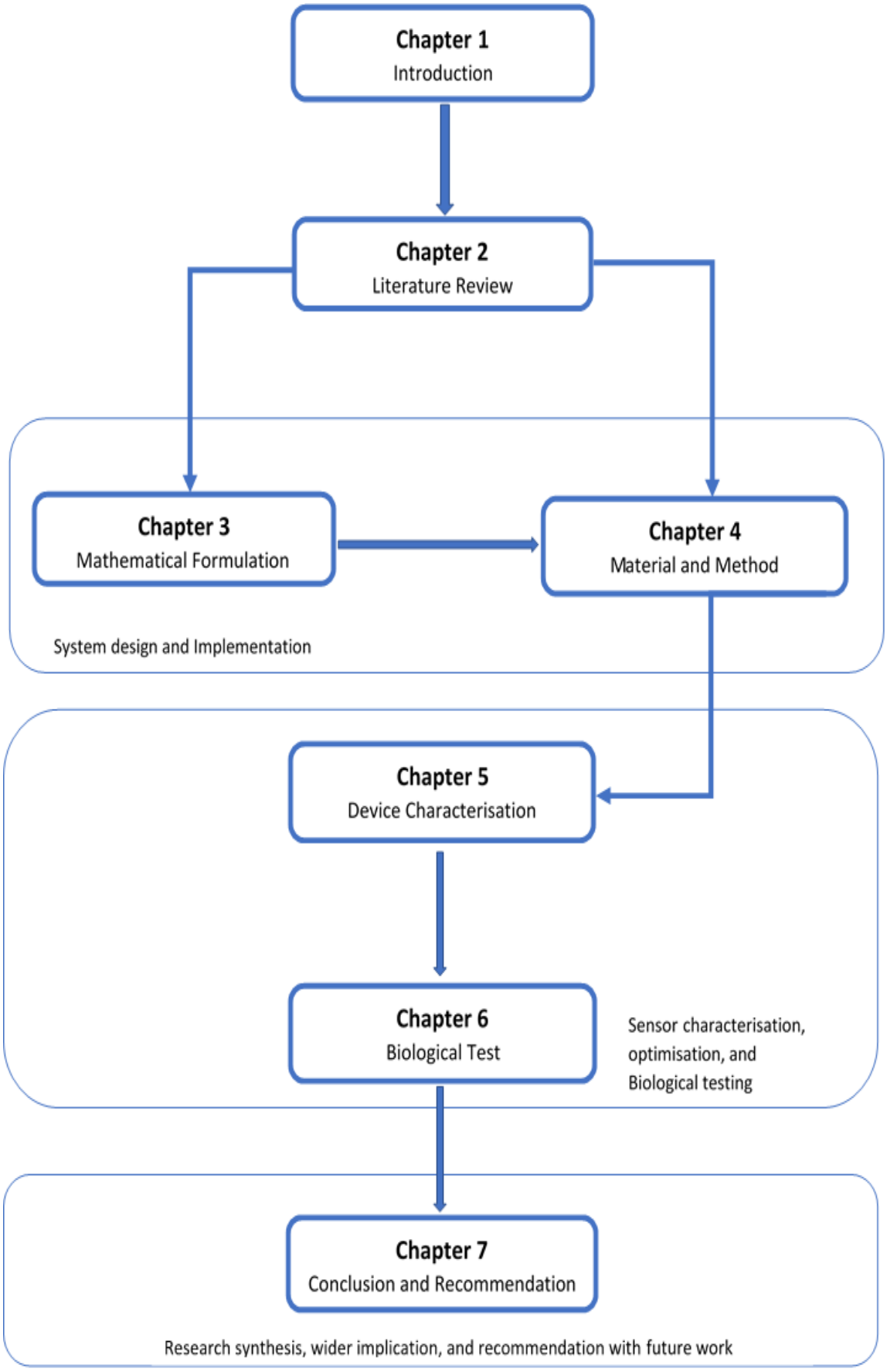

Figure 1. 1 The Thesis structure.

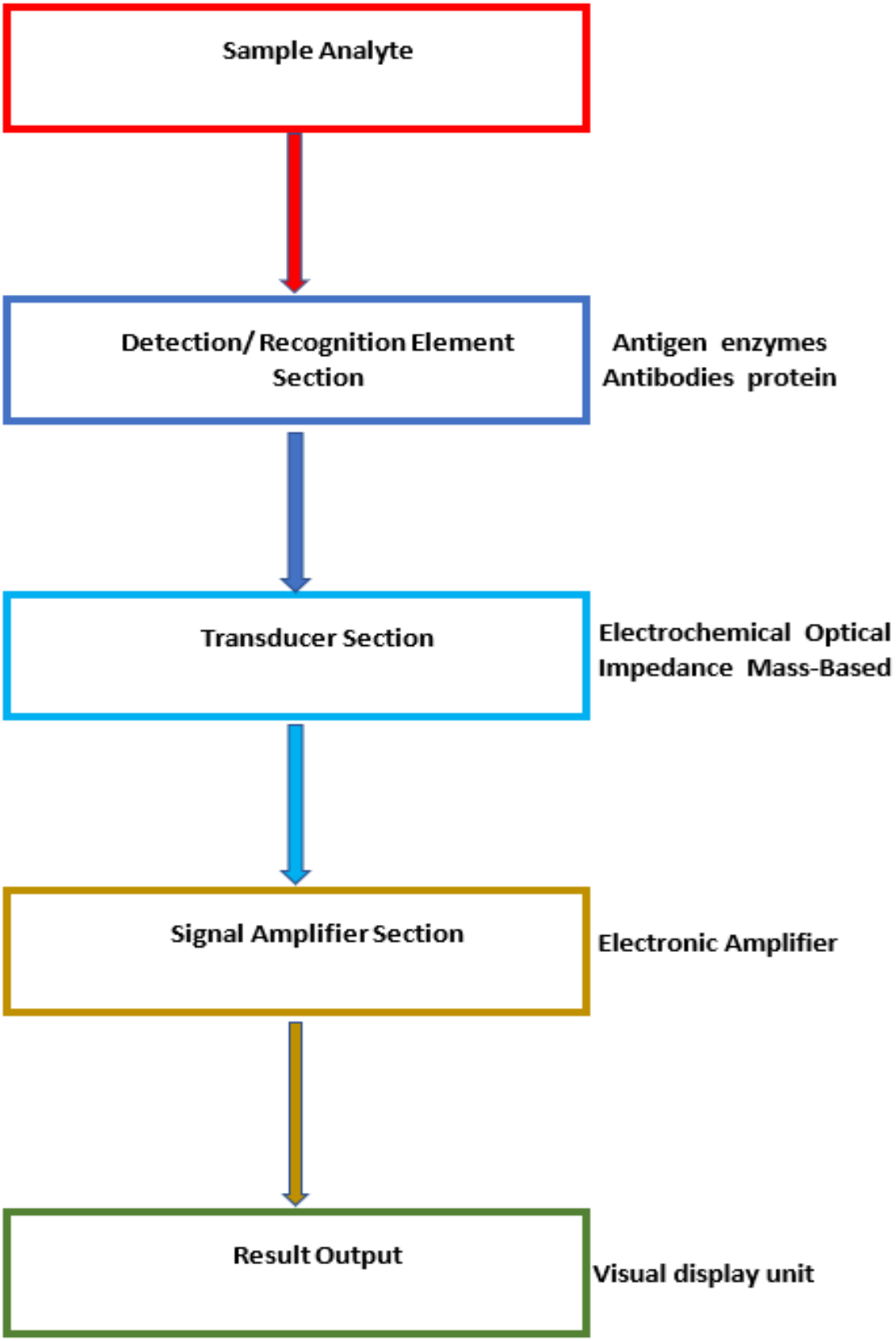

Figure 1. 2 The structure of a biosensor.

Chapter 2. Literature Review

2.1 Introduction

In this chapter, the study starts by looking at the technical background and an extensive review of the RF biosensor. The general overview of the technical background is presented first by looking at radio frequency design in general. This background discusses Planar transmission Line, radio frequency filter, microstrip filters, and stepped impedance filter. Then the focus was shifted to discuss biosensor background, types of biosensor, radio frequency biosensors, and microwave Microelectromechanical Biosensor. The background was then expanded by looking at Material wherein; materials used in RF designs, materials used in biosensors, and graphene-based Biosensor, were discussed. The chapter was then concluded with the summary and by identifying challenges that need to be addressed leading to the intended task to be undertaken in this research to mitigate these challenges. The technical background is presented in the next section.

2.2 Radio Frequency Design

Operating at higher frequencies (MHz to GHz) for low loss transmission of signal in modern digital communication is one of the big challenging tasks[11]. The miniaturization of microwave circuits was done to overcome this problem through the development of planar transmission lines [11], these miniaturized devices and structures are used to design modern circuit boards which have attracted features like; light weight, low profile, low cost and ease of integration with other devices on a single board [3]. This higher frequency range falls within the Radio Frequency (RF) spectrum, which is basically any frequency within the range of 20KHz to 300GHz, and most communication systems require an RF front end where analogue signal processing is done by RF filters and low noise amplifiers [12]. Filters are basically resonant circuit that is used practically in every transmitter, receiver or piece of test and measuring system [13, 14]. They are necessary building elements and components in many areas of RF/microwave engineering. They are two ports network used to select or control the frequency response at certain points in an RF/microwave system by providing transmission at frequencies contained in the passband of the filter and attenuate signal transmission in the filter stop band [13, 15].

The complete transmission line circuit can be fabricated and realized by thin film or photolithography technology [11].

However, for low loss transmission of signal at high frequency, the waveguide and other transmission lines were developed. Waveguide, two wire lines and coaxial lines were depended upon for the design of early RF and microwave transmission. Although high power handling capability and low loss are the benefits of using waveguide, but they are bulky and expensive, while a two wire line is inexpensive but lack shielding as a demerit as well as having high radiation losses at high frequencies [16], while coaxial transmission lines have better shielding but they are a difficult medium in which complex microwave components can be fabricated from.

All impedance elements are assumed to be lumped constants in ordinary circuit theory, for a transmission line over a high frequency this is not true. If the frequency of operation is so high that the inductance of short conductor lengths and the capacitance between short conductors and their surroundings cannot be ignored, it then means that these capacitances and inductances are distributed along the conductor length and at each point of the conductor their effects combine. Since the wavelength at this frequency is short in comparison to the physical line length, then distributed parameters cannot be adequately represented by means of lumped parameters equivalent circuit. As such microwave transmission lines can be analysed in terms of voltage, current and impedance only by the distributed circuit theory [16]**.**The miniaturization of microwave circuits was done to overcome this problem through the development of planar transmission lines [11], these miniaturized devices and structures are used to design modern circuit boards which have attracted features like; light weight, low profile, low cost and ease of integration with other devices on a single board[3].

2.2.1 Planar Transmission Line and Stepped Impedance microstrip filter

One of the essential prerequisite for a transmission line structure to be suited for a circuit element in a microwave integrated circuit (MIC), is that the transmission structure should be planar in configuration (set-up or make-up) [17]. A planar set-up means that the

elements characteristics can be determined by the dimensions in a single plane, for instance the impedance of a microstrip line can be controlled by simply adjusting its width, as such when the impedance can be controlled by adjusting the dimension in a single plane, then the fabrication of the circuit can easily be carried out by the method of photolithography and photoetching of thin films. The development of hybrid monolithic MICs has been brought about by the use of this techniques at microwave and millimeter wave frequencies [17]. There are several transmission lines that fulfil the requirement of being planar in structure these are; Microstrip line, coplanar waveguide, parallel-plate, slot lines and coplanar strips [13, 18]. The most popular of these planar transmission lines is the microstrip transmission line. This is mainly because the mode of wave propagation in it is almost transverse electromagnetic (TEM), which is termed quasi-TEM. This quasi-TEM mode allows for an easy approximate analysis and produces wide band circuit and also easy transition to coaxial circuit is possible[17]. Being one of the most popular and frequently used type of planar transmission lines the microstrip line can primarily be fabricated by photolithographic processes and is easily miniaturized and integrated with both passive and active microwave devices and circuit components.

One of the most suitable means of fabricating the passive microwave biosensors is for them to be fabricated as a planar transmission line structure. Planar transmission line can be designed in many forms as stated above. Each topology is characterized by the modal distribution of its fields, as well as achievable levels of characteristic impedance, phase velocity, and number of modes supported by the structure [13, 17]. However, The main difference between circuit theory and transmission line theory is that, in circuit theory analysis of the physical dimension of a network is assumed to be smaller than it electrical wavelength (of the transmission line /network) [19]. This means lump elements such as capacitors and inductors mainly used in electronic circuits are generally available in limited range of values and are also difficult to implement at RF/Microwave frequencies, where distance between individual components is not negligible. More so lump capacitor and inductor components introduce stray inductances and capacitances from their leads and the materials from which they are made from[20].

However, transmission line structures can suitably be used to approximate lumped circuit elements and they could conceptually be useful starting point to see how various design functions can be realized. For instance, a capacitor can be approximated by using an electrically short section of low impedance line, in the same vain, an inductor can be approximated by a high impedance section with electrical delay less than ~ $\pi/4$[21]. Since lumped elements are made up of components that have connecting leads, it means their usage for high frequency filter design and application will result in unwanted losses due to these lead conductors. This is in part due to the skin effect in these leads that is caused by increase in resistance in the lead conductors as frequency of application increases [14], and also in part due to the fact that at high frequencies, the materials used in the producing these lumped circuit elements tends to play a role in their resultant value, as such the value will change and this change will affect the overall circuit resulting in incorrect response [14].

A transmission line on the other hand is characterized by two or more parameters (i.e., its characteristic impedance, propagation velocity, and physical length). The transmission line size may be a fraction of a single or several wavelengths, thus it can be referred to as a distributed parameter network where voltages and currents over the length of the network can vary in magnitude and phase[19, 21]. These differences that exist in the dimensionality between ideal and physically realizable components can lead to a breakdown in applicability of simple circuit. The required fabrication tolerances needed by lumped element designs can potentially lead to challenges in terms of component performance. Alternatively, by changing the characteristic impedance, phase velocity, and mode shape of the guiding scheme base on length at a scale so small as compared to the wavelength in the transmission media, in this manner responses over inherently large bandwidths can be achieved which can be quite insensitive to fabrication tolerances[11, 13]. Furthermore, advancements in semiconductor technology, in the production of high quality organic materials or ceramics that possesses a low loss factor, and the convenience of low cost printed circuit boards (PCBs) has swung open the latest stage in transmission line expansion [22]. Low losses, negligible signal distortion, high transmitted power capability, electromagnetic (EM) compatibility, a wide operational frequency band, high electromagnetic resistance and pure dominant mode propagation are essential

requirements set on any kind of transmission line, along with easy and low cost production, and high integratability with various passive circuits and active devices[22, 23].

Because of these flaws and the need to have a planar structure, the distributed or planar transmission lines were utilized to approximate the susceptances and reactances of the lumped element filters [15]. Hence the essence of the planar filter is to obtain an approximate microstrip realization that estimate the lumped element filter. For this work the microstrip transmission line was explored to implement the transduction section (transducer of the biosensor), because of the benefits of planar technology that has enabled the fabrication of printed circuit lines, which are however, relatively easy to produce (although potentially difficult to make into a useable biosensor). Microstrip technology (which is planar transmission line technology) is a technique for filter design and implementation owing to its advantages of light weight, low cost, planar structure, compact size, and ease of integration with other components on a single board [24, 25].

Filter networks on the other hand are essential building elements in many areas of RF/microwave engineering. Which essentially control the frequency response of a signal by allowing the transmission at all frequencies within the passband and attenuation at all frequencies in the stop band [15, 25]. In most modern microwave and RF communication systems, especially radar and satellite communication which requires high performing filter with very high selectivity and low insertion loss. Microstrip filters are gaining popularity among researchers due to constant design improvements as well as their need in many microwave systems including wireless communication like satellite communication and in filters design, there are a few parts that need to be improved or upgraded in order to produce a more efficient and better product. Based on requirement and specification filters can be implemented using either lumped elements or distributive elements, and microstrip structures have been good alternatives when used as an RF and microstrip filters in terms of selectivity, size, insertion loss just to mention a few [26].
The microstrip technology is a good means for the design and implementation of filters due the advantages that all its components can be fabricated by photolithographic technology in a planar form thereby resulting in structures that possess the

aforementioned benefits, and ease of integration with other components on a single board to form a microwave integrated circuit (MIC) [25]. The configuration of a microstrip line is such that a conductor of width W is fabricated on a thin, grounded dielectric substrate of thickness h and relative permittivity (dielectric constant εr), If the dielectric substrate were not present (εr = 1), this would have resulted in a two-wire line consisting of a flat strip conductor over a ground plane, inserted in a homogeneous medium (air in this case). This would constitute a simple TEM transmission line with phase velocity $V_p = C$ (c is speed of light) and propagation constant β = k0. Pozar in [13] stated that it is for this reason that microstrip line cannot support a pure TEM wave since the phase velocity of TEM fields in the dielectric region would be $C/\sqrt{(\varepsilon_r)}$ and that in the air region will be C, so a phase-matching condition at the dielectric–air boundary would not be possible to impose, in actuality, the exact fields of a microstrip line constitute a hybrid TM-TE wave and require more advanced analysis techniques. Microstrip line, short stubs and sections whose physical lengths are smaller than a quarter of a guided wavelength at the frequency which they operate, are the most common components for approximate microwave realization of lumped elements in microstrip filter structures[27]. From the above it is obvious that a planar transmission line could be implemented by employing a microstrip filter technique which comes with these stated merits and the benefits of planar filter configuration, which appears suitable for the intended biological and biomedical application

The lumped element filter dimensions are almost the same as their wavelength consequently they are not suitable for high frequency filter construction, because if used at this frequency, there would result a circuit performance degradation [28]. Thus, to arrive at practical filters, the lumped component filters must be converted into distributed element realizations. Filters can be realized in lumped type or microstrip line type. Various alternative methods have been developed by several researchers to ease simulation effort when converting prototype low pass filter into microstrip and one of such is the stepped impedance implementation. These filters are formed from the series connections of high and low impendence microstrip transmission lines [18, 29], they are simple in design and possesses the benefits associated with all planar transmission line structures which

includes; low cost simplicity, ease of fabrication [30]. Stepped impedance low pass microstrip filters offer better stop band characteristics and are simpler to design.

The cascade structure of alternating high and low impedance transmission line act as a semi-lumped element. The high impedance lines act as series inductor where low impedance transmission line act as a shunt-capacitor. The steps to design the stepped impedance microstrip low pass filter is clearly highlighted in chapter three but includes [31]; specifying the filter type, then from standard tables obtain the low pass filter prototype values, after which they are then transform into real values of reactive components via frequency scaling, the next step is to convert this physical filter design analytical or via software tools into a microstrip stepped impedance filter for onward implementation on a preselected substrate.

The main advantage of the stepped impedance filter is it simplicity but it is however plagued with low attenuation in the stop band, low selectivity, susceptible to noise, susceptible radiation , it does not possess a sharp transition band and high stop band [13], and basically, the conventional stepped-impedance LPF is suffering from narrow stopband, gradual transition and large dimension due to the high order filter in order to obtain sharp response as drawbacks [15]. Several research groups have published details on their development of these types of filters, Rajasekaran et al [28] used Advanced Design System (ADS) tool to design an X-band stepped impedance Butterworth low pass filter at a center frequency of 10GHz and an attenuation of 60dB. Their filter stepped impedance filter which showed harmonic suppression in the stop band was intended to be used for wireless application. In the work of Aditi and Pravesh [32], they designed a 6th order microstrip stepped impedance Chebyshev filter with a cut-off frequency of 2.5GHz on an FR4 substrate. This design was tested using both a Vector Network Analyser (VNA) and Integral Equation Three-Dimensional (IE3D) full wave electromagnetic simulator. The simulated responses of the IE3D software and the VNA slightly differs from the designed value, but overall, their responses were quite similar as expected.

A seventh order microstrip stepped impedance Chebyshev low pass filter was designed by Garvansh et al [31] at a cut-off frequency of 5GHz. The sizes of the filter were determined via calculations but was also verified using the IE3D software tool. The resultant filter was fabricated using conventional process and the test results indicated the Chebyshev response that exhibits the equal ripple pass band and a maximally flat stop band. The simulation results also showed that the cut-off frequency was 3.7GHz which is less than the designed value of 5GHz. Similarly, a stepped impedance filter was designed by Homayoon et al [33] where they used the least square method to design a stepped impedance low pass filter, their designed filter frequency response matches those they obtained from HFSS simulator software. In a similar vein, a sixth order, 2.5GHz cut-off frequency microstrip stepped impedance low pass filter was designed by Sudipta and Chowdhury [29], their filter was fabricated on an FR4 while the design and simulation was performed using the 3D full wave electromagnetic simulator IE3D. The fabricated filter was tested with a VNA which gives a response whose cut-off frequency is just short of the designed cut-off frequency. Artificial Neural Network (ANN) was used to design a stepped impedance microstrip low pass filter by Vivek et al[27]. This is a 3rd order Chebyshev filter with a cut-off frequency of 1.8GHz. The results of the ANN filter parameters when compared with the IE3D electromagnetic simulation software tool was found to be a match and the cut-off frequency of the response matches it designed value. From the foregoing is clear that the stepped impedance form could serve as a good means for the deployment of the propose microstrip filter owing to all the state advantages and note should be taken, of any flaws that might arise and the possible reasons for such flaws.

2.2.2 Radio Frequency Filter

A filter is a network that provides perfect transmission for signal with frequencies in certain passband region and infinite attenuation in the stopband regions. Such ideal characteristics cannot be attained, and the goal of filter design is to approximate these ideal requirements to within an acceptable tolerance. Filters are used in all frequency ranges and are categorized into three main groups[13-15]; Low-pass filter (LPF) transmits all signals between DC and some upper limit (the cut-off frequency ωc) and attenuate all signals with frequencies above ωc. High-pass filter (HPF) passes all signal with frequencies

above the cut-off value ωc and reject signal with frequencies below ωc. Band-pass filter (BPF) passes signal with frequencies in the range of the passband (ω1 to ω2) and reject frequencies outside this range. The complement to band-pass filter is the band-reject or band-stop filter. In each of these categories the filter can be further divided into active and passive type. The output power of passive filter will always be less than the input power while active filter allows power gain[14].

At frequency below 1GHz, filters are usually implemented using lumped elements such as resistors, inductors, and capacitors. For active filters, operational amplifier is sometimes used. There are essentially two low-frequency filter syntheses techniques in common use, these are referred to as the image-parameter method (IPM) and the insertion-loss method (ILM). The IPM provides a relatively simple filter design approach but has the disadvantage that an arbitrary frequency response cannot be incorporated into the design [13]. The insertion-loss method begins with a complete specification of a physically realizable frequency characteristic, and from this a suitable filter schematic is synthesized. The IPM will be ignored for this work and attention will only be given to the ILM, whose design procedure is based on the attenuation response or insertion loss of a filter method [13-15]. There are a number of standard approaches to designing a filter, among the well-known methods are[13, 14]: Maximally flat or Butterworth function, Equal ripple or Chebyshev approach, Bessel and the Elliptic function Method. The ILM permits a high degree of control over the passband and stopband amplitude and phase characteristics, with an organized way to synthesize a desired response. The essential design trade-offs can be estimated to best meet the intended application requirements. If, for instance, a minimum insertion loss is of most importance, then a binomial response could be used; a Chebyshev response would satisfy a requirement for a very sharp cut-off. If it is possible to sacrifice the attenuation rate, a better phase response can be obtained by using any of the linear phase filter design [28]. In addition, in all cases, the insertion loss method allows filter performance to be improved in an easy way, at the expense of a higher order filter.

RF filters are filters designed to operate in the RF frequency range (20KHz to 300GHz) [34]. Filters designed for low frequency applications are realized using lumped elements

comprising reactive and resistive parts. But at microwave and RF frequencies different types of resonators and cavities are used to achieve filter characteristics for ease of fabrication. The commonly used filter implementation is the microstrip filter structure which is planar in design. Conventional filter structures like Bessel, Chebyshev, and Butterworth low pass filters have requirements for special fabrication technique [31]. With more efficient software and faster computers, it is now possible to simulate planar microwave circuits using electromagnetic software simulation tools. These electromagnetic field solvers have given RF and microwave engineers a new means of handling and simulating difficult filter design problems. The visualization capabilities of these software tools can reveal new insights into microwave components behavior at their designed frequencies, and also microstrip geometry and structures are suitable for these field solvers to obtain valuable analytical data to aid the visualization of concepts and the resultant response of the designed structure[35].

2.3 Biosensor Background

Fundamentally sensors also called transducers are devices that register a physical, chemical, or biological change and convert that into a measurable signal [9]. Sensors are of myriad types which includes; pressure sensors, microphones, accelerometers, gyroscopes, optical and image sensors, microfluidics, flow meters, and temperature sensors[36]. In addition, devices like RFID, strain sensors, energy harvesting devices and biological/chemical sensors are rapidly emerging. These may be digital or analogue, in addition to those that can measure temperature, flow, motion, speed, light, barometric pressure, physiologic pressure, humidity, sounds, magnetic fields, chemicals and gases[36]. While a chemical sensor can be termed a device responding in a fast and reversible way to chemical stimuli (i.e., changes in concentration of a biochemical species) [10]. Electrochemical biosensors, which are subclass of chemical sensors, combine the sensitivity, as shown by low detection limits, of electrochemical transducers with the high specificity of biological recognition processes [9]. These devices contain a biorecognition element (enzymes, proteins, antibodies, nucleic acids, cells, tissues or receptors) that selectively reacts with the target analyte and produces an electrical signal that is related to the concentration of the analyte of interest [9]. From the foregoing the biosensor

whose basic structure is shown in figure 2.1 below, can be defined as stated by IUPAC "A device that uses specific biochemical reactions mediated by isolated enzymes, immunosystems, tissues, organelles or whole cells to detect chemical compounds usually by electrical, thermal or optical signals" [37].

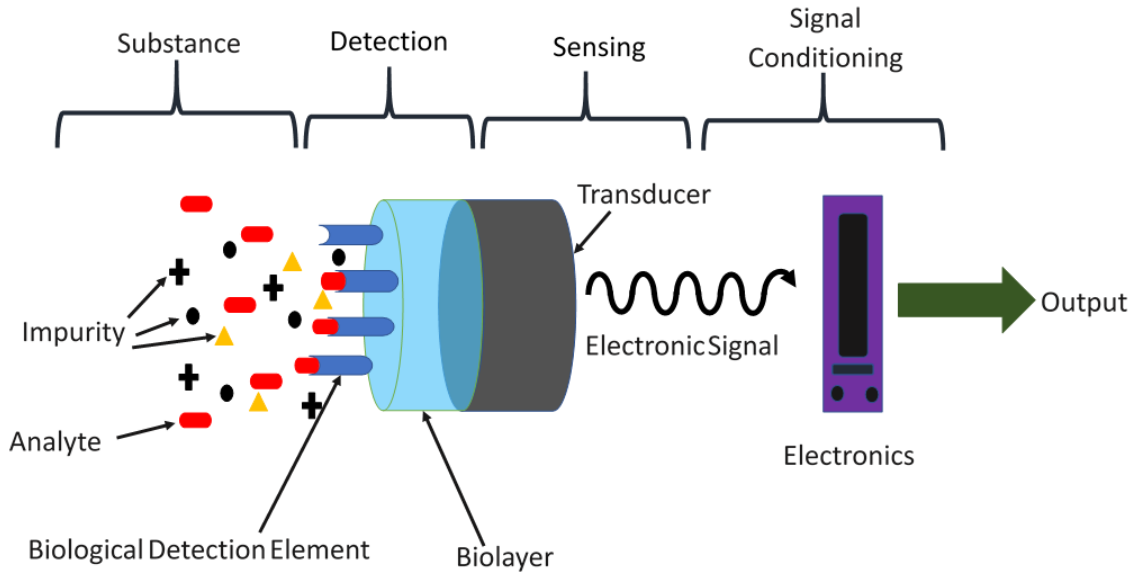

Figure 2. 1 The structure of a biosensor

The basic idea of the biosensor was first explicated by Leyland C. Clark in 1962, in his seminal description of an "enzyme electrode"[1]. Building on his earlier invention of the Clark oxygen electrode, he opined that electrochemical detection of oxygen or hydrogen peroxide (H2O2) could be used as the basis for broad range of bioanalytical instruments, by the integration of appropriate immobilised enzymes [1]. In general when biological molecules interact specifically and reversibly there is a change in one or more physicochemical parameters associated with the interaction and especially so if this reaction is accompanied by catalysis[8]. Two basic biosensors categories exist these are catalytic and affinity biosensors[10]. The transducer element of a typical biosensor can be categorize into four electronic configurations namely: amperometric, optical, potentiometric and other devices[38]. Biosensor instruments are specific, rapid, simple to operate, easily fabricated with little sample pre-treatment involved[39]. The heart of the biosensor is it sensing element; hence a lot of materials has been employed as sensing elements, ranging from metals to semiconductor. There has been an interest in the use of nanomaterial for the development of biosensor, and non-metals are currently finding

applications as sensing elements because of their unique physicochemical properties. Carbon base materials especially carbon nanotubes (CNTs) are at the forefront of this explosion. The interest is partly motivated by the ability to improve macroscale biosensors by incorporating CNTs and partly by a desire to develop completely new biosensing platforms. Carbon materials are useful as the sensing element of biosensors since the environmental sensitivity of carbon-based molecules can be efficiently tailored by synthetic chemistry techniques[40].

Biosensor's usage brings about a mixture of advantages. Firstly, they are highly sensitive, this is because biomolecules often possess high affinity toward their targets, for instance, antibodies capture antigens with a dissociation constant at the nanomolar scale, and DNA to DNA interactions are even stronger than antigen-antibody. Secondly, biological recognition is usually a very selective process. An example is that enzyme and substrate are just like lock and key, such high selectivity always results in selective biosensors. Thirdly, owing to the development of modern electronic industry, there is now considerable potential in developing inexpensive, integrated and ready-to-use point-of-care biosensor devices[41]. These biological sensors certainly improve the ability to detect pathogens or perform genetic analysis in hospitals; and more importantly, they are particularly useful for small clinics and even for point-of care analysis[41]. The developing area of nanotechnology together with the elegant and multi-disciplinary research involving new sensing concepts is well suited to provide a combinatorial sensing motif like point-of-care array detection methodologies. Such capability would certainly open the door for the development of highly sensitive, multi-analyte and multi-metabolite sensing platforms. This is expected to provide the user with not only the ability to monitor common disorders but also determine which of his/her daily habits exacerbate metabolic imbalances[41].

From the foregoing, it is possible to explore the construction of selective and sensible biosensors for the analysis of numerous biochemically and clinically important compounds by coupling the catalytic power of enzyme systems to the apt transducers [42]. However in certain cases whole bacterial, sub-cellular fractions or other cells or tissue slice might prove to be a better medium biocatalyst activity by supplying complex

multi-enzyme pathways, allowing the stabilization of the catalytic activity, thereby enhancing the amount of biocatalyst subsequently simplifying the construction of the electrode (transducer)[42].

Enabled by rapidly emerging nanotechnologies (nanoparticles, nanotubes, and nanowires) and microfabrication techniques (microelectromechanical systems (MEMS)), microfluidics, and complementary metal-oxide-semiconductor (CMOS)), several new sensing platforms have been proposed and tested for biomedical applications. Despite these inroads, there remains a need to develop practical assay methodologies that (1) have higher sensitivity and specificity, (2) can minimize sample preparation, (3) can measure widely different types of molecules using the same format and instrument and (4) can be ran in a single tube point-of-care or high-throughput screening formats[42]. These stringent prerequisites are necessary for translation to clinical settings, because molecular measurements will have to be performed on smaller and smaller samples to enable multiplexing and longitudinal monitoring so that treatment strategies can be tailored to individual patients in real time[42].

Numerous clinical trials and intensive research efforts have indicated that continuous metabolic monitoring holds great potential to provide an early indication of various body disorders and diseases. In view of this, the development of biosensors for the measurement of metabolites has become an area of intense scientific and technological studies for various research groups across the world [41]. These studies are driven by the need to replace existing diagnostic tools, such as glucose test strips, chromatography, mass spectroscopy and enzyme linked immunosorbent assays (ELISA), with faster and cost effective diagnostic devices that have the potential to provide an early signal of metabolic imbalances and assist in the prevention and cure of various disorders like diabetes and obesity just to mention a few [41].

2.3.1 Types of Biosensor

Ever since the discovery of Biosensor in the early 1960's they have increasingly find significant applications in our day-to-day life. Take the case of routine practice, for

instance the health sector. It is interesting to state that one of the laudable technological objectives that is challenging science and technology is the effective maintenance of health, and one of the ways to actualize this objective is to seek means by which disease can quickly, easily, and effectively be detected, prevented, and treated. The importance of the prevention and treatment of disease is one of the driving forces that leads to the development of specific Biosensor types. Lots of research has been carried out to improve the sensitivity and overall performance of Biosensors, these several research have led to the development of different classes of Biosensors. These classes of Biosensor can be categorized either by the kind of biological signalling mechanism (Bioreceptors) that are employed or based on the type of sensing/ transduction technique deployed. Biosensor's category that are due to the type of bioreceptors employed are: enzyme based, antibody, DNA, cell based, microbial, and tissue. And those categories that are based on the kind of transducer employed are: electrochemical, electrical, optical, piezoelectric, and thermometric.

The type of Biosensor whose design is to be explored in this work is the one based on the mode of implementation of the transduction mechanism and in this case, it is generally the electrical type and particularly the Radio Frequency (RF) Biosensor. The concept of sensing in this kind of Biosensor is that it makes use of the shift in the frequency of the transducer (the sensing element), to signal the presence of the target analyte and the intensity of shift from this designed frequency is being used to indicate the concentration of the target analyte in the sample introduced unto it.

2.3.2 Radio Frequency Biosensors

The sensing scheme that is applied for biological purpose is application specific, hence it is difficult to design a universal biosensing scheme for Point of care (POC) devices [4]. the optical sensing scheme is feasible for a large sensing applications like Enzyme Link Immunosorbent Assay (ELISA) technique, and electrochemical sensing technique is suitable for applications like blood analysis monitoring systems [4], another feasible sensing technique is the use of electromagnetic waves (EM) that are not in the optical frequency range [4]. EM wave in the GHz to THz frequency range are highly sensitive to

changes in the water content in any sample and this can be used to detect biological target in the sample based on the changes in the water content at certain high frequencies [4]. Biosensors operating in the microwave and RF frequency range (1GHz to 100GHz) of the electromagnetic spectrum have recently gained interest [4]. The interaction between EM wave and biological materials can be exploited for the design of highly sensitive biosensors.

When we consider RF design, charge interaction is a very important factor, considering the main RF characteristics which are; frequency, phase shift, amplitude, S-parameters and power loss [43]. The advantage of microwave filter architecture is that it allows the reaching of very high sensitivity capabilities [44]. Frequency based biosensor has the potential for wireless remote sensing application, where it can be employed as a biosensing node in an RF transmit system which can transfer real-time measured information for biomolecular sensing in a biofluidic state. It can also be employed for the detection of other specific biomolecular binding that is involved in antigen-antibody reaction and DNA hybridization [45]. Most RF biosensors have been mainly based on RF passive devices and circuits having a simple structure such as various types of resonators, transmission line (TL), and interdigital capacitors (IDCs), although in recent years, active systems based on radio frequency integrated circuit (RFIC) and hybrid PCB circuits have been studied for biomolecular detection [46]. In case of biosensors using RF passive devices and circuits as well as nano-sized RF biosensors, they can be simply measured by using complex measurement system like a test fixture system connected with a VNA [46]. On the contrary, measurements on the biosensing platform associated with an RF active systems can easily be performed by employing a simple, less complex and cost-effective equipment, such as a digital multimeter [46].

In a work that showcases how silicon radio frequency integrated circuits (RFICs) was used for detecting certain protein in a blood sample, CMOS RF transceiver were designed for the fast detection of biological substances. Its main function is to manipulate and monitor RF dynamics of protons in water via nuclear magnetic resonance (NMR) since target molecules alter the proton dynamics, this is the basis for this biosensing platform [47].

The outstanding physical phenomenon of this sensing scheme is nuclear magnetic resonance (NMR) where nanoscale magnetic particles coated with antibodies that specifically bind to the target proteins are suspended in the sample [47]. If the proteins (target molecule) exist, the magnetic particles self-assemble into clusters around the proteins, this self-assembly can be detected by performing proton NMR due to the presence of target proteins, the magnetic particles self-assemble into larger magnets, the resonant interaction between RF magnetic fields and protons in water, which is altered by the presence of target biological objects will then be used to detect the presence of, and the concentration of the target molecule in the sample [47]. The result was satisfactory as it showed lower detection limit of the biosensor. Its main demerit is that it is relatively large and bulky as compared to more potable handheld device.

The IDC is a type of planar RF passive device, which are known to produce a considerably large capacitance due to its periodic metal-dielectric gap-metal configuration [46]. This sensing technique is a well-known transducer and is widely used at low frequency region [46]. In high frequency region, when the frequency increases, the IDC device transforms into inductance at a certain frequency [48]. This device act like a resonator at certain frequencies, hence their usage in biosensing platforms [45]. In order to enhance their sensitivity and improve on their detection limit, carbon nanomaterials CNTs, Graphene nano Ribbons (GNRs), and graphene, as well as Graphene oxide (GO) could be incorporated with this IDCs device [46]. Since this carbon nanomaterials are biologically compatible and suitable for the detection of small biomolecules due to their large surface areas.

Label-free diagnostics remain attractive, since they simplify sample preparation, decrease assay costs, and eliminate potential artefacts from label instability or perturbation of assay thermodynamics [49]. Barry et al in [49] demonstrated that, near-field microwave imaging (NFMI) can achieve noncontact, label-free detection of low surface coverage analyte species at sensitivities comparable to conventional fluorescence bioassays [49]. The main advantage of NFMI over other label-free detection methods is that it has outstanding sensitivity, thus removing a central obstacle to label-free diagnostics [49]. Similar to other label-free schemes, a significant disadvantage is its susceptibility to

nonspecific background [49]. In the absence of a label to enhance contrast between species of interest and other material, such as water or salt residue, a label-free technique requires stricter control over sample preparation and measurement [49]. The sensitivity level of the NFMI has shown that RF biosensing platforms detection techniques can approach if not exceed the sensitivity level of conventional fluorescence diagnostics scheme. As such RF biosensor can be design and implemented for several tailored applications.

Metamaterial has also find application in the designing of the sensing element of biosensors, Metamaterial was used to design an LC resonator in the form of an asymmetric split ring resonator (aSRR) based biosensor for the detection of stress biomarker in the microwave region [50]. The results indicate a device sensitivity up to 1ng/mL and as low as 0.26ng/ml. The advantage of using a metamaterial is because they possess sharp resonance peak in dispersion and this could be useful since they may indicate sensitivity increase of a sensor [50]. For rapid label free detection they may improve the performance of a biosensor at the desired frequencies [50]. The results for this work were quite interesting but they assumed that the inductive and capacitive component of the aSRR is small. More so, the simulation results slightly differ from that of the experimental results, it also has the demerit that the samples should be dried before usage and this could take time and effort thereby increasing the test time. The substrate of the aSRR based biosensor is lossy since it is copper with an outer coating of gold.

An RF biosensor based on coplanar waveguide (CPW) and distributed MEMS transmission lines (DMTL) was proposed in [51], this biosensor was used to detect the presence of E. coli bacterium cell, the result of this detection technique was successful, since the presence of E. coli was detected on both the CPW and the DMTL, but with an improve detection observed on the DMTL. However, the selectivity of this device is a point of concern since noticeable change in the measured parameters is dependent on the volume/quantity of the target molecule present. In addition, the result of this device is based on simulation which may not indicate the actual response when implemented. In the work of Chen, et al [52] cancer cell was dielectrically characterized with an RF

biosensor which makes use of microwave coplanar waveguide (CPW) transmission line at a frequency range of 40GHz. This is to ensure that dielectric sensitivity of cells is exposed to broader bandwidth. The cancer cell used in this case is the hepatoma G2 where its frequency dependent cell based dielectric parameters like microwave attenuation and dielectric constants were measured [52]. One disadvantage of the CPW is that it has a potential for lousy heat dissipation, also a lot of CAD program do not support it and its application is yet to be well understood by microwave designers [53]. This biosensor has a very low limit of sensitivity, its selectivity is also a major drawback. Gold (Au) was used to design its electrode owing to its biocompatibility and superb electrical properties but with inherent associated flaws.

A MEMS RF-integrated biosensor (MIB) was proposed to measure the pH and Brix (glucose concentration) in grapes using a microfabricated biosensor structures [54]. The device was designed to be a powerless and wireless communication device, where the changes in the tank oscillator circuit can be determined by using RF interrogation employing a passive technique which when compared with a standard pH curve for the functionalized sensitive substance can determine the changes in the pH value or brix and communicate these changes unto a network. The limitation to this sensor design which can also be made to include environmental data measurement like temperature and humidity is that it is quite difficult to correctly estimate the parasitic resistance in its integrated circuit design. A model of an RF circuit for a biosensing element (carbon nanotube) combined with an interdigital capacitor (IDC) was designed where the electrical properties of both the sensing element and the analyte was determined from an RF circuit model [45]. It has been discovered recently that, in order to construct an accurate RF equivalent circuit model, so as to enable better understanding of the resonant frequency variation as a function of biomolecular binding in the biosensor, the modelling approach should consider the resonant frequency behaviours of S11-parameter, S21 (S12) as well as the RF characteristics of the approach (IDC, CPW, microstrip) at high frequencies. The frequency shift upon biomolecular binding indicates that, the biosensing mechanism can be an excellent candidate for specific biomolecular sensing in the microwave region.

To better understand the electrical properties of the biosensing element that is responsible for the change in resonant frequency upon the addition of an analyte unto the sensing element (biomolecular binding), an accurate and reliable RF circuit model is necessary. If the circuit model is accurately constructed for the sensing element based biosensor, it electrical quantities can quantitatively be established to explain the cause of frequency shift [45]. In the sensing platform of [45], an RF equivalent circuit model for a biosensing element (carbon nanotube) at microwave frequency was presented. The biomolecular sensing element was investigated in terms of the self-resonant frequency (SRF) of an RF passive component (IDC), where it was established that the SRF shift of the sensing element is due to the changes in capacitance, which is in turn due to change in the biomolecular binding process [45]. A bio-detection technique and device based on RF electrical signal and MEMS was proposed, in order to study the effect of analyte (protein) on the RF characteristics of the device, a 50Ω transmission line, a series inductance device and a shunt capacitance device were design and fabricated as a coplanar waveguide (CPW) [43]. The RF parameters of interest were the phase shift, power loss and S-parameters. The changes observed upon the introduction of the analyte was clear and visible for the transmission line (since it has both capacitive and inductive components like a resonator hence their results are multiplied by the synergy effect) than those for capacitive and inductive devices that reported smaller changes in the interested RF parameters. The limitation is that, although copper (Cu) was replaced with Gold (Au), but the conductance loss of the biomolecule on the metal surface in the resonator has an effect on the result and as such, a means of controlling it should be devised, another issue is how many biomolecules can be immobilized and bounded on the device.

2.4 Material

The material used for the implementation of microstrip filter is of paramount importance since it is to serve as the base transduction material for the biosensor. Several materials like gold, graphene, carbon nanotubes (CNT), multiwall CNT just to mention a few, have been deployed for use as the sensing elements of sensors and biosensors. A diverse range of chemical and biochemical analytes have been detected using carbon materials as electrodes, or components of electrodes, in electrochemical assays. Remarkably, the rate

of electron transfer and analytical performance of these electrodes are vividly influenced by the structural nature of the carbon material itself. Considering carbon-based materials rich history in electrochemical sensing it is hardly surprising that graphene has become a focal point of electro-chemical research over recent years. Various functional carbon materials have been studied as electrodes for the detection of biological and chemical analytes in electrochemical assays [55]. The electroanalytical performance of these investigated materials is strongly influenced by the structural properties of the carbon itself which is a function of the density of electronic states as well as the edge plane sites obtainable on the surface [56].

To fabricate sensors and biosensors that are cheaper and compatible with disposable biosensor format, research on the viability, performance, and usage of the laser scribed Graphene (LSG) material has been on the rise to explore possible area of applications. Since the early 1980s laser ablation of polymers has been studied, the consequence of which has led to the scalable approach of producing and patterning porous graphene from commercial polymer film (polyimide) using CO2 infrared laser, the resulting laser induced graphene (LIG) exhibits high electrical conductivity and was deployed as a microsupercapacitor (MSC) [57]. In comparison to the conventional lithographic techniques, the laser-scribing technology is simpler, lower-cost, and higher throughput [58]. This has led to an inexpensive commercially available standard light scribe CD/DVD optical drive used to irradiate graphite oxide (GO) film with an infrared laser to reduced GO to LSG [59]. Graphene film was also obtained by reducing graphene oxide film in a light-scribe DVD burner to produce a graphene material [60]. Laser scribed graphene electrode was also used by Katie Griffith et al as an electrode in an electrochemical sensor [61]. All the performances and ease of tailored application as exhibited by LSG materials has made it a viable option for the fabrication of disposable sensing platforms and has opened a whole new opportunity for it to be deployed in many other sensing applications.

Nanomaterials, particularly carbon nanomaterials also have an important role to play in new developments in each of the biosensor size domain category. This significance stem from the fact that Nanomaterials can help address some of the key issues in the development of biosensors, such issues include: the design of biosensing interface so that

analyte of interest selectively interacts with the biosensing surface, the achievement of efficient transduction of the biological recognition event, the increase in the sensitivity and the selectivity of the biosensor and the improvement of response time in very sensitive systems[62]. More specific challenges include: making biosensor compatible with biological matrices, so that they can find application in complex biological samples even in vivo [62].

2.4.1 Materials Used in Biosensors

The strategy for biosensor enhancement and construction could be said to includes five features: the sensed or measured parameter and the matrix, the transducer working principle, the chemical/biochemical model, the field of application and, the technology and materials for the sensor fabrication [63]. Materials used for biosensors are generally classed as: materials for the electrode and transducer, materials for the substrate, materials for the immobilization of biological recognition elements and, the biological elements [64]. Materials used for the electrode and transducer are usually conductive materials, some of the most frequently used materials for this purpose may be included the following: metals (mercury, platinum, gold, silver and stainless steel), metal oxides (indium tin oxide, ITO), carbon-based materials (glassy carbon, graphite, carbon black and carbon fibre), new hybrid materials, and organic electroconductive polymers or salts. Boron-doped diamond is a special case of material because bare diamond is a non-conducting, allotropic form of carbon[65].

Recently the class of nanomaterials that has attracted investigation are metal oxides such as TiO_2, ZnO, Fe_2O_3, RuO_2, IrO_2 or various colloidal particles on various substrates, comprising conducting tin oxide glass, Si wafers, polymers, and Teflon [66]. One of the problems related to these materials is that it has been very difficult to control the agglomeration and aggregation. These impediments are created by the existence of strong particle to particle interaction involving various chemical bonds, such as ionic, hydrogen or strong dipole interactions. To overcome these problems, these interactions must be lessened to van der Waals forces or bonds that are easily controllable in an

appropriate media, this modification will improve the reactivity of the nanomaterials in many ways and, in consequence, enhance their conductivity [66]. For this reason, a surface modification of the nanoparticles is needed to effectively apply these nanomaterials for biosensor device development.

Advances in materials chemistry have greatly affected the design of analytical sensor and biosensor devices in the last two decades. Recent progress in biosensor technology involves interdisciplinary studies involving physics, chemistry and surface chemistry, biology, biochemistry, material science, nanotechnology, and computer science. To this end a rapid, cheap, and easy-to-use methods, biochemical sensors have emerged as a dynamic technique for qualitative and quantitative determination of diverse analytes, essential in many areas such as environmental, clinical, agricultural, food or military investigations [66]. When designing biosensors, it is essential to study and understand each section of this complex system as well as its limitations and all the factors that influence its unique performance. Despite a great deal of publications in the biosensor field, some aspects need further improvements and optimization; several of these could be tied to inadequate materials and insufficient understanding of the underlining mechanism. Since the properties and the type of material used are largely connected with the transducer and the transducer/detector interface, a considerable attention has been paid to the nature of the electrode material.

The varieties of the elements used as electrodes have led to variations in terms of sensitivity of the electrodes and the length of the detection time of the sensor. In consideration of these factors, the ideal electrodes are those with high sensitivity and fast response time. The rapid technological development of new electrode materials has expanded the range and classes of detectable compounds. An emerging area of research is the implementation of new materials for the development of a unique class of biosensors, biochips, nano sensors, and other transducers. Efforts are focused on discovering the ideal material to ensure optimal characteristics of the sensor system. In the construction of biosensors there are several requirements for selecting an electrode material: biocompatibility with the biological element, absence of diffusion barriers, stability with changes in temperature, pH, ionic strength, sufficient sensitivity, and

selectivity for the analyte of interest as well as ease of mass production. These materials should possess either the necessary functional groups needed for the attachment of biomolecules or they should be able to be easily functionalized [65, 66]. Some sensors require operation in harsh conditions and, in this case, materials with special mechanical and chemical resistance, almost inert are vital. The most important materials for chemical and biochemical sensors include organic polymers, sol-gel systems, semiconductors, and other various conducting composites. A few of these are discussed below.

Polymers were the first materials in sensor development for the purpose of increased sensitivity and selectivity [66]. Conducting electroactive polymers (CEPs) are the most used in advanced biosensors and are recognized for their biocompatibility, allowing the microfabrication of low cost and disposable devices [66, 67]. CEPs have been described and used for their remarkable sensing characteristics, by being able to be reversibly oxidized or reduced after applying an electrical potential [66]. Materials like Polyaniline (PAni), polypyrrole (PPy), polythiophenes (PTs) and their spin-offs have been of much interest for scientific applications [68].

In a neuron recording application, the polymer SU-8 was employed in the electrode fabrication to improve biocompatibility and to remove the tissue-electrode gap filled with a passivation layer [69]. Similarly, to anchor the biotinylated proteins and the Deoxyribonucleic acid (DNA), the Nitrilotriacetic acid (*NTA*) functionalized PPy has been coated on a Pt electrode. This reaction was proven to be as efficient as biotin-avidin reaction but avoiding the avidin layer [54].The immobilization of glucose oxidase (GOX) in a PPy matrix signifies the first biosensor comprising biomolecules trapped in an electropolymerized film [66]. In a separate but similar case, functionalized polymer films which represents another category of materials used in biosensor design, which are appropriate for enhancing their analytical characteristics. One of the most popular use of electro-functional polymers is in the development of new materials in the biosensors field. For instance, Oureghi et al. [70] developed an impedimetric immunosensor for group of a N-substituted PPy bearing cyano (CN) and the hydroxyl groups on the heavy chains of the Antibody (Ab). Another material kind is the polymeric sorbents with selectivity for a

distinct analyte or groups of similar analytes have been developed as biosensing materials obtained by molecular imprinting method [66]. This is a copolymerization process between monomers of desired functional groups and the target analyte, which acts like a molecular template. A practical approach based on polymer imprinted materials is the development of biosensors for the detection of the herbicides atrazine, which is based on conductimetric detection and it uses an atrazine selective polymeric matrix generated from triethylene glycol dimethacrylate and oligourethane acrylate while the 2,4-dichlorophenoxyacetic acid (2,4-D) one was prepared on a Zinc selenide (ZnSe) surface and reported to be able to detect 2,4-D in the ppb concentration range [66].

Sol-gel processes have long been used for the powderless processing of glasses and ceramics. Intermediate between glasses and polymers, sol-gel materials have opened new possibilities as biosensor material proving a versatile way for bio-immobilization. Thus, antibodies, DNA, Ribonucleic acid (RNA), antigens, plant and animal cells and bacteria have been attached on various supports using this method. The sol-gel technique is based on the ability to form a solid metal or semi-metal oxide via the aqueous processing of hydrolytically labile precursors, rather than by high temperature chemistry [66]. With rapid advances in sol-gel precursors, nanoengineering polymers, encapsulation protocols and fabrication methods, novel sol-gel nanocomposites have been developed during the past few years. In biosensors, this technique could result in development of novel strategies to generate advanced materials for the immobilization of biological receptors within silica, metal oxide, organosiloxane and hybrid sol-gel polymers [66]. Dong et al. synthesized a self-gelatinizable grafting copolymer of poly(vinyl alcohol) and 4-vinylpyridine (PVA-g-PVP) and hybridized this polymer into a silica sol or a titanium oxide generating inorganic-organic hybrid thin film composites [44, 71]. Based on this hybrid material, amperometric glucose and tyrosinase biosensors have been developed [71].

Other widely used organic biosensing materials are carbon and its derivatives graphene, carbon nanotubes (CNTs), and electrogenerated polymers. Carbon is one of the most common chemical elements and is used in a wide range of applications. Given the carbon electrochemical properties, several studies on the biosensor application have been

conducted. Carbon electrodes have been used in many forms. Their most common forms are carbon paste and glassy carbon, both of which have been widely used in biosensor applications [72]. The use of advanced electrochemical techniques, such as scanning electrochemical microscopy, electrochemical AFM, and spectro-electrochemistry, have widened our understanding of the interfacial properties of traditional carbon electrode materials [111]. Carbon paste electrodes were first introduced in the 1950s for analytical purposes, specifically in anodic polarography [112]. Carbon paste electrodes (CPE) have been extensively studied, characterized, and modified. Pravda et al. [73] conducted an experiment to determine dopamine, 3,4-dihydroxyphenylacetic acid, norepinephrine, and homovanillic acid, by the development of an amperometric biosensor with carbon paste electrode. The result showed that the biosensor response was fast and well reproducible with high sensitivity and linearity over the concentration range from 0.09 mM to 1mM. Glassy carbon electrodes have also been extensively characterized and customized to perform several types of tests. They have been employed as electrode material for the fabrication of sensors given the special configuration and orientation of glassy carbon surface. One of the earlier implementations of glassy carbon was when Sanz et al. [74] introduced a new tyrosinase biosensor based on glassy carbon electrodes to determine the bioelectrochemical polyphenols index in wines. Their biosensor was reported to have a longer lifespan of up to 18 days. However, glassy or carbon paste electrodes are disposable.

The first important group of nanomaterials with application in sensors and biosensors field is represented by the carbon nanotubes (CNTs) [114]. It is worth briefly adding that their nano-dimensions, surface chemistry and electronic properties make this material an ideal candidate for chemical and biochemical sensing. Since their discovery in 1991, they have been the target of numerous investigations as nanoscale building blocks for analytical devices [75]. The ability to control the particle size and morphology is of crucial importance in nanostructured materials for chemical sensors and biosensors for both fundamental and industrial applications. The ability of CNTs to promote the electron transfer reactions of NADH and hydrogen peroxide has been used for the development of dehydrogenase- and oxidase-based biosensors [75]. Carbon nanotube electrodes (CNTE)

have been widely used in electrochemical biosensors because of their exceptional chemical ability to bind to other materials, high electrical conductivity, and mechanical properties such as high electrocatalytic activity, large surface area, and the ability to alleviate surface fouling.

The CNT-modified electrodes shows higher performance because of the presence of oxygen groups on the CNT surface and also due to the small dimensions and electronic structure of CNTs, as a result Biomolecules (e.g., proteins and DNA) can also be easily adsorbed onto the surface of CNTs and can be attached directly to functional groups on CNTs [76]. The modification of electrode surfaces with CNTs or gold nanoparticles (AuNPs) is commonly applied to enhance the stability and the analytical performance of biosensors. As a result CNT-enzyme-based biosensors had lower limit of detection (LOD) values [76]. Applications of technology at the nanoscale (e.g., incorporating CNTs in biosensors) have increased over the last 20 years, and they represent one of the emergent areas of research. However, several challenges associated with it use at that scale need to be overcome before the implementation of CNTs in active biosensors becomes common practice, some of these challenges include; a cost effective method for separating different types of NTs, miniaturization of sensors, technological difficulty in fabrication and multi-analyte determinations. That is why graphene is gaining recognition by the day, because current studies have dissociated graphene from some of this demerit.

Carbon has been widely employed in most electrocatalysis and electroanalysis, since carbon nanotubes used as biosensors have shown remarkable performance, it has also shown excellent performance in its application in biofuel cells, polymer electrolyte membrane (PEM) fuel cells [77]. Chemical/biological sensors based on carbon nanotubes (CNTs) have already been extensively studied. However, the diversity associated with CNTs' structure and chirality may results in varied device characteristics, which could lead to device reliability issues[40]. The biosensor application of CNT is illustrated in the work of Zhang et al [78] where an ultra-sensitive and label free cancer marker biosensor was synthesized for the detection of Prostate Specific Antigen (PSA) in a wide detection range by using a suspended self-assembly of graphene composite. The result of this graphene-

based biosensor is compared to that of a carbon nanotube (CNT) based biosensor with the same design and fabrication conditions. In this work, the sensitivity of the suspended graphene was shown to be more than that of its unsuspended counterpart. The changes in the ‘‘normalised conductance’’ of the sensing material because of the lowering of its resistance was used to determine the concentration of the analyte of interest and the sensitivity of the suspended graphene. It is important to note that trapped charges at the interface between the unsuspended graphene and the substrate and in the substrate decrease the transport characteristics (electron Mobility) of a single layer unsuspended graphene. Their research has as a result highlighted that suspended graphene is highly sensitive than its unsuspended counterpart.

The sensitivity of CNT sensor manufactured under the same condition as the self-assembly graphene sensor above was compared when used as a cancer sensor. The results indicated that the CNT was able to detect a few levels of pg/ml concentration of PSA cancer marker which is less sensitive when compared to the graphene-based sensor whose detection limits were in the region of few fractions of fg/ml. The difference in the detection limits of these two sensors could be due to the inherent pink noise (Flicker *noise*, also known as 1/f *noise*) in the CNT, this noise fluctuation could be attributed to trapped charges in the antibodies or due to the presence of defects within the tube network [78]. It is also worthy of note that to highlight the fact that low frequency (<1KHz) noise are dominant in limiting the performance of nanodevices [78]. Graphene effectively screen charge fluctuations from external impurity charges due to the high quality of its crystal lattice and its two-dimensional honey comb structure, this screening effect could be the reason for the reduction of an electrical noise level exhibited by graphene [78].

Material selection should result from a process of comparing several material parameters, since they tend to be inter-related. For instance, a material that possesses a high dielectric constant enables miniaturized circuits; but, in the case of a power amplifier, it may lack the thermal conductivity to efficiently dissipate excess heat from the active circuitry. Additionally, a circuit material with dielectric constant that exhibits a broad frequency variation may fit a narrowband design but may not work well for broadband circuitry. A

wide range of naturally occurring and engineered materials are used in the construction of active and passive RF/microwave components and circuits. Whether those materials are part of the packages, the substrates, the printed-circuit boards (PCB), or even the thermal pathways for heat dissipation, they are essential to electronic circuits ranging from DC to optical wavelengths. In the semiconductor part of the RF/microwave industry, another set of materials supports the miniature devices and integrated circuits (ICs), including silicon, silicon carbide (SiC), gallium arsenide (GaAs), and gallium nitride (GaN) [79]. GaN, with its excellent high-frequency capabilities, has become one of the more popular semiconductor materials for RF/microwave device developers. Other materials occasionally used in RF/microwave applications are high-temperature-superconductor (HTS) materials, typically built around yttrium barium copper oxide (YBCO) or niobium materials [79] . Such materials can achieve required temperature levels without a cryocooler and can provide extremely low-loss performance, such as for bandpass filters with negligible passband insertion loss and a fraction of the size of conventional room-temperature filters [79].

The substrate supporting the circuit is a dielectric with metallisation on either side. The circuit pattern is printed on one or both sides by photolithographic process. As opposed to the low frequency circuits the dielectric substrate do not just support the circuit pattern but also actively contributes to the functioning of the circuit. The dielectric constant and thickness of the substrate decide the impedance of the transmission lines. For any given dielectric substrate, the width of the conductor pattern decides the impedance of the transmission line which is typically 50 ohms. Tight tolerances are demanded on the uniformity of the dielectric constant (The dielectric constant is a measure of a material's capability to store charge, as in a capacitor fabricated on that material. Higher dielectric constants denote greater charge-storing capacity for a given voltage) and thickness over the substrate area to achieve the required circuit performance. The basic requirements for the substrate materials are [80]: High DC resistance, easy machinability for sizing and holes making, provide smooth surface for metallization, dimensional stability over the temperature of the operation, low dielectric loss, stable electrical properties such as

dielectric constant, high thermal conductivity for high power applications, and uniformity of these properties over the substrate area.

2.4.2 Graphene Based Biosensor

Graphene material which is a 2-dimentional layer material of SP2 bonded carbon [81], is made up of a single layer of carbon atoms bonded together in a honeycomb lattice structure and has attracted strong scientific and technological interest in recent years due to its unique physicochemical properties such as excellent electrical and mechanical conductivity, high surface area, electronic, optical, thermal and properties, as well as high mechanical strength and ease of functionalization [77]. This one atom thick material, has a unique chemical structure and excellent properties that made it suitable for several engineering application [81]. Graphene indicates strong adsorptive capability tendencies since every atom in a graphene sheet is a surface atom, molecular interaction and electron transport through graphene can be highly sensitive to adsorbed molecules [82]. This means all the atoms can take part in the reaction, therefore electron transport through it can be highly sensitive to adsorbed molecules [83]. This phenomenon has enable the fabrication of sorption based sensors capable of detecting trace levels of vapour using conventional low power electronics [83].

Being very stable material with remarkable ranges of physicochemical properties which is why it can be deployed in the design of many different types of sensors, it is also known to offer the best surface to volume ratio, since every of its atom is a surface atom, which signifies that every graphene atom is a possible agent for reactive species [84]. The result of its interaction could effect changes in the bonding forces which would to a reasonable level cause a disturbance in the electronic system of the pure graphene. These changes can be exploited to enable the usage of graphene to detect chemical or gases [85]. It fast response rate (sensitivity) to surface charge or ion density makes it suitable to be applied in solution-gated, ultra-low noise, ultra-fast biosensors and chemical sensors [84]. The carrier density of a graphene conductor is easily modified by the application of an electric field this lend it usage as an electric field sensor [9]. Base on the fact that it is a mono layer

material, which means that, it can be taken very close to the charge source where the field is strongest to enable measurement that would give a relatively better signal-to-noise ratio and allow for better special resolution as compared to other systems [84].

Graphene has shown immense performance, since graphene based electrode displays better performance when used in the area of electrocatalytic activity and microscopic scale conductivity than carbon nanotubes based ones [77]. These has shown that, since carbon nanotubes can be used in electrochemical analysis then graphene also has similar opportunities since it is the basic building block for graphite which is an allotrope of carbon. As aforesaid, carbon materials application in electrocatalysis and electroanalysis is broad, hence, the potential for some carbon materials to find application in electrochemistry lie in its basic electrochemical properties, which should first be examine to ascertain several essential parameters of such carbon materials (electrodes) like; electrochemical potential window (EPW), Electron transfer rate, and Redox potential [86]. Graphene shows a wide EPW of Ca. 2.5v in 0.1MPBS (pH 7.0) which can be comparable to that of graphite glassy carbon (GC) and even electrodes like boron doped diamond and it charge transfer resistance as established by AC impedance spectra is far less than graphite and GC electrodes [87]. The electron transfer behavioural study of graphene using cyclic voltammetry (CV) of redox pairs like [Fe(CN)6]3-/4- and [Ru(NH3)6]3+/2+ was reported to show a clearly visible redox peak [86, 88]. It showed that both cathodic and anodic peak currents in CV are linear with the square root of the scan rate, as such highlighting that the redox processes on graphene base electrode are predominantly diffusion controlled thus indicating the electrochemistry of graphene [88].

Another important characteristic of graphene base electrode that could lead to it high selectivity and sensitivity is its structural defects. Since chemically reduced graphene oxide is endowed with structural defects and functional groups (oxygen containing groups like carboxylic group which increase the activity of graphene) [89-91]. This is as a result of the fact that the two graphitic planes (edge and basal planes) of the structured layer of graphene shows different electrochemical properties, as it was observed that the kinetics of the electrons at the edge plane is higher than that at the basal plane [77]. Hence the

high density edge-plane-like defective plane or site on graphene is endowed with high rate of electron transfer and could provide many active sites for electron transfer to biological species [92]. The selectivity/sensitivity of the edge plane can also be attributed to functional groups such as those containing oxygen groups like carboxylic group which plays an important role in the improved activity of graphene.

The level of sensitivity in the lower limit range as displayed by graphene is due to it superb electronic properties owing to its delocalized pie-bond structure and zero band gap which is extremely sensitive to molecular doping (bonding with other metals) [93]. Delocalization gives it the advantage of spreading electron density over a large area and creates stability for the molecule of the material. This creates charge distribution and makes the material more conductive, and also ensures that a stable product is formed in terms of a reaction [94]. Charge transfer as a result of interaction of molecules with graphene causes a change in its Dirac point and therefore it resistance [93]. This high electron mobility of graphene enables it to be used for high frequency application [95]. To make graphene more active and hydrophilic, oxygenate groups like carbonyl and carboxyl groups are attached to the graphene which would yield graphene oxide. Other chemicals such as hydrogenated (CH) or amines (NH2) could be attached to it to make it chemically reactive [96]. The low capacitance it exhibits makes it suitable in biosensor and /or chemical sensors fabrication because of its low signal to noise ratio [96].

Graphene clearly reveals itself in a pronounce ambipolar electric field effect such that charge carriers can be tuned continuously between electron and holes in concentration n as high as 103cm-2 and their mobility μ can exceed 15,000 cm2v-1s-1 even under ambient conditions[97]. In graphene, mobility remains high even at high n (1012cm2) in both electrically and chemically doped device, which translate to ballistic transport on the sub-micrometre scale (currently up to ≈ 0.3μm at 300k) [97]. A further indicator of its extreme electronic quality which is an equally important reason for interest in graphene is the particular unique nature of its charge carriers, they mimic relativistic particles and are more easily and naturally described starting with Dirac equations rather than Schrödinger equation (which is usually being sufficient for describing electronic properties in materials

in condense matter physics) [97]. These quasi-particles that are accurately described by (2+1) dimension Dirac equation with an effective speed of light Vf ≅106ms-1 are called massless Dirac fermions [97]. Graphene potential for electronics is justified owing to its highly mobile charge carriers. The truly excellent feature of graphene is that mobility remains high even at high electric field induced concentration, and seems to be slightly affected by chemical doping and this resulted into ballistic transport on a sub-micrometre scale at 300k [97].

The unique electrochemical response of graphene to target molecules are, from its planar geometric structure and it special electronic property [81]. Graphene and graphene based materials are promising materials for the production of state-of-the-art nanoscale sensors or biosensors [81]. Their excellent conductivity and large surface areas make graphene based sensors and biosensors to have high accuracy, rapidness, high sensitivity and selectivity, low detection limit and long term stability [81]. They have attracted immense scientific and technological interest recently, and has shown great promise in many areas of application like in electronics, energy storage and conversion, fuel cells, solar cells, batteries as well as biotechnology and bioscience [77]. Graphene including pristine graphene and it analogues of graphene oxide and reduced graphene oxide is revolutionizing the way we design high performance devices particularly in the areas of environmental remediation, biosensing and energy conversion and storage [98]. Several devices have been produced using this material like the work of Huang, et al [99] who developed a fast label free high sensitive and selective graphene based biosensor for the detection of E.coli bacteria, which achieved a detection limit as low as 10 cfu/mL. In their work they demonstrated a Nanoelectronics sensor based on antibody modified chemical vapour deposition grown graphene to detect the bacteria (E.coli) [99]. The field effect transistor (FET) designed Nanoelectronics biosensor was used for the rapid and label free detection of the bacteria by measuring the change in conductance as the concentration of the bacteria increases.

Similarly, In the work of Wu et al [100], a Surface Plasmon Resonance (SPR) based graphene biosensor was postulated. This biosensor uses attenuated total reflection (ATR)

method to detect a change in refractive index near the sensor surface, which is due to the adsorption of biomolecules. Surface Plasmon Polariton (SPP) is a perpendicularly confined evanescence electromagnetic wave which propagate at the interface between a metal and a dielectric (i.e. the sensing medium) [101]. The change in the concentration of biomolecules in the sensing medium results in a local change in the refractive index (RI) near the metal surface , this change in RI will lead to a change in the propagation constant of the SPP which can be measured by ATR method [101]. The results showed several times improved sensitivity than the traditional one. The specificity of the sensor is questionable, and this work is only a proof of concept as the result is mainly from simulation. The work showed the biocompatibility property of graphene hence its usage as a biorecognition element.

Changes in Haemoglobin (Hb) concentration in blood can lead to several diseases and can even result to death [102]. Hb is the most important part of blood responsible for transporting O2 throughout the circulatory system [102]. Therefore, accurate determination of Hb content in blood is medically essential, that is why in their work Liu et al [103] functionalized graphene nanosheets (PDDA-G) was synthesized with poly (diallyl-dimethylammonium chloride) (PDDA) and used to Combine with room temperature ionic liquid (RTIL). The resulting RTIL/PDDA-G composite Showed enhanced ability for the immobilization of Hb to realize its direct electrochemistry. Their biosensing scheme displayed a fast-direct electron transfer of Hb. This approach has highlighted the need for the functionalization of graphene sheets with good biocompatibility and solubility, thereby establishing a novel and promising platform for the study of the biological application of graphene [103].

In univariate calibrations, where the concentration of a single analyte of interest is predicted from a single instrumental signal, the quantification of figures of merit is rather simple, well known and well defined [76], whereas, in multivariate calibrations, the complexity of data makes the evaluation of figures of merit much more difficult [76]. This is such an important point to note in the design of a biosensor of choice. For biosensors the figures of merit may include but not limited to concepts that relates to the methods,

to the analyte (e.g. sensitivity, selectivity, LOD and signal-to-noise ratio (SNR)) and to concepts pertaining to the final results (e.g. traceability, uncertainty, representativity) [76]. For this work the figure of merit that are of interest are those related to the methods and the analytes. However, to show the reliability of the device those relating to the results would also be looked at. Improvements in sensitivity and selectivity of the sensors have always been of paramount interest, and chemical modifications of the electrode surface (e.g., deposition of nanoparticles (NPs) and/or nanotubes (NTs) and the incorporation of enzymes in transduction system) have been identified as excellent opportunities for improvements [104].

2.5 Summary

Based on the technical background and literature review of the research work done on biosensors thus far, the following challenges have been identified:

Typically, the main goal for virtually all the current work is to develop a portable and an improved biosensing platform that can effectively and efficiently produce accurate test results in the shortest time possible, with a very low sample volume that is label free and require no sample pre-treatment. In most cases some of these goals have not been satisfactorily achieved.

A cost-effective biosensing platform that possess an extremely low limit of detection (sensitivity) and selectively detect the concentration of the analyte of interest (selectivity) so as to meet the current demand for a quick, accurate and reliable test result required.

The utilisation of systems and materials that possess minimal loss at microwave and radio frequency, leading to reliable test results, needed for the effective, timely and economic management of critical biological systems, biological processes, and other fields where their application may be deemed necessary.

In the light of these challenges identified, this research work aim is to investigate an opportunity to combine RF biosensor with graphene and to explore the potential of this approach, this will be investigated by designing and implementing an RF biosensor transducer that is portable and possesses considerably high sensitivity and selectivity and requires no sample pre-treatment for the detection of the quantity of the biomarker of interest. Quartz is a hard substrate as stated above, and hard substrates though do not lend themselves to easy mechanical working. However due to their smooth surface for metallization, dimensional stability over the temperature of the operation, stable electrical properties such as dielectric constant, high thermal conductivity for high power applications, and uniformity of these properties over the substrate area, as well as excellent mechanical and electrical properties, Quartz is a suitable substrate in realizing the proposed RF sensing platform. In addition, this material is cheap and is found to show low dielectric loss at microwave frequency.

The research will also look at the utilisation of different filter systems and types of materials (Quartz, Graphene, RGO, and Gold) used for the implementation of these filters in a bid to employing the most effective means and material of achieving a sensitive and selective sensing device for biosensor implementation.

Chapter 3. System Design and Mathematical formulation

3.1 Introduction

It is important to begin this chapter with a background on the under-laying principle behind the reason for not utilizing lumped elements for the implementation of filters at frequencies higher than 800MHz. With respect to the intended purpose for the design of filter in this work, lumped element filter is not suitable, one of the chief reasons is that the filter is intended to be deployed as the sensing (transduction section of the biosensor) medium of the proposed biosensor, and in order to perform this task it designs and make up should be such that will allow easy contact or access with the introduced sample(s) for testing. This primary function of the sensing element means that it has to be planar in structure and should be designed in such a way that will make its functionalization easy to achieve so as to improve its efficacy for the intended biosensing application. The second reason is that, with planar structures there is room to vary the materials used for their fabrication, enabling for the testing of several materials whose properties are apt for the intended biological application. Below are some of the under-laying reasons for planar structures utilisation as well as the size and geometry of the filter, this chapter also discusses the volume and concentration of the functionalization protocol . The following abbreviation were used in this chapter:

$\omega =$ The frequency at which the attenuation is desired, $\omega_c =$ The cut-off frequency of the filter.

Figure 3.1 below illustrates the systematic schematic diagram for the biosensor design. The design phase was accomplished in chapter 3, while in chapter 4 the fabrication and test of the devices were presented, in chapter 5 the full detail of the device characterisation was illustrated.

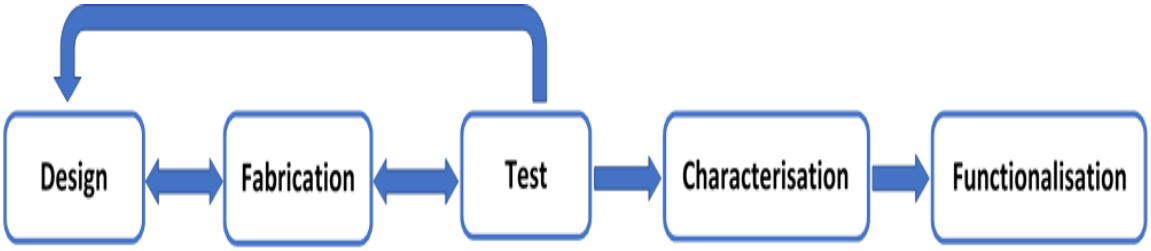

Figure 3. 1 Schematic diagram for the biosensor design

3.2 Skin Effect

At low frequencies, a conductor utilizes all its cross-sectional areas. But as frequency increases, though there will be an increase in magnetic field at the center of the conductor, this field present an impedance to the charge carriers, thereby decreasing the current density at the center of the conductor and increasing the current density around the perimeter of the conductor since impedance to the current density is less. This phenomenon is called skin effect and it occurs in all conductors including leads of resistors, capacitors, and inductors. The depth at which this current flow in a conductor because of the frequency of the signal is called skin depth. Skin depth is the depth into the conductor at which the charge carrier density falls to 1/e or 37% of its value along the surface. This is dependent on frequency of the signal, the permeability of the conductor and its conductivity, as such different conductors have their distinct skin depth. This effect results in essentially a decrease in the cross-sectional area of the conductor and increases its net resistance. The effect of skin depth on the leads of components is also one of the reasons why lumped elements was not employed in the design of high frequency filter.

3.3 Parasitic Effect of Lump Elements

Magnetic field exist in any medium surrounding a current carrying conductor. If the current flowing is an alternating current (AC) then the field is alternately expanding and contracting, this action will produce a voltage on the wire which will oppose any current flow. This opposition to current flow is called self-inductance. Any material that possesses this quality is called an inductor. This quality becomes pronounced as we go higher in frequency. The inductance in a straight wire depends on its length and diameter [14]. The

concept of inductance is important since all conductors at Radio Frequencies (RF) (including hook-up wires, components lead etc.) exhibits the property of inductance. With respect to the above stated phenomena let's look at what traditional components (resistor, inductor, and capacitor) used for the fabrication of circuits will appear to be in the RF frequency range.

The Resistor equivalent circuit at RF is made up R which is the resistor value itself, L is the lead inductance, while C is the combination of parasitic capacitance (it varies from resistor to resistor and their structure, for instance carbon composition resistors contains tightly packed particulate of carbon granules and between each pairs of granules there is a parasitic capacitor their aggregate results in C) [14]. The carbon composition resistors are very poor at high frequencies, while the wire wound ones are also not good at RF frequencies because they have varying impedances over various frequencies in RF[14]. The metal film resistors produce some of the best characteristics over ranges of frequencies, their impedances tend to reduce with frequencies above say 10MHz, at high frequencies say RF and with low value (say under 50Ω) the lead inductance and the skin effect might become pronounced. The current trend of resistor technology is to greatly reduce or remove the stray (parasitic) reactance associated with resistors. This has brought about the development of thin film resistors. They are mainly produced on a substrate of Alumina or Beryllia and they offer negligible stray reactance at frequencies ranging from DC to 2GHz[14].

The equivalent circuit of a capacitor at RF is made up C being the capacitance of the capacitor, Rs is the heat dissipation loss, Rp is the insulation resistance and L is the inductance of the leads and plates[14]. As the frequency of operation increases the lead inductance becomes pronounced and important. At certain resonant frequency this inductance becomes series resonance with the capacitor and above this frequency the capacitor behaves like an inductor[14]. The formula for capacitive reactance is given as Xc $=1/W_c$, this might show that larger C value would have less reactance than smaller C values at given frequency, the opposite may be true at RF frequencies. This is something that must be given consideration to when designing circuits at frequencies above 100MHz.

Inductors are so designed in such a manner as to increase the magnetic flux linkage between the turns of the coil. This increase flux linkage increases the inductance of the wire beyond what it would have been if it were not wound. Inductors are extensively employed for RF designs like in filters, resonant circuits, phase shift and delay networks, and are also used as RF chokes to prevent or reduce the flow of RF energy along a certain path.

The equivalent circuit of a typical inductor at RF is made up of Rs as the series resistance owing to the resistance of the conducting element of the wire, L is the inductance value of the inductor, while Cd is the aggregated distributed capacitance which is brought about by the individual distributed capacitance that resulted from the adjacent pair of coil conductors separated by air with a potential difference between the two conductors [14]. At low frequencies the inductor reactance is equal to that of an ideal inductor, however, as the frequency increases the reactance rapidly increases and depart this ideal value until it reaches a peak at the inductor's parallel resonant frequency, above which the inductor's reactance begins to drop with increase in frequency and begins to look like a capacitor[14]. The ratio of the inductor's reactance to its series resistance (X/Rs) is often used as a measure of its quality, the larger this value the better the inductor, this ratio is often regarded as the quality factor and sometimes Q. These lump element components are the primary components used in the designing of filter circuit of all kinds which finds applications in various field of electronics engineering, all these inconsistencies in quantities associated with these traditional lumped is militating against their deployment for use in the design of filters at microwave and radio frequency. Let us look at a simple filter circuit and see what their structures are like.

3.4 Filter Circuit

A filter is an electronic system that provides perfect transmission of signal with frequencies in certain passband region and provides infinite attenuation in the stopband regions. Such perfect characteristics are not attainable, and the aim of filter design is to

approximate the ideal requirements to within an acceptable tolerance. Filters are used in all frequency ranges and are categorized into three main groups:

- Low-pass filter (LPF) that transmit all signals between DC and some upper limit ω_c and attenuate all signals with frequencies above ω_c.
- High-pass filter (HPF) that pass all signal with frequencies above the cut-off value ω_c and reject signal with frequencies below ω_c.
- Band-pass filter (BPF) that passes signal with frequencies in the range of ω_1 to ω_2 and reject frequencies outside this range. The opposite of band-pass filter is the band-rejection or band-stop filter.

In each of these categories the filter can be further divided into active and passive type[14, 105]. The output power of passive filter will always be less than the input power while active filter allows power gain[105]. This work will only discuss the passive filter. The characteristic of a passive filter can be described using the transfer function approach or the attenuation function approach. In filter circuits used in low frequency, the transfer function ($H(\omega)$) of equation 3.1 depiction is used, while at microwave or RF frequency the attenuation function of equation 3.2 description is preferred [105], in both cases V_1 is the input while V_2 is the output voltage. Figure 3.1a to 3.1c illustrates the characteristics of the three filter categories. Note that the characteristics shown are for passive filter.

$$H(\omega) = \frac{V_2(\omega)}{V_1(\omega)} \tag{3.1}$$

$$Attenuation = -20Log_{10}\left(\left|\frac{V_2(\omega)}{V_1(\omega)}\right|\right) \tag{3.2}$$

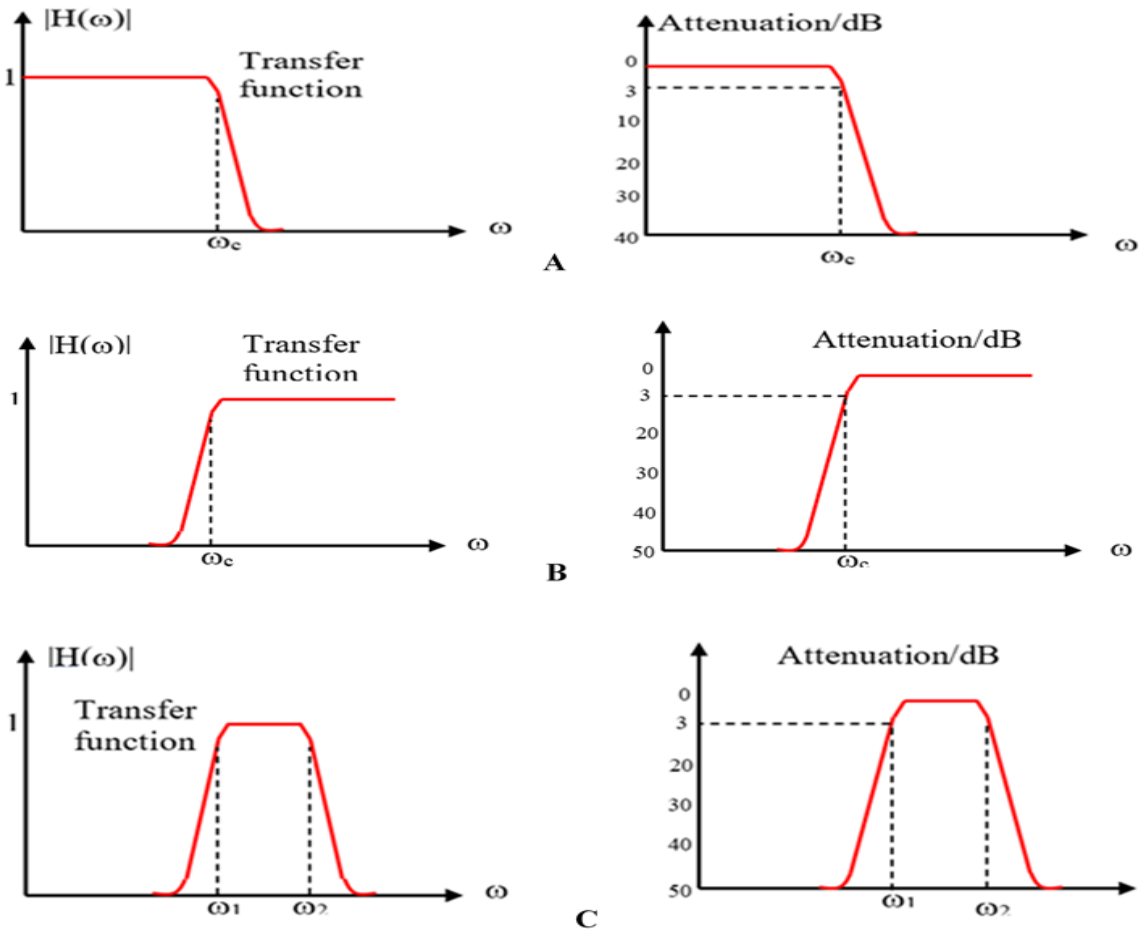

Figure 3. 2 Frequency responses for A) Low-pass filter, B) High-pass filter, C) Band-pass filter.

3.4.1 Realization of Filters

At frequency below 1.0 GHz, filters are usually realized using lumped elements such as resistors, inductors, and capacitors. For active filters, operational amplifier is occasionally employed. There are essentially two low-frequency filter syntheses methods commonly used. These are known as the Image Parameter Method (IPM) and the Insertion Loss Method (ILM)[13, 106]. The IPM provides a comparatively simple filter design approach but has the drawback that an arbitrary frequency response cannot be incorporated into the design, and also this approach divides a filter into a cascade of two-port networks, and attempt to come up with the schematic of each two-port, such that when combined, gives the required frequency response [106]. The IL technique begins with a complete specification of a physically realizable frequency characteristic, and from this a suitable filter schematic is synthesized. In this work the ILM will be concentrate on, whose design

procedure is based on the attenuation response or insertion loss of a chosen filter type. The insertion loss of a n two-port network is given by [13]:

$$P_{IL} = \frac{Power\ available\ from\ Source}{Power\ delivered\ to\ load} = \frac{P_{in}}{P_{Load}} = \frac{1}{1-|\Gamma(\omega)|^2} \quad (3.3)$$

where Γ is the reflection coefficient.

The design of a filter using the IL method typically begins by designing a normalized filter. The normalized filter for a start is a low-pass filter with source and load resistance of 1Ω and cut-off frequency of 1 Radian/s. Figure 3.2 shows the characteristics, impedance transformation and frequency scaling are then applied to de-normalize the Low Pass Prototype (LPP) and synthesize different type of filters with different cut-off frequencies.

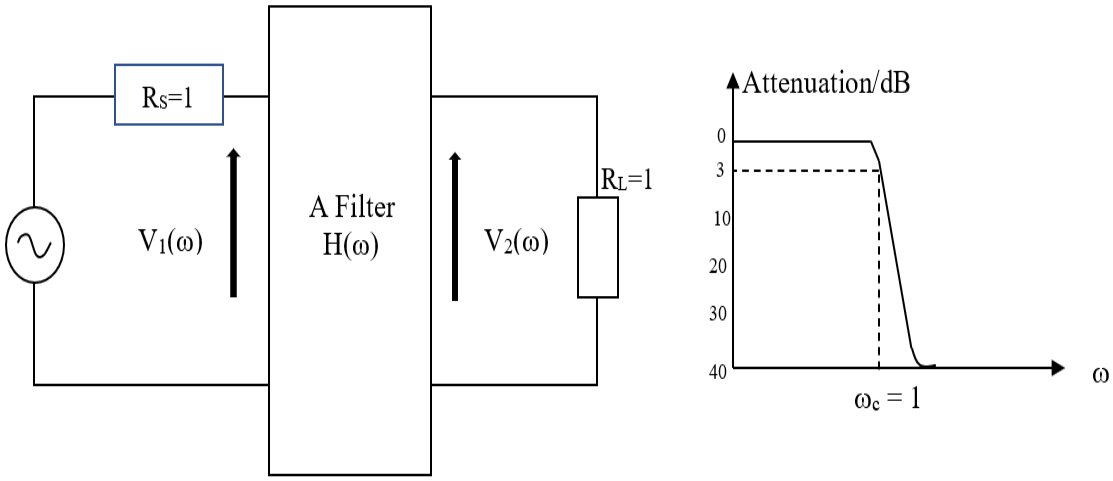

Figure 3. 3 A normalized LPP filter network with unity cut-off frequency (1Radian/s).

LPP filters have the form shown in Figure 3.3 (An alternative network where the position of inductor and capacitor is interchanged is also applicable). The network consists of reactive elements forming a ladder, usually known as a ladder network. The order of the network corresponds to the number of reactive elements. Impedance transformation and frequency scaling are then applied to transform the network to non-unity cut-off frequency, non-unity source/load resistance and to other types of filters such as high-pass, band-pass or band-stop.

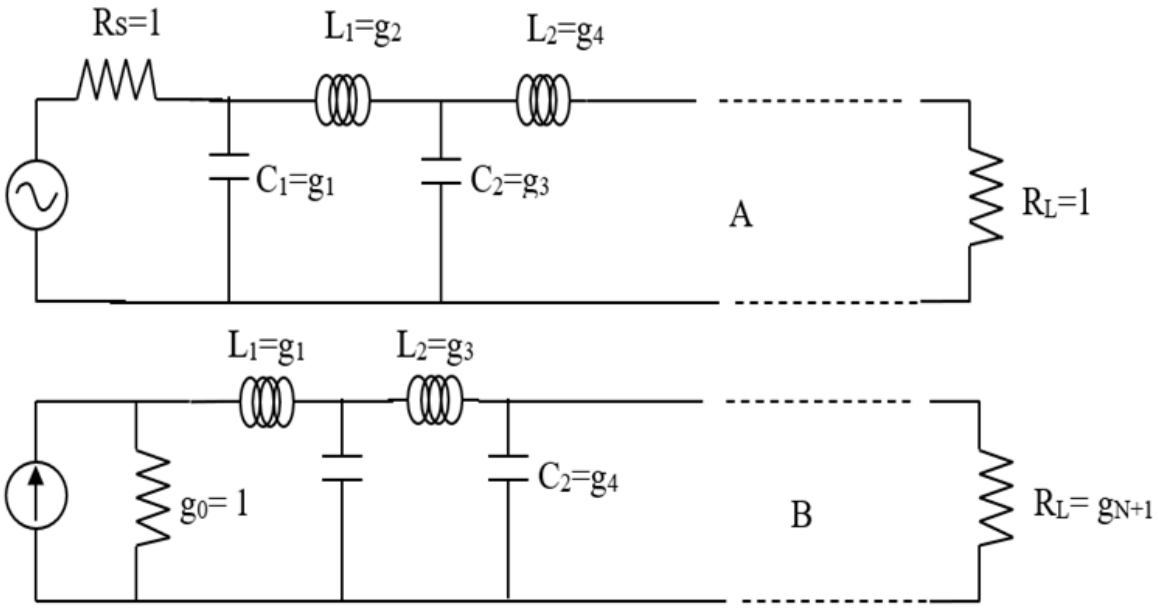

Figure 3. 4 LC elements prototype circuit A) Low-pass filter, B) High-pass filter

3.4.2 Low-Pass Prototype Filter Design Using Lumped Elements

There are several standard approaches used for the designing of normalized Low-Pass Prototype (LPP) that approximate an ideal low-pass filter response with cut-off frequency of unity. Among the popular methods are [13, 14, 107]: Maximally flat or Butterworth function, Equal ripple or Chebyshev approach, and Bessel. The basic idea is to approximate the ideal amplitude response of the filter such as Butterworth, Chebyshev, Bessel, and other orthogonal polynomial functions. A comparison of approximating the LPP amplitude response with Butterworth, Bessel and Chebyshev polynomials is illustrated in Figure 3.4 [108].

The Butterworth low pass filter response has the flattest pass band response available with no ripples, and it is a medium Q filter, this means that the stop band attenuation steepness is not as good as some filters but better than some. It is most often referred to as the “middle of the road design”. The attenuation of this filter is given by [14]:

$$A_{dB} = 10\log\left(1 + \frac{\omega}{\omega_c}\right)^{2n} \tag{3.4}$$

The element values for the normalized Butterworth LPF operating between 1Ω terminations can be determined by[14]:

$$A_k = 2\sin\frac{(2K-1)\pi}{2n} \tag{3.5}$$

The Bessel filter initial stop band attenuation is very poor and can be approximated by the following equation below[14]:

$$A_{dB} = 3\left(\frac{\omega}{\omega_c}\right)^2 \tag{3.6}$$

The expression in equation 3.5 is not accurate above a $\frac{\omega}{\omega_c}$ that is more than 2. For values of the ratio $\frac{\omega}{\omega_c}$ greater than 2, a straight-line estimation of 6 dB per octave per element can then be made.

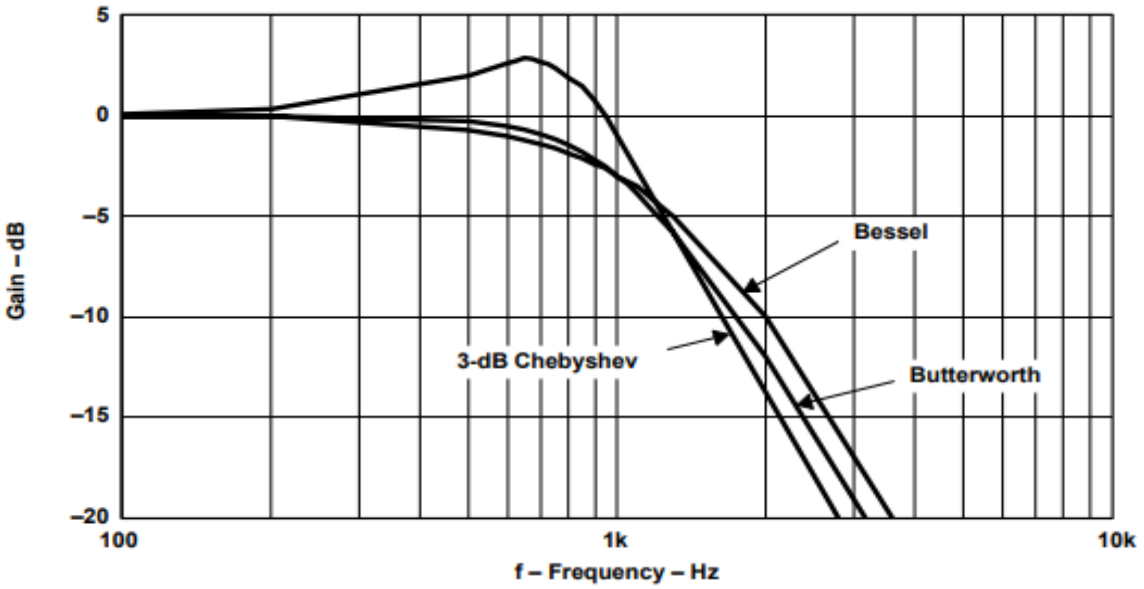

Figure 3. 5 Second order (N=2) response of Butterworth, Chebyshev, and Bessel filters [14].

The need to strike a balance between a filter which possesses a desired passband ripple which could be of importance when deployed as a sensor for sensing biological samples in microns and the stop band steep attenuation which could lead to sharp resonant peak of the filter has led to the choice of the Chebyshev filter as the filter of choice in the design of the microstrip filter element.

3.4.3 The Chebyshev Filter

This filter is often referred to as equal-ripple filter that is mainly desired for used when ripple can be allowed in its pass band. The attenuation of a Chebyshev filter can be determined by the following expression[14];

$$A_{dB} = 10\log\left(1 + \varepsilon^2 C^2{}_n\left(\frac{\omega}{\omega_c}\right)'\right) \quad (3.7)$$

Where; $C^2{}_n\left(\frac{\omega}{\omega_c}\right)'$ = Chebyshev polynomial to the order n evaluated at $\left(\frac{\omega}{\omega_c}\right)'$,

$\varepsilon = \sqrt{((10)^{R_{dB}/10}) - 1}$, R_{dB}= pass band ripple in decibels and $\left(\frac{\omega}{\omega_c}\right)'$ can be found by defining a parameter B. But $B = \frac{1}{n}\left(\cosh^{-1}\left(\frac{1}{\varepsilon}\right)\right)$, n= the number of reactive elements in the filter (or the order of the filter), and ε= same as above, $\left(\frac{\omega}{\omega_c}\right)' = \left(\frac{\omega}{\omega_c}\right)\text{coshB}$, $\cosh x = 0.5(e^x + e^{-x})$.

A typical Chebyshev polynomial table for determining the attenuation of the filter response is shown in table 3.1 below [14];

Table 3. 1 Chebyshev Polynomials to the order n

n	Chebyshev Polynomial
1	$\left(\frac{\omega}{\omega_c}\right)$
2	$2\left(\frac{\omega}{\omega_c}\right)^2 - 1$
3	$4\left(\frac{\omega}{\omega_c}\right)^3 - 3\left(\frac{\omega}{\omega_c}\right)$
4	$8\left(\frac{\omega}{\omega_c}\right)^4 - 8\left(\frac{\omega}{\omega_c}\right)^2 + 1$
5	$16\left(\frac{\omega}{\omega_c}\right)^5 - 20\left(\frac{\omega}{\omega_c}\right)^3 + 5\left(\frac{\omega}{\omega_c}\right)$
6	$32\left(\frac{\omega}{\omega_c}\right)^6 - 48\left(\frac{\omega}{\omega_c}\right)^4 + 18\left(\frac{\omega}{\omega_c}\right)^2 - 1$
7	$64\left(\frac{\omega}{\omega_c}\right)^7 - 112\left(\frac{\omega}{\omega_c}\right)^5 + 58\left(\frac{\omega}{\omega_c}\right)^3 - 7\left(\frac{\omega}{\omega_c}\right)$

The equations above are used to derive families of attenuation curves, each categorised according to the quantity of ripple allowed in the filter passband. Several of these family of curves include 0.01dB, 0.1dB, 0.5dB, and 1.0-dB ripple[14]. Each curve begins at $\omega/\omega c$ =1, which is the normalized cut-off, or 3-dB frequency. The passband ripple is, however,

not shown. For this work the curve with the passband ripple of 1dB shown below was chosen for the design of the filter used, this was done for the reason stated above.

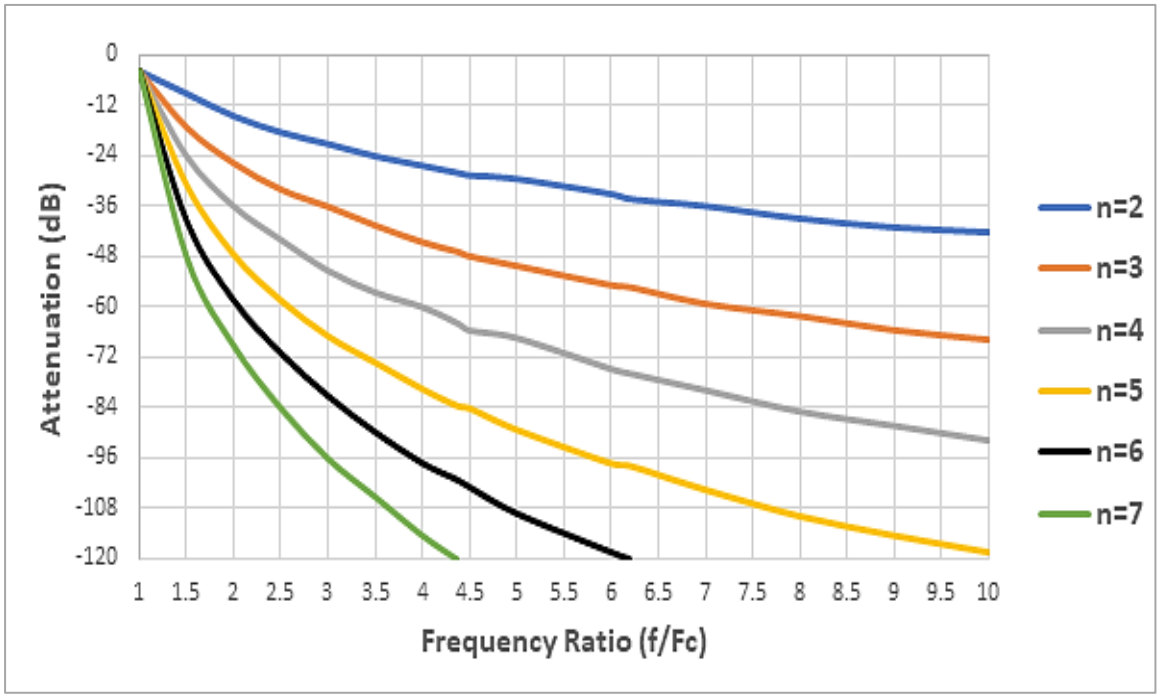

Figure 3. 6 Attenuation characteristics for a Chebyshev filter with 1 dB ripple [14]

To further highlight the pass band ripple of the Chebyshev lowpass filter with 1dB ripple, examples of a few of filter responses of figure 3.5 (the attenuation characteristics for a Chebyshev low pass filter with 1dB ripple) [14] are shown below, the simulated responses for n=3 in figure 3.6a, n=4 in figure 3.6b and n=5 shown in figure 3.6c clearly indicate that the number of passband peaks is related to the filter order, and also that the number of peaks increases as the number of active elements of the filter increases. In all the cases it was also observed that the passband ripple between peak to peak of the response corresponds to the 1dB as the attenuation characteristics stipulates in figure 3.5.

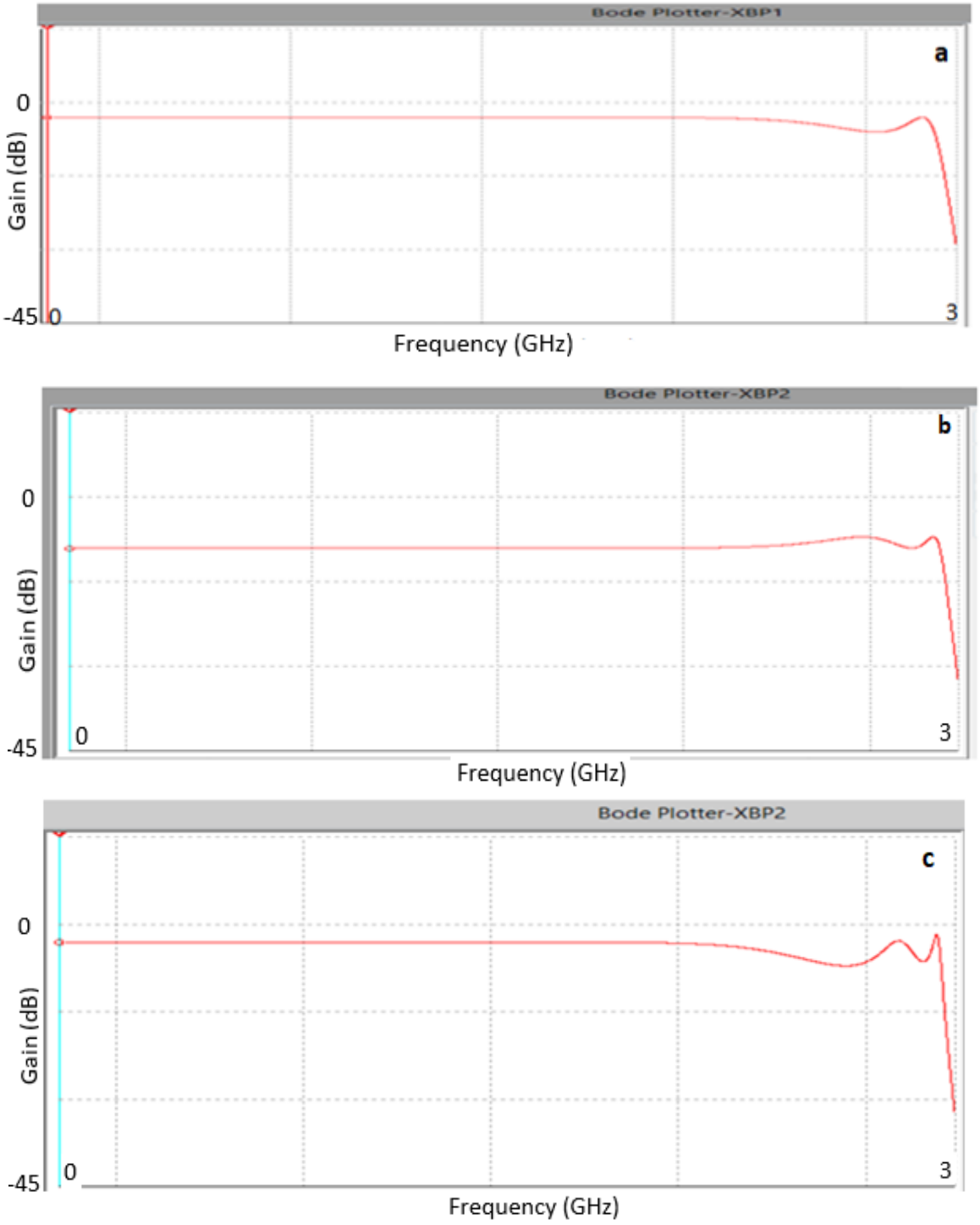

Figure 3. 7 The Chebyshev Lowpass filter response a) for n=3, b) for n=4, c) for n=5

3.4.4 Filter Transformations

The LPF prototypes discussed above were normalized designs having the source impedance *Rs* = 1Ω and the cut-off frequency of ωc = 1 rad/sec. These designs can be scaled in terms of impedance and frequency, and converted to give high-pass, bandpass,

or bandstop filter characteristics. On the whole, the specific desired filter design can be obtained base on certain interested characteristics particular to a filter type that best suits the intended application. Using the above stated techniques in filter design will yield a prototype filter which still needs to be scaled, to enable its implementation with values of reactive elements that can be designed or obtained for use that ensures the expected required results of the filter is obtained. To convert this prototype filter to the reactive element filter, some frequency and impedance scaling needs to be done and this is explained below.

3.4.5 Frequency and Impedance Scaling for Low pass Filter

In the prototype design as shown above, the source and load resistances are unity (only for the exception of equal-ripple filters with even *N*, which have non unity load resistance). Thus, after obtaining the prototype values from tables, the next thing is to convert these normalized values into actual components values to be used to obtain the lowpass filter design. In Impedance scaling however, a source resistance of R_0 (usually 50Ω) can be obtained by multiplying all the impedances of the obtained prototype design by R_0 [13].This can be shown in the equations below where the items on the left hand of the equations denote the impedance scaled quantities, as such the new filter impedance scaled components values are given by [13, 14];

$$\mathrm{L} = R_0 L_n \tag{3.8}$$

$$\mathrm{C} = \frac{C_n}{R_0} \tag{3.9}$$

$$R_s = R_0 \tag{3.10}$$

$$R_L = R_0 R_l \tag{3.11}$$

Where L_n, C_n, and R_l are the normalized prototype components values.

More so, it is important to know that the cut-off frequency of the prototype circuit is 0.159Hz (ω =1 rad/sec) and this frequency operates between a source and a load resistance that are normalised so that R_L=1Ω [14]. To transform the cut-off frequency of a low-pass prototype from unity to ωc entails that the frequency dependence of the filter is scaled by the factor $1/\omega_c$ (Frequency scaling for low-pass filters), which is accomplished

by replacing ω by ω/ω_c, where ω_c is the cut-off frequency, this cut-off occurs when $\omega/\omega c = 1$, or $\omega = \omega_c$ [13]. These new element values are determined by applying the substitution to the series reactance, $j\omega L$, and shunt the susceptance, $j\omega C$, of the prototype filter[13]. Hence:

$$jX_n = j\frac{\omega}{\omega_c}L_n = j\omega L_n \quad (3.12)$$

$$jB_n = j\frac{\omega}{\omega_c}C_n = j\omega C_n \quad (3.13)$$

With the frequency scaling this indicate that the new element values are given as:

$$\mathrm{L} = \frac{L_n}{\omega_c} \quad (3.14)$$

$$\mathrm{C} = \frac{C_n}{\omega_c} \quad (3.15)$$

When both frequency and impedance scaling are applied to the prototype values the actual component value that can be used for the implementation of the filter can then be obtained by the combination of equations 3.6, 3.7,3.12, and 3.13 for the reactive components which will yield[13, 14];

$$\mathrm{L} = \frac{R_0 L_n}{\omega_c} = \frac{R_0 L_n}{2\pi f_c} \quad (3.16)$$

$$\mathrm{C} = \frac{C_n}{R_0 \omega_c} = \frac{C_n}{2\pi f_c R_0} \quad (3.17)$$

Where, C is the final circuit capacitor value, L the final circuit inductor value, C_n a low pass prototype element value from table, $L_n$is a low pass prototype element value from table, R_0 is the final load resistor value, and $f_c$is the cut- off frequency of the filter. The source resistor is transformed to its actual value by multiplying it by the load resistor.

3.4.6 Band Pass Filter Design

The most difficult task that a band pass filter (BPF) designer would encounter if the design is to be derived from a low pass prototype (LPP) is in specifying the band pass attenuation characteristics in terms of the low pass response curve. The frequency response of a BPF exhibit geometric symmetry i.e. it is only symmetric when plotted on a logarithmic scale [14, 109]. As such the centre frequency of a geometric symmetry filter is given by[14, 109];

$$f_0 = \sqrt{f_1 . f_2} \quad (3.18)$$

Where f_0= Centre frequency, f_1 =-3dB cut off Frequency below the centre frequency in the passband, and f_2= 3dB cut off Frequency above the centre frequency in the passband.

In design it is better to know the ratio of the frequencies, so that it can be used to obtain the number of the elements needed for the design of the filter when looked up in the standard curve (response) of the LPF type. This can also be a guide to aid in the determination of the component (elements) values in the filter circuit. The frequency ratio is given as:

$$\frac{B\omega}{B\omega_c} = \frac{f}{f_c} \tag{3.19}$$

Where $B\omega$= Bandwidth at the required value of attenuation, $B\omega_c$= the -3dB bandwidth of the bandpass filter.

The LPF can be transformed to a BPF by resonating each low pass element in the circuit with an element of opposite type and of same value. This is done in such a manner that, if an element is in series, the added opposite element should be in series, similarly, while if an element is in parallel the added opposite element should be in parallel. In other words all shunt elements of a LPP circuit becomes parallel resonant circuit and all series elements becomes series resonant circuits as shown below[14].

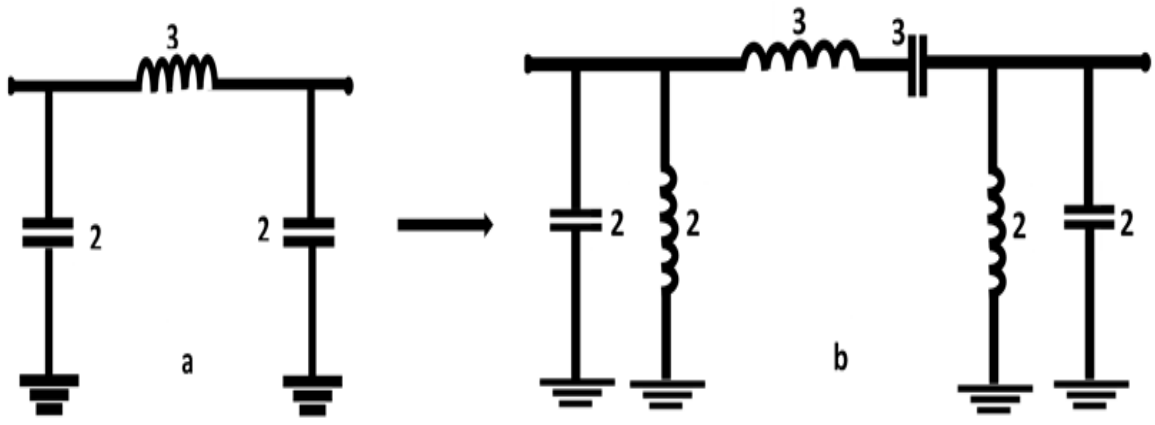

Figure 3. 8 Filter transformation, a) Low pass circuit, b) bandpass circuit

Figure 3.8a is a low pass filter while 3.8b is a bandpass filter, to complete the design, the transformed filter (figure 3.6b) is then frequency and impedance scaled using the following sets of equations. For the parallel resonance branches:

$$\mathrm{C} = \frac{C_n}{2\pi B \mathrm{R}} \tag{3.20}$$

$$\mathrm{L} = \frac{RB}{2\pi {f_0}^2 L_n} \tag{3.21}$$

For the series resonance branches:

$$\mathrm{C} = \frac{B}{2\pi {f_0}^2 c_n R} \tag{3.22}$$

$$\mathrm{L} = \frac{RL_n}{2\pi B} \tag{3.23}$$

Where R is the final load impedance, $B\omega_c$ is the -3dB bandwidth of the final design, f_0 is the Geometric centre frequency of the final design, C_n is the normalized capacitor bandpass element values, and L_n= the normalized inductor bandpass element values.

3.5 Low pass Filter Design

The process of the LPF filter design by insertion loss method was adopted for this work. This filter design is made up of several stages with each stage working for the ultimate achievement of actualising the filter. The stages for LPF design are stated in the figure 3.9 below [12, 14];

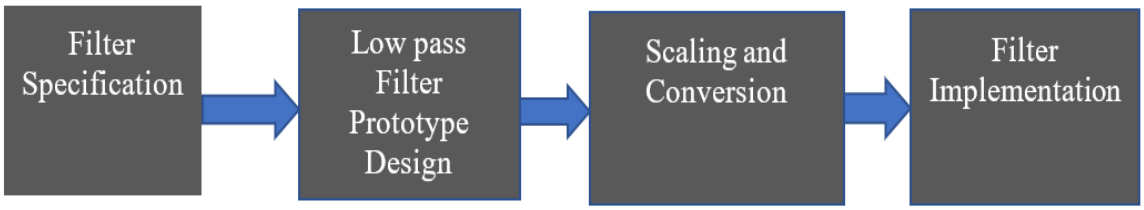

Figure 3. 9 The stages of low pass filter design

3.5.1 Chebyshev Low Pass Filter Design

For this work the Chebyshev low pass filter of 1dB passband ripple was chosen. This is because from its response characteristics it is endowed with ripple in its pass band, this

ripple can be particularly useful for the intended application at a micro scale. It is also helpful to bear in mind that the higher the filter order the steeper its attenuation (knowing that it naturally has attenuation better than both Butterworth and Bessel filters of same order as shown in figure 3.4 above). The maximum frequency of the available vector network analyser in the Laboratory is 3GHz, this means a filter that should operate within this maximum frequency value should be designed and its response including the pass band, cut-off frequency and the attenuation all within this frequency range of 0 to 3GHz.

Filter Specification is the first stage of design where the frequency of operation of the filter is being defined, the cut-off frequency is also defined (for LPF), the bandwidth of the filter is defined (in the case of bandpass filter), the kind of filter to be implemented subject to the filter characteristics suitable for the intended application as well as the degree of ripple (if it is a Chebyshev filter). Having determined the type of filter, the attenuation of choice is also defined, the next step is to determine from the aforementioned parameters above the number of reactive elements (filter order) of the filter as well as specifying the filter source and load resistance. From the above summation the following filter was designed. A Chebyshev low pass filter with the following characteristics: Fc=2.5GHz, Passband ripple =1dB, Rs=R_L=50Ω, Rs/R_L=1, and $\frac{f}{f_c}$=1, N=5.

Low pass Filter Prototype Design is the next stage of the design, In this stage of the filter design the specifications made above is being used to determine the exact filter element prototype values as well as determining the source and load resistance (Rs/R_L) ratio which will help in determining the circuit schematics for usage in the filter design and also the point where the prototype filter elements values will be read from in the standard tables of the chosen filter. The final step in this stage is the implementation of the prototype filter element with the normalised resistance as a circuit from the chosen schematics. The above information was used to determine the prototype elements and the schematics shown in the circuit of figure 3.9 below.

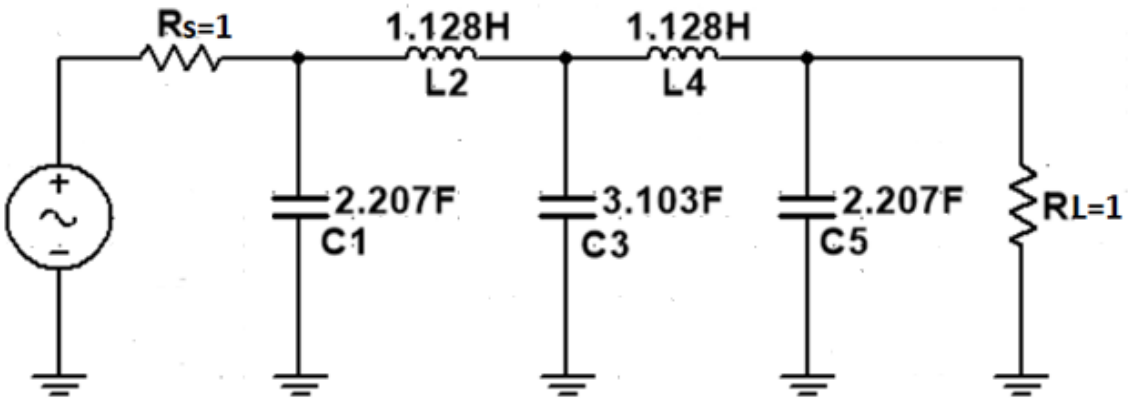

Figure 3. 10 Designed low pass filter with prototype element values (N=5)

Scaling and Conversion section follows in the process of the design, this is the stage where impedance and frequency scaling were done to obtain the actual filter element values, this stage entails the usage of equations 3.16 and 3.17 for the transformation of the Chebyshev prototype filter into an implementable filter to actualise the filter circuit hence, Table 3.2 below shows the designed element (component) values that was then used to implement the filter when scaling low pass filter.

Table 3. 1 Calculated element values for a 5th order filter at 2.5 GHz cut-off frequency

Element	Value
C1	2.81pF
L2	3.591nH
C3	3.951F
L4	3.591nH
C5	2.81pF

The filter implementation stage is a simple follow up from the immediate previous stage, since all that is required to implement the filter has been designed and their actual values has been determined then the implementation of the circuit on a circuit board is done based on the schematics of design, after which test are then done to observe if the results obtained meets the design specifications. From the scaling and table above the filter circuit suitable for implementation is shown in figure 3.10 below.

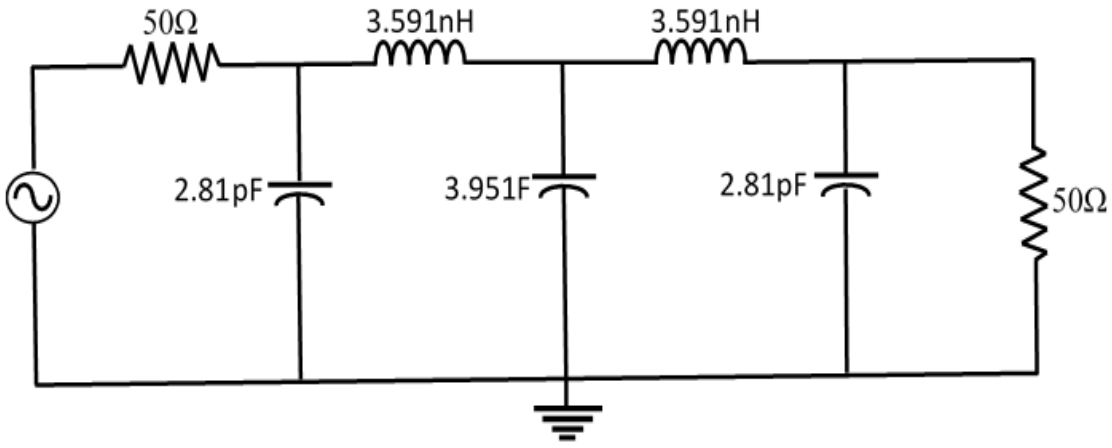

Figure 3. 11 The designed five elements Chebyshev low pass filter at 2.5GHz

The above design was used to accomplish the actual component values for the filter which will now then be used to design the Microstrip (Distributed) filter equivalents which is to be used as the conducting strip of the Microstrip transmission line that is intended to serve as the transduction section of the proposed biosensor. To achieve this, the next step of design is to transform this network filter design into a microstrip filter equivalent via the representation of the filter in a planar form as a stepped impedance filter for the low pass filter and a parallel coupled filter for a bandpass filter. The approach used above to derive the 5^{th} order lowpass filter at a cut-off frequency of 2.5GHz can be replicated in designing lowpass filters of different range of cut-off frequencies and any order of filter desired. For this research work the seventh order LPF was also designed at a cut off frequency of 2.5GHz using the same analytical method above.

3.5.2 Stepped Impedance Low Pass Filter

In the microwave frequency region filters can be designed using distributed transmission lines. A relatively easy way to implement low-pass filters in the microwave frequency range as a microstrip or stripline is to use alternating sections of very high and very low characteristic impedance lines. The series inductors of a lowpass filter can be replace with a high impedance line sections (of characteristics impedance (Z_0), where $Z_0=Z_{High}=Z_H$), and the shunt capacitors can be replaced with a low impedance line sections (of characteristics impedance (Z_0), where $Z_0=Z_{Low}=Z_L$)[15, 110]. When alternating line sections of very high and very low characteristic impedance are used for making microwave microstrip lowpass

filters design, such filters are usually referred to as stepped-impedance filter, or hi-Z, low-Z filters, and are popular because they are easier to design and take up less space[13, 15]. The stepped-impedance lowpass microstrip filters uses a cascaded structure of alternating high- and low impedance transmission lines. The high-impedance lines act as series inductors and the low-impedance lines act as shunt capacitors. Therefore, this filter structure is directly realizing the L-C ladder type of lowpass filters of circuit schematics shown above. Some initial design information must be provided about the microstrip lines because the expressions for inductance and capacitance depend upon both characteristic impedance and length. It would be practical to initially fix the characteristic impedances of high and low impedance lines by taking into consideration[15];

- $Z_L < Z_0 < Z_H$, where Z_L and Z_H denote the characteristic impedances of the low and high impedance lines, respectively, and Z_0 is the source impedance, which is usually 50Ω for microstrip filters.
- A lower Z_L results in a better approximation of a lumped-element capacitor, but the resulting line width must not allow any transverse resonance to occur at the operation frequencies.
- A higher Z_H leads to a better approximation of a lumped-element inductor, but Z_H must not be so high that its fabrication becomes inordinately difficult as a narrow line, or its current-carrying capability becomes a limitation.

The ratio of Z_H/Z_L should be as high as possible so that values of Z_H and Z_L are usually set to the highest and lowest characteristics impedance that can practically be fabricated[13]. Figure 3.12 below shows the general structure of a stepped impedance lowpass microstrip filter.

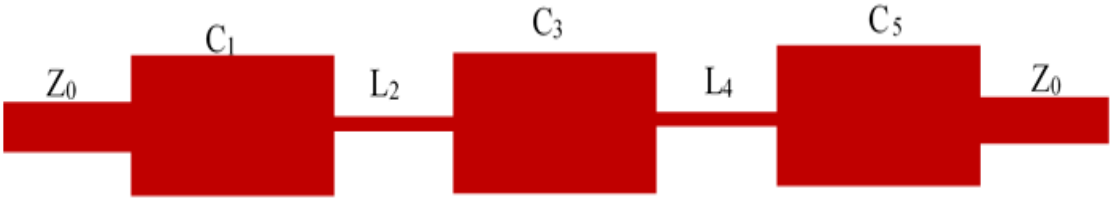

Figure 3. 12 General Structure of the 5th order stepped impedance lowpass microstrip filters.

To obtain the stepped impedance filter of the LPF from the circuit schematics (Circuit components value after frequency and impedance scaling) the following objectives needs to be achieved.

1. The characteristic impedance of each element (transmission line section) must be specified.
2. The length of each transmission line section (element) must be designed.
3. The width of each transmission line section (element) must be designed.
4. The thickness of each transmission line section (element) should be defined.

The rule of thumb is that $Z_L < Z_0 < Z_H$, Z_0 is the source impedance, which is usually 50Ω for microstrip filters. It is important to note that a higher characteristic impedance chosen for the design of the inductive lines will move any unwanted transmission peak up to a higher frequency[15]. The use of inductive lines with higher characteristic impedance and shorter lengths tends to achieve better approximation of the lumped elements inductor, and also the narrow inductive lines have a better stopband performance than a wide one[15].

With respect to the above-mentioned considerations the characteristic impedance of the lowpass filter for this work were chosen as; for the high impedance line Z_H=93Ω, and for the low impedance line Z_L=24Ω. The other design parameters were also determine using previous equations. These parameters and the above assumptions were then used to design the width and length of both the inductive and capacitive microstrip sections of the planar filter (distributed element).

From previous equations it is important to derive the essential parameter (guided wavelength of the inductive (λ_{gL}), capacitive (λ_{gc}), and resistive (λ_{g0}) part of the circuit) for the design as shown below. For this work quartz was utilised as the substrate of the of the microstrip filter, the dielectric constant (ε_r) of this substrate of choice the is 3.8, with a thickness of 1mm. In most microstrip design the width (W) of the microstrip conductor is wider than the thickness (h) of the substrate. Hence the effective dielectric constant (ε_{re}) in the case where w/h ≤2 is mostly employed, as such the equation below [15]was

used to obtain the ε_{re}. to do this however, the width to thickness ratio was first determined.

Given that; h=1mm, ε_r=3.8

$$\varepsilon_{re} = \frac{\varepsilon_r+1}{2} + \frac{\varepsilon_r-1}{2}\left(1 + 12\left(\frac{h}{w}\right)\right)^{-0.5} \quad (3.24)$$

From equation 3.24 w is unknown, to determine w, it is best to take the condition of width to thickness ratio where w/h ≤ 2, as such:

$$\frac{w}{h} = \frac{8Exp(A)}{Exp(2A)-2} \quad (3.25)$$

But the A in equation 3.25 can be determined using equation 3.26 below where:

$$A = \frac{Z_0}{60}\left(\frac{\varepsilon_r+1}{2}\right)^{0.5} + \frac{\varepsilon_r-1}{\varepsilon_r+1}\left(0.23 + \frac{0.11}{\varepsilon_r}\right) \quad (3.26)$$

For the resistive part of the filter, we have:

$Z_0 = 50\Omega$, $\varepsilon_r = 3.8$, h=1mm. Now solving for A in equation 3.30 above we have:

To determine the appropriate width to height ratio, firstly coefficient A is calculated from equation 3.26 giving a value of $A = 1.442$. Substituting this into equation 3.25 above we can determine the value of w as shown below where $\frac{w}{h} = 2.12978$, and with h=1mm, then $w = 2.13mm$

To determine the effective dielectric constant equation 3.24 above was used

$$\varepsilon_{re} = \frac{\varepsilon_r + 1}{2} + \frac{\varepsilon_r - 1}{2}\left(1 + 12\left(\frac{h}{w}\right)\right)^{-0.5}$$

Resulting in the effective dielectric constant of $\varepsilon_{re} = 2.944$

The effective dielectric constant as calculated above was then be used to determine the guided wavelength (λ_{g0}) of the resistive part of the microstrip filter which is one of the essential parameters in the designing of the microstrip filter.

The guided wavelength can be determined by the general equation below where[15];

$$\lambda_g = \frac{300}{F_{(GHz)}\sqrt{\varepsilon_{re}}} \quad (3.27)$$

Where $F_{(GHz)}$ is the Cut-off frequency in GHz and ε_{re} is the Effective dielectric constant.

To determine the guided wavelength (λ_{g0}) of the resistive part of the microstrip filter equation 3.27 above is made to suit the purpose as shown below.

$$\lambda_{g0} = \frac{300}{F_{(GHz)}\sqrt{\varepsilon_{re}}}$$

For this Microstrip filter design the cut-off frequency was chosen as 2.5GHz and the effective dielectric constant of the resistive part has been evaluated above, hence, $\lambda_{g0} = 70$. The same procedure followed above was then used to determine the guided wavelength of the inductive (λ_{gL}) and capacitive (λ_{gc}) parts of the microstrip filter as shown below, using equations 3.24 to 3.27.

For the inductive part of the filter, we have:

$Z_{0L} = 93\Omega$, $\varepsilon_r = 3.8$, h=1mm, solving for A in equation 3.26 above it was determined to be $A = 2.5523$, Placing this value of A in equation 3.25 above we can determine the value of w where, $\frac{w}{h} = 0.631$, and h=1mm, so $w = 0.631mm$. To determine the effective dielectric constant equation 3.24 above was used as such $\varepsilon_{re} = 2.7129$. this value was then substituted into equation 3.27 to determine the guided wavelength (λ_{gL}) of the inductive part of the microstrip filter,

$$\lambda_{gL} = \frac{300}{F_{(GHz)}\sqrt{\varepsilon_{re}}}$$

For this Microstrip filter design the cut-off frequency was chosen as 2.5GHz and the effective dielectric constant of the resistive part has been evaluated above, hence: $\lambda_{gL} = 73$

For the capacitive part of the filter, we have;

$Z_{0c} = 24\Omega$, $\varepsilon_r = 3.8$, h=1mm,

To determine the width of the planar capacitor equations 3.28and 3.29 below were used:

$$B = \frac{60\pi^2}{Z_c\sqrt{\varepsilon_r}} \tag{3.28}$$

$$\frac{w}{h} = \frac{2}{\pi}\left((B-1) - \ln(2B-1) + \frac{\varepsilon_r - 1}{2\varepsilon_r}\left[\ln(B-1) + 0.39 - \frac{0.61}{\varepsilon_r}\right]\right) \tag{3.29}$$

Where from evaluation $B = 12.6575$, substituting this value into equation 3.29 the width by thickness ration is determined as $\frac{w}{h} = 6.02$, since h=1mm, so w becomes $w = 6.02mm$. To determine the effective dielectric constant equation 3.24 above was used and $\varepsilon_{re} = 3.21$. To determine the guided wavelength (λ_{gL}) of the inductive part of the microstrip filter, equation 3.18 above is made to suit the purpose as shown below

$$\lambda_{gc} = \frac{300}{F_{(GHz)}\sqrt{\varepsilon_{re}}}$$

For this Microstrip filter design the cut-off frequency was chosen as 2.5GHz and the effective dielectric constant of the resistive part has been evaluated above, hence the capacitive guided wavelength is $\lambda_{gc} = 67$

From the above evaluations the design parameters for this microstrip filter at a cut-off frequency of 2.5GHz is tabulated as shown in table 3.3 below:

Table 3. 2 The calculated parameter of the Microstrip filter at 2.5GHz

Characteristic Impedance (Ω)	$Z_{0c} = 24$	$Z_0 = 50$	$Z_{0L} = 93$
Guided wavelength (mm)	$\lambda_{gc} = 67$	$\lambda_{g0} = 70$	$\lambda_{gL} = 73$
Microstrip width (mm)	$W_c = 6.02$	$W_0 = 2.13$	$W_L = 0.63$

After the calculation of some of the useful parameters in the designing of the stepped impedance Microstrip filter as shown in table 3.3 above, the next step was to determine the length of the high and the low impedance line. In order to do this the following equations below was utilised [15];

$$l_L = \frac{\lambda_{gL}}{2\pi}\sin^{-1}\left(\frac{\omega_c L}{Z_{0L}}\right) \quad (3.30)$$

$$l_c = \frac{\lambda_{gc}}{2\pi}\sin^{-1}(\omega_c C Z_{0c}) \quad (3.31)$$

Where l_L is the length of the high impedance line, λ_{gL} is the guided wavelength of the high impedance line, Z_{0L} is the characteristic impedance of the high impedance line, ω_c is the cut-off frequency, L is the lumped element inductor value from the designed circuit, l_c is the length of the low impedance line, λ_{gc} is the guided wavelength of the low impedance line, Z_{0c} is the characteristic impedance of the low impedance line, and C is the lumped element capacitor value from the designed circuit.

Equations 3.30 and 3.31 do not take into account the series reactance of the low impedance line and the shunt susceptance of the high impedance line, to include these effects, equations 3.32 and 3.33 are the adjusted to satisfy the following equations below[15];

$$\omega_c L = Z_{0L}\sin\left(\frac{2\pi l_L}{\lambda_{gL}}\right) + Z_{0c}\tan\left(\frac{\pi l_c}{\lambda_{gc}}\right) \quad (3.32)$$

$$\omega_c C = \frac{1}{Z_{0c}}\sin\left(\frac{2\pi l_c}{\lambda_{gc}}\right) + \frac{2}{Z_{0L}}\tan\left(\frac{\pi l_L}{\lambda_{gL}}\right) \quad (3.33)$$

Solving for l_L and l_c in equations 3.32 and 3.33 respectively yielded the desired length of the respective impedance line. The above equations from 3.30 to 3.33 was then used to design the stepped impedance microstrip filter as illustrated below. For uniformity of the geometry of the stepped impedance filter, the elements, and parameters of table 3.4 was chosen for design the proposed LPF filter.

Table 3. 3 The elements, and parameters of the proposed 5th order LPF filter

Parameter	Value
ω_c	2.5GHz
Filter Order (n)	5
Inductor (L)	3.591nH
Capacitor (c)	2.81pF

It is important to note that to design the length of the line, the trigonometric portion should be calculated in radian, else the correct length would not be achieved (or the trigonometry portion should be solved in degree and convert it to radian and complete the calculation). From Equation 3.30 the length of the inductive part was found to be $l_L = 7.57mm$. Similarly, the length of the low impedance line that is capacitive part l_c was determined using equation 3.31 to be $l_c = 16.75mm$. Now to include the effect of the parasitic element in the design which is firstly, to compensate for the parasitic element of the inductor arm, the true length of the planar inductor section was then obtained by using equation 3.32 and was determine to be $l_L = 4.14mm$, while using 3.33 the true length $l_c = 11.6mm$. So, the parameters that are being used to implement the microstrip filter at a cut-off frequency of 2.5GHz for a fifth order filter is shown in table 3.5 below.

Table 3. 4 The calculated parameter of the 5th order Microstrip filter at 2.5GHz

Characteristic Impedance (Ω)	$Z_{0c} = 24$	$Z_0 = 50$	$Z_{0L} = 93$
Guided wavelength (mm)	$\lambda_{gc} = 67$	$\lambda_{g0} = 70$	$\lambda_{gL} = 73$
Microstrip width (mm)	$W_c = 6.5$	$W_0 = 2.13$	$W_L = 0.63$
Length of impedance line (mm)	$l_c = 11.6$	$l_0 = 8$	$l_L = 4.14$

Before the fabricati0n of a filter with these designed values in table 3.5, a simulation of the designed filter was done in software package utilising the obtained values in the above to verify the design. The initial result of this simulation indicated that the cut-off frequency of the simulated microstrip filter is not same as the designed cut-off frequency value, hence there need to be improvements done on the filter to readjust the cut-off frequency to the designed value of 2.5GHz. The modification and improvement of the cut-off frequency of this filter was achieved by modifying the length of the inductive arm. Therefore, to modify the inductor length to obtain an improved or desired cut-off frequency as the design frequency, the equation below was used:

$$l_{ind}^{mod} = \left(\frac{{F_c}^{mod}}{{F_c}^{specify}}\right)^2 \times l_{ind}^{initial} \quad (3.34)$$

Where l_{ind}^{mod} is the modified inductor length, ${F_c}^{mod}$ is the obtained cut-off frequency from simulation result, ${F_c}^{specify}$ is the designed cut-off frequency, and $l_{ind}^{initial}$ is the evaluated inductor length.

Using equation 3.34 above for several iteration of simulation and evaluation, resulted in the desired inductor length, at a desired simulated cut-off frequency of 2.507GHz. The modified inductor length as shown in table 3.6 below was used to implement the microstrip LPF in figure 3.12.

Table 3. 5 Improved parameter of the 5th order Microstrip LPF filter at 2.5GHz with modified inductor length

Characteristic Impedance (Ω)	$Z_{0c} = 24$	$Z_0 = 50$	$Z_{0L} = 93$
Guided wavelength (mm)	$\lambda_{gc} = 67$	$\lambda_{g0} = 70$	$\lambda_{gL} = 73$
Microstrip width (mm)	$W_c = 6.02$	$W_0 = 2.13$	$W_L = 0.63$
Length of impedance line (mm)	$l_c = 11.6$	$l_0 = 8$	$l_L = 6.08$

The parameters calculated as shown in the above table were then used to implement a distributed filter of a cut-off frequency of 2.5GHz and for a 5th order LPF type show in figure 3.13 below.

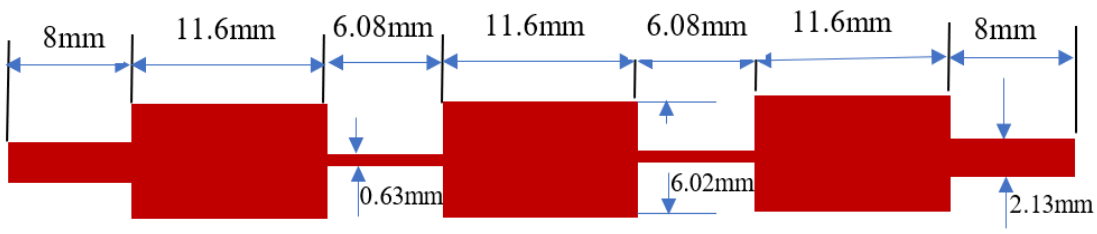

Figure 3. 13 The structure of the 5th order stepped impedance microstrip LPF with cut-off frequency of 2.5GHz.

The same procedure used to design the fifth order microstrip lowpass filter above was similarly employed in designing the seventh order microstrip LPF with the following design parameters, where table 3.7 shows the values of both the inductor and capacitor was chosen to be these values due to uniformity of the geometry of the stepped impedance filter.

Table 3. 6 The elements, and parameters of the proposed 7th order LPF filter

Parameter	Value
ω_c	2.5GHz
Filter Order (n)	7
Inductor (L)	3.6001nH
Capacitor (c)	2.8062pF

Using the same approach used in determining the fifth order Microstrip low pass filter (MLPF) stated above including inductor length modification, the seventh order filter was also designed, and the results are tabulated in table 3.8 below.

Table 3. 7 The designed parameter of the 7th order Microstrip filter at 2.5GHz

Characteristic Impedance (Ω)	$Z_{0c} = 24$	$Z_0 = 50$	$Z_{0L} = 93$
Guided wavelength (mm)	$\lambda_{gc} = 67$	$\lambda_{g0} = 70$	$\lambda_{gL} = 73$
Microstrip width (mm)	$W_c = 6.02$	$W_0 = 2.13$	$W_L = 0.63$
Length of impedance line (mm)	$l_c = 11.54$	$l_0 = 4$	$l_L = 6.81$

The recorded results of table 3.7 were then used to produce the designed Microstrip low pass filter as shown in figure 3.14 below.

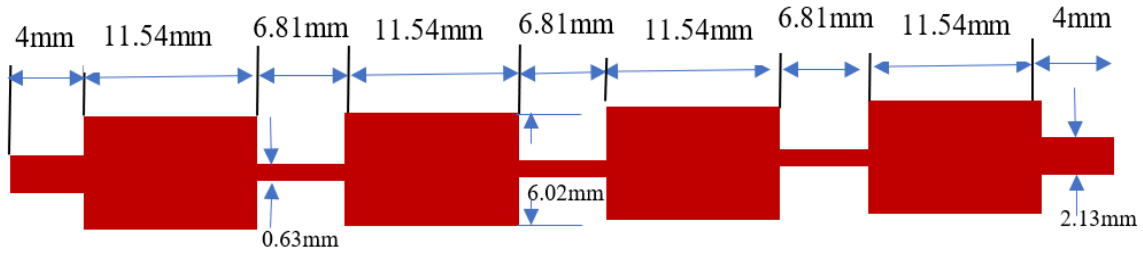

Figure 3. 14 The structure of the 7th order stepped impedance microstrip LPF with cut-off frequency of 2.5GHz

This design method can be used in the designing of microstrip LPF of any order of choice and any cut-off frequency that is required. The next section will look at how the microstrip bandpass filter was designed.

3.6 Microstrip Bandpass Filter

There are two methods for designing a planar bandpass filter which can be used for the implementation as the sensing element of a biosensor, these are, the end coupled and parallel (edge) coupled microstrip bandpass filter. The end coupled microstrip bandpass filter operates like a shunt resonator type filter because its J-inverter (also referred to as the Admittance inverters) tends to reflect high impedance levels to the end of each of the half wavelength resonators and this causes the resonators to show a shunt type resonance. In this work only the parallel coupled microstrip bandpass filter would be design and implemented as the sensing element of the proposed biosensor. The parallel coupled microstrip bandpass filter uses half wavelength line to represent each open end microstrip resonator. They are so positioned in such a way that the adjacent resonators are parallel to each other along half of their length. Their parallel arrangement provides large coupling for a spacing between each resonator, as such this type of filter is mostly employed when constructing filters that have wider bandwidth as compared to its end coupled microstrip counterpart. The general structure of the parallel coupled microstrip bandpass filter is given below in figure 3.15.

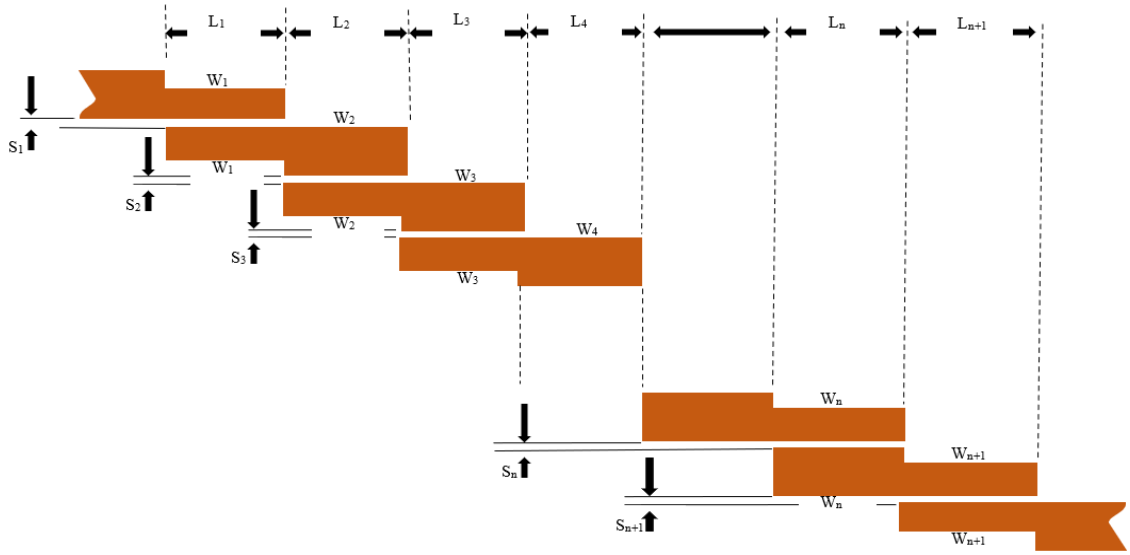

Figure 3. 15 The General structure of a parallel coupled microstrip BPF

These coupled microstrip lines are characterized by the characteristic impedances as well as effective dielectric constants of two modes (odd and even modes). To design a planar bandpass filter the following steps and sets of equations are used:

The first thing was to determine the filter of choice and the prototype LPF component values. The next step was to determine the fractional bandwidth, this can be set by choice in percentage or by the formula below: FBW is the fractional bandwidth of the BPF which is given by: $FBW = \frac{\omega_2 - \omega_1}{\omega_0}$

Where ω2 is the upper frequency of the passband, ω1 is the lower frequency of the passband and ω0 is the center frequency of the passband.

The next was to determine the J-Inverter of all the components of the filter given by:

$$\frac{J_{0,1}}{Y_0} = \frac{J_{n,n+1}}{Y_0} = \sqrt{\frac{\pi FBW}{2 g_n g_{n+1}}} \tag{3.35}$$

$$\frac{J_{j,j+1}}{Y_0} = \frac{\pi FBW}{2} \frac{1}{\sqrt{g_j g_{j+1}}} \tag{3.36}$$

Equation 3.35 was used to determine the first and the last J-inverters, while equation 3.36 was used to determine the J-inverters between the first and the last J-inverters.

$$J = 1 \; to \; n-1$$

Where, $g_0, g_1 \ldots\ldots\ldots\ldots\ldots g_n$ are the ladder type LPF prototype values with normalized cut-off frequency of ω_c. J_j,J_{j+1} is the characteristic admittance of the J-inverters, Y_0 is the characteristic admittance of the terminating lines.

It is imperative to note that both the end coupled, and the edge coupled filters can have the same lowpass network, but their implementation will differ.

The J-inverters obtain from above can be used to determine the even and odd modes characteristic impedance of the edge coupled microstrip line resonator as given below.

$$(Z_{oe})J_j,J_{j+1} = \frac{1}{Y_0}\left[1 + \frac{J_j,J_{j+1}}{Y_0} + \left(\frac{J_j,J_{j+1}}{Y_0}\right)^2\right] \quad (3.37)$$

J=0 to n

$$(Z_{oo})J_j,J_{j+1} = \frac{1}{Y_0}\left[1 - \frac{J_j,J_{j+1}}{Y_0} + \left(\frac{J_j,J_{j+1}}{Y_0}\right)^2\right] \quad (3.38)$$

J=0 to n

While the length of the coupled line can be determined by:

$$L_j = \frac{\lambda_0}{4\sqrt{(\varepsilon_{re})_j \times (\varepsilon_{ro})_j}} - \Delta l_j \quad (3.39)$$

Δl_j is the equivalent length of microstrip open end.

The above equations with other equations were then used to design the microstrip BPF in this work to be used as the sensing element of the biosensor. The design of the planar BPF is as shown below.

For this microstrip bandpass Filter Design the following Parameters were used to actualize the size of the resonators. Relative permittivity ε_r=3.8, The thickness of the quartz substrate h=1mm, The characteristic impedance of the source and load resistor Z_0=50Ω, The cut-off frequency F_c=2.5GHz, and FBW=0.2. The Chebyshev filter with a ripple loss of 1dB was chosen which has elements value for a normalized prototype filter as follows: g_0=1; g_1=2.207;g_2=1.128;g_3=3.103;g_4=1.128;g_5=2.207;g_6=1. Table 3.8 below summarizes all these parameters.

Table 3. 7 Microstrip bandpass Filter Design Parameters

Parameter	Value
Relative permittivity	3.8
Substrate Thickness	1mm
Z_0	50Ω
Fc	2.5GHz
FBW	20%
Chebyshev filter ripple loss	1dB
Normalised prototype elements value	g0=1; g1=2.207; g2=1.128; g3=3.103; g4=1.128; g5=2.207; g6=1.

The coefficients for this filter were calculated using equations 3.35 to 3.59. It has a characteristic admittance of Y_0=(1/50), The J-inverters of the resonators were determined using equations 3.35, 3.36 further details of which can be found in Appendix A. To determine the EVEN mode characteristic Impedance of the BPF equations 3.37 and 3.38 were used. Where $(Z_{oe})_{j,j+1}$ is the characteristic impedance of the even mode for the $J_{j,j+1}$ element, and $(Z_{oo})_{j,j+1}$ is the characteristic impedance of the odd mode for the $J_{j,j+1}$ element.

The single Microstrip line EVEN and ODD characteristic Impedance were determined using:

$$(Z_{ose})_{j,j+1} = \frac{(Z_{oe})_{0j,j+1}}{2} \tag{3.40}$$

While for the ODD single Microstrip line it was determined using:

$$(Z_{oso})_{j,j+1} = \frac{(Z_{oo})_{j,j+1}}{2} \tag{3.41}$$

To determine the single line shape ratio of Width and Thickness for the EVEN mode the equation below was used.

$$(A_e)_{j,j+1} = \frac{(Z_{ose})_{j,j+1}}{60}\left(\frac{\varepsilon_r+1}{2}\right)^{0.5} + \frac{\varepsilon_r-1}{\varepsilon_r+1}\left(0.23 + \frac{0.11}{\varepsilon_r}\right) \tag{3.42}$$

$$(w/h)_{se(j,j+1)} = \frac{8Exp(A_e)_{j,j+1}}{Exp\left(2(A_e)_{j,j+1}\right)-2} \tag{3.43}$$

While to determine the single line shape ratio of Width and Thickness for the ODD mode is done using the equation below:

$$(A_o)_{j,j+1} = \frac{(Z_{oso})_{j,j+1}}{60}\left(\frac{\varepsilon_r+1}{2}\right)^{0.5} + \frac{\varepsilon_r-1}{\varepsilon_r+1}\left(0.23 + \frac{0.11}{\varepsilon_r}\right) \tag{3.44}$$

$$(w/h)_{so(j,j+1)} = \frac{8Exp(A_o)_{j,j+1}}{Exp\left(2(A_o)_{j,j+1}\right)-2} \tag{3.45}$$

Then to determine the single line shape ratio of space and Thickness the approach was done using the equations below.

$$(A)_{j,j+1} = \cosh\left(\left(\frac{\pi}{2}\right)(w/h)_{se(j,j+1)}\right) \tag{3.46}$$

$$(B)_{j,j+1} = \cosh\left(\left(\frac{\pi}{2}\right)(w/h)_{so(j,j+1)}\right) \tag{3.47}$$

$$(s/h)_{j,j+1} = \left(\frac{\pi}{2}\right)\cosh^{-1}\left(\frac{\left((A)_{j,j+1}+(B)_{j,j+1}\right)-2}{(B)_{j,j+1}-(A)_{j,j+1}}\right) \tag{3.48}$$

To determine the single line shape ratio of width by Thickness of the element the approach was done using the equations below.

$$(C)_{j,j+1} = \left(\frac{\pi}{2}\right)(s/h)_{j,j+1} \tag{3.49}$$

$$(D)_{j,j+1} = \left(\frac{\pi}{2}\right)(w/h)_{se(j,j+1)} \tag{3.50}$$

$$(E)_{j,j+1} = \cosh(C)_{j,j+1} \quad (3.51)$$

$$(F)_{j,j+1} = \cosh(D)_{j,j+1} \quad (3.52)$$

$$(w/h)_{j,j+1} = \frac{1}{\pi}\cosh^{-1}\left(\frac{1}{2}\left((C)_{j,j+1} - 1\right)\right) + \left(\left(\left(\cosh(C)_{j,j+1} + 1\right)\left(\cosh(D)_{j,j+1}\right)\right) - (C)_{j,j+1}\right) \quad (3.53)$$

From the above results the Effective dielectric constants of each elements was determined using:

$$(G)_{j,j+1} = 12\left(\frac{1}{(w/h)_{j,j+1}}\right) \quad (3.54)$$

$$(H)_{j,j+1} = \sqrt{1 + (G)_{j,j+1}} \quad (3.55)$$

$$(I)_{j,j+1} = \frac{1}{(H)_{j,j+1}} \text{ (3.56)} \quad (3.56)$$

While the individual relative dielectric constant is given by:

$$\varepsilon_{r(j,j+1)} = \left(\frac{\varepsilon_r + 1}{2}\right) + \left(\frac{\varepsilon_r - 1}{2}\right)(I)_{j,j+1} \quad (3.57)$$

And the individual element guided wavelength is given by:

$$\lambda_{g(j,j+1)} = \frac{300}{F_c\sqrt{\varepsilon_{r(j,j+1)}}} \quad (3.58)$$

The length of each of the element is a quarter of a wavelength given by:

$$Length_{(j,j+1)} = \frac{\lambda_{g(j,j+1)}}{4} \quad (3.59)$$

Finally, the results of calculated coefficients are summarized in table 3.10 below, from this table the design of the microstrip BPF was implemented in ANSYS high-frequency structure simulator (HFSS) program for the device simulation, and it is from these results that the fabrication of the sensor devices were derived.

Table 3. 8 Parameters needed for the implementation of a BPF of 2.5GHz cut-off frequency

Resonator element	Space (mm)	Width (mm)	Length(mm)
01	0.0106	1.5418	17.7011
12	0.0766	2.1134	17.4911
23	0.1162	2.2274	17.4550
34	0.1162	2.2274	17.4550
45	0.0766	2.1134	17.4911
56	0.0106	1.5418	17.7011

These results derived for the analytical design of the microstrip BPF was adjusted a little bit because it was challenging fabricating a device that space between resonators to be this small. Therefore, after comparing the simulation results of several devices the, it then became evident that setting the spacing between resonators to be 1mm will still give the same results as the designed space distances arrived at from the analytical design. The new table for the microstrip BPF that was employed for the fabrication of the devices is given in table 3.11 below.

Table 3. 9 New parameters needed for the implementation of a 5th order BPF of 2.5GHz cut-off frequency

Resonator element	Space (mm)	Width (mm)	Length(mm)
01	1	1.5418	17.7011
12	1	2.1134	17.4911
23	1	2.2274	17.4550
34	1	2.2274	17.4550
45	1	2.1134	17.4911
56	1	1.5418	17.7011

The results from the evaluation recorded in table 3.11 above was then used to fabricate the 5th order microstrip BPF (MBPF). It can be observed that the structure in terms of elements arrangement slightly differs from that of the standard parallel coupled MBPF of figure 3.15. The reason for this change in elements geometry is because of the substrate size used in the implementation of this sensing element. Since quartz was chosen as the substrate of the MBPF, it then means that there is a constraint with respect to the size of

the substrate, this is because a standard quartz size of 75mm X 25mm was employed for the implementation of this sensing element, but from the result of the design above it indicates that the substrate needed to implement the designed filter would have a dimension of 121.44mm X 36mm. Therefore, an alternative geometrical structure was needed to implement this filter, hence an improvised parallel coupled V-Shaped filter geometrical structure was proposed and simulated to compare with the standard parallel coupled MBPF, the result observed indicated that this improvised filter response was identical with the standard parallel coupled MBPF. Following from the above, the structure of the improvised 5th order MBPF called the "V-shaped MBPF" was implemented as shown in figure 3.16 below.

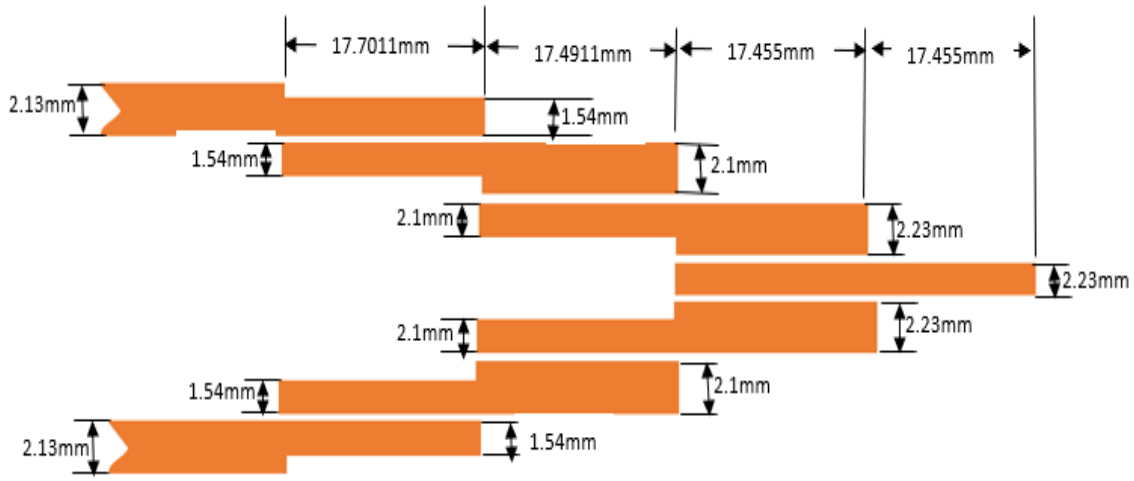

Figure 3. 16 The implemented 5th order MBPF

The same approach used in designing the 5th order MBPF was also employed in designing the 3rd order equivalent with the following design parameters. The Chebyshev filter with a ripple loss of 1dB was chosen which has elements value for a normalized prototype filter as follows: g_0=1; g_1=2.216; g_2=1.088; g_3=2.216; g_4=1, With a characteristic admittance of Y_0= (1/50). The results were recorded, and the final structure is as shown in figure 3.16, while table 3.9 is the results of the evaluation of the filter element parameters. The structure of this 3rd order filter used is same as the standard MBPF, this is because for this filter all the elements of the 3rd order MBPF was easily accommodated on the quartz substrate.

Table 3. 10 The parameters needed for the implementation of a 3rd order BPF of 2.5GHz cut-off frequency

Resonator element	Space (mm)	Width (mm)	Length(mm)
01	0.0107	1.544	17.7002
12	0.0734	2.1019	17.4949
23	0.0734	2.1019	17.4949
34	0.0655	2.0708	17.5050

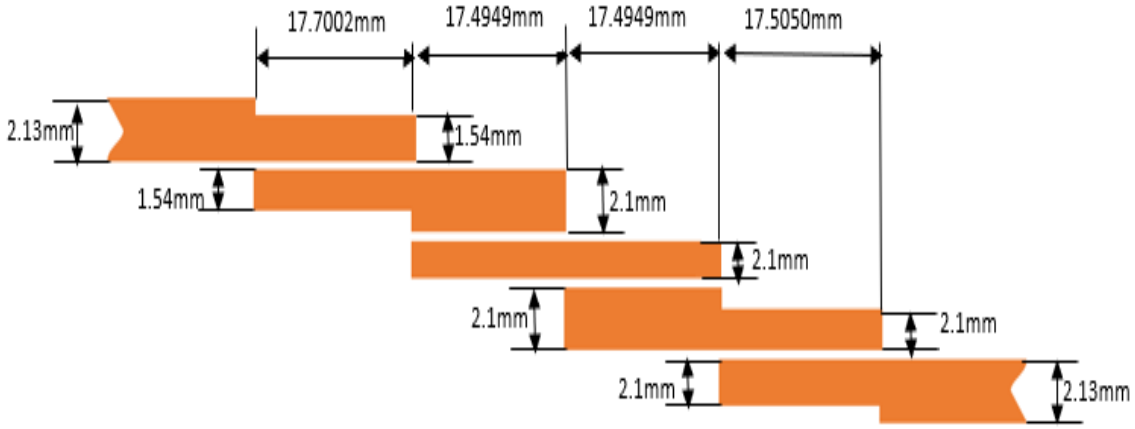

Figure 3. 17 The implemented 3rd order MBPF

3.7 Modelling and Simulation

To ensure the simulated results are reliable, the model should be designed in the software as required with the evaluated designed dimensions and chosen ground and substrate materials with their required thickness. For this work the model was design in ANSY HFSS Electromagnetic suite 17.1 software tool, it was employed because of its reliability. The material used for both the LPF and the ground plane in the simulation was Gold, while for the substrate a quartz was used. To implement this design in ANSYS HFSS, the ground and the substrate were drawn and assigned materials as shown in figure 3.18a, this structure is the base on which the filter of choice will be implemented upon. Figure 3.18b highlights the 5th order LPF (it could also be used for any other microstrip filter) implemented on the base structure of figure 3.18a (ground and substrate).

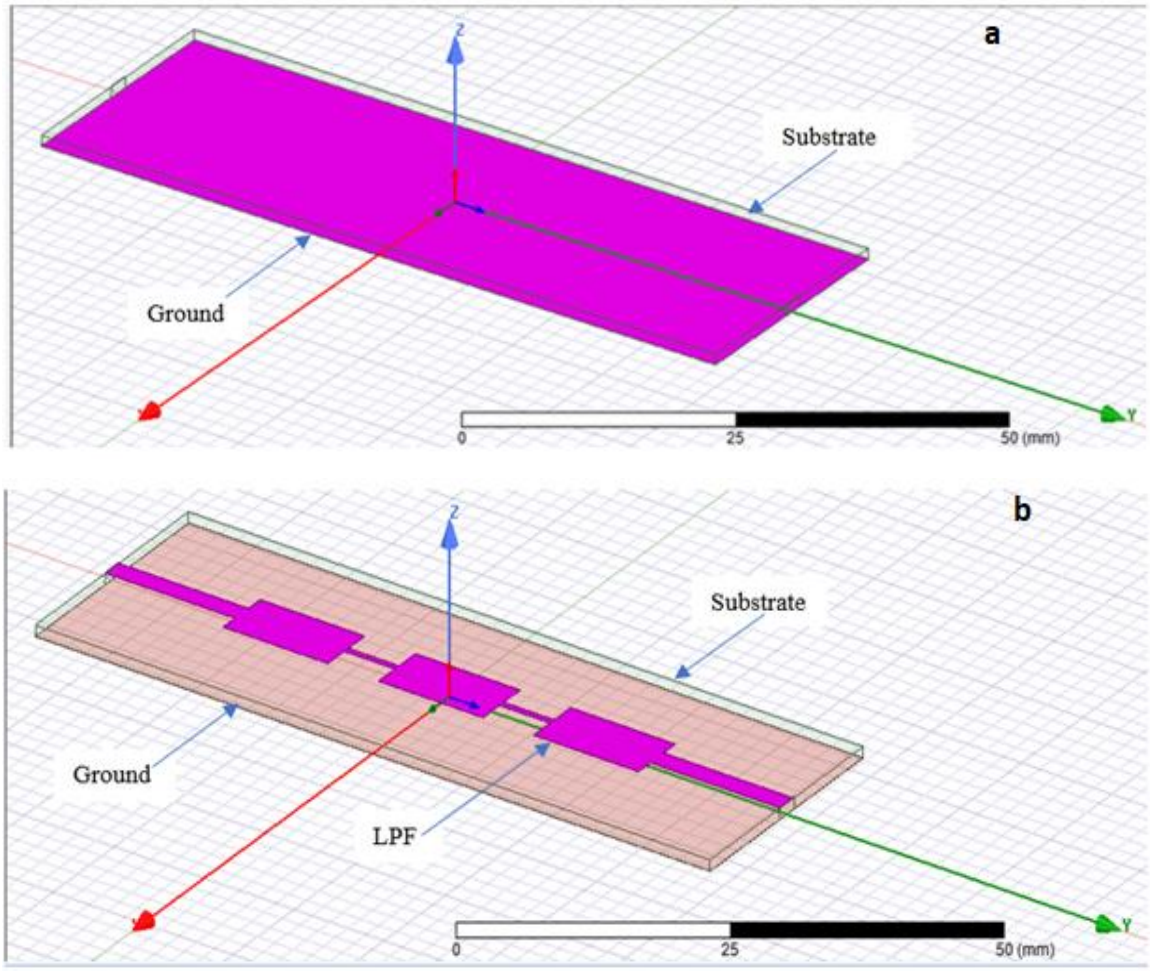

Figure 3. 18 Implementation of the 5LPF a) the substrate and ground plane of the microstrip filter, b) the substrate, ground plane and the LPF element of the microstrip filter

Prior To fabricating the filter with these designed values, simulation of this designed filter was done on ANSY HFSS software using the designed values. The results of these simulations shown in figure 3.19 a, b and c are for the filter response starting with the calculated values of table 3.5, shows the results for a gold filter, results for other materials will be discussed in chapter 5. The simulation results using these values indicates a cut off frequency of 2.77 GHz as seen in figure 3.19a, which is higher than the designed value. This initial simulation result indicated that the cut-off frequency of the simulated microstrip filter is slightly higher than the calculated value, hence there need to be improvements done on the filter to readjust the cut-off frequency to be same as the designed value of 2.5GHz.

The modification and improvement of the cut-off frequency of this filter was achieved by modifying the length of the inductive arm. Therefore, to modify the inductor length to obtain an improved or accurate cut-off frequency as the design frequency, equation 3.34 above was used for several iteration of simulation and evaluation, to obtain a suitable modified inductor length and cut-off frequency of 2.51GHz. This value was however not immediately arrived at, because after the first modification the cut off frequency was observed to be 2.58GHz as shown in figure 3.18b, this cut off frequency is slightly above the designed value, therefore another modification was done using the new cut-off frequency and equation 3.34, this yielded a cut off frequency of 2.51GHz as shown in figure 3.19c. This iteration was used to realise the desired filter dimension at the desired cut off frequency. This is an essential aspect of the design of the microstrip filter, since from simulation results the desired response of the filters are viewed to ascertain that they meet the design requirements such as the cut-off frequency.

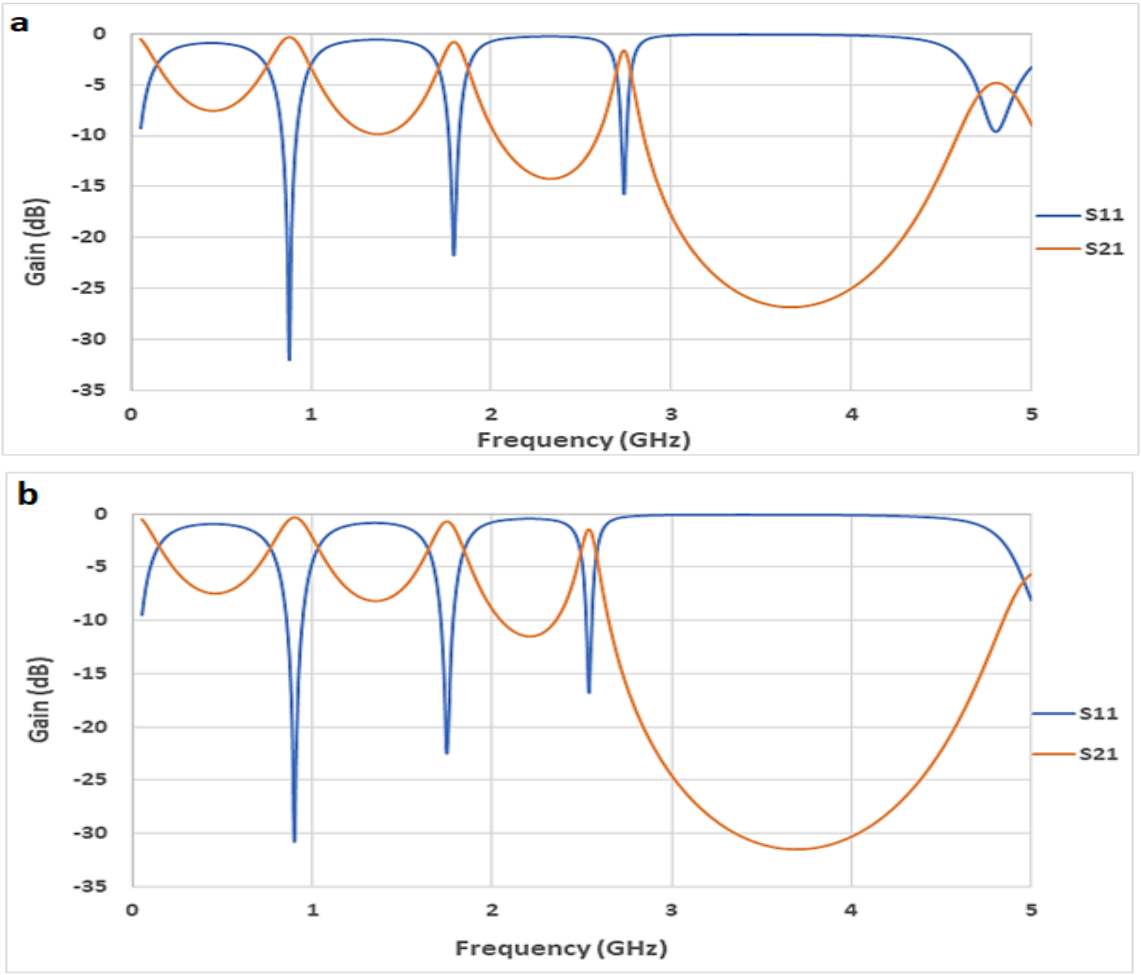

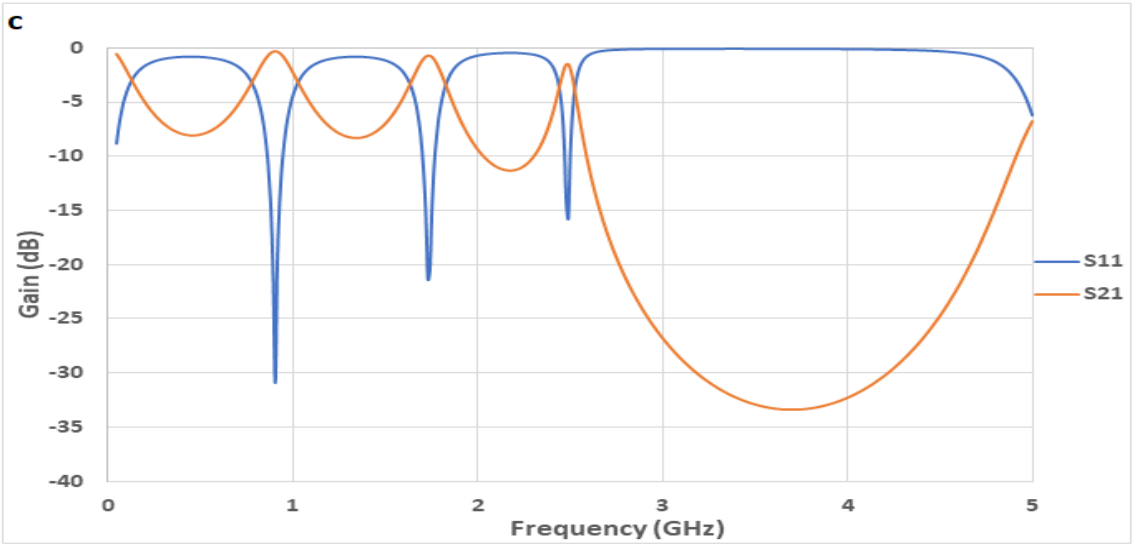

Figure 3. 19 Response of microstrip filter LPF response with analytical values, a) without modification, b) after the first modification, c) after the second modification.

This simulation involves using the designed geometry to simulate the response of the microstrip filter so as to observe the filter response as a microstrip filter and also observe the response to know if the response obtained can suit the intended application. This simulation can also help determine what section of the filter has the highest current density so that it can be selectively targeted for the intended application. One of the main advantages of the distributed filter design is that, if implemented, the results of simulation can be compared with those of test equipment (Vector Network Analyzer (VNA)).

3.8 Summary

The beginning of this chapter seeks to give a brief background as to the reason why a planar system was needed for the implementation of the sensing element of the biosensor. The next section briefly highlighted the different types of filters and the approach used in designing the Chebyshev filter. From this the 5^{th} order MLPF was designed, and the results modified to obtain a planar filter that represents the lumped elements filter, the same approach was utilized in designing the 7^{th} order MLPF. The 5^{th} MBPF was designed in the next section making use of the LPF prototype element values, from the results obtained an innovative element geometry was derived to enable the ease of positioning of the sensor element on the substrate of choice. This section also indicated

the utilization of the same method in designing the 3rd order MBPF, where it was illustrated that for this order the standard parallel coupled structure was utilized for its implementation. The MLPF is characterized by the stopband where the signal attenuates as is evident from the LPF responses, and passband with the accompanying ripples which is dependent on the order of the filter. These ripples tend to produce sharper and well-defined resonant peaks as the filter order increases. The MBPF just like the traditional type is characterized by the bandpass signal and the attenuated sections of the response. For the case of the 3rd order MPBF the standard parallel coupled arrangement of elements was achieved, while for the 5th order MBPF the parallel coupled arrangement was improvised in the form of a V-shaped arrangement. This geometrical change in elemental arrangement was due to the size of the substrate of choice, and this new parallel arrangement did produce a suitable bandpass filter response.

Chapter 4. Materials and Methods

4.1 Introduction

This chapter gives an insight into the materials used for the fabrication of the sensor devices and the methods of implementation such as how the manufacture of devices was done and how equipment was used for characterization. Some of these materials used for the transducer (sensing element) includes Kapton tape and graphene oxide, while materials used for the substrate were FR4 and quartz slides. This chapter also highlighted that the devices made out of gold material was fabricated using an evaporator, while the devices that are made from Kapton tape was fabricated using a laser machine, more so, the devices made out of the chemically reduced graphene material employed the inkjet printing scheme. The chapter also explains some of the equipment settings used for the implementation of these devices and their types. All of this was done to give a clear understanding of the detailed requirement necessary to produce the sensor devices. The different ways used in the characterization of the sensor types was also detailed, thus, allowing for clear insight into the production procedure.

4.2 Quartz Slides

Quartz microscope slides are made of a high purity fused quartz. The slides used for this work were obtained from PI-KEM limited and they are available in the standard 1mm thickness but for this work the size of slides used was the 75mm x25mm x1mm. These slides have high chemical purity, low coefficient of thermal expansion with excellent electrical insulation. They are intended to serve as the substrate of the circuit. Table 4.1 shows some useful property of quartz which are relevant to this research needs [111, 112].

Table 4. 1 Property of quartz

Property	Quantity
Electrical resistivity	$7\times10^{7}\,\Omega$cm
Dielectric constant	3.8
Insulated strength	5×10^{7} V/m

4.3 SMA Connectors

In order to connect the fabricated filter to the VNA for characterisation and biological testing, a Sub Miniature version A (SMA) connector was used, the SMA which is a coaxial cable connector with a semi-precision minimal connector interface with a screw-type pairing mechanism for coaxial cables. This SMA connectors was connected to the sensor device by soldering its centre contact to the filter (the sensor) while the ground plane of the device was soldered to the outer contact of the SMA. For this work the SMA connector used features a 6.35mm-36-thread-type coupling mechanism and is considered a semi-precision, sub-miniature and high-frequency connector that is rated to deliver reliable broadband performance from DC to 18 GHz, with a constant impedance of 50 ohms and low reflection [113]. This connector has Length of 17.45mm, diameter of 9.53mm, height 7.92mm and weight 82.78g. The main features of this connector are its high mechanical strength and high durability, this SMA connector was obtained from RS components.

4.4 Laser cutter

CO_2 laser engraving and laser cutting machines are extremely popular due to their relatively low cost and incredible flexibility and accuracy. They are especially well suited to cutting and engraving a wide range of materials such as woods, plastics, leather, paper, and card. The engraving ability of the machine was what it was needed for, so that the Kapton tape can be engraved upon to produce the graphene-like material that could be used as a sensing element. For this work the HPC Laserscript CO_2 laser cutter LS6840 PRO laser was used. It has a cutting bed area size of 680mm x 400mm (slightly reduced for engraving), fitted with a 50W tube as standard and is available with a 60W tube upgrade[114]. This machine has a maximum cutting thickness of 20mm but with a recommended maximum cutting thickness of 10mm. The speed of this machine ranges from 200-400mm/s and it is fitted with a Laser source of water-cooled CO_2 gas filled glass tube and has a focus spot size of 2mm, for this work however, the speed used were 300, 350 and 400mm/s. The Z axis (table height) adjustment is up to 130mm and is fitted with a Stepper motor drive system while having a location precision of <0.01mm.

4.5 Airbrush and compressor

This multi-purposed and gravity feed dual action Voilamart airbrush compressor kit was used for this task of spraying the graphene oxide on the substrate. This spray-gun sprays an entire range of stipple effects from very fine to coarse textures. The complete kit comes with a lightweight and portable air compressor that operates at low noise with adjustable pressure, has auto start / stop function, has air flow control knob for adjustment of air volume, an over-pressure protected, a constant pressure and zero pulsation, and can be plugged with AC transformer or DC 12V battery. The airbrush has a 10.5ml permanently mounted colour cup that allows easy spraying. The speed of spray was maintained at 6 seconds for each to-and-fro action (pass), the number of passes was dependent on the type of filter being produced and the distance of the spray gun from the quartz substrate was set to be at an average of 20cm. For a 5^{th} order LPF made from 5 passes the thickness was observed to be 0.67mm. In a bid to improve conductivity, controlled steps were taken to produce a better filter from the spraying techniques employed. Refer to section 4.3 above to see how it was used for the fabrication of GO LPF device.

4.6 Balzers E-beam Deposition Machine

All the gold samples in this work were deposited by e-beam evaporation with a Balzers BAK 550 Evaporator machine. This apparatus can solely provide e-beam evaporation deposition process of films. The starting material was the Ti of 99.995% purity provided by Testbourne Ltd, UK. The samples were deposited on the quartz substrate, with substrate temperature not too high to be monitored and samples were grown up to a thickness of 50nm, controlled by a quartz crystal microbalance (QCM). The deposition rate was automatically controlled and set at 1.5Å/s. The second layer of gold (Au) with percentage purity of 99.99% was also deposited using the same approach with the deposition rate being controlled at 3Å/s (but does have a variation of ~+/-0.5Å/s), this was also grown up to a thickness 300nm. The chamber of this machine was pumped down to a working pressure of below 5 $x10^{-7}$mbar, at the end of processing, the chamber was vented using nitrogen. Based on the above equipment settings, the filter designs were sent to INEXMicro for production, and it was done using their Balzers BAK 550 evaporator,

with the device deposition thicknesses of 300nm for Au overlaying a 50nm for Ti being the desired device outcome.

4.7 Surface Profiler

Portable surface roughness tester is a portable measuring instrument that allows you to measure surface roughness easily and accurately. For this work the Mitutoyo Surftest SJ-410 was used to measure the portion of the Kapton tape that was irradiated with the laser machine so that the width and height of the irradiated part can be measured accurately. For this device, the specifications are: The X axis measuring range is 50mm, while the Z axis measuring range is 800µm, 80µm, 8µm and up 2400µm with an optional stylus. The measuring resolution of this equipment is 0.01µm (800µm range), 0.001µm (80µm range), and 0.0001µm (8µm range). The measuring force is 0.75mN, with a radius of skid curvature of 40mm, the measuring speed is 0.05, 0.1, 0.2, 0.5, 1mm/s, with a drive speed of 0.5, 1, 2, 5mm/s. The measuring speed used for this work is 0.5mm/s, and the Z-axis measuring range was set at 2400µm.

4.8 Vector Network Analyzer

A network analyser generates a sinusoidal test signal that is applied (transmitted signal) to the device under test (DUT) as stimulus and measures the response (reflected signal) of the DUT. It measures the amplitude and the phase of the wave quantities and uses these values to calculate the S-parameter. They are used to test component specifications and verify design simulations to make sure systems and their components work properly together. For this work, a two port R&S@ ZVL vector network analyser with a frequency range from 9KHz to 3GHz was used. In this work the settings used for the measurement of the characteristics of the device under test are: number of sweep points used was 3900 points, the power gain setting was set to -10dBm, the average factor (sweep average) was set to 36, the frequency span was from 9KHz to 3GHz (specialized range was selected when sensing and control devices were being measured). The through, open, short, match (TOSM) (also called SOLT or 12-term error correction model) calibration was done on the equipment at the beginning of every series of measurement: this calibration type

uses four known standards reflection and transmission measurements on DUTs with 2 ports, it is characterized by high accuracy. To characterise and conduct biological testing, the equipment was turned On, the above calibration and settings were then implemented, then the device of choice was connected to the equipment, after the average factor has reached the set value, then measurements of the S-parameters were taken. This process is repeated for all the device connected for either characterisation or biological testing.

4.9 Semiconductor Device Analyzer

The semiconductor device analyser (SDA) is a characterisation device that integrate multiple measurement and analysis capabilities for accurate and quick device characterization into a single instrument. For this work the Agilent B1500A semiconductor device analyser was used for the characterization of the produced devices by determining their conductance. The complete SDA is made up of two sections, The Agilent B1500A EasyEXPERT electronic system and the outer conductors of the manipulators/positioners. This device has resident graphic user interface (GUI)-based software running on the it embedded Windows 7 platform and is equipped with the 15-inch LCD with touch panel, hard disk drive, DVD-ROM/CD-ROM/CD-RW drive, and USB/LAN/GP-IB interfaces. The USB keyboard, the USB mouse, and the stylus pen are available as option.

This equipment can operate from any single-phase AC power source supplying 90 to 264 V at 47 to 63 Hz. To characterize the DUT for conductance measurement a voltage range of -2V to 2V was set, then the DUT is place in the device holder section where easy connection is achieved between the device and the outer conductors of the manipulators/positioners. After this arrangement, the calibrate/measure button was activated on the Agilent B1500A electronic system for the parameter characterization, and onward exporting of the results into an external storage device. A typical conductance measurement on rGO filter using the SDA is shown in figure 4.1 below.

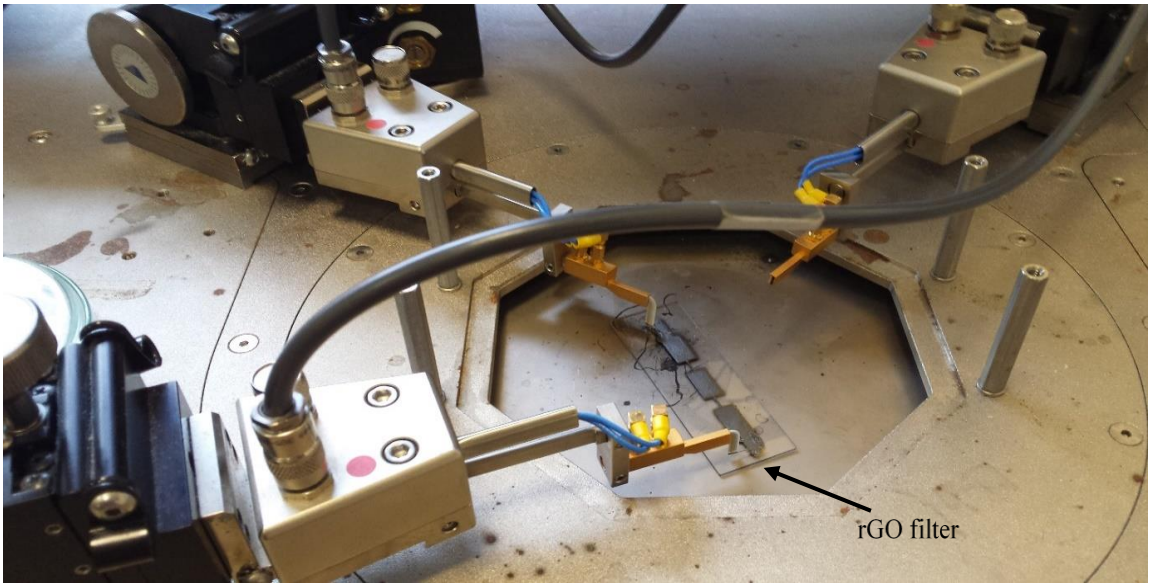

Figure 4. 1 SDA testing of a rGO filter

4.10 Scanning Electron Microscopy

The scanning electron microscope (SEM) can make images of solid samples and can determine the elemental composition of the said sample (when the EDX scan result is of interest). The maximum magnification is generally determined by the size of the electron beam and can be as high as one million. The best resolution of a high-end SEM is on the order of 0.5 nm. In addition to collecting imaging data to show the morphology of a sample, SEMs also generate and can collect X-rays that are characteristic of the elements in the sample. This is usually done with an energy dispersive X-ray spectrometer (or EDS system). EDS X-ray data can be used to determine the elements in the sample. If the X-ray data is mapped as a function of spatial position, an X-ray map showing the distribution of the elements in the sample can be created. The detection limit for EDS is generally on the order of 0.5% by weight within the X-ray generation volume. For this work the Hitachi TM3030 SEM system was used, this system has an accelerating voltage of 5 kV and 15 kV, with a magnification range from 15x to 60,000x, the maximum specimen size to be use with this system is 70mm diameter, and a maximum specimen thickness of 50mm. The main unit has a recording pixel of 1280×960 pixels (max.) / 640×480 pixels.

The working height in this system is 8.6cm, the sample thickness and diameter are stated in the specification above, the initial magnification was set from 18,000 to 50,000 times, after which it was then reduced to zoom in as needed. This equipment was used in this work to take a high-resolution 3D image of a section of the sensor element produced, while the EDX result of the system was used to determine the availability of carbon on a substrate, which indicates the presence of graphene (since graphene is the carbon material that was used to fabricate the device).

4.11 Kapton Tape

The need to explore the production of cost-effective materials that can find application in the area of biosensor especially in the disposable types, that can lead to the cheap mass production of sensing element, has led to the quest to investigate a graphene-like material that is derived from a polymer, particularly the Kapton tape. This Kapton tape is a Tesa® 51408 orange coloured masking tape with silicone adhesive, with the backing material being made of polyimide (Kapton). The tape chosen for this work is 0.07mm thick, 25mm wide, and 33m long obtained from RS Components . This high-grade masking tape polyimide is ideal for masking applications with permanent high temperature [115]. They are classed as a flame retardant material with a dielectric breakdown voltage of 7500V and has a strong chemical resistance property [115]. The Kapton tape was used to fabricate a lowpass sensing filter element as illustrated below.

There are two basic categories of material (Kapton tape), with different processing condition, from which eight samples of this material with varying parameters were produced. The two categories of samples are: the multiple strip line and the single strip line. The two main parameters that were varied during the production were the speed at which the laser engraves on the Kapton tape and the width of the strip line. The multiple strip line material involves rewriting the single strip pattern 5 times at 2mm distance apart on the chosen face of the Kapton tape. The multiple strip line sample is made up of four set of samples, where each sample is made up of five engravings with varying laser power settings ranging from 26% to 34% in increment of 2% (this was determined based on test

carried out on the pre-test samples to ascertain the power settings that would produce a material with suitable property). This fabrication principles also applies to the single strip line, it has the same fabrication principles and the same parameters as its multiple strip counterpart but differs by the number of strip line on it (in its case it is just a single strip line). Figure 4.2 illustrate the laser irradiation process by the laser machine, where it shows initially the substrate, it then showed the Kapton tape on the substrate and finally the end material derived as a result of the laser irradiation by the laser machine.

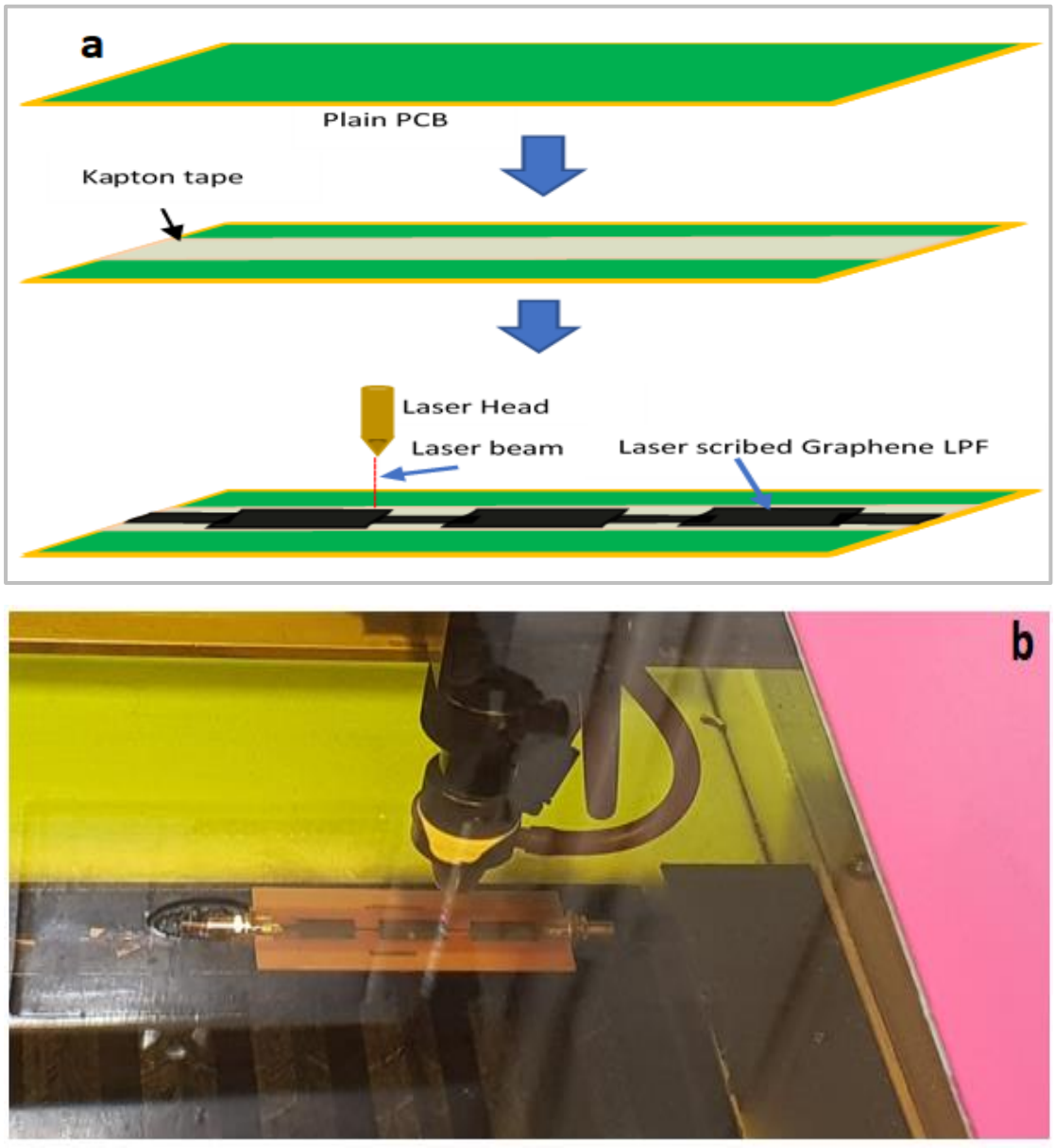

Figure 4. 2 The HPC laser machine engraving on Kapton tape to produce an LIG, a) The fabrication phase, b) The device fabrication from the LIG material.

For the multiple strips, the two main parameters which are the speed at which the laser engraves on the Kapton tape and the width of the microstrip, were chosen and set. These parameters change from sample to samples to produce the four sets of samples for each category of samples. The same principle applies to the single strip samples, but in this case the strip was a single strip of engraved line. For both the multiple strip line and the single strip line the samples main fabrication parameters are shown in table 4.2 below.

Table 4. 2 Settings used to produce the microstrip laser scribed graphene

Parameter	Sample 1	Sample 2	Sample 3	Sample 4
Speed (mm/s)	300	300	400	400
Width (mm)	300	350	300	350
%Power	26,28,30,32,34	26,28,30,32,34	26,28,30,32,34	26,28,30,32,34

These sets of settings were employed for both the multiple strip line and the single strip line, which resulted in samples amounting to 40 in total, which means once for each power setting. To achieve the design of these samples after the mathematical design as shown for a LPF as described in section 3.5.2.

1. Kapton tape was attached to the FR4 substrate material and placed into the HPC laser engraver.
2. Then the system was set with appropriate settings.
3. The taped sample was then introduced into the working area of the laser machine for the engraving process.
4. The laser machine was then switched ON to commence the engraving of the taped sample, this process produced a graphene-material to be used for filter design.
5. The same procedure was repeated from the first step to the fourth steps for all the two categories to produce the entire 40 samples.

The result of the above procedure and the fabrication procedure is shown in figure 4.2 above, but for implementation the multiple strip line design was used for the LPF fabrication.

4.11.1 Printed Circuit Board

The FR4 substrate is simply a printed circuit board (PCB) which provides the needed electrical isolation between the signal carrying microstrip and the ground plane. The PCB will provide both the mechanical and thermal support. The use of the PCBs for this work was to serve as the substrate of the irradiated Kapton tape. The AD16, single-sided plain copper ink resist board FR4 with 35µm copper thick, 100 x 160 x 1.6mm was obtained from RS components and used for the fabrication of the LIG LPF.

4.12 Graphene Oxide

Graphene Oxide (GO) is the oxidized form of graphene, with oxygen containing functional groups decorating both edge and basal planes [116, 117]. Its physical properties can be modified from those of fully oxidized GO to, almost those of graphene by simply removing the functional groups from its surface. This process allows it to be transformed from an insulating material to a semi-metal [116]. The investigation of this concept to exploit the change in the material conductivity for the mass production of sensitive and cost-effective sensing element is a research objective. The product used for this work is a dark brown, odourless liquid with a pH of 1.8 to 2 and a concentration of 6.2mg/ml in a 1000m container from supplier (Graphenea, Spain). The product is chemically stable under standard ambient conditions. This product was used for the fabrication of an electronic filter devices, the fabrication technique is as illustrated figure 4.2, starting from the preparation of the substrate.

Before using the quartz substrate for the fabrication of the rGO sensing element, it was thoroughly cleaned using the following procedure; It was first washed using distilled water and cotton bud to scrub away any sticky dirt, it was then rinsed with ethanol, and then also washed with isopropanol, after which they were further cleaned by putting them in a glass box with a mixture of ethanol and Isopropanol and covered, then this glass box was the put in a Sonicator for 15 minutes. Upon taking them out of the Sonicator, they were then dried using nitrogen gas, further cleaning was done using an oxygen plasma for 10

minutes, this process ensured that the surface of the substrate was free of contamination so as to allow for the administering of the GO using the designed mask.

The next step was to then make a solution of the GO to be used for the filter implementation. This solution was made by simply diluting the concentrated GO with distilled water to get the required concentration of GO for the proposed device production. The concentration of the GO from supplier is 6.2mg/ml, this concentration is quite high for the intended spraying application where a microstrip of the material is required to produce the sensing surface, this concentration was then diluted to 1mg/ml and 10ml of this was then loaded into the spray gun for the sensor element production. Where an average of 3mL was used to produce each filter element.

There are two basic reason for diluting the concentrated GO:

- To reduce the viscosity so that GO can easily be sprayed using the spray gun for the filter production.
- To ensure that only a thin uniform layer of GO was produced on the surface of the substrate, to achieve layers that are highly sensitive for the proposed biological application.

After the GO has been prepared, the mask (mask fabrication details given in sections 4.4.1 and 4.4.2) was then transferred onto the surface of the substrates. These masks were allowed on the surface for a few minutes before the introduction of the GO. While the masks were settling on the substrates, a hot plate was switched ON and its temperature was set and maintained at 120^{o} (this was to ensure that the GO ink dry off immediately (and not flow) once it hits the surface and for the fabricated filter to have a uniform flat surface all through its length). The prepared GO was then poured into a spray gun, then the union of the substrate and mask were then placed on the hot plate. With the help of the spray gun the GO was then sprayed on the surface of the substrate containing the mask, at a predetermined speed of 6 seconds for each to-and-fro action (pass), the number of passes done was dependent on the filter being produced. After the spraying

was over, the resultant unit of the substrate, the mask and the GO was then left on the hot plate for another 5 minutes before taking it off, this was then allowed to cool down before the mask was taken off the substrate, leaving on it the traces of the GO filter geometry on the surface of the substrate.

At this stage, the produced filter is a GO filter, so in order to chemically reduce it, the now fabricated GO filter was then place in a glass dish, wherein drops of Hydrazine Hydrate of ~80% in H_2O was introduced in the glass dish without it touching the filter. The dish was then sealed using a glass cover and a paraffin tape to make it as airtight as possible. This arrangement was then placed back on the hotplate at the same temperature of 120^0 and was then heated for 20 minutes all of which was done in a fume cupboard. Upon taking them down from the hot plate the filters were then allowed to cool down. The resultant filter produced from the reduction of GO using hydrazine hydrate is now the reduced graphene oxide (rGO) filter. This filter is ready to be used as the sensing element of the sensor after characterisation. Figure 4.3 below illustrates the procedure explained above.

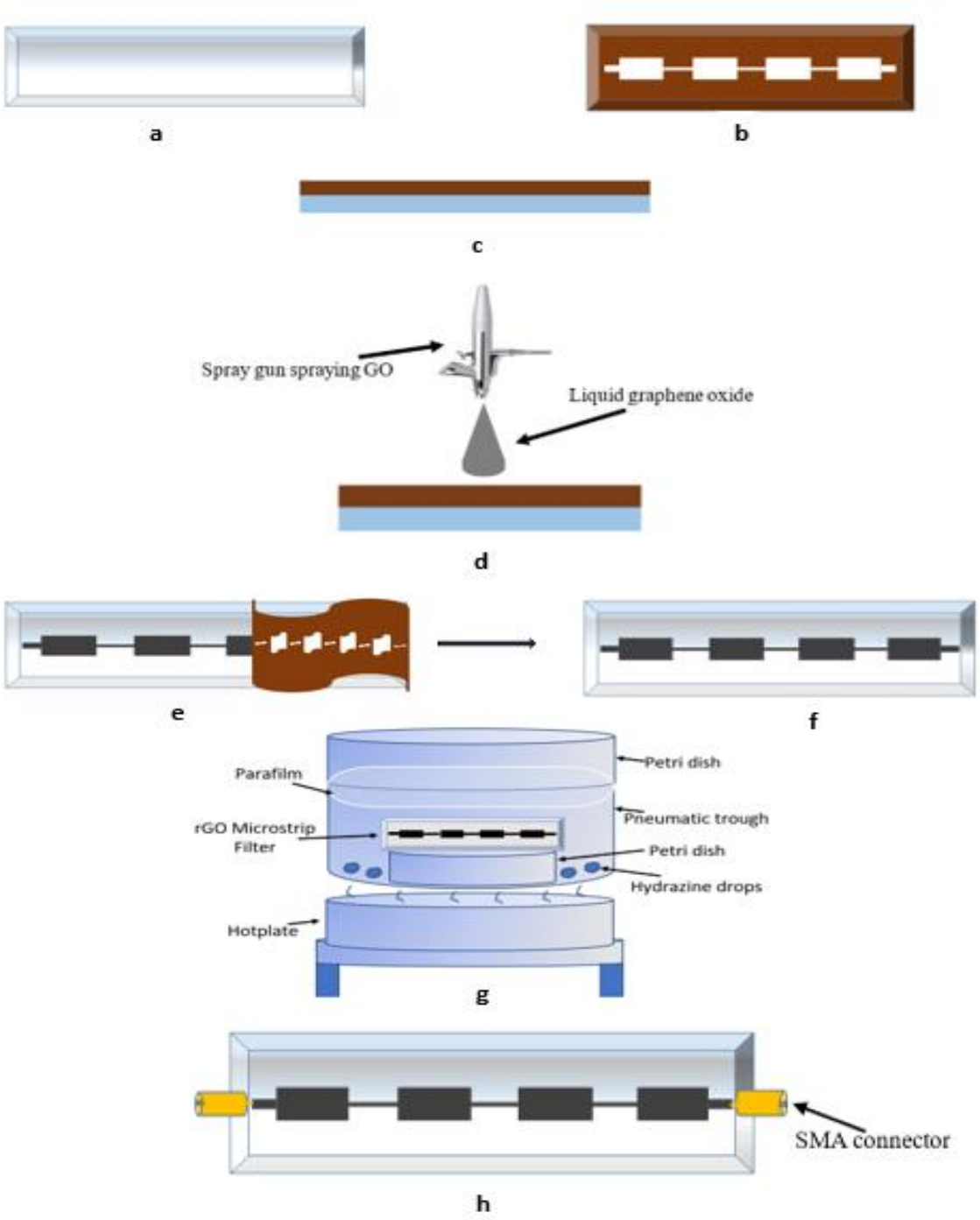

Figure 4. 3 The reduced Graphene oxide microstrip LPF fabrication procedure, a) the cleaned quartz substrate, b) Patterned Mask, c) Quartz substrate attached to patterned Mask, , d) Spraying process, e) Removal of mask from GO, f) GO on quartz substrate after the r

The procedure for implementing the filter element on the surface of the substrate is illustrated in figure 4.3a to 4.3g, this shows the step-by-step method on how to produce the microstrip filter on the chosen substrate. Figure 4.3h however shows the rGO filter on the substrate and an SMA connector attached. This arrangement was done to provide a

means by which the filter can be characterised and subsequently used for the proposed biological sensing.

4.13 Mask Fabrication

For the MLPF (microstrip lowpass filter) most produced from rGO and MBPF (microstrip bandpass filter) to be implemented on the desired substrate there need to be a shadow mask used as a guide for the filter fabrication. This section deals with how the masks used for designing the structure and geometry of the line element filter was fabricated. To implement the filter as a sensor its planar equivalent was designed, where the dimensions of the planar filter was determined. The sensor geometry to be fabricated was cut out on masks made of different materials because of their unique fabrication methods. The MLPF devices were produced from rGO (although a few MLPF mask were made from Perspex where some gold MLPF samples were produced), while the MBPF devices were produced from gold.

4.13.1 The MLPF Mask

The masks for the rGO sensors were specifically cut out on a sticky paper obtained from Poundland, this is so that it can easily be removed after the administration of the GO liquid. The sensor is basically a filter which was designed as a planar type, which was then produced on the thoroughly cleaned surface of the substrate (for this work, a quartz substrate was used). The geometries of the MLPF were designed in AutoCAD software. This designed was then transferred to an HPC laser machine (the same laser machine used for the engraving on Kapton tape in section 4.2 above), which was then used to cut out the geometry on the material (for rGO it is a sticky paper), several of these masks were made for the number of substrates that was available. They were then taken to the lab to be used to fabricate the precise sensor geometry on the substrate using the spraying technique. Figure 4.4 below shows the geometry of the paper cut out mask used to produce a MLPF.

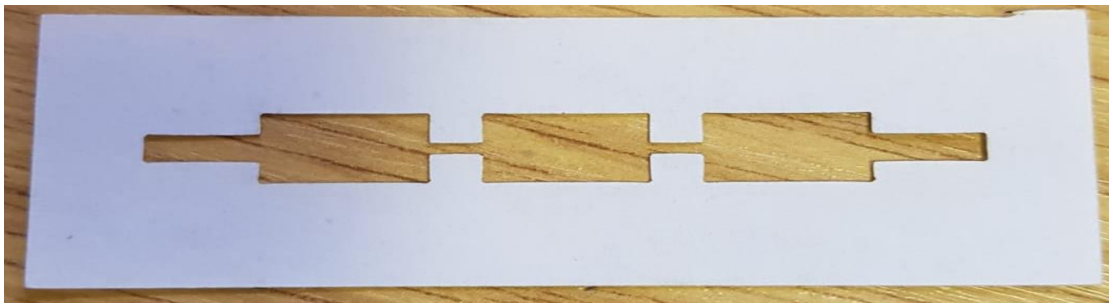

Figure 4. 4 A 5th order LPF made on a sticky paper

4.13.2 The MBPF Mask

As for the shadow mask used for the implementation of the gold sensor devices their fabrication is a little different. To make the gold film filter, the first step was the same as that of the rGO filters of the MLPF above (the mask for these sets of filters were different) because they were designed using AUTOCAD Inventor, and was then transferred for cutting using the milling machine, this CNC milling machine (Datron micro milling machine) was then programmed for cutting a circular Aluminium plate cut as a disc, from this disc the filter geometry and arrangement was also cut out, a sample of this disc, filter arrangement and geometry used for MBPF is shown in figure 4.5a below (the actual disc used had space for 6 slides even though this one is showing space for three slides). Although the initial mask was made from Perspex shown in figure 4.5b but, because the evaporator could not pump down to a low enough pressure, this was changed to an aluminium disc. The actual disc used has a diameter of 150mm (this is due to the shape and size of the holder in the evaporator), on each of these discs, 6 standard quartz glass of 75mm X 25mm was made to fit on each (these quartz slides were arranged on the discs to accommodate as many slides as possible) by creating a recess of 0.5mm depth.

There were 8 of these discs produced each disc has a face that is the structure and geometry of the desired filter and has no covering at the back that allows for the back of each of the quartz to be easily reached by the gold film during evaporation, this back thin gold film will serve as the ground plate on the other side of the substrate. These metallic shadow masks of 8-disc having 6-quartz slides on each disc held in place by a photoresist was then transferred to a Blazers e-beam deposition machine for the final process of thin-film deposition of gold, the result of the deposition was then used for the proposed sensor

element. Less attention was paid to the Perspex disc because their design and the mode of extracting the quartz sample needs to be improved upon too.

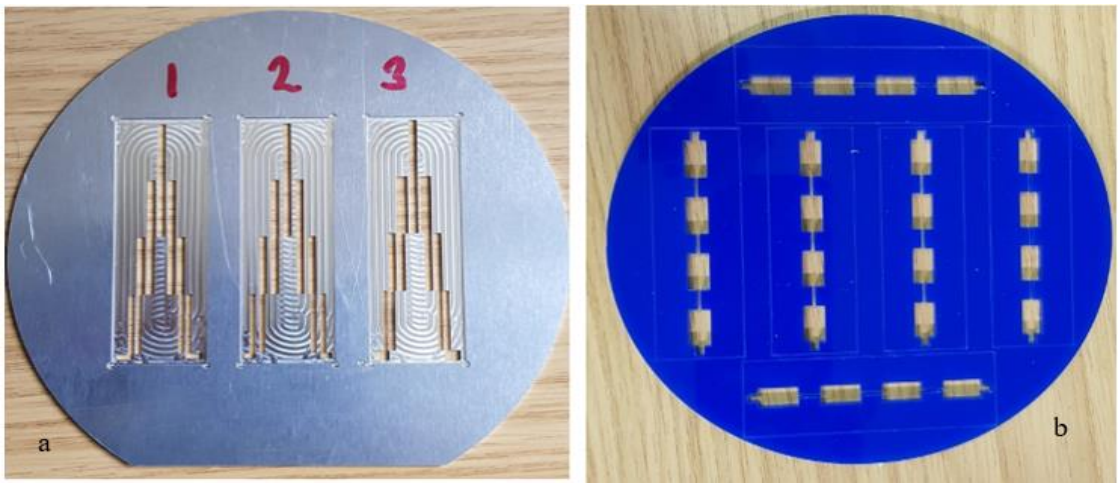

Figure 4. 5 Circular disc for gold microstrip filter fabrication, a) the circular disc of the Aluminium mask, b) the circular disc of the Perspex mask

4.14 Electrical Characterisation of Device

The above discussed material characterisation techniques were needed to be highlighted in order to state the techniques by which other materials used for the implementation of the microstrip filter can be verified and their characteristics validated, this is to give an insight into their suitability for their intended application. However, the Electrical Characterisation of Devices in this work involves using a vector network analyser (VNA) to determine the filter response characteristics with and without the application of the sample of interest on the point of interest to the DUT. These characteristics include the insertion loss between ports n and was obtained from the S-parameter (S_{12} or S_{21}) called the transmission coefficients and the return loss at ports n, that was obtained from the S-parameter (S_{11} or S_{22}) called the reflection coefficients. The determination of this electrical characterisation of the devices aided establishing that the filter response is a true representation of the designed filter from which the sensitive and most responsive point of interest was decided.

Having obtained these characteristics, the next phase was the determination of the sensing site on the filter. This point was determined by the application of known solution (for this work a mixture water and alcohol solution was used). This exercise was done repeatedly on various spots on the filter to help determine the most suitable point for use in the proposed biological application. The procedure for the characterisation of devices is that, from the first fabrication run (comprising both LPF and BPF), different devices were chosen, and liquid applied on them to test their sensitivity. Results from this indicated the most optimum design which was manufactured in a second fabrication run. From this second run (all being 5^{th} order BPF) one device was selected to be used as a sample for the characterisation exercise. Since all the devices of the second run were of the same design, the idea of selecting one was so that repeatability of results was expected on all the devices. The selected device (the DUT) was then connected to the already calibrated VNA noting which point was connected to port 1 and port 2 respectively (this was to ensure that the test results remain consistent for each device connected in the same manner), the result of this connection indicated the response of the filter on the graphic user interface (GUI) of the VNA. To see which part of the device was most sensitive to change in conditions (which is the characterisation of the device), a fixed amount of solution was added to specific points of the device. The procedure was as follows.

1. VNA calibration was done to choose the desired equipment settings and to reduce measurements error
2. Frequency range was set from 9KHz to 3GHz
3. A reservoir was attached to the surface of the device, this contained specific areas in which a defined volume of fluid could be held as shown in figure 4.6
4. Using a pipette add 60 µl of water at point A of figure 4.6
5. Measure and record results of the S11 and S21 parameters separately.
6. Remove water from point A.
7. Repeat step 4 to 6 for six times.
8. Change reservoir location to a predetermined point on the device.

9. Repeat steps 4 to 7 for each of the defined reservoir locations.

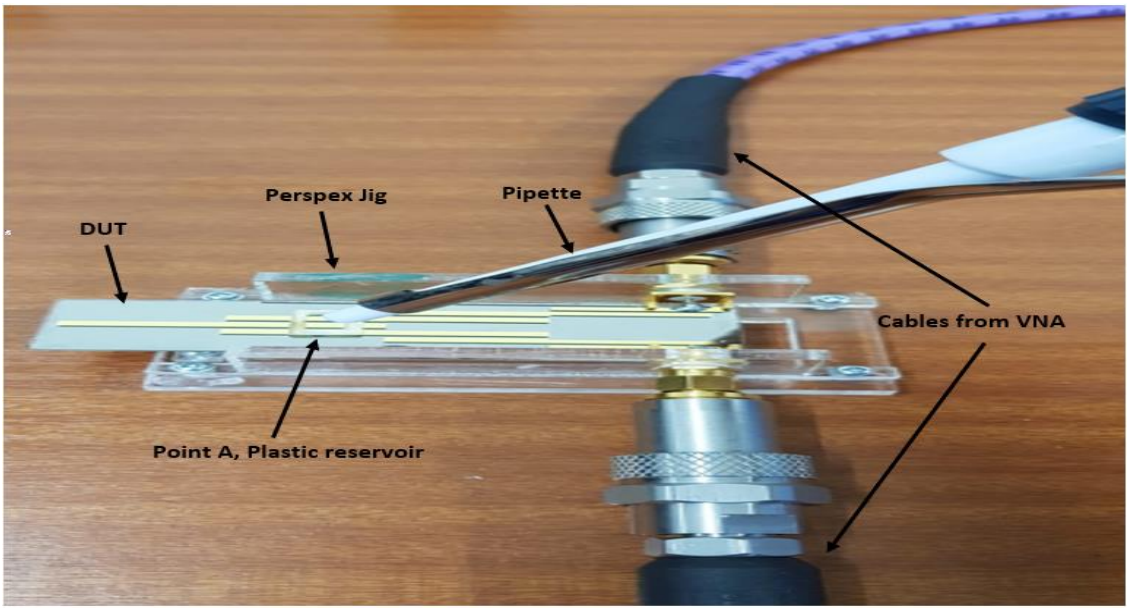

Figure 4. 6 A DUT connected to VNA with attached reservoir at point A

The purpose of this test was to identify the point that produce the most significant change in the filter frequency and gain responses caused by the introduction of the liquid sample being tested on the device under test. The test sample was administered into a rigidly fixed reservoir attached to the same points on the filter, this was exclusively done on several chosen points (that were determined from the results of simulation and prior test sample devices) on the filter surface. The test results were observed and recorded in the form of an S-parameter as a CSV file for onward processing. Figure 4.7 below gives a simple illustration of the connection between the DUT and the VNA equipment used in the characterisation of the connected filter.

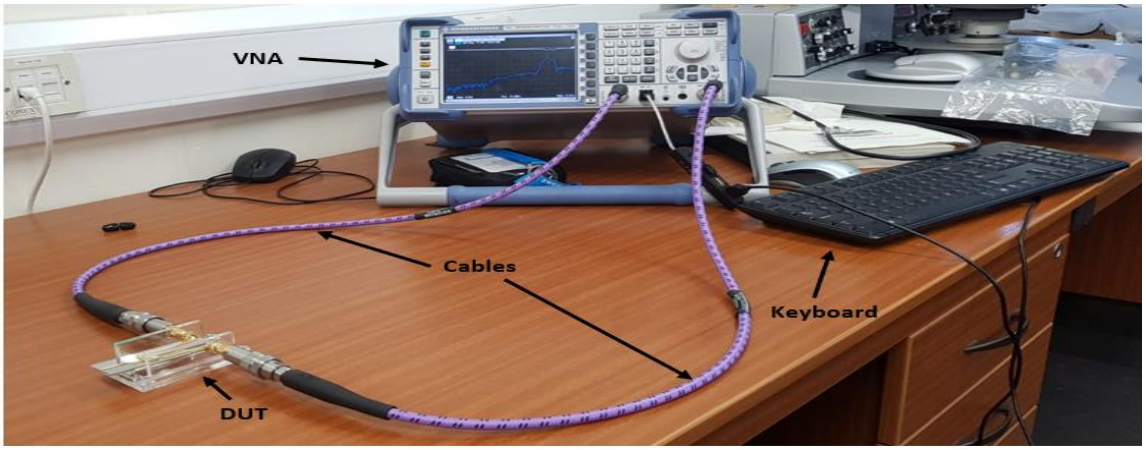

Figure 4. 7 Typical connection between the DUT and the VNA used for both characterisation and testing

4.15 The reservoir

This is the hollow rectangular shaped plastic that was attached to the selected point on the device, where the chosen sample was held-in to allow for constant interaction between the sample and the sensing element of the fabricated device, this is to allow for any changes due to this sample-sensor interaction to be observed on the measuring device (the VNA in this case). To fabricate the reservoir the first step was to get the sizes of the points of interest on the device(s), for this work the size is 7mm x 5mm, having determined the desired sizes, a hollow rectangular shape of these sizes was then cut out from a plastic using the HPC laser cutter already discussed in section 4.4. This hollow reservoir was cleaned and then glued to the surface of the device at the chosen points where the sample was intended to be introduced to allow for measuring of the response of the devices.

4.16 Summary

This section of the work looked at the materials and methods used in the fabrication of the microstrip devices, beginning with the initial Kapton tape material that was used to fabricate a graphene-like material (i.e. LIG), with a brief procedure of how it was achieved. Then the graphene oxide which was used to produce a reduced graphene oxide sensor was discussed, by outlining the fabrication procedure as well as the fabrication of mask

types. This chapter also talked about the substrate used which was mainly quartz, where some of its relevant useful properties were listed. The usage of FR4 (the PCB) as the substrate for the initial design was also talked about as well as the SMA connectors being used for connecting the DUT to the VNA. Also deliberated upon was the fabrication and characterization equipment used. Three types of fabrication process where demonstrated, issues identified were low conductivity for the LIG and lossy substrate due to the usage of FR4. The rGO showed improved conductivity as compared to the LIG, but conductivity value was not as high as that of the gold material. Each fabrication procedure produced sensors of the required geometry to an accuracy of ±0.05mm. A test procedure was used to identify the most suitable areas on the sensor for the gold device, this result then informed the point to implement the functionalisation protocol for the biological sensing application. The results of this testing are detailed in chapter 5.

Chapter 5. Characterisation of Devices

5.1 Introduction

This chapter illustrates the characterisation of the sensor devices, which was done so that the point with the highest sensitivity on the device can be identified and selectively targeted for use as the point to be functionalised for the biological sample to be introduce for the proposed specific biosensing. Since characterization is a necessary step to determining the physical, chemical, and biological properties of materials before industrial applications. For this work however, the characterization was mainly electrical using a VNA and ANSYS simulations. To do this, the chapter is divided into 3 major subsections; the Gold devices, the Graphene (Kapton Tape) devices and the Graphene oxide (Ink Jet) devices, and in each subsection a preamble of the fabrication process was briefly given. The characterisation results were presented by placing on the same plot the response of the fabricated and the simulated results to enable easy assessment. The next section gives the characterisation of the devices produce using several selected materials.

5.2 Gold Film Sensor Fabrication

The gold device fabrication method is quite different from the rGO method, the only common denominator is their substrate cleaning process. To properly clean the quartz substrates to rid the surface of any metal or impurities the following procedures were used. The samples were rinsed using DI water in a weir, then further cleaned using N-Methyl-2-Pyrrolidone (NMP) which was heated to 70°C and the quartz samples were left in the NMP for at least 30mins with ultrasonic cleaning being used for some of the time. Isopropyl Alcohol (IPA) was used to rinse the NMP off the samples and this dries usually without residues. After the substrate has been cleaned, they were then taken to the laboratory for microstrip production.

It is important to note that the shadow mask made of Perspex as shown in figure 4.4b was initially used for the gold sensor device, but due to the fact that with Perspex mask, the desired sharp edges of the filter were not achieved and also in the process of detaching

the devices from the mask, there was difficulty experienced because of the glue used in holding the substrates in place, thereby leading to some of them breaking. More so, the Perspex melts in Acetone when cleaning, and more importantly the e-beam evaporator could not go to a low enough pressure with the Perspex. With these reasons the Perspex shadow mask was replaced with an Aluminum equivalent.

Before introducing the quartz slides into the evaporator, a means of keeping the slides fix in the designed recess of the Aluminum shadow mask was devised which was coating the quartz wafers with photoresist and they were then taped to the mask used in holding the slides down for the filter geometry to be fabricated. This technique was used instead, as photoresist would not scratch the Gold (Au) and it is easier to clean over than adhesives. This way the slides were easily cleaned using Acetone or similar reagent. For the metal deposition on the samples a Balzers e-beam deposition machine was used to put down 50/300nm of Ti/Au on the slides with the Ti being deposited first and then the Au film was then laid over. In the evaporator machine for the Ti/Au depositions, the samples were held above the crucibles used for metal evaporation and were manually turned this required 2 evaporation runs, so that the metal was also deposited on the bottom side of the slides as well. The result of this metal deposition process is shown below, figure 5.1 shows the gold 7th order MLPF device to be used as the sensing element of the biosensor.

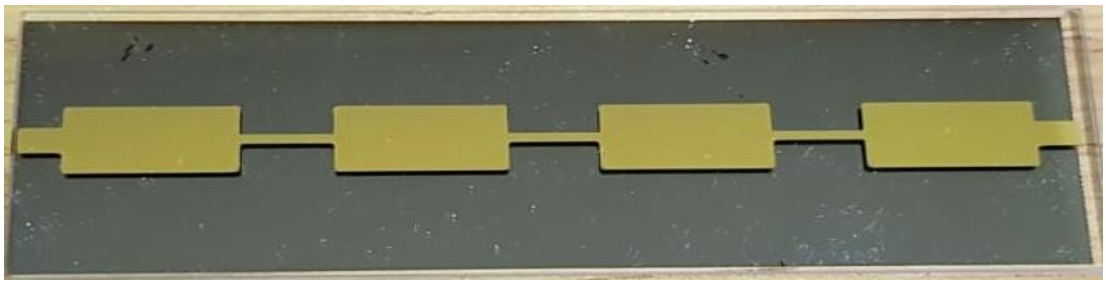

Figure 5. 1 The 7th order gold film filter (sensor)

5.3 Characterization of Gold Device

After the fabrication of the devices there is a need to characterize them so that their response characteristics can be determined, this is so that the most suitable point on the device is used for the sensing purpose so as to achieve the intended selectivity and

sensitivity and as well ensured that the fabricated devices meet the design requirements. For these devices, the electrical characterization was done using a VNA, the observed response of the filter after the introduction of the test sample into an attached (with glue) rectangular reservoir at different points on the device under test (DUT) was recorded in an effort to locate the point of best/maximum resonance response. The results of the characterization of these devices are as shown in figure 5.2. To obtain these results two sets of parameters were recorded, the insertion loss between ports n obtained from the S-parameter S12 or S21 called the transmission coefficient and the return loss at port n obtained from the S-parameter S11 or S22 called the reflection coefficient, from the responses observed, the transmission coefficient did not indicate useful significant changes during characterisation hence, most of the reported results are the reflection coefficients. To locate the most suitable point on the device, two sets of devices were manufactured.

The first sets of gold devices (which comprises both lowpass filters of 5^{th} and 7^{th} order as well as the band pass filter comprising the 5^{th} and the 3^{rd} order) saw 1/3 of the devices characterised. This method would enable more samples to be characterised and ensured the response from individual characterised device is a representation of the set of devices fabricated, the results of the characterization of some of these devices is shown below.

5.3.1 Results for 5th order Lowpass filter

The observed results of this device are as shown below starting with an overlay of the simulated results with that of dry VNA measurements of the fabricated device as shown in figure 5.2. This is then followed by the results for water placement at various points on the device as seen in figure 5.4 below.

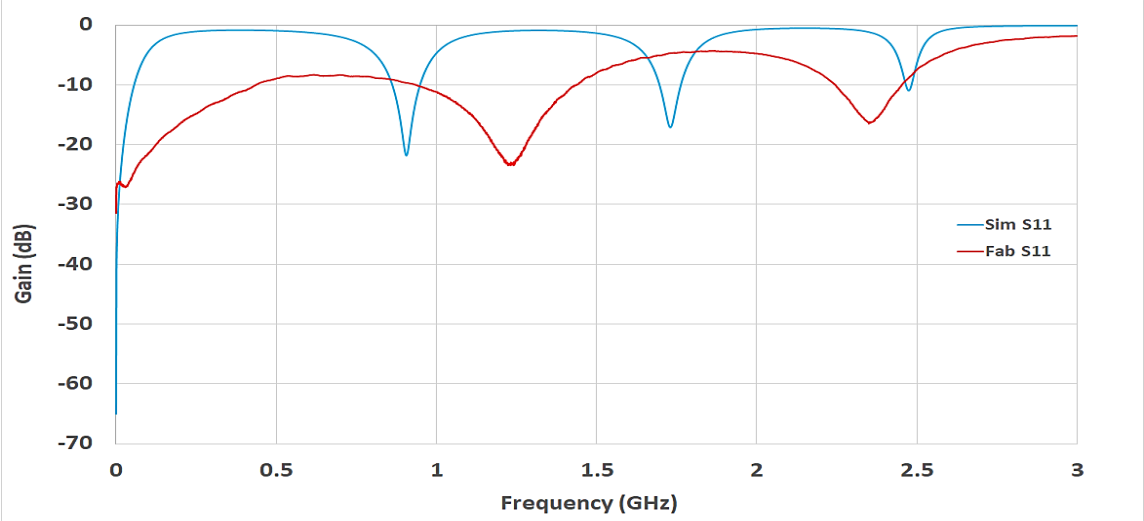

Figure 5. 2 The combine S11 plot of the fabricated and the simulated gold devices of a 5LPF

From the figure 5.2 above of the S11 plot for both the simulated (S11 Sim) and fabricated (S11 Fab) device response, the simulation response shows an ideal lowpass filter response with little loss and a greater number of resonant frequency peaks as observed from the plot, while the fabricated device shows a response that has resulted from losses associated with the conductor, the dielectric and loss to air, since it is not all the electromagnetic wave that travels through the microstrip device. This results also show how the fabricated device tends to show significant similarities with the simulated device, since the simulated response indicates an ideal behaviour of the device. The S11 of the fabricated and simulated response of the device was chosen because it is characterised by sharp peaks at its resonant frequency, making it a good way to use the device response for the intended biomedical application. The results of the response from figure 5.2 informed the frequency range for which the characterisation of the devices was carried out. The observed response of the characterised 5LPF is as shown in figure 5.4 below.

In order to get the desired point on the device for biological sample introduction, a means of determining the point on the device that gives the best response (measured on a VNA) as a result of the introduction of a sample onto it, thereby by making it the suitable, and the point with the most change in terms of shift in frequency (and gain). To achieve this, a sample (for this case tap water) was introduce to various parts of the device and their response recorded as observed. Then these recorded results were then combined to

enable the selection of the point that showed the desired response, so that it can be used as the testing site of the desired sample for the required biomedical application. Figure 5.3 below shows the points on the device where the test sample was introduced to enable the device characterisation.

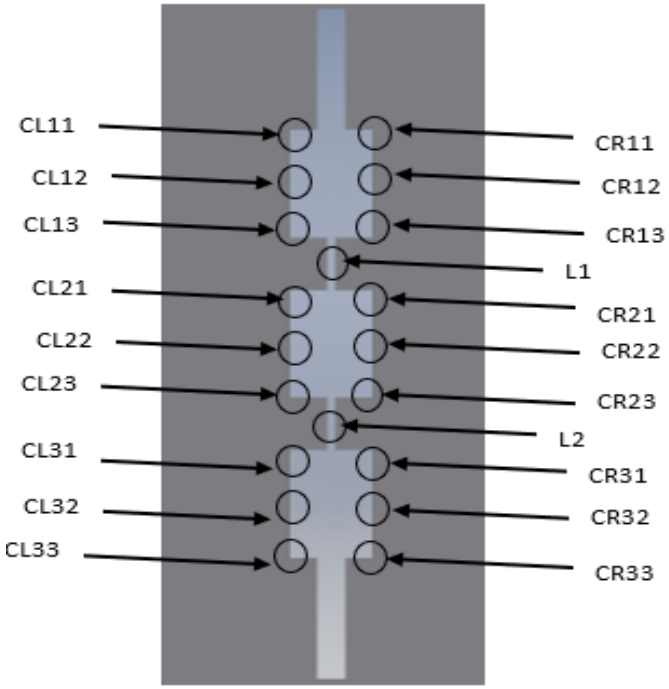

Figure 5. 3 Points on the 5LPF where sample was introduced for device characterisation

The results of the combined response of the several tests carried out when water was introduced at different points on the 5LPF device is shown in figure 5.4a below where result of 15LCL11 in the legend of the same figure refers to the measurement at point CL11 of figure 5.3, this was done up to the result of 15LCL33 of figure 5.4 referring to the measurement at point CL33 of figure 5.3. Similarly, the result of 15LCR11 in the legend of the same figure refers to the measurement at point CR11 of figure 5.3, this was done up to the result of 15LCR33 in the legend of figure 5.4 referring to the measurement at point CR33 of figure 5.3. Then the results of 15LL1 and 15LL2 in figure 5.4 are the measurement of the points L1 and L2 respectively, and finally, Plain means the result of the response on the plain device without the addition of water on the device for characterisation.

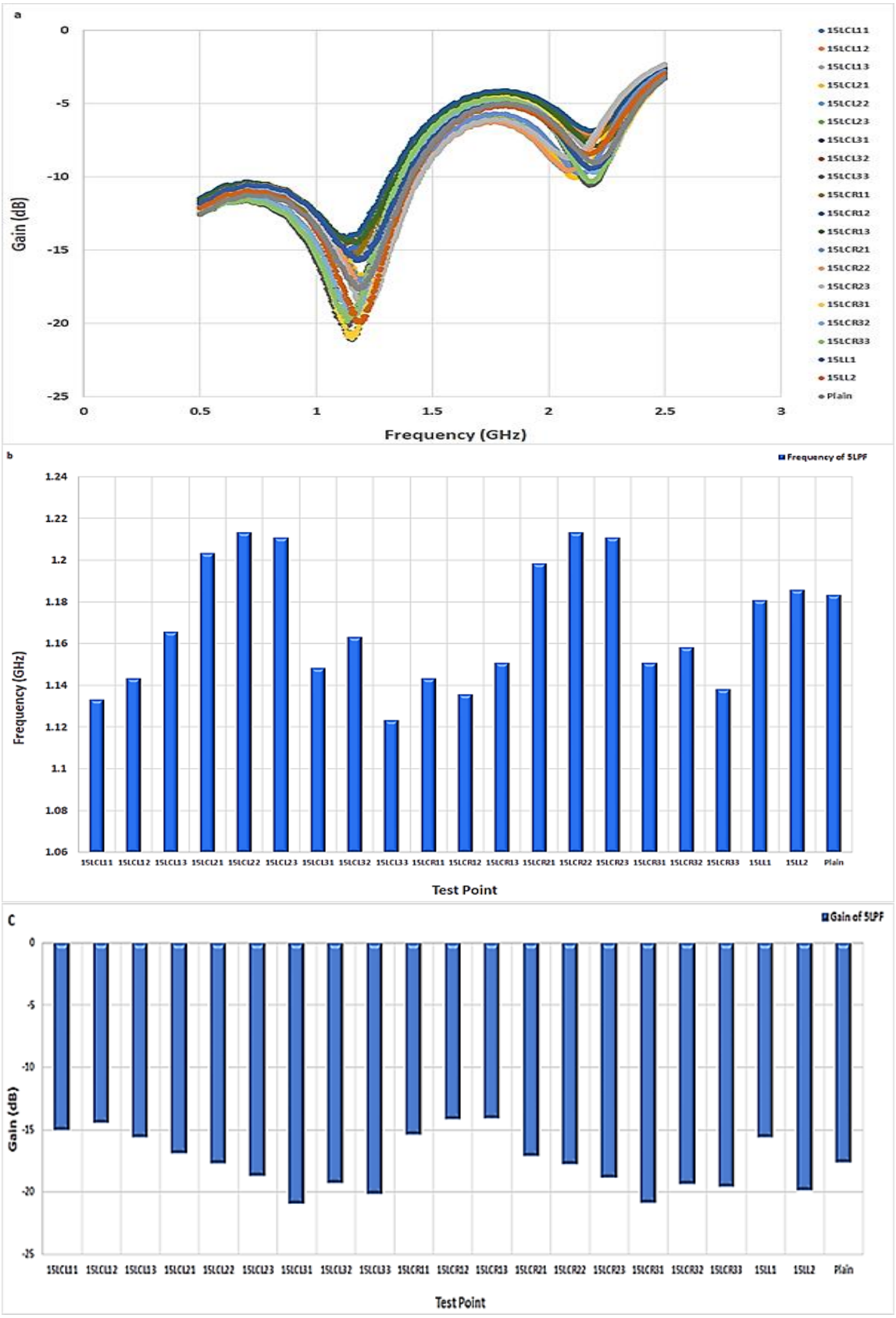

Figure 5. 4 The results of the combined response, a)The VNA response for S11 of 5LPF, b) the plot of frequency shift for each point , c) the plot of gain change for each point.

It is important to state that in order to process these results the lower frequency section of the plot in figure 5.4a was chosen because it indicated the desired gain peaks for the propose 5LPF and 7LPF devices. To elaborate these characterisation results, a histogram plot of the frequency shift for each position was done as shown in figure 5.4b. From this frequency plot however, it can be observed that the highest frequency was exhibited by test points 15LCL22 and 15LCR22 at 1.20GHz, but the mean value of the frequency of these test points is 1.17GHz, with a standard deviation of 30.1MHz. similarly, a histogram plot of gain change for each position was also plotted as shown in figure 5.4c wherein the peak gain was observed to occur at test point 15LCL31 at -20.86dB, while the mean value for all the test points is -17.53dB, and the standard deviation for the test point is 2.23dB indicating close gain values for the points. From the histogram plots of figure 5.4b and 5.4c it can be observed that the results show symmetry in their response and also the results of 15LCL11 and 15LCR11 are closer in value, so slight variation indicates repeatability (in terms of manufacture, positioning of fluid and measurement accuracy).

5.3.2 Results for 7th Order Lowpass Filter

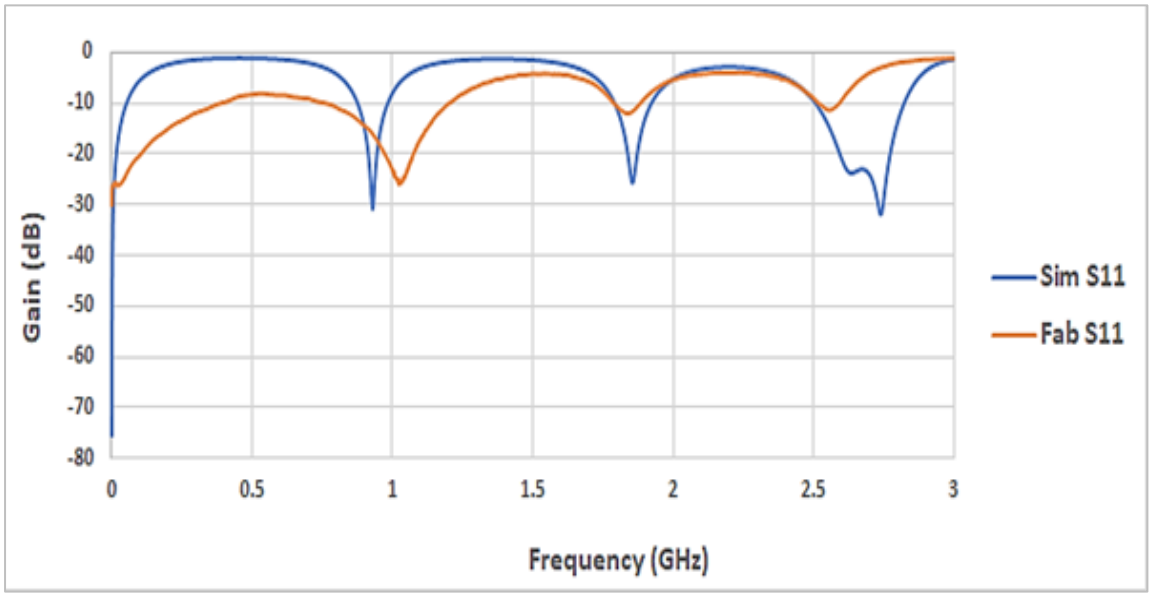

Figure 5. 5 The S11 plots of the fabricated and the simulated gold device of a 7LPF

From the figure 5.5 above of the S11 plot for both the simulated (S11 Sim) and fabricated (S11 Fab) device response, the simulation response just like the 5LPF response in figure

5.2 shows an ideal lowpass filter response with little loss and more number of resonant frequency peaks as observed from the plot. While the fabricated device response, when compared to the simulation response shows a response that has resulted from losses associated with the conductor, the dielectric and to air. These results also show how the fabricated device bear significant similarities with the simulated device, since the simulated response can be considered to exhibit an ideal behaviour of the device, without the losses associated with fabricated device. The results of the response from figure 5.5 informed the frequency range for which the characterisation of the devices was carried out.

In a similar approach like that done for the 5LPF a means of determining the point on the device that gives the best response as a result of the introduction of a sample onto it and indicating the point with the most change in terms of shift in frequency (and gain) was done. These points where characterisation was done is shown in figure 5.6. The observed results of the characterised responses of the 7LPF shown in figure 5.7, were recorded and then combined to enable the selection of the point that showed the desired response, to enable it usage for the required applications.

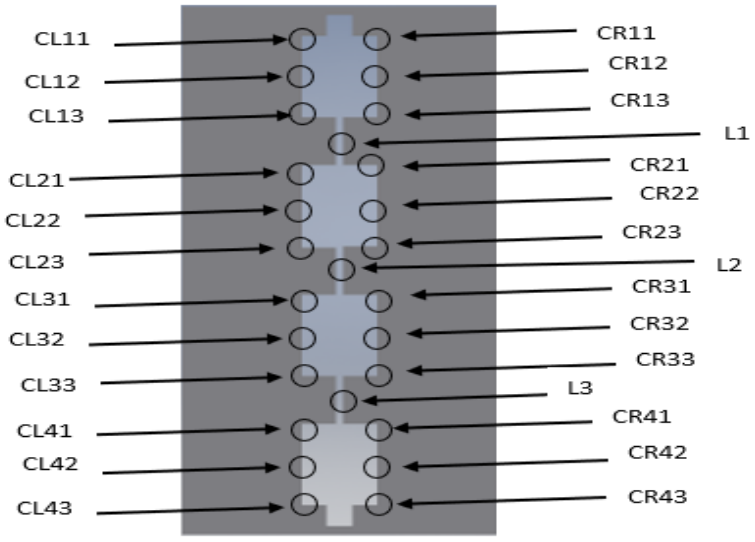

Figure 5. 6 Points on the 7LPF where sample was introduced for device characterisation

The results of the combined response of the several tests carried out at different points on the 7LPF device is shown in figure 5.7 below where below where the result of 17LCL11

in the legend of the same figure refers to the measurement at point CL11 of figure 5.6, this was done up to point 3 of the fourth capacitor where the result of 15LCL33 of figure 5.7 refers to the measurement at point CL43 of figure 5.6. Similarly, the result of 17LCR11 in the legend of the same figure refers to the measurement at point CR11 of figure 5.6, this was done up to point 3 of the fourth capacitor where the result of 15LCL33 of figure 5.7 refers to the measurement at point CR43 of figure 5.6. Then the results 17LL1, 17LL2 and 17LL3 are the are the measurement of the points L1, L2 and L3 respectively, and finally Plain means the result of the response on the plain device without the addition of waster on the device for characterisation.

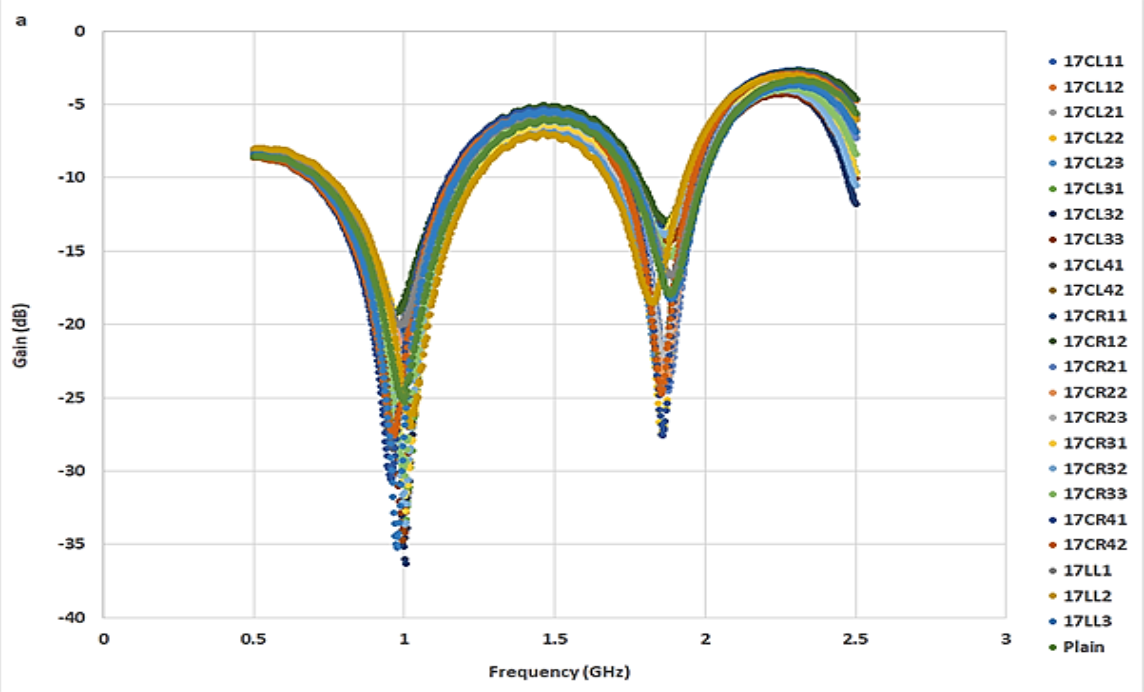

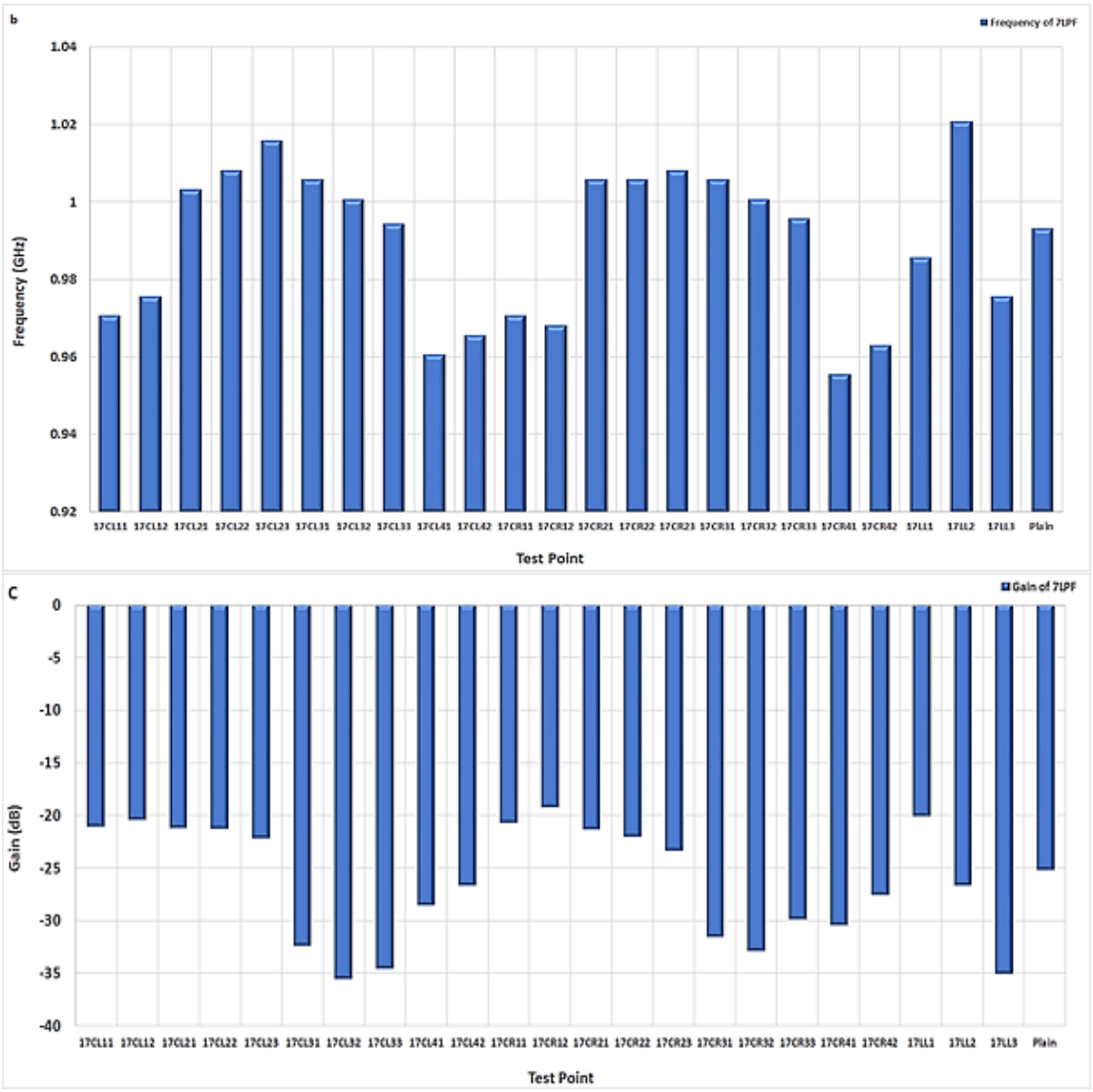

Figure 5. 7 The results of the combined response, a)The VNA response for S11 of 7LPF, b) the plot of frequency shift for each point, c) the plot of gain change for each point.

To simplify the characterisation result of figure 5.7a, an elaboration of the results was done as shown in figure 5.7b, where a histogram plot of the frequency shift for each test point was done as shown, from this plot it can be observed that the peak frequency was recorded at test point 17LL2 with a value of 1.02GHz. However, the mean value of the frequency peaks of the test points was recorded to be 0.99GHz with a standard deviation of 19.5MHz. In a similar manner figure 5.7c shows the histogram plot of the gain value for each test point, from which the point 17CL32 indicated a gain value of -35.45 dB, but the mean value of the peak gain for all the points is -26.18dB and a standard deviation of 5.42dB. From the histogram plots of figure 5.7b and 5.7c it can be observed that the results indicate symmetry in their response and also the results of 17CL11 and 17CR11 are

closer in value, so slight variation indicates repeatability (in terms of fabrication, positioning of fluid and measurement accuracy).

5.3.3 Results for 3rd order Bandpass Filter

From the figure 5. 8showing the S11 plot for both the simulated (S11 Sim) and fabricated (S11 Fab) device response, the simulation response shows an ideal bandpass filter response clearly showing the passband notch that is synonymous with an actual band pass filter. The fabricated device response also bears similar response, but its notch-shape at the expected passband has disappeared when compared to its simulated counterpart. The result of the simulated device response shows little loss and sharper frequency peaks as observed from the plot while the fabricated device shows a response that has resulted from losses associated with the fabricated microstrip devices. Since there is a trend of the combined plots from 0 up to 1GHz, this results also show how the fabricated device tends to show slight similarities with the simulated device, since the simulated response indicates an ideal behaviour of the device.

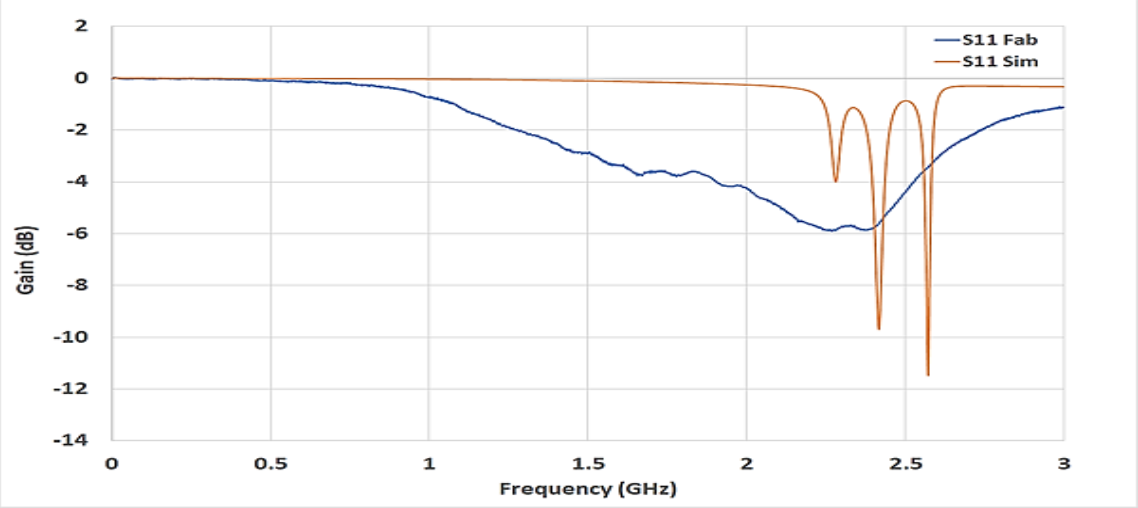

Figure 5. 8 Combine S11 plot of the fabricated and simulated gold devices of a 3BPF

Similarly, just as done for the LPF, a means of determining the point on the device that gives the best response as a result of the introduction of a sample (tap water) onto it and indicating the point with the most change in terms of shift in frequency (and gain) was

done. The observed results recorded, were combined to enable the selection of the point that showed the desired response, to be used for the required applications.

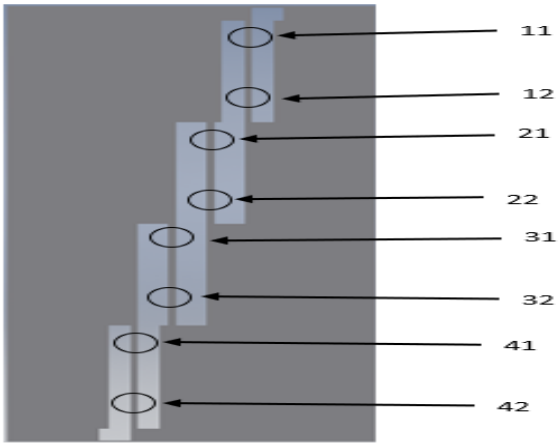

Figure 5. 9 Points on the 3BPF where sample was introduced for device characterisation

The results of these combined response of the several tests carried out at different points on the 3BPF device is shown in figure 5.10 below where the result of 13B11 on the legend of figure 5.10 refers to the measurement at point 11 in figure 5.9, this was done up to point 2 of the second slot and all through to point 2 of the fourth slot (point 42). And finally, the result of Plain on the legend of figure 5.10 which means the measurement of the response of the plain device without the addition of water on the device for characterisation.

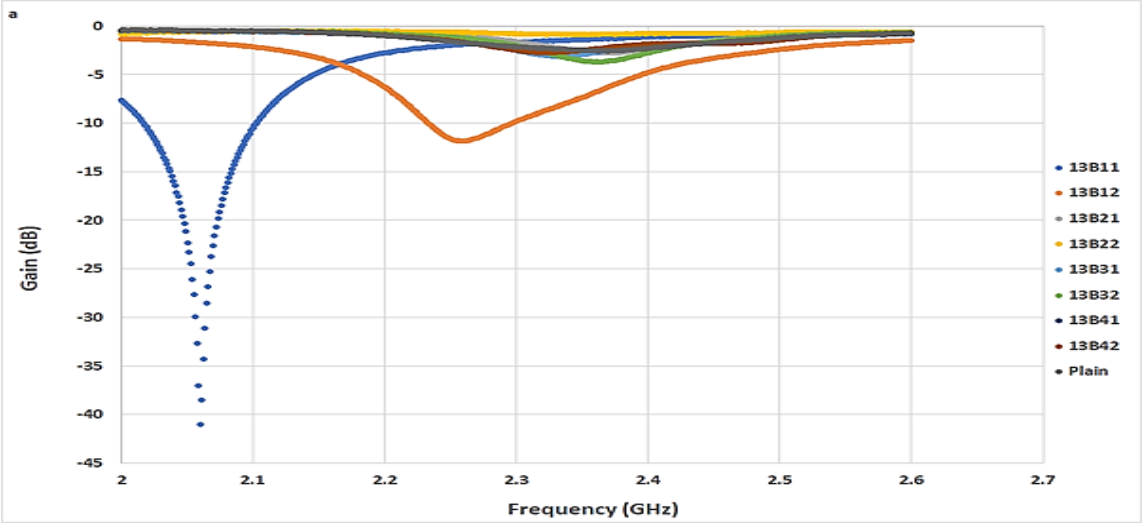

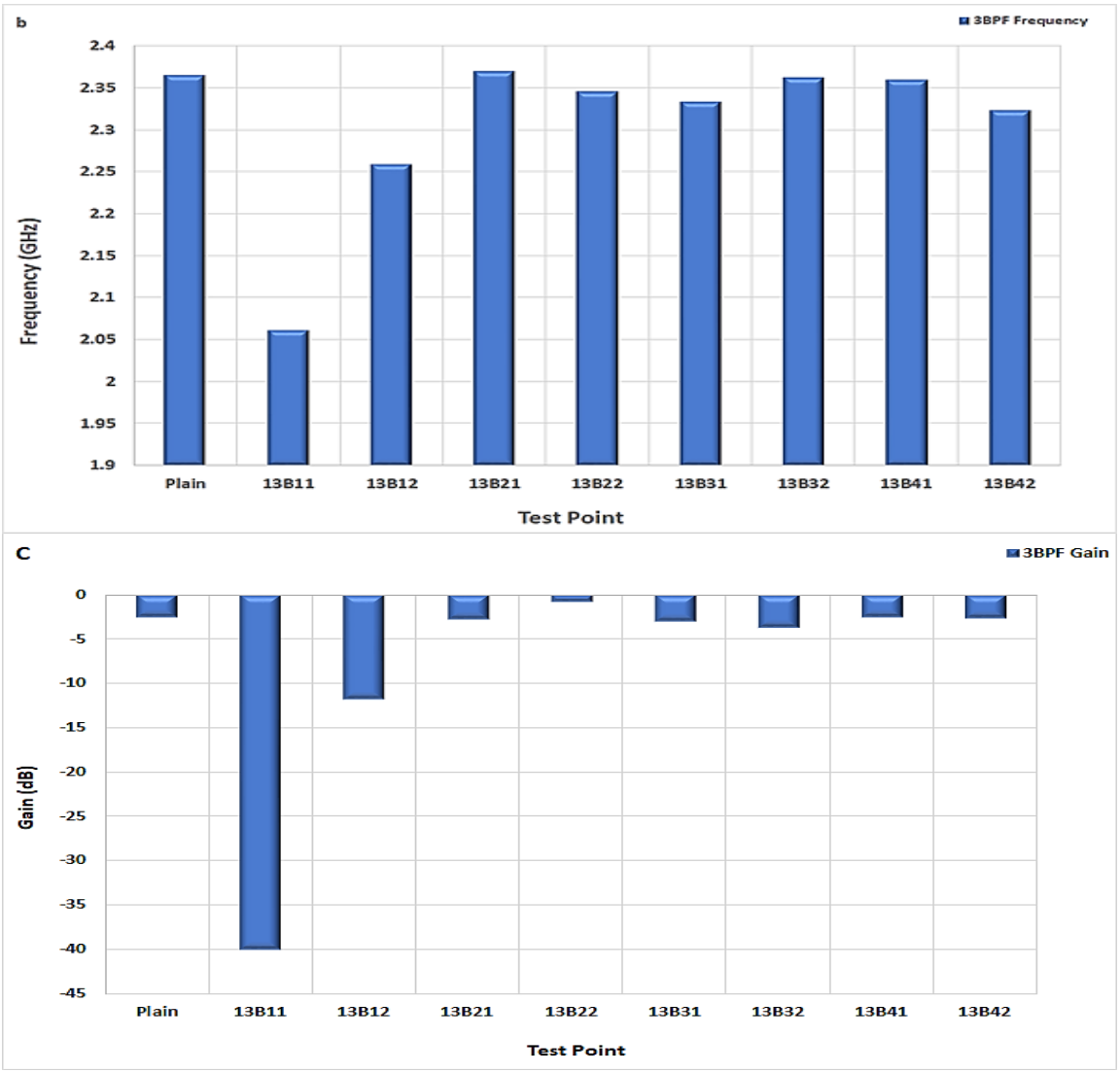

Figure 5. 10 The results of the combined response, a) The VNA response for S11 of 3BPF, b) the plot of frequency shift for each point, c) the plot of gain change for each point.

The histogram plot for figure 5.10a was done for the frequency shift for each test point on the device as shown in figure 5.10b, from this plot it was observed that the test point that exhibit the highest frequency shift is 13B21 at a frequency of 2.37GHz, however, the mean value of the frequency shift for all the test points is 2.31GHz and a standard deviation of 98.9MHz. Similarly, figure 5.10c is the histogram plot for the change in gain for the test points of the device wherein the peak gain value was observed to occur at test point 13B11 with a value of -40dB, but the mean value of this gain values is -7.78dB and a standard deviation of 12.48dB.

5.3.4 Results for 5th Order Bandpass Filter

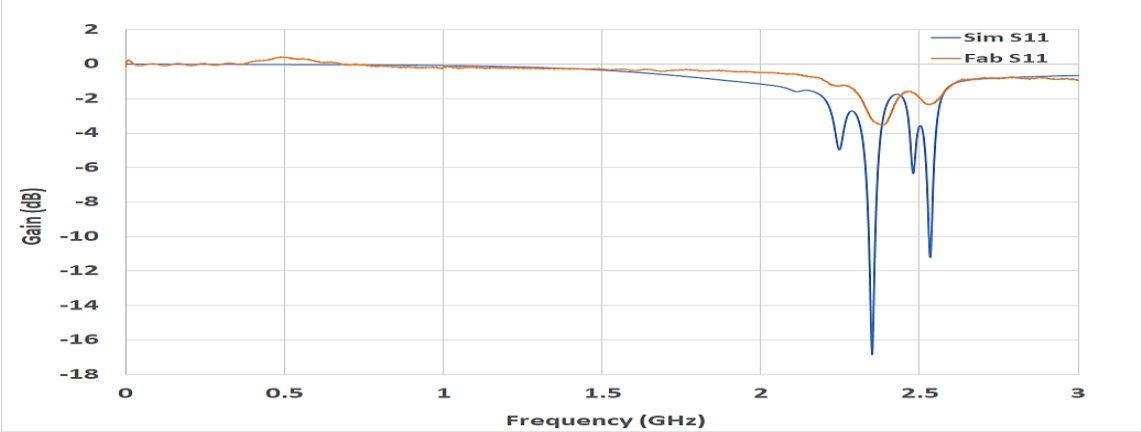

Figure 5. 11 The combine S11 plot of the fabricated and the simulated gold devices of a 5BPF

From the figure 5.11 above which shows the S11 plot for both the simulated (S11 Sim) and fabricated (S11 Fab) device response, the simulation response shows an ideal bandpass filter response with little loss and more resonant frequency peaks as observed from the plot while the fabricated device shows a response that has resulted from losses associated with a fabricated microstrip filter. The significant similarities between the fabricated device and the simulated device is shown by these results since the simulated response indicates an ideal or close to ideal behaviour of the device. From figure 5.11 it can be observed that the expected bandpass filter notch is more visible on the simulated response as compared to the fabricated device response, but the frequency at which the notch occurs for the simulated device tend to be at a slightly lower frequency (between 2.4GHz to 2.55GHz with a centre frequency of 2.475GHz) as compared to that of the fabricated device (between 2.46GHz to 2.55GHz with a centre frequency of 2.505GHz), indicating a response that bear similarity with the expected bandpass filter.

Just like in previous devices, a means of determining the point on the device that gives the most suitable response as a result of the introduction of the chosen sample (tap water for this work) onto it and indicating the point with the most change in terms of shift in frequency (and gain) was done. The observed results as recorded were combined to enable the selection of the point that showed the desired response that made it suitable to be used for the required biomedical applications.

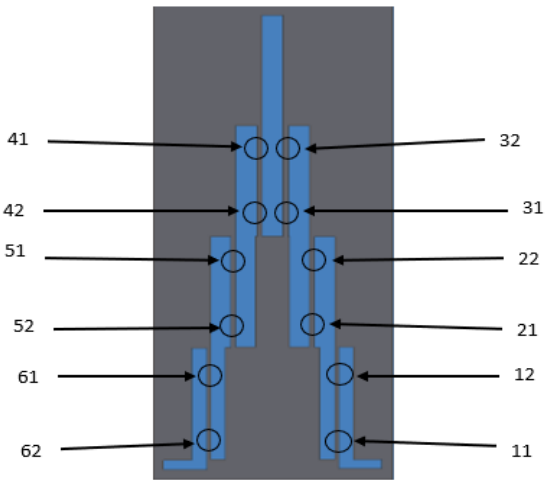

Figure 5. 12 Points on the 5BPF where sample was introduced for device characterisation

The results of these combined response of several of the tests carried out at different points on the 5BPF device is shown in figure 5.13 below where 15B11 on the legend of figure 5.13 refers to the measurement at point 11 in figure 5.12, this was done up to point 2 of the second slot and all through to point 2 of the sixth slot (point 62). And finally, the result of Plain on the legend of figure 5.10 means the measurement of the response of the plain device without the addition of waster on the device for characterisation.

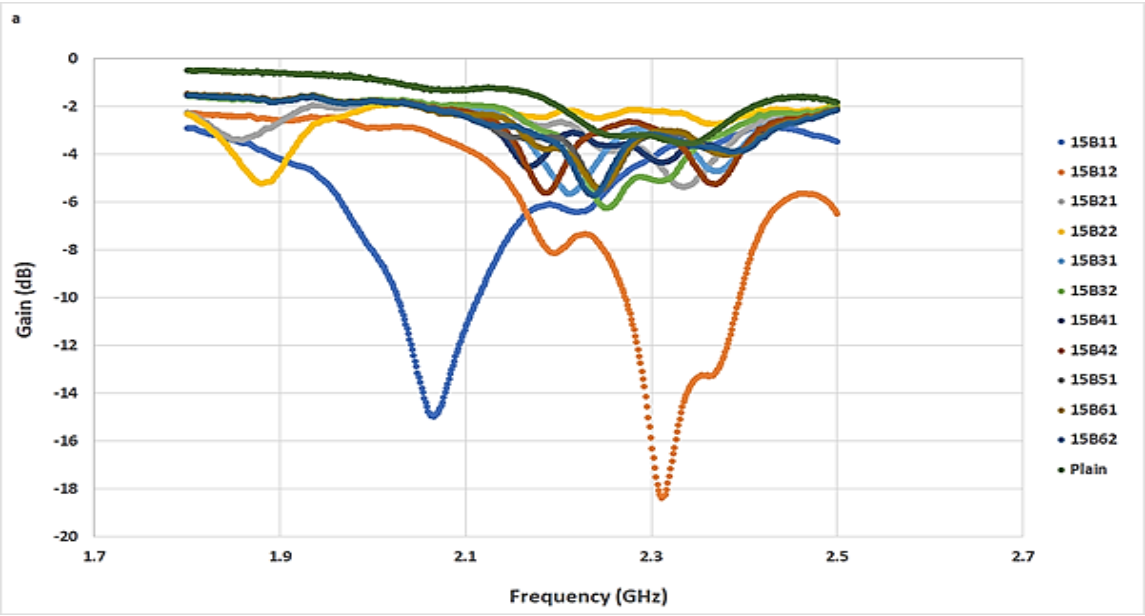

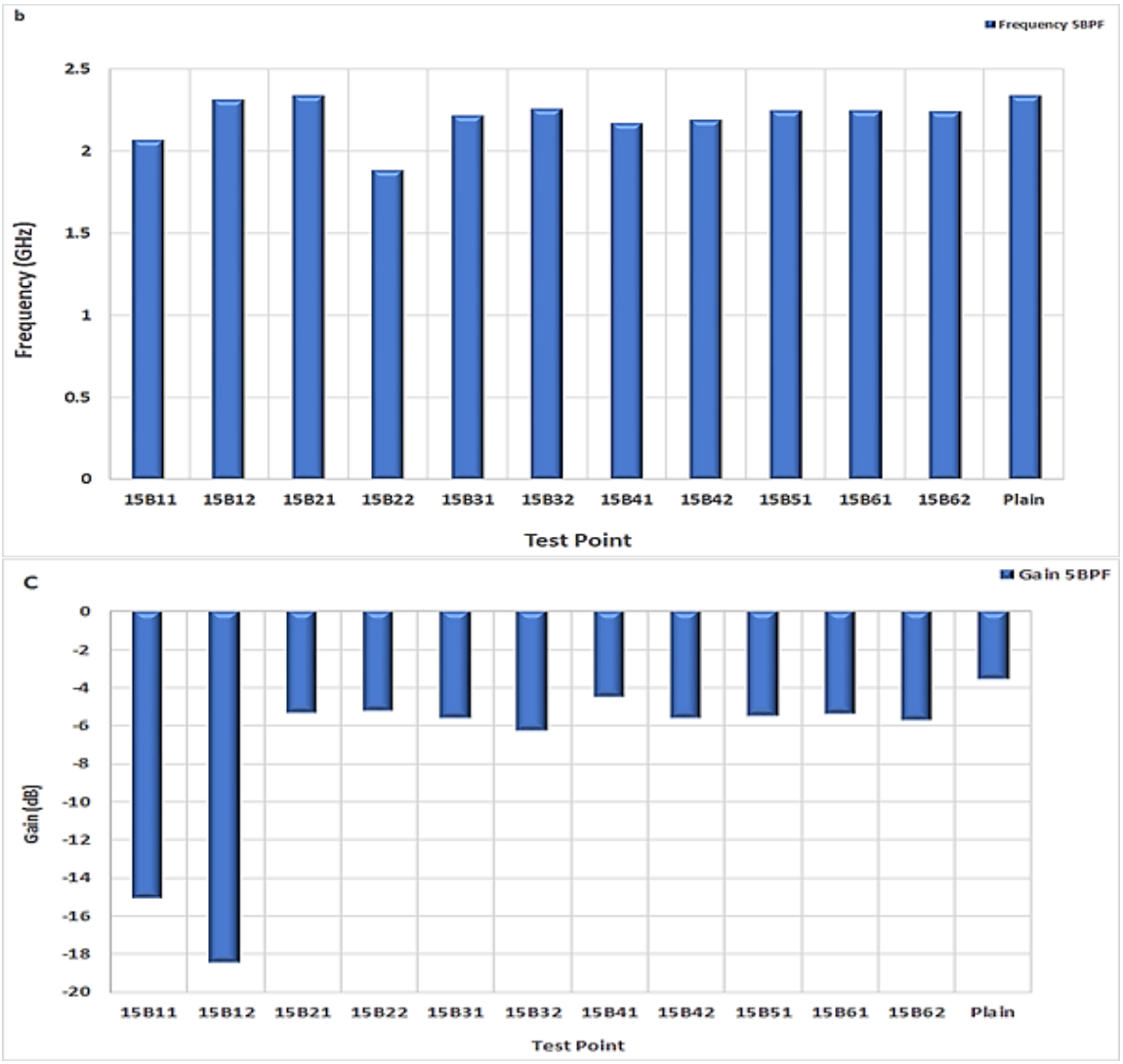

Figure 5. 13 The results of the combined response, a) The VNA response for S11 of 5BPF, b) the plot of frequency shift for each point, c) the plot of gain change for each point.

The Characterisation results of figure 5.13a above was expounded, firstly, with the histogram plot for the frequency shift for each test point on the device as shown in figure 5.13b, from this plot the test point that was observed to exhibit the highest shift in frequency is 15B21 at 2.33GHz, but the mean value of the frequency shift for all the test points is 2.21GHz and a standard deviation of 127MHz. Similarly, figure 5.13c shows the histogram plot for the change in gain for the test points of the device in which the peak gain value was observed to occur at test point 15B12 with a value of -18.38dB, but the mean value of this gain values is -7.19dB and a standard deviation of 4.55dB.

5.3.5 The Second Set of Manufactured Devices

The above method of characterization involves testing all the points on each device, this approach would not only contaminate the surface of the device but would also mean more results to process, longer characterisation time and faults like scratches on the device could result due to the excessive handling of the devices. More so, it was observed that from the first sets of the fabricated filters the BPF indicated better response that would make it suitable for the design of a sensing element. Additionally, it is also important for all the devices to be used for the sensing element to be made from the same filter design to enable easy analysis of results. For these reasons, a second fabrication run was made, which were mainly the 5th order band pass filter. From this second set, a random sample from the fabricated devices was selected and characterized, since all of these devices were fabricated from the same mask design and having the same geometry and size. Furthermore, to enable the identification of the point which produce the desired change in frequency and gain upon the introduction of the test sample (for this case water + ethanol), pilot tests was carried out on few initial devices. From the results of these preliminary characterisation tests, the points that were observed to show higher changes in frequency and gain were narrowed down to 4, these are point 12, point 3M, point 4m and point 3M+4M.

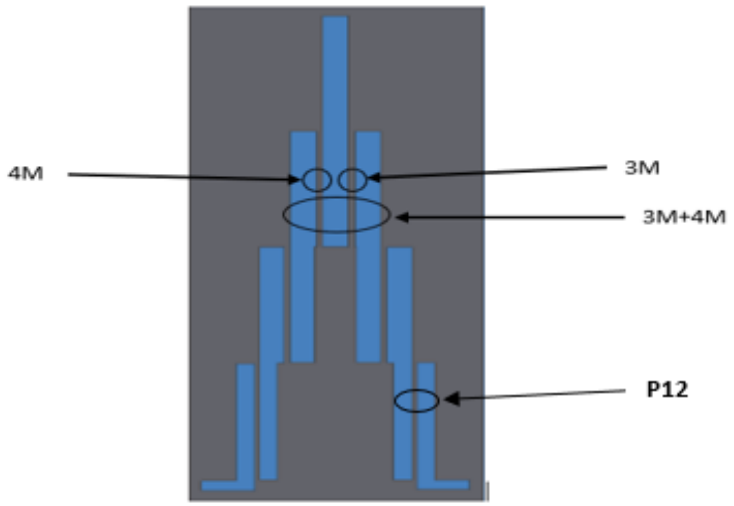

Figure 5. 14 Points on the 5BPF where sample was introduced for device characterisation

5.3.5.1 Characterisation of Point 12

Since the results from the initial characterization of the points has resulted in narrowing down the number points on the device to be characterised. However, for each of the selected points to be characterized effectively, 12 readings were taken at an interval of 5 minutes between each reading, this is to ensure repeatability of the readings. To characterize this device a mixture of tap water and ethanol was used in a ratio 1:1 (that is 50% water 50% ethanol), the results of which are presented below. Figure 5.15 shows the results of point 12 on the device where the test liquid sample was introduced for characterization.

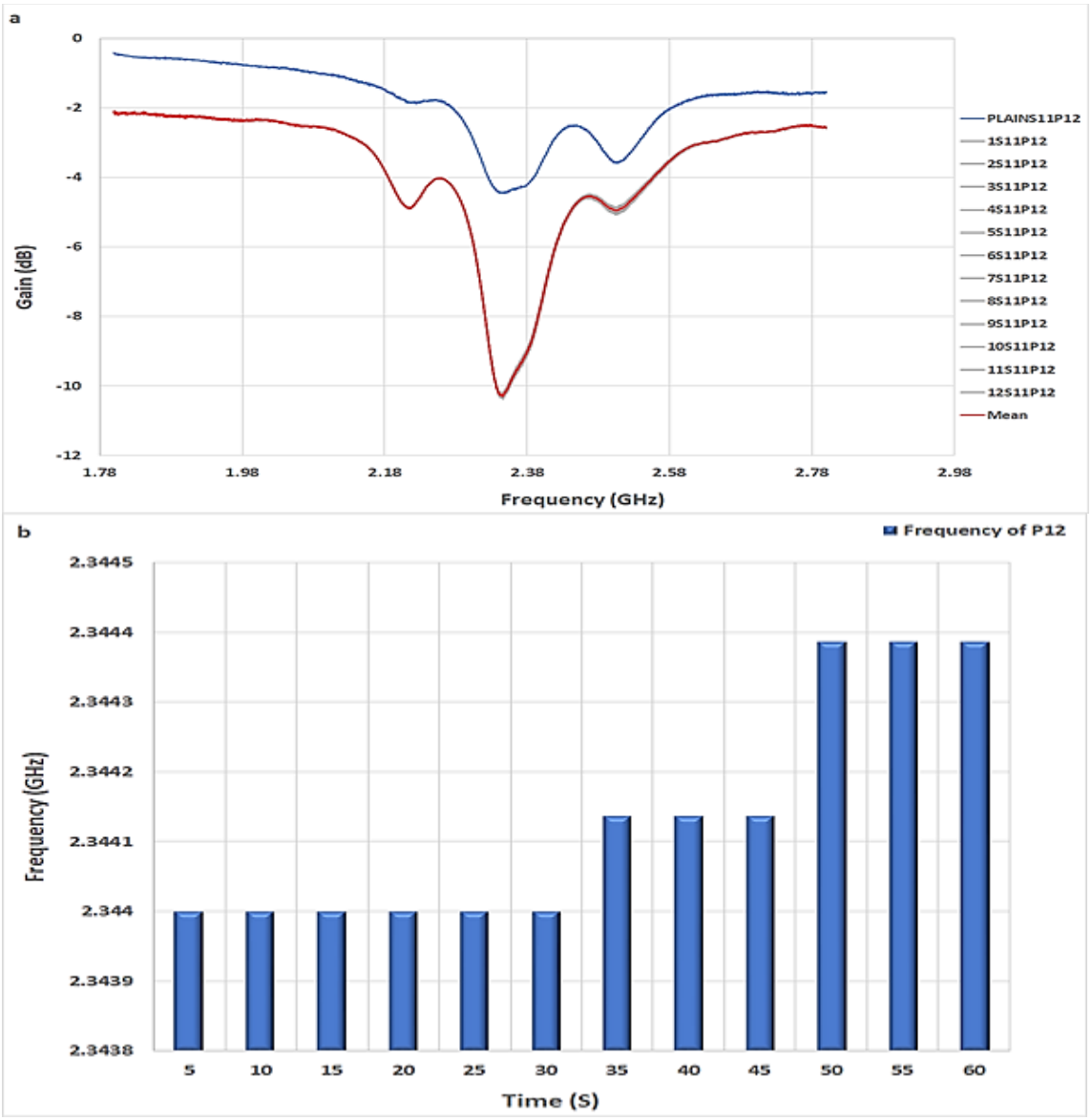

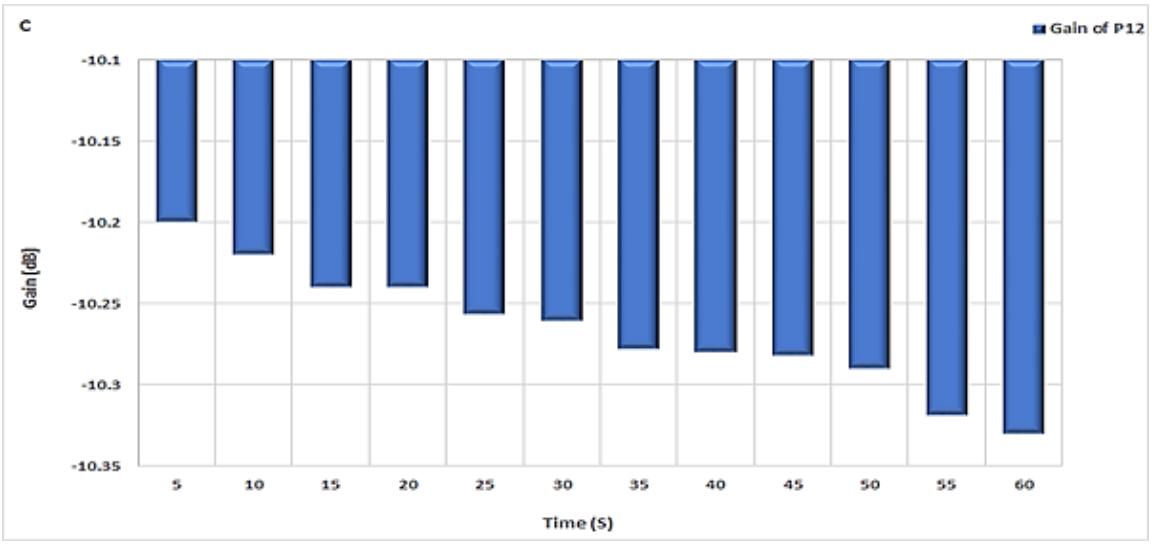

Figure 5. 15 The results of the combined response, a) The S11 characterization result for the 12 readings at point-12 on the DUT, the plot in red is the mean of the 12 plots, b) the plot of peak frequency for each reading, c) the plot of peak gain for each reading.

The characterisation results of the point-12 on the DUT as shown in figure 5.15a highlighted the mean result plot in red as the average of these 12 results, while the result in blue is that of the device without added sample. Then for clarity, the peak frequency from each result was extracted, and a histogram of each was plotted as shown in figure 5.15b. Although from this plot it can be observed that the peak frequency appears to increase with increase in the number of tests consequently with time, to a maximum value of 2.3444GHz. However, the Mean peak frequency for all the 12 results was 2.3441GHz and the standard deviation is 0.1647MHz. These results indicate that the peak frequency of the 12 plots occurred very closely thereby indicating good repeatability of response from the test point. Similarly, a histogram of the peak gain of the 12 readings was plotted as shown in figure 5.15c, wherein an increase in the peak gain of the results was observed to have a maximum value of -10.33dB, but the mean of all the gain values was -10.27dB and a standard deviation of 0.04dB. This is also an indication of closely repeatable results with a favourable measurement accuracy of this test results for this point. The next section will look at the results of point 3M on the device under test.

5.3.5.2 Characterisation of Point 3M

For this selected point to be characterized effectively, 12 readings were taken at an interval of 5 minutes between each reading, this is to ensure repeatability of the readings. To characterize this device a mixture of tap water and ethanol was used in a ratio 1:1 (that is 50% water 50% ethanol), the results of which are presented below. Figure 5.16 shows the results of point 3M on the device where the test liquid sample was introduced for characterization.

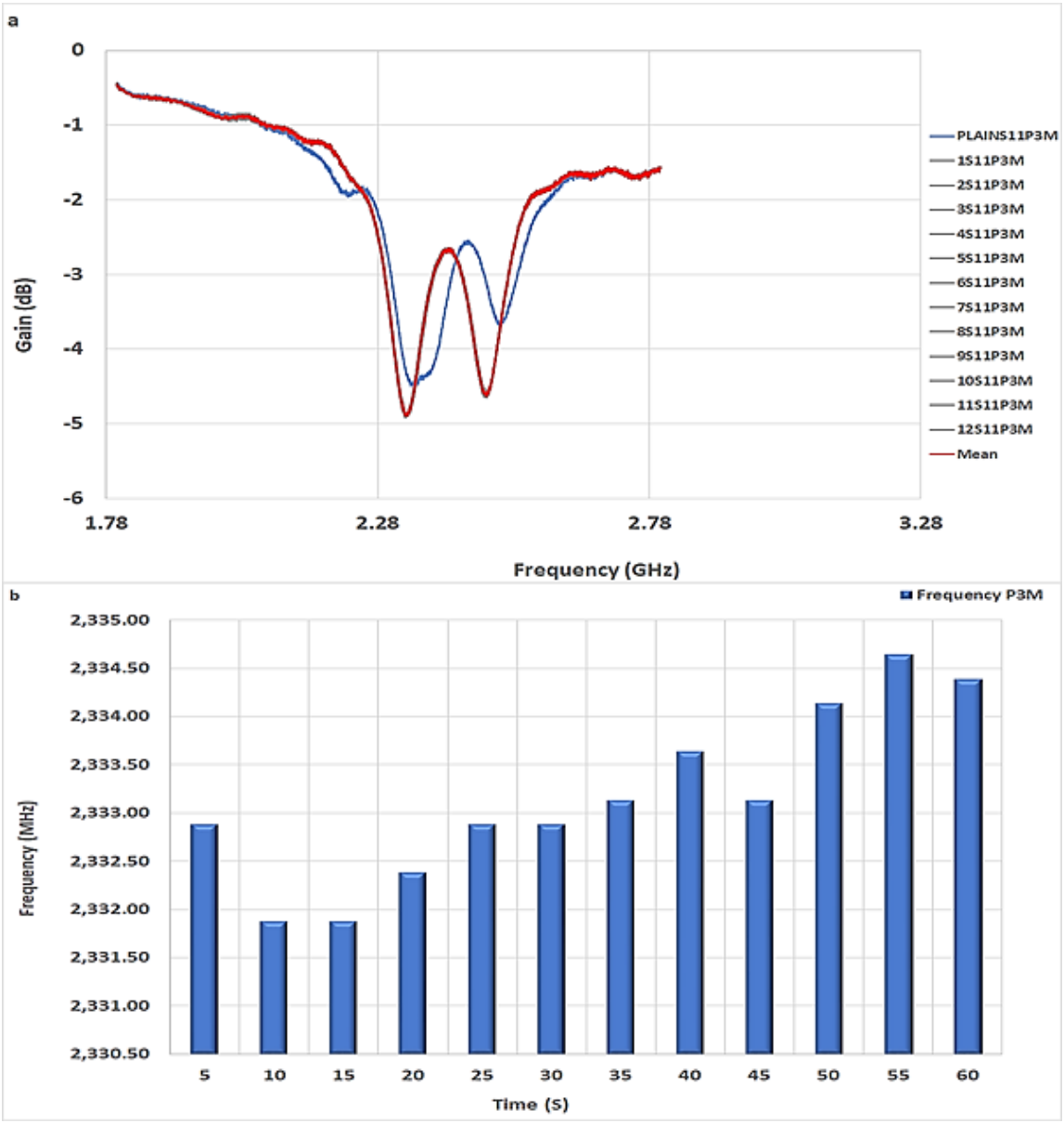

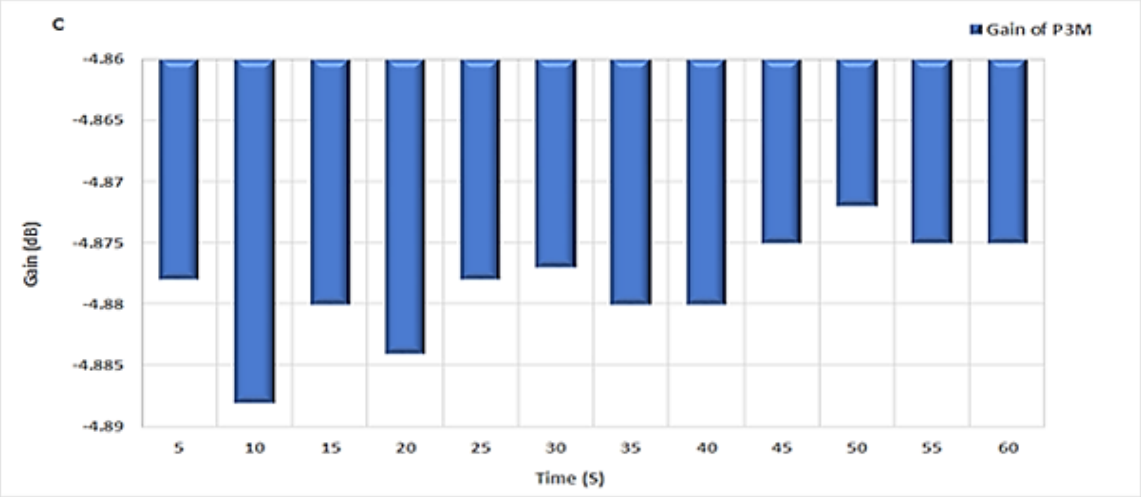

Figure 5. 16 The results of the combined response, a) the S11 characterization result for the 12 readings at point-3M on the DUT, the plot in red is the mean of the 12 plots, b) the plot of peak frequency for each reading, c) the plot of peak gain for each reading.

The highlighted plot in red of figure 5.16a is the mean plot which represents the average of these 12 results, while the result in blue is that of the device without added sample. The peak frequency from each result was then extracted, and figure 5.16b shows the histogram plot. Although from this plot the peak frequency shows an increase trend with the number of tests and also with time, to a maximum value of 2.3346GHz. The Mean peak frequency for all the 12 results was 2.3332GHz and the standard deviation is 0.9MHz. These results indicate that the peak frequency of the 12 plots occurred closely thereby indicating repeatability of result from the test point. Correspondingly, a histogram plot of the peak change in gain of the 12 readings shown in figure 5.16c, in which an observed maximum gain value of -4.89dB was recorded, but the mean of all the gain values was -4.88dB and a standard deviation of 0.004dB. This is also an indication of closely repeatable results for this point.

5.3.5.3 Characterisation of Point 3M + 4M

For this selected point to be characterized effectively, 12 readings were taken at an interval of 5 minutes between each reading, this is to ensure repeatability of the readings. To characterize this device a mixture of tap water and ethanol was used, the results of which are presented below. Figure 5.17 shows the results of point 3M on the device where the test liquid sample was introduced for characterization.

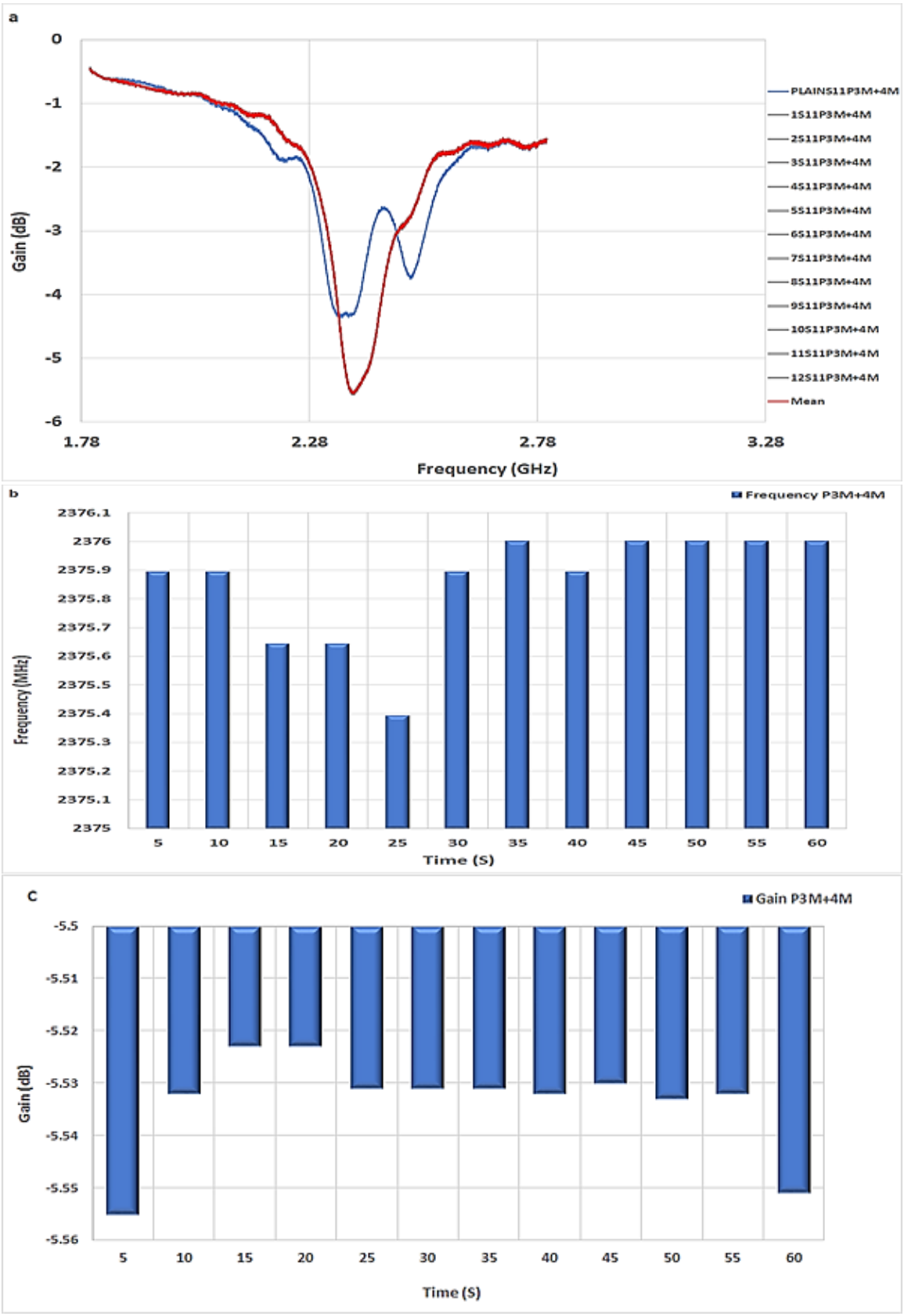

Figure 5. 17 The results of the combined response, a) The S11 characterization result for the 12 readings at point-3M+4M on the DUT, the plot in red is the mean of the 12 plots, b) the plot of peak frequency for each reading, c) the plot of peak gain for each reading

In a like manner, the characterisation results of the point-3M+4M on the DUT as shown in figure 5.17a, accentuated the mean result plot in red colour as the average of these 12 results, while the result in blue is that of the device without added sample. Then to elaborate, the peak frequency from each result was extracted, and a histogram of each was plotted as shown in figure 5.17b. From this plot it can be observed that the peak frequency appears to have a fairly equal value even with increase in the number of tests and also increase with time but maintain a maximum value of 2.376GHz. However, the Mean peak frequency for all the 12 results was 2.3759GHz and the standard deviation is 0.1938MHz. These results indicate that the peak frequency of the 12 plots occurred at a very close frequency thereby indicating good repeatability of response from the test point. Similarly, a histogram of the peak gain of the 12 readings was plotted as shown in figure 5.17c, in which an increase in the peak change in gain of the results was observed to have a maximum value of -5.555dB, but the mean of all the gain values was -5.533dB and a standard deviation of 0.009dB. This is also an indication of very closely repeatable results with a good measurement accuracy of this test results for this point. The next section will look at the results of point 4M on the device under test.

5.3.5.4 Characterisation of Point 4M

To effectively characterized this selected point, 12 readings were taken at 5 minutes interval between readings, this is to ensure repeatability of the readings. To characterize this device a mixture of tap water and ethanol was used, the results of which are presented below. Figure 5.18 shows the results of point 3M + 4M on the device where the test liquid sample was introduced for characterization.

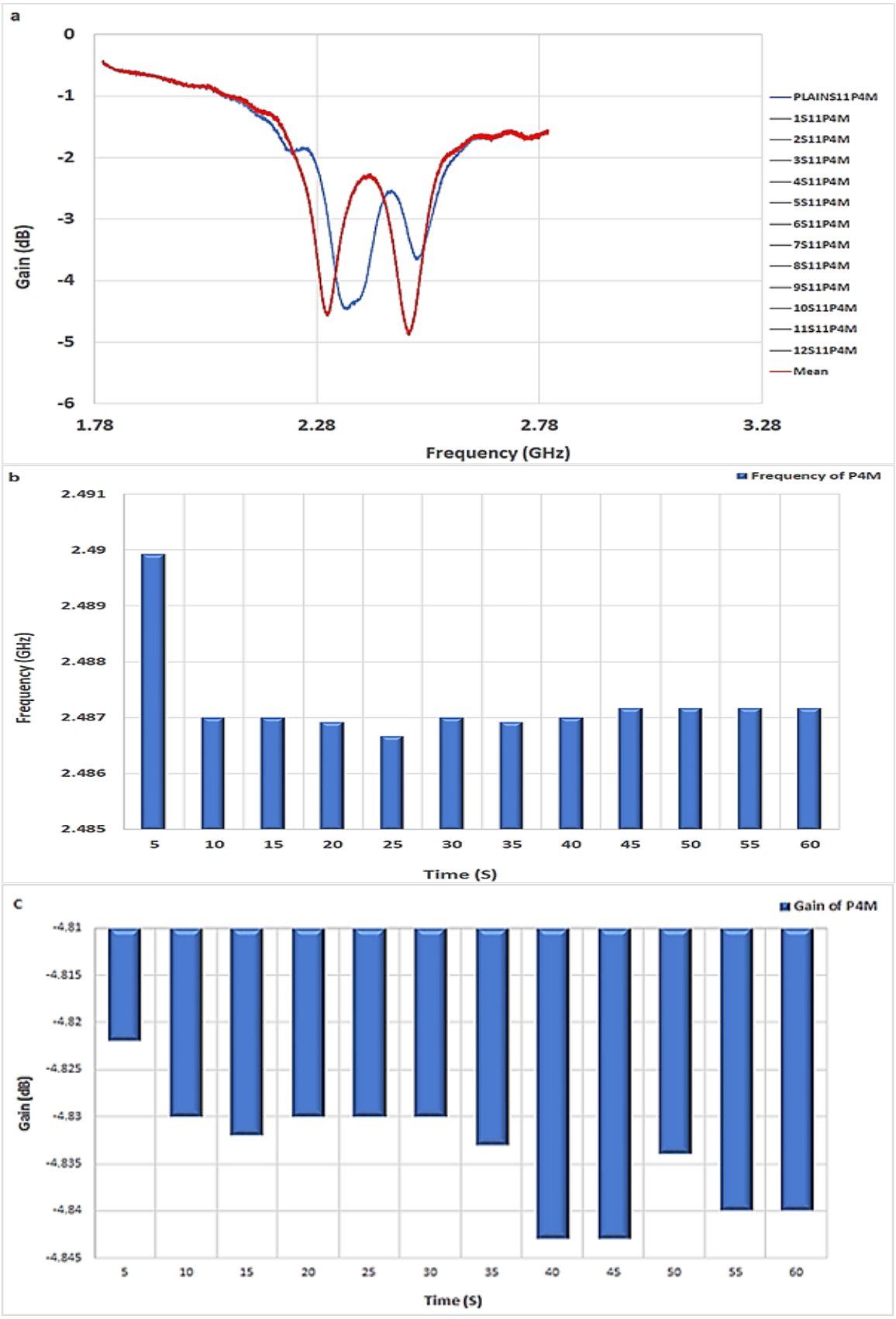

Figure 5. 18 The results of the combined response, a) The S11 characterization result for the 12 readings at point-4M on the DUT, the plot in red is the mean of the 12 plots, b) the plot of peak frequency for each reading, c) the plot of peak gain for each reading.

In a similar manner, the characterisation results of the point-4M on the device as shown in figure 5.18a, highlighted the mean result plot in red colour as the average of the 12 results, while the result in blue is that of the device without added sample. Then, the peak frequency from each result was extracted, and a histogram of each was plotted as shown in figure 5.18b. From this plot it can be seen that the peak frequency appears to have an initial high value and then fairly constant equal value even with increase in the number of tests and also increase with time, nevertheless, it maintains a maximum peak frequency value of 2.4899GHz. However, the Mean peak frequency for all the 12 results was 2.4873GHz and the standard deviation is 0.851MHz. These results indicate that the peak frequency of the 12 plots occurred at a close frequency thereby indicating good repeatability of response from the test point. Similarly, a histogram of the peak gain of the 12 readings was plotted as shown in figure 5.18c, in which a slight increase in the peak gain of the results was observed to have a maximum value of -4.843dB, but the mean of all the gain values was -4.834dB and a standard deviation of 0.006dB. This is also an indication of very closely repeatable results with a good measurement accuracy of this test results for this point.

The mean results for the frequency and gain were then plotted together in a histogram plot to compare results of all the test points. Similarly, the results for the maximum frequency and gain were then plotted together in a histogram plot to compare results of all the test points. This was done to aid the selection of the point on the device that indicate the best response and is considered to suitable for use on the sensing device.

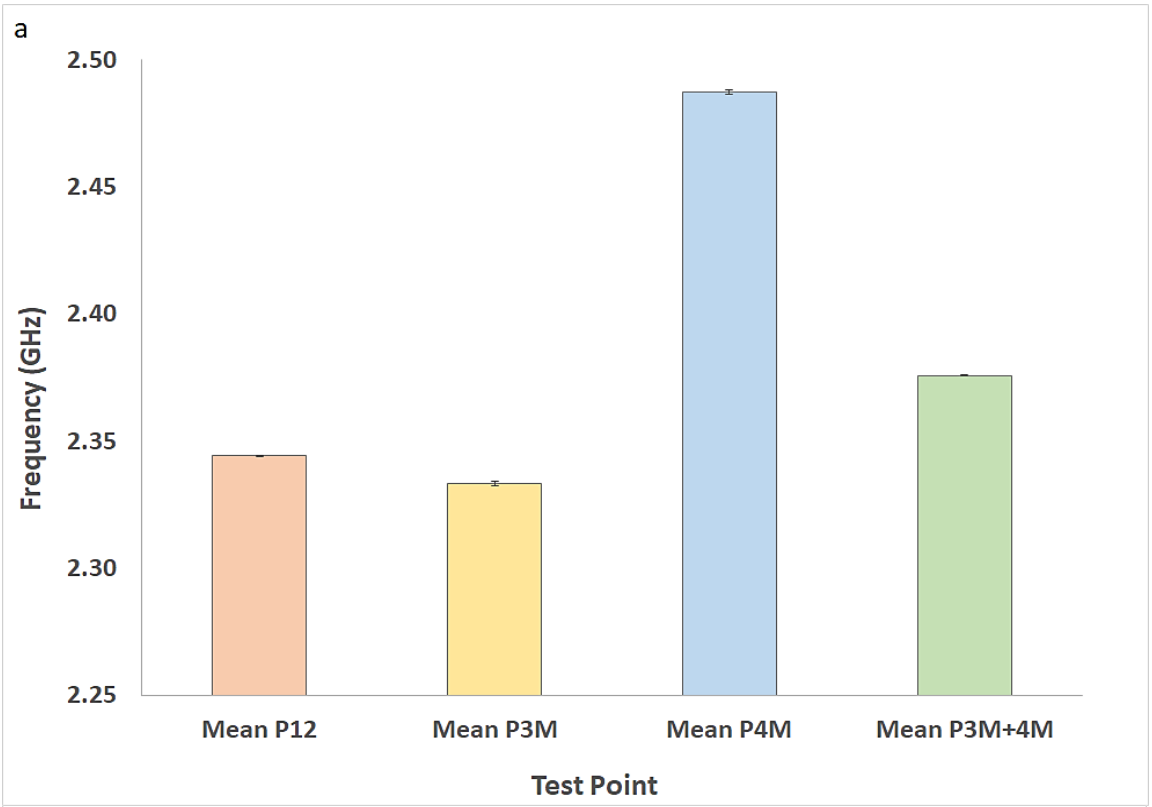
a
2.50
2.45
2.40
2.35
2.30
2.25
Frequency (GHz)
Mean P12
Mean P3M
Mean P4M
Mean P3M+4M
Test Point

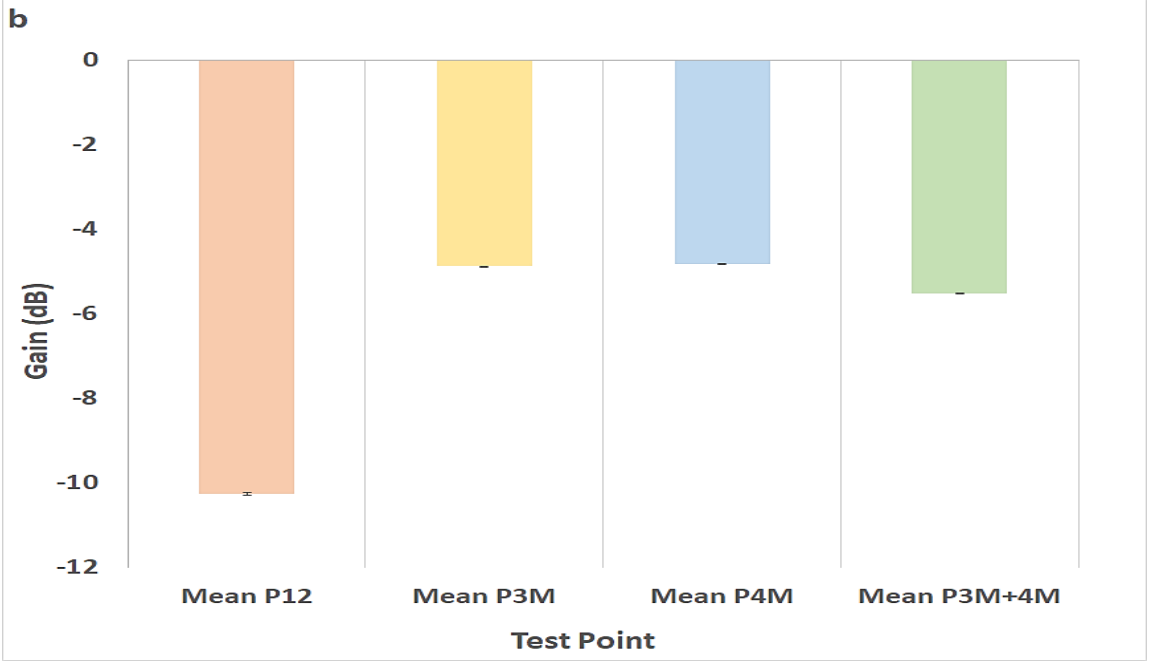
b
0
-2
-4
-6
-8
-10
-12
Gain (dB)
Mean P12
Mean P3M
Mean P4M
Mean P3M+4M
Test Point

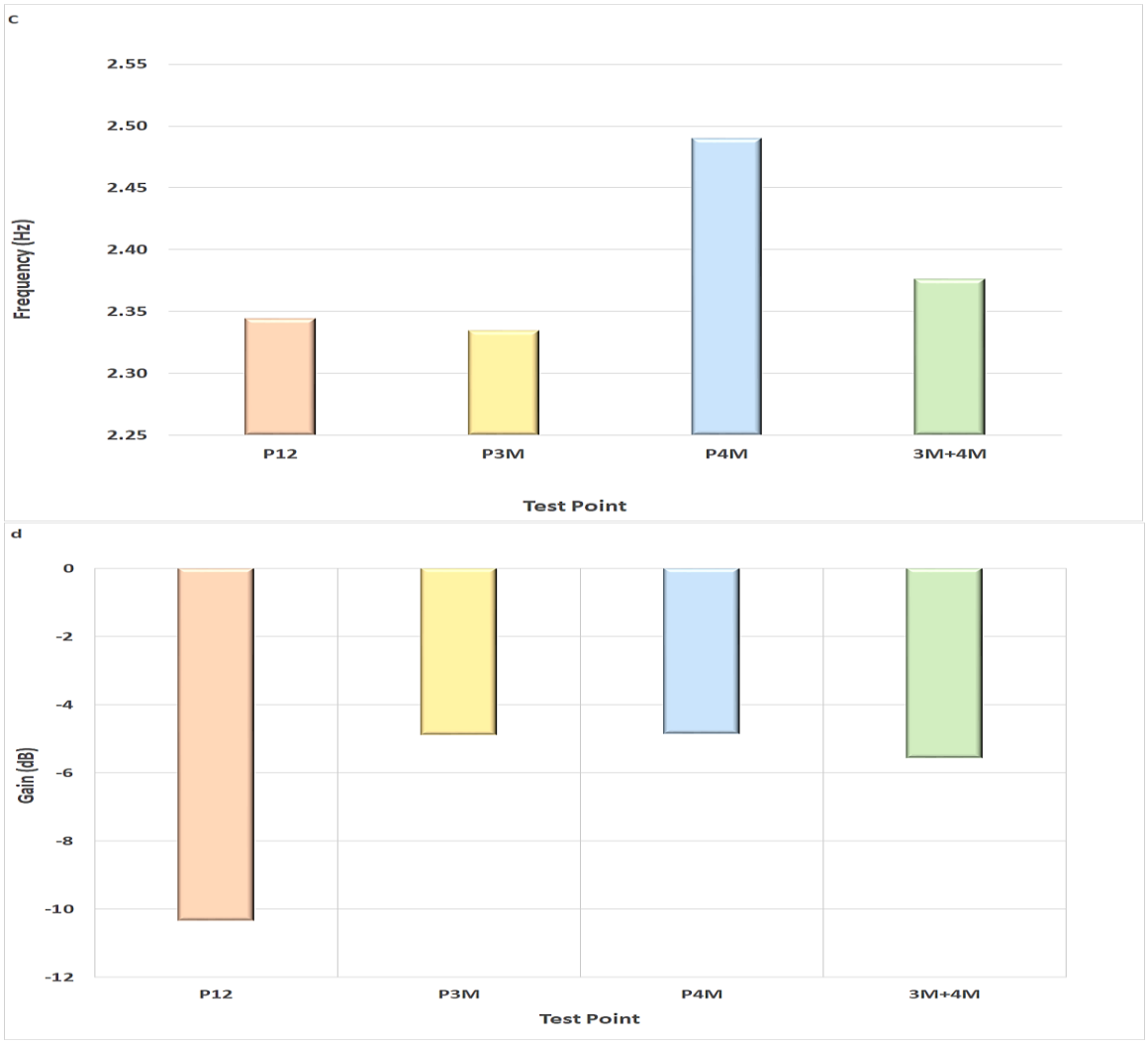

Figure 5. 19 The maximum and mean value of all the test point results, a) the mean of the frequency value, b) the mean of the gain value, c) the maximum frequency value of each test [point, d) the maximum gain value of each test point.

It is important to select the test point with the most appropriate response that would make it the most suitable point on the device to be used for the sensing application. To achieve this a further processing of the results presented above was done. Firstly, the histogram plot of the mean value of the peak frequency shift for all the 12 results for each test point is presented in figure 5.19a, where it showed that the test point that exhibit the highest mean frequency response is P4M, but that of P12 is significantly lower and that of P3M+4M which is the next highest frequency value from the plot. However, from this plot point P12 showed the smallest deviation in measurements indicating this point was the most insensitive to variations in fluid level, and the point with next lowest deviation value being P3M+4M, this quite interesting because the deviation from the mean value of the frequency is desirable and quite small at these points. Similarly, the mean value of the

peak change in gain for all the 12 results for each test point is presented in figure 5.19b, although, the histogram plot indicates that P12 has the highest mean gain value, but that of P3M+4M is more than half its value and not far from it. However, from this plot point P3M showed the smallest deviation in measurements representing the point that is most insensitive to changes in fluid level with the next lowest point being that of P4M and closely followed by that of P3M+4M, these results illustrated that the change from the mean value of these change in gain value is quite small at these points.

A further comparison was done, this time with the maximum values of the shift in frequency response of the test points, it was observed that P4M exhibited the highest frequency response from all it 12 results recorded as compared to other test points, this is illustrated in the histogram plot of figure 5.19c. This high frequency value is quite close to the earlier stated mean frequency value of all its 12 results. Although, the maximum gain value from the 12 results for each test points as shown in figure 5.19d indicated that P12 showed the highest gain value, however, the maximum gain value for point 3M+4M is closer in value to the mean value of all its 12 results indicating a fairly repeatable results for the test point. By and large it can be observed from the analysis done above that point 3M+4M has a result that illustrates a high peak frequency and high level of repeatability in its response as compared to other test points on the device, making it the most suitable point to be used as the sensing point for the device, alternatively point 4M could be used as a second option.

5.4 Graphene (Kapton Tape) Fabrication

The mathematical design of the microstrip was done in section 3.5.2, where the design of the width and expected thickness was made. The implementation of this design was achieved using the laser scribe technique for making graphene oxide. This method of graphene oxide production is one of the do-it-yourself (DIY) methods of producing graphene. This technique has introduced a new way of making a graphene oxide material. To achieve this task several experiments were conducted, and the materials that were initially used were: Kapton tape, silver paint, plywood (as a base), digital multimeter and laser machine (Laserscript HPC laser) for the fabrication of the LIG.

From these samples produced several tests were carried out on them using a digital multimeter to obtain necessary resistance values from the resulting materials (graphene oxide-like). The reason for carrying out this test is to determine the resistivity of the resultant material so as to ascertain its viability in its being employed as a material that has the required property for use as the sensing element of the proposed biosensing platform. The two categories of samples (the multiple strips and the single strip) were tested to explore which material from any of the two sets of materials (twenty different materials for the multiple strip and twenty for the single strip) is a viable material for the sensing element design. The results of these tests carried out were recorded, from these results several plots were also derived, and with further data processing, it led to the determination of the particular material with the optimum conductivity and is suitable for the design of the material of interest. Some of the observed results are presented below. To obtain these results the laser machine was used to engrave a number of strips (for the case of a multiple strip material) at chosen power settings and speed rate of engraving (full details of the fabrication procedures can be obtained in chapter four).

5.4.1 The Multiple Strips

The results of the test carried out for the different parameters of the different materials produced was recorded as measured using the aforementioned equipment and the results of this measurement was recorded in a tabular form. Table 5.1 below shows the recorded value of a typical resistance measurement along the length of a multiple strip line of the produced material. of a typical resistance measurement along the length of a multiple strip line of the produced material.

Table 5. 1 Typical Result of the Measurement of Resistance along the length of a multiple strip line. Results in red are resistance values that do not increase linearly with increase in length

MULTIPLE STRIP (n=5) Each Strip Width (ESW)=0.30mm, Speed=300mm/s						
% POWER		% power of 26	% power of 28	% power of 30	% power of 32	% power of 34
	Length(mm)	Resistance (Ω)	Resistance (Ω)	Resistance (Ω)	Resistance (Ω)	Resistance (Ω)
1	30	553	777	336	308	70200
2	60	1060	1340	684	633	69000
3	90	1710	1940	1050	925	69100
4	120	2300	2470	1430	1580	70000
5	150	2900	2930	1850	1910	70600
6	180	3580	3380	2230	2240	71300
7	210	4340	3870	2610	2640	70900
8	240	5570	4340	3050	2980	72000
9	270	6660	4870	3480	3310	73400
10	300	7380	5340	3940	3690	73900
11	320	8030	5620	4310	3970	12000000

From the tables of results obtained above it can be observed that certain column has resistance values that do not increase linearly with increase in length (i.e. they are irregular), these values are highlighted for easy identification. As such, these results have started giving an idea of which material from these set of samples might possess the needed property for the intended usage. From these tabulated results, a plot of the resistance against the length was done for each percentage (%) power settings, a typical plot is shown in figure 5.20.

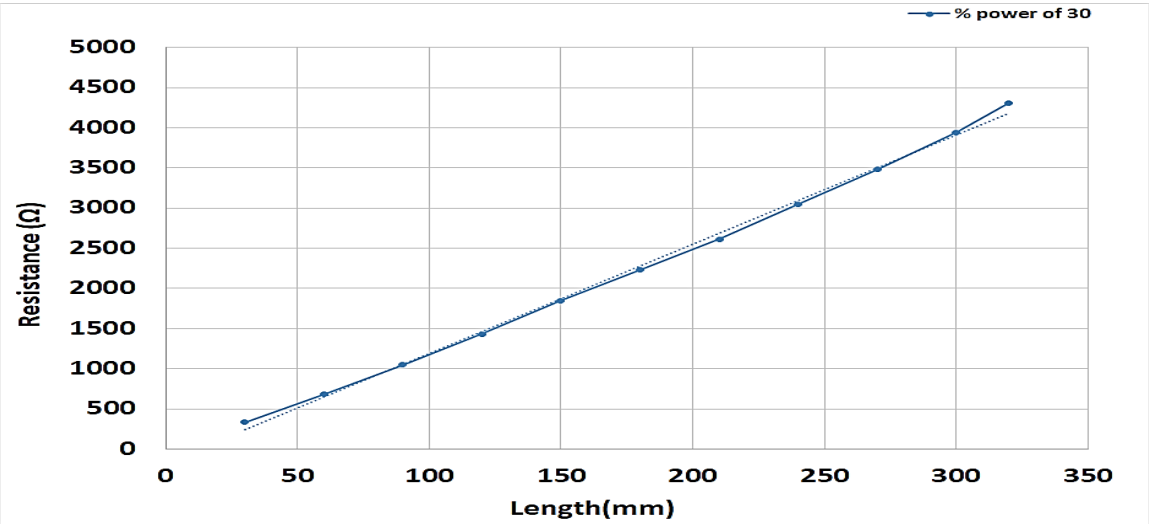

Figure 5. 20 The plot of the resistance against the length for a multiple strip material for %power of 28

These plots were then used to determine the resistance per unit length of the produced material for each power setting for individual material produced. From these resistance per unit length obtained, then the resistivity of each material was determined using equation 5.1 [118]. Where ρ is the resistivity, R the resistance, A the area and ℓ the length.

$$\rho = \frac{RA}{\ell} \tag{5.1}$$

In order to determine the suitable resistivity of the materials produced, the areas of each material was determined, and to achieve this task, the thickness and the width of the individual materials were measured using the Surftest SJ-410, with this device the measurement were done to the nearest micron. From these determined areas, the resistivity for each material was determined using equation 5.1. The result of the resistivity of each material was then used to individually determine the conductivity of each setting for the multiple strip material using equation 5.2 [118], Where ρ is the resistivity and σ is the conductivity of each material.

$$\sigma = \frac{1}{\rho} \tag{5.2}$$

The result of the conductivity for each setting is as shown in figure 5.21 below, form which the multiple strip material with the optimum conductivity can be observed.

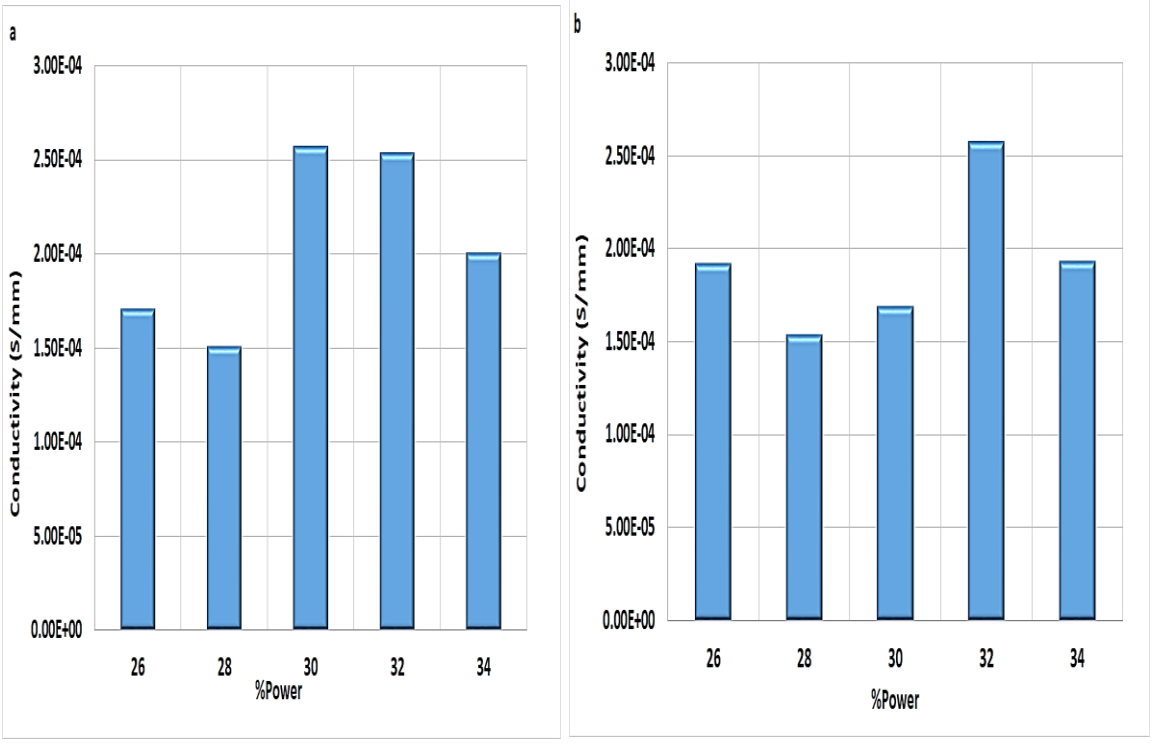

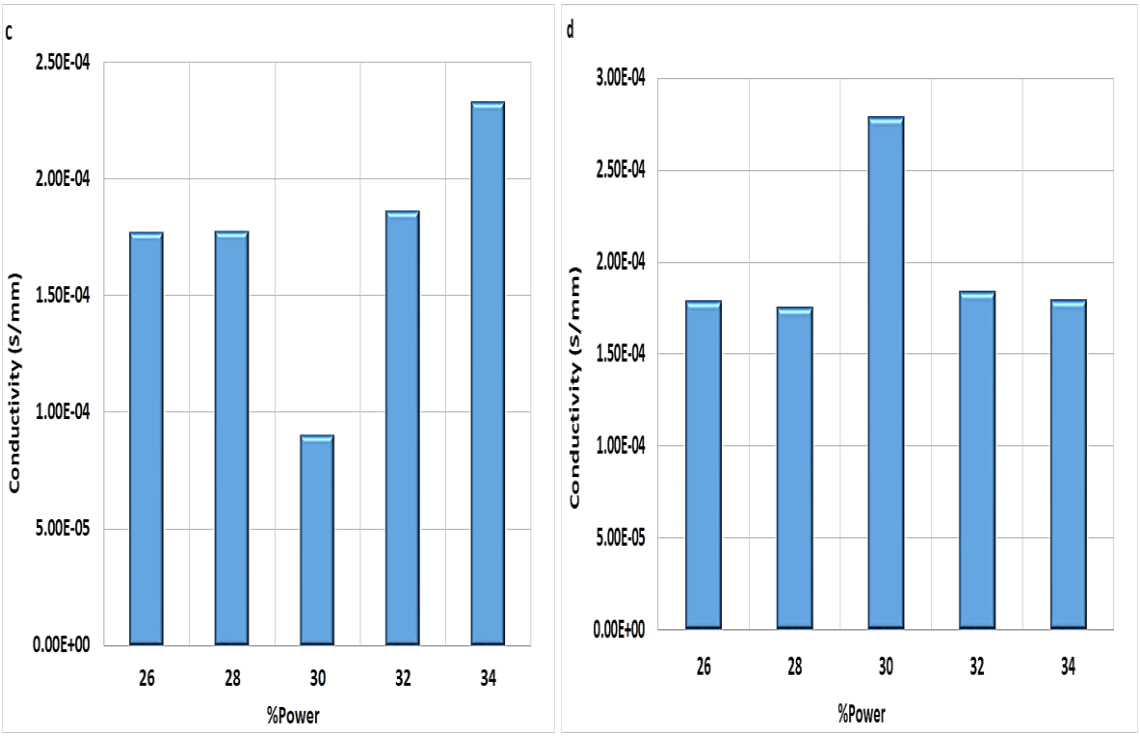

Figure 5. 21 Conductivity plot for multiple strip material , a) width of strip is 0.3mm at engraving speed of 300mm/s, b) width of strip is 0.35mm at engraving speed of 300mm/s, c) width of strip is 0.3mm at engraving speed of 400mm/s, d) width of strip is 0.35mm

The results of the conductivity for each setting is as shown in figure 5.21, from which the multiple strip material with the optimum conductivity can be observed. From the results presented, figure 5.21a shows the conductivity results for a setting where the width of each strip is 0.3mm at an engraving speed of 300mm/s, this approach produced a material that has a maximum conductivity at a %power of 30. While figure 5.21b shows the conductivity for a setting where the width of each strip is 0.35mm an engraving speed of 300mm/s, this method produced a material with a maximum conductivity at a %power of 32. Furthermore, figure 5.21c is the conductivity results where the width of each strip is 0.3mm at an engraving speed of 400mm/s, this method yielded a material with a maximum conductivity at a %power of 30. Finally, figure 5.21d is the conductivity results where the width of each width of strip is 0.35mm at an engraving speed of 400mm/s, which produced a material with a maximum conductivity at a %power of 30. From these results presented it can be observed that the optimum production approach for the multiple strip material is the method which yielded a material with the highest conductivity, and this is the technique that has each width of strip of 0.35mm, and engraves at a speed of 400mm/s at a %power of 30. This is the approach that was used for the production of the LIG MLPF in this research.

5.4.2 The Single Strip

The same procedure was followed to obtain results of the single strip line, using the same equipment as used for the multiple strip line above, results were obtained and recorded as shown in table 5.2 below, which represents a typical resistance measurement along the length of the single strip line.

Table 5. 1 A typical Result of the Measurement of Resistance along the length of a single strip line

SINGLE STRIP Width of Strip (WOS)=0.30mm, Speed=400mm/s						
% power		% power of 26	% power of 28	% power of 30	% power of 32	% power of 34
	Length(mm)	Resistance (Ω)	Resistance (Ω)	Resistance (Ω)	Resistance (Ω)	Resistance (Ω)
1	30	132000	57400	5000	5920	197000
2	60	713000	65200	9500	15300	206000
3	90	720000	71600	13550	20000	211000
4	120	726000	76300	17400	23500	230000
5	150	734000	80800	21400	27400	242000
6	180	738000	87700	26300	31000	935000
7	210	745000	101400	31700	37200	940000
8	240	760000	1200000	39300	59400	950000
9	270	772000	38800000	51400	67800	950000
10	300	779000	39000000	59200	71300	950000
11	320	0	39000000	63200	0	950000

From these results certain column has resistance values that do not increase linearly with increase in length they are highlighted for easy identification. From these results a plot of the resistance against the length was done for each percentage (%) power settings, a typical plot for these results is shown in figure 5.22.

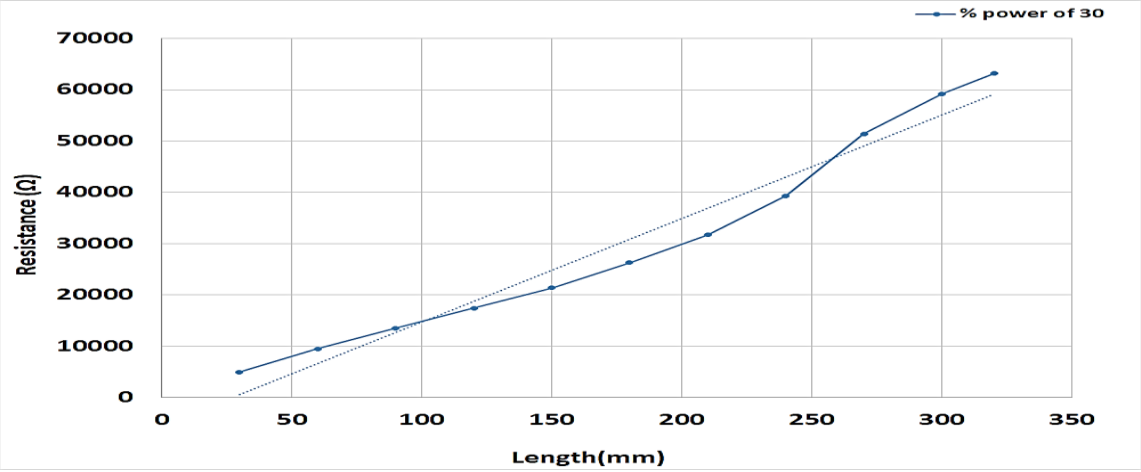

Figure 5. 22 The plot of the resistance against the length for a single strip material for %power of 28

These plots were also then used to determine the resistance per unit length of the produced material for each power setting for individual single strip material produced. From these resistance per unit length obtained, then the resistivity of each material was determined using equation 5.1 above in a similar manner. In order to determine the suitable resistivity of the materials produced, the areas of each material were determined, to achieve this, the thickness and the width of the individual materials were measured using the Surftest SJ-410. From these determined areas, the resistivity for each single strip material was similarly determined using equation 5.1. The result of the resistivity of each material was then used to individually determine the conductivity of each setting for the multiple strip material using equation 5.2. The result of the conductivity for each setting is as shown in figure 5.22 below, from which the single strip material with the optimum conductivity can be observed.

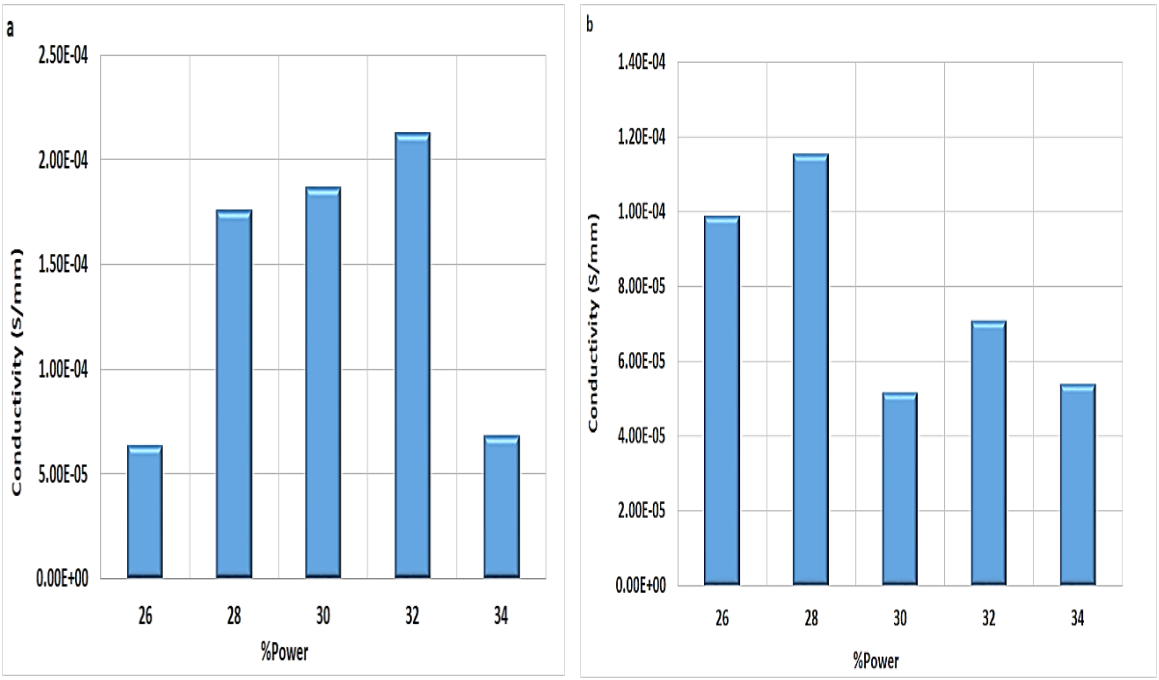

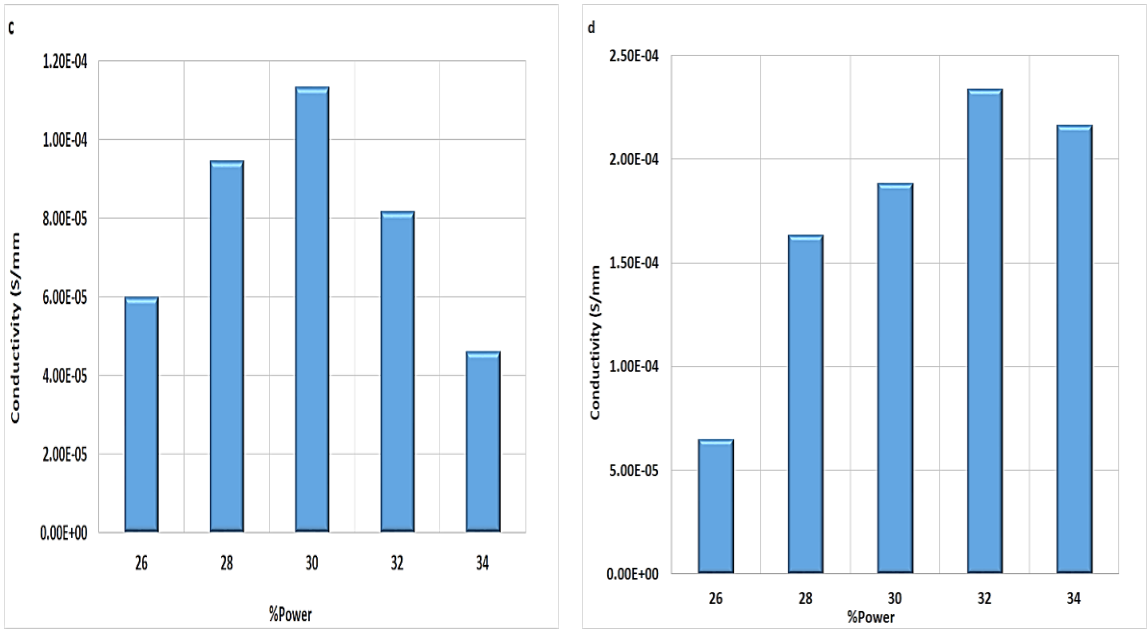

Figure 5. 23 Conductivity plot for single strip material , a) width of strip is 0.3mm at engraving speed of 300mm/s, b) width of strip is 0.35mm at engraving speed of 300mm/s, c) width of strip is 0.3mm at engraving speed of 400mm/s, d) width of strip is 0.35mm a

The results of the conductivity for each setting is as shown in figure 5.23, where the single strip material with the optimal conductivity was illustrated. From these results figure 5.23a is the conductivity results for a setting where the strip width is 0.3mm at an engraving speed of 300mm/s, this method yielded a material that has a maximum conductivity at a %power of 34. While figure 5.23b shows the conductivity for a setting where the strip width is 0.35mm at an engraving speed of 300mm/s, this method produced a material with a maximum conductivity at a %power of 26. Furthermore, figure 5.23c is the conductivity results where the strip width is 0.3mm at an engraving speed of 400mm/s, this method yielded a material with a maximum conductivity at a %power of 28. Finally, figure 5.23d is the conductivity results where the strip width is 0.35mm at an engraving speed of 400mm/s, and produced a material with a maximum conductivity at a %power of 32. From these results presented it can be observed that for a single strip production, the method which yielded a material with the highest conductivity, is the technique that has the strip width of 0.35mm, at an engraving speed of 400mm/s, and produced a material with a conductivity a %power of 32.

Both materials can be used for flexible, stretchable, and wearable sensors and biosensors for point-of-care (POC) testing. However, the thinner structure of the single strip materials

which is potentially better for biological work makes them appeal as being able to operate by being directly attached to a system – either externally (e.g., to human skin, or even surfaces of fruits and vegetables) or internally (e.g., on soft tissue) to deliver accurate, reliable, and real-time measurement of physiological parameters or biomarkers, but it has problem with producing continuous strips. Whereas, from the results of the conductivity of both materials in figure 5.21 and 5.22, the multiple strip material showed better electrical conductivity and the advantage of their fabrication and design strategies can make them find application where larger surfaces and electrical conductivity is a requirement for their biomedical applications in healthcare, fundamental biomedical research, and environmental monitoring. These materials can find application in flexible and wearable devices, they present unique characteristics inherent in their design that could inspire and improve designs for smart and effective devices in the future.

5.5 Graphene (Kapton Tape) Characterization

The implementation of the microstrip filter was done so that characterisation of the fabricated device can be achieved to examine the performance of this newly produced material for the intended application. It should however be stated that to implement this MLPF, the Laser irradiation technique was employed, where the designed geometry (length and width of each equivalent element) was transferred to a laser machine, the machine then inscribed this geometry on the Kapton tape based on laser setting of 400mm/s as the machine engraving speed, and at a percentage power (%power) setting of 30, to produce the distributed filter shown below in figure 5.26 for test, so that it response can be observed and recorded for effective characterisation.

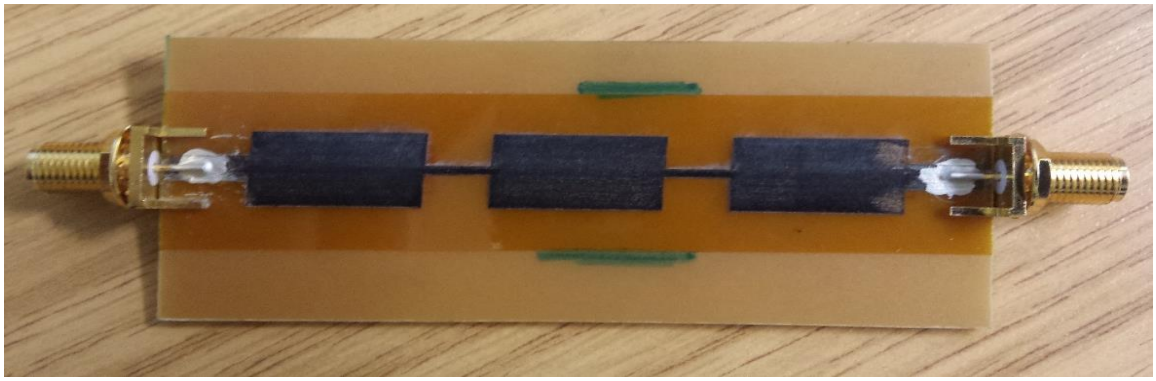

Figure 5. 24 Laser induced graphene distributed filter with SMA connectors

The fabricated MLPF (in this case a 5LPF device) was then connected to a VNA for test to observe and compare results. The preliminary results were to illustrate the viability of the usage of the irradiated material for the intended biological application. This preliminary microstrip filter observed result was recorded. Figure 5.25 shows the responses as observed from the VNA and simulation results of the S11 response of the device. From figure 5. 25a it can be observed that in both results (for the fabricated and simulated device), there was no resonance observed when compared to figure 5.2 above for a pure gold device (which is the desired response of the potential device), this is mainly due to the low conductivity value of the LIG material used for the device fabrication, the lossy RF-4 substrate material used as well as the lossy coper ground plane used. However, from the same figure the reflection coefficients of the material show similar response characteristics but with low loss associated with the response of the fabricated device. From figure 5.25b it can be observed that the gain of the simulated device dropped from an initial high value to a lower value and then rose from this value to a constant and remained at this new constant value. While the fabricated devices response as shown in figure 5.25b indicate a deep in resonant frequency as the frequency to lower gain value and rose incrementally as frequency increase. This response behaviour exhibited by the S21 response of the LIG filter shows a tendency of the material to have better response characteristics if further improvements and fine tuning of parameters can be made in its fabrication process.

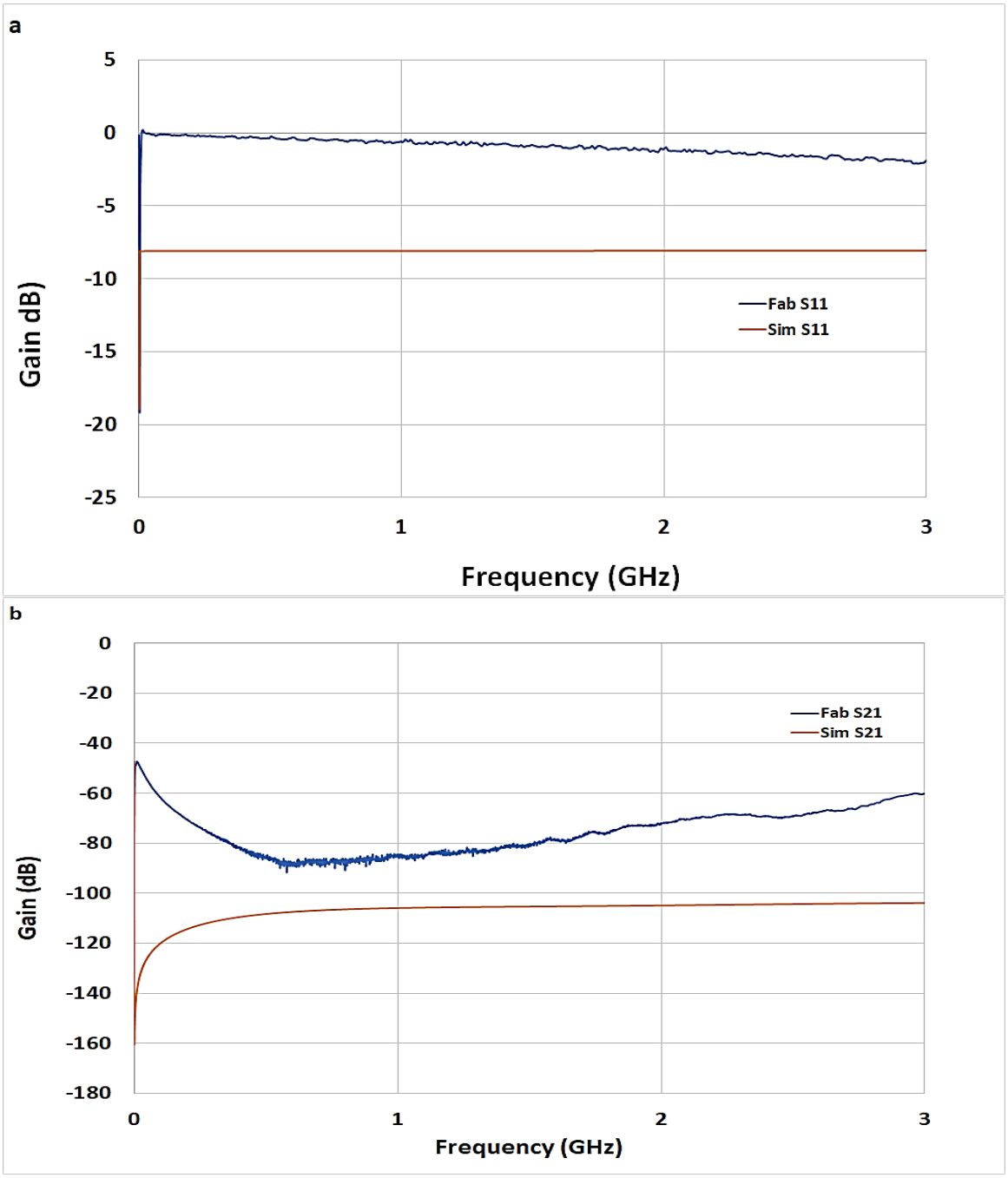

Figure 5. 25 LIG 5LPF device response, a) S11 plot for both the fabricated and the simulated, b) S21 plot for both the fabricated and the simulated.

The idea behind this characterization test, observation and results recording is to gain an understanding of the process so that if the observed results of the fabricated filter is satisfactory and tends to be in alignment with the design parameters, and yield favourable conductivity results and values, then such material use for filter design can now be implemented for the intended biological sensing application as is the aim of this work. From the above result it has become imperative to device techniques in improving the

conductivity of the LIG material since its conductivity is very low as compared to a gold material that has traditionally been used, and to look at ways of using a low loss substrate material for its substrate and ground plane. However, from simulation carried out on the LIG MLPF using HFSS, it was observed that for the LIG MLPF device to produce a response identical to the response of the gold MLPF device while maintaining the substrate as FR-4 and the ground plane as copper, the conductivity would range from 80,000S/m to 1,000,000S/m, this is quite a high conductivity value to be derived from this polyimide material, but ways of improving the conductivity of this LIG material would be explored. This may require alternative ways of preparing the material before engraving and/or the treatment of the LIG material after the laser irradiation.

5.6 Graphene (Ink Jet) Fabrication

Inkjet printing is a common method for printing text and images onto porous surfaces, paper, or transparencies. The recent advancement of a free-form fabrication methods for the building of parts layer-by-layer has led to interest in production of multilayer parts and circuits by inkjet printing. The past few years have seen growing efforts, especially in organic transistors, light emitting diodes, ceramics, and biopolymer arrays [119]. This is illustrated in the work of Lee et al [120] where a graphene oxide support system, comprising functionalized graphene oxide (GO) ink that was inkjet-printed to fabricate a field effect transistor (FET) biosensor. In the last few years however, this technique has been used as a free-form fabrication method for the building of three-dimensional parts and is also being investigated as a way of printing electrical and optical devices, especially where these involve organic components. The need for a versatile inkjet technology for free-forming materials and for multilayer devices raises several materials problems that do not apply to conventional printing of images [119]. This approach would have afforded the graphene oxide device fabrication the obvious benefits of more accurate shape, uniform device dimension, reduced production inaccuracies and better size reproduction. However, owing to the unavailability of the inkjet printer, an alternative manual method was employed for the device fabrication, this is called the spray gun approach. This is a similar technique to the inkjet printing but manually using a spraying system to achieve similar results. This fabrication technique is as illustrated in chapter four.

5.7 Graphene (Ink Jet) Characterization

After the GO filters were reduced, tests were carried out on them to measure their individual conductance, to gauge their conductivity and hence their suitability for the proposed application. These tests were done using the semiconductor device analyser (SDA) to measure the conductance of the produced rGO sensing filter.

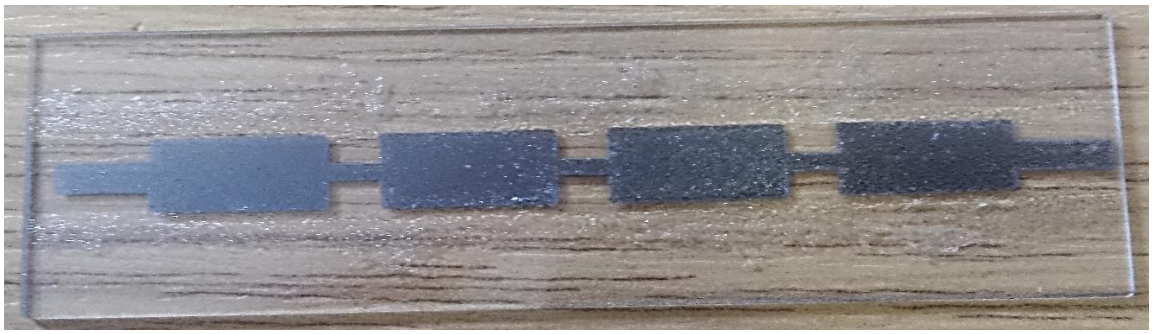

Figure 5. 26 The 7LPF made from rGO before characterisation with an SDA

Figure 5.26 above is the filter made from rGO, the filter was tested for conductivity using the SDA equipment and the result of the equipment was exported in the form of a CSV file, and a typical plot obtained is shown in figure 5.27. The typical conductivity of this produced rGO is 10,000S/m. From fabrication and simulation results it can be stated that this conductivity value is not as high as that of gold, when used to produce similar a MLPF devices. However, from simulation carried out on the rGO MLPF using HFSS, it was observed that for the rGO MLPF device to produce a response identical to the response of the gold MLPF device while maintaining the substrate as quartz and the ground plane as copper, the conductivity would range from 90,000S/m upwards.

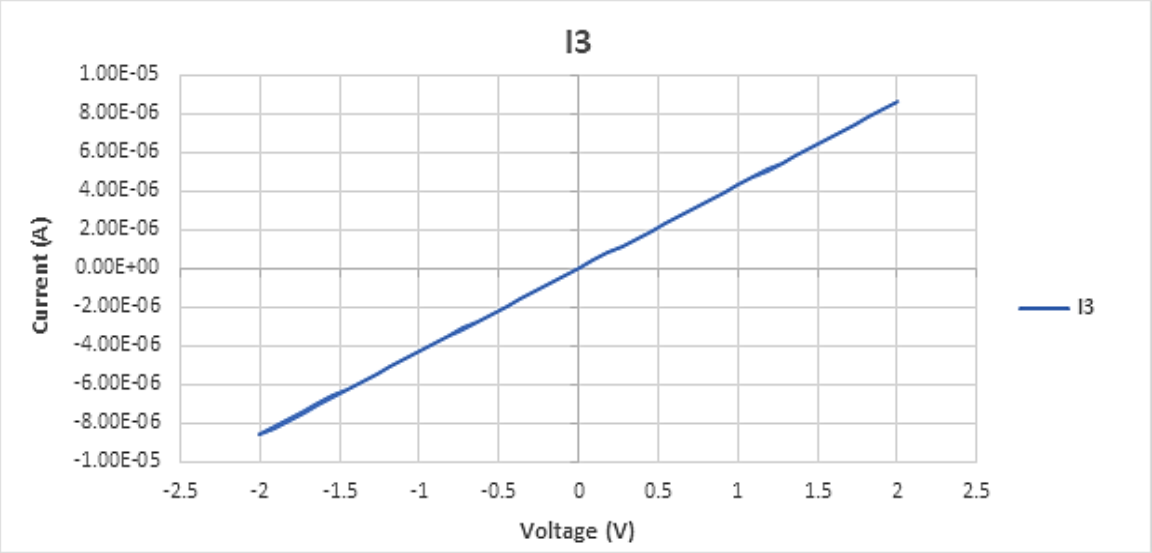

Figure 5. 27 The conductance plot of 5LPF rGO

Further characterization was done using a VNA to study the sensitivity and selectivity of the fabricated devices. The essence of this characterization is to observe if experimental results agree with the expected and simulated results, thereby, illustrating the possible deployment of the filter for the intended application. The results of both the VNA results and the simulation results are shown in figure 5.31 below.

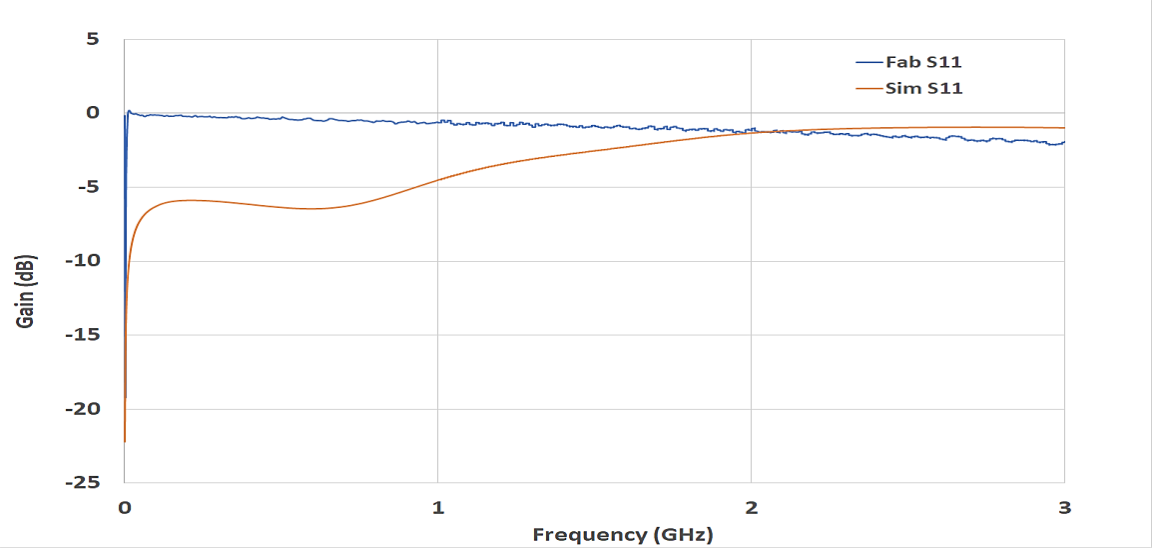

Figure 5. 28 The S11 response for both the fabricated and the simulated rGO 5LPF device

From the figure 5.28 above which compares the response the S11 plot for both the simulated (S11 Sim) and fabricated (S11 Fab) device, it was observed that the response of the simulated device shows a change in gain value as the frequency increases. This is

indicating that the material used for their fabrication has some improved conductivity as compared to the Kapton tape material. While the response of the fabricated device as observed showed less changes in gain as the frequency increases but with little loss. These differences could be attributed to the difference in the actual conductivity and the simulated conductivity of the device, and the value is significant to indicate this variation in their responses. However, their similarities are observed at the high frequency section where they both tend to show low loss in the device. From figure 5.31 above it is clear to see that it is important to come up with techniques on how to improve the conductivity of the rGO material since its conductivity is very low as compared to its gold counterpart, which has traditionally been used, and to also look at ways of using a low loss ground plane for the device.

There are several ways by which the conductivity of GO can be increased thermal annealing is a possible option, but the substrate needs to carefully consider. One of the ways of increasing the conductivity of this material is to increase the time and temperature it takes to carry out the chemical reduction of the GO as well as the kind of chemical used for their reduction. For this work the chemical reduction of the GO was done using hydrazine for 20 minutes at 800C. This reduction chemical, time and temperature could not have significantly improve the conductivity of the GO since it has been reported from literature that the type of chemical used, a higher reduction temperature and longer reduction time leads to improve conductivity of GO. This is because one downside with the method used for this work is that the hydrazine agents tend to leave behind C-N groups, in the form of hydrazones, amines, and aziridines, which may have negative effect on the electronic structure and property of rGO[121]. Therefore, improved chemical reduction method is an option to explore, this is because in the work of Chen et al [122] where thermal reduction of 4500C and hydroiodic acid reduction were used to directly reduce a Graphene oxide/Nanofibrillated Cellulose Composite Film. Similarly, Rao et al [121] reported that dried films of GO were treated with 48% hydrobromic acid (HBr), 95% hydrochloric acid (HCl) and 66% hydroiodic acid (HI) for 2 h, 24 h or 48 h respectively. The experimental analysis indicates that the electrical resistivity of GO is highly dependent on the type of acid treatment and the samples treated with HI

acid exhibited the lowest resistivity value of ~0.003 W.cm. The reduction of GO films and single GO sheets via a simple, low-cost method at moderate temperature was reported by Liu et al [123], they reported an in-situ synthesis of highly electrically conductive reduced graphene oxide films and single sheets using Lawesson's reagent (LR) as a reducing reagent at moderate temperature of 3000C.

To get a clearer picture of all the devices produced for this work it is important to make Comparison of the three different microstrip filters and their advantages/disadvantages as well. Table 5. 3 compares the devices produced using the three different materials. While their advantages and disadvantages are then presented.

Table 5. 2 Comparison of the fundamental parameters of the devices produced from the 3 materials.

Material	Conductivity	Cut-off frequency for LPF (GHz)	Centre Frequency for BPF (GHz)
Chemically reduced Graphene	8.7mS/m	N/A	N/A
Graphene from Kapton tape	0.28 mS/mm	N/A	N/A
Gold	44.2MS/m	2.51	2.35

The advantages of chemically reduced graphene are: Cheap to produce devices, has less complex device fabrication methods, has alternative device fabrication approaches, Devices can relatively be mass produced, and Has better conductivity as compared to the Kapton tape counterpart. The disadvantages of chemically reduced graphene are: Device fabrication requires specialised environment, Device fabrication requires specialised skills, Long substrate preparation process, Device fabrication requires specialised and advanced equipment, and Possess low conductivity.

The advantages of graphene from Kapton tape are: The cheapest to fabricate device from, devices are easily and cheaply mass produced, Device fabrication requires little skill to achieve, the device fabrication machine is easier to operate. The disadvantages of graphene from Kapton tape are: Device fabrication cannot be achieved on certain substrate (like quartz, glass, etc.), It produces the lowest conductivity material, Materials

produced are laterally segmented at micro and nano scale implementation which could lead to discontinuity of material, Devices are easily contaminated during fabrication.

The advantages of Gold devices are: Possess the highest conductivity, Smother end devices, Reliable devices, Controlled fabrication process, Controlled fabrication environment, and hence less prone to contamination during production. The disadvantages of Gold devices are: The most expensive fabrication approach, Device fabrication requires specially trained skilled personnel, requires expensive device fabrication equipment, and Fabrication must follow strict guidelines.

5.8 Summary

This chapter is basically about the characterisation of devices, it began with brief detail of the gold film sensor production. The chapter was then split into 3 major subsections; the Gold devices, the Graphene (Kapton Tape) and the Graphene (Ink Jet) and in each subsection a preamble of the fabrication process was briefly given. The characterisation results obtained from VNA measurement and the ANSYS simulation results for each device was presented on plot to compare the responses for each material. For the gold devices two sets were produced, the first sets comprise a combination of the 5th and 7th order LPF and the 3rd and 5th order BPF.

For the 5th order LPF the characterization results indicated that the highest frequency was exhibited by test points 15LCL22 and 15LCR22, and a mean frequency just some megahertz away, and a standard deviation of 30.1MHz. while, the peak gain was observed to occur at test point 15LCL31, with a mean value of about -3dB away from this maximum value, and a standard deviation of 2.23dB. For the 7th order LPF, the peak frequency was recorded at test point 17LL2 with a value, having the mean value of frequency peaks close to 1GHz and a standard deviation of 19.5MHz. While the peak gain value was at point 17CL32, but the mean value of the peak gain is -26.18dB and a standard deviation of 5.42dB. The 3rd order BPF has its highest frequency shift on point 13B21, with a mean value of the frequency shift of 2.31GHz and a standard deviation of 98.9MHz. While the

maximum change in gain occurred at test point 13B11, with mean value of -7.78dB and a standard deviation of 12.48dB. The 5th order BPF, exhibit its highest shift in frequency on point 15B21, with a mean value of 2.21GHz and a standard deviation of 127MHz. While the change in gain has a peak gain value on point 15B12, and a mean value is -7.19dB and a standard deviation of 4.55dB. The characterisation results of these filters were presented and discussed.

Based on the results of characterization of the first set of devices, a second set was then produced consisting mainly of 5th order BPF. For these new devices, a random sample from a dozen of identical devices was chosen and characterized. As for the filter device produced from LIG material obtained from Kapton tape, the characterisation steps were presented based on the measurement results. For a multiple strip material, it was observed that the conductivity results for a setting where the width of each width of strip is 0.35mm at an engraving speed of 400mm/s at a %power of 30, exhibit better result as compared to the rest. While for the single strip material, the conductivity results where the strip width is 0.35mm at an engraving speed of 400mm/s at a %power of 32, is better as compared other results.

From the results presented and the analysis of results the 5th order BPF gold devices were taken forward for biological testing. This is because from the sets of the fabricated filters the BPF indicated better response that would make it suitable for the design of a sensing element. And between the 3BPF and the 5BPF devices the 5BPF device indicate better performance based on the analysis done in section 5.3. Additionally, it is also important for all the devices to be used for the sensing element to be made from the same filter design to enable easy analysis of results.

Chapter 6. Biological Testing

6.1 Introduction

This chapter looks at the use of these filters towards measurement of the target biological sample (Anti-mouse IgG). The chapter discusses the production of the reservoir, protocols for the cleaning of the devices, then the process of functionalisation, the MES (4-morpholinoethanesulfonic acid) buffer solution and the mouse IgG preparation. The sensing procedure is also discussed where the devices used for measuring and control were stated. This chapter also highlighted the results of both the measuring and control devices for each filter devices, after which device selection was done based on the results obtained illustrating the sensitivity and selectivity of the device. Finally, a brief summary of results and analysis was presented.

6.2 Device Preparation

This section deals with the preparation of the fabricated devices prior to the implementation functionalisation protocol. This includes the production and attachment of the reservoir, the device cleaning method used and the pre-functionalisation procedure. These undertaking are discussed in the sections below.

6.2.1 Device Cleaning

The first stage was to clean the devices to ensure the surface was free from any form of dirt prior to functionalisation. There are three methods by which the devices can be cleaned, these are: using Piranha, Plasma Ashing (Oxygen plasma) and UV Ozone. The Piranha is regarded as the best cleaning method and it is made up of 70% H_2SO_4 and 30% H_2O_2 (i.e., concentrated sulphuric acid and hydrogen peroxide in a ratio of 7:3). To prepare the Piranha solution, 0.7ml of the sulphuric acid was mixed with 0.3ml of hydrogen peroxide in a beaker. However, it was observed that the Piranha solution attacked the reservoir when used, as a result the next best cleaning technique being the Plasma Ashing (this is simply washing off any impurities on the device surface and further cleaning is

done by placing them in an Oxygen plasma machine, to remove any residual impurities) was then used for the cleaning of the surface of the devices.

6.2.2 Pre-functionalization

After the cleaning of the surface of the devices using the plasma Ashing technique, then, ethanol was poured into the reservoir on the device surface and covered with a glass lid, this arrangement was then placed on a wet paper towel to create a humid surrounding (to prevent evaporation) all of this was put in a small plastic box and then into another bigger plastic box as shown in Figure 6.1. This box was then left in a cold room at 4^0C for 24 hours. This was done for two reasons, the first was to ensure that the reservoir is firmly bonded to the device surface without any leaks, the second was to certify the first layer of the functionalisation scheme can be firmly bonded to the gold surface. This is because the reagent to be used as the first layer of the functionalisation protocol is always prepared using ethanol since it can only dissolve in ethanol. If the ethanol does not vaporise then the first layer can be assumed to have bonded to the device surface.

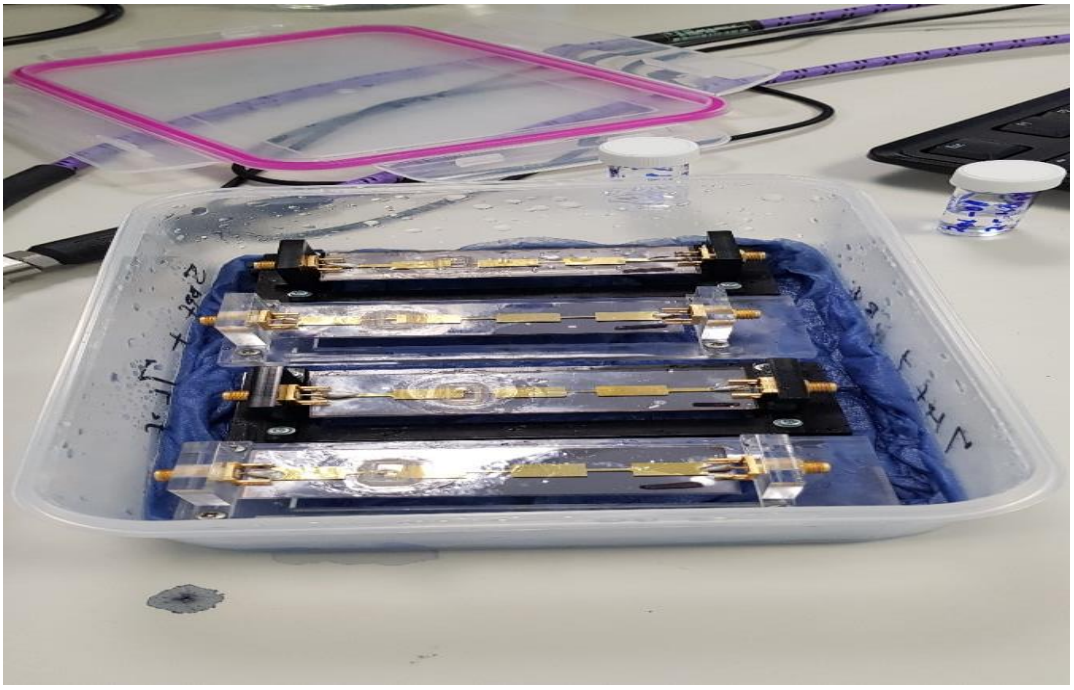

Figure 6. 1 Sensor devices being placed in a humid surrounding

6.3 Functionalisation Protocol

The functionalisation protocol takes several steps to be achieved, this is the preparation of the surface of the device to selectively respond to the analyte of interest as a result of the specific binding action of the anti-body being tested for. The first step is to know before-hand the material from which the devices is made from. Having known this, then chemical protocols can be designed to ensure the effective functionalisation for the intended application. For this work, the devices were made from gold, as such the functionalisation protocol has been known. To begin the process, the thiol-carboxylic (Sigma-Aldrich, United Kingdom) with Molecular weight (MW) of 526.73 or the thiol-hydroxy (Sigma-Aldrich, United Kingdom), with MW of 336.53 reagent stored with Nitrogen gas in a freezer was taken out and allowed to warm up to room temperature. The thiol reagents have the chain as shown below in figure 6.2.

To effect control, i.e., to ensure that the devices were selectively working, these two reagents were used to functionalise the surface of two selected sets of devices. The first sets of devices were functionalised using the hydroxy group reagent while the second sets were functionalised using a combination of both hydroxy (OH) group and carboxylic (COOH) group reagent in a ratio proportion.

6.3.1 Self-Assembly Monolayer

This has to do with the laying of the first layer of the functionalisation protocol. The first assembly type being the formation of the 100% hydroxy group in a 1:1 ratio with ethanol (being used for the control devices), for this group, a concentration of 0.5mM was chosen from the concentrated solution of the OH group of 1mM. For 100% OH assembly, with a desired volume of 2ml of the working solution (containing reagent + ethanol). This means 1ml of the OH reagent is required in the 2ml blocking OH solution, as such the remaining 1ml is the volume of the ethanol. Hence the required resultant blocking reagent was made up of 1ml OH + 1ml ethanol, with total being 2ml working Blocking reagent. Having determined the volume of the working OH reagent and the required volume of ethanol, the stock solution for the OH reagent was then prepared, where 10ml of ethanol was

poured in a glass container using a sterile plastic pipette and then 4µl of OH reagent was also then poured in the glass container using a micro pipette, this mixture was thoroughly mixed and stored as the stock solution.

The second assembly type comprises a ratio of the hydroxy and the carboxylic group (for this work an 80%: 20% ratio was chosen) for this combination the ratio is 0.4mM:0.1mM totaling 0.5mM. The sum of the OH and COOH reagent equals 4.5ml the remaining 0.5ml was made up for using ethanol, the composition for the working reagent is; the OH is 2ml, COOH is 2.5ml, Ethanol is 0.5ml making a total of 5ml. The OH in this mixture is acting as a blocking reagent, blocking the surface of the device not covered by the COOH reagent. While the stock solution (out of which the working or test reagents were then taken from) for the COOH reagent was prepared, where 2.5µl of the COOH reagent was poured in glass container containing 20ml of ethanol this mixture was then stirred to mix properly, and the mixture was safely stored. The working solution for both reagents is what was used for the self-assembly monolayer (SAM) on the devices when functionalising the first layer for either the control device (with 100% OH) or the measuring device (with 80% COOH and 20% OH). Both SAM were left to incubate in a humid environment for 24 hours in a cold room of 4^0C.

These working reagents were then used to modify the surface of the devices for the purpose of selective binding with the analyte of interest. The step-by-step procedure is as shown in figure 6.3 below, however, the SAM of the control device is shown in 6.2 this is made by the application of the 100% OH reagent. Figure 6.3 illustrates the functionalization procedure for the measuring device starting with figure 6.3a as the first layer of the measuring device that has the COOH and the OH reagents on the device, with the OH blocking all the surfaces not covered by the COOH. Figure 6.3b shows the second layer of the measuring device, where the amine (NH_2) linkage is connected to the receptive COOH reagent, Figure 6.3c shows the attachment of the mouse IgG to the amine group. While in figure 6.3d shows the anti-mouse IgG connecting with the mouse IgG indicating selectivity of the measuring device.

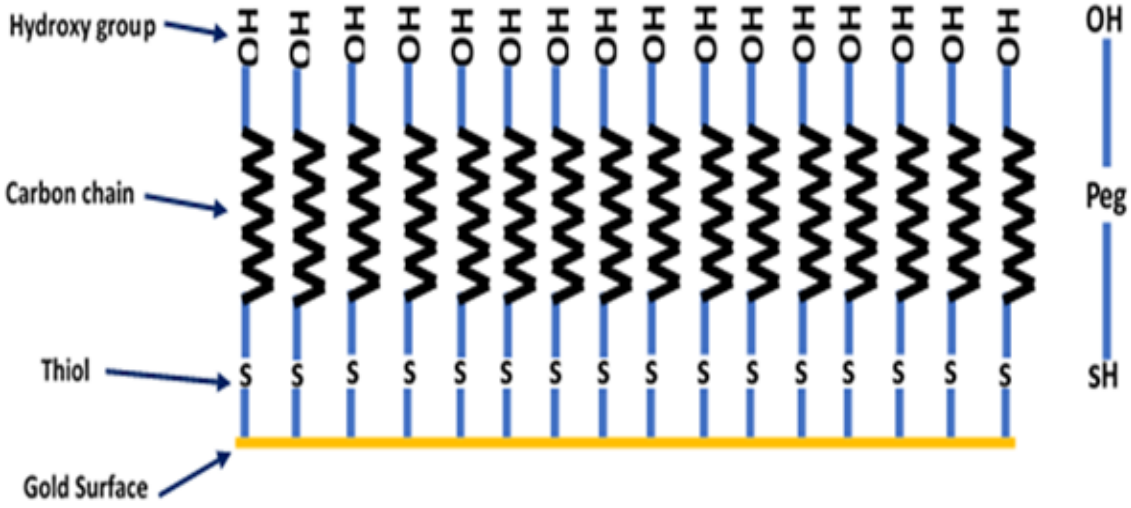

Figure 6. 2 The SAM of the control device used as the blocking OH reagent on gold Surface

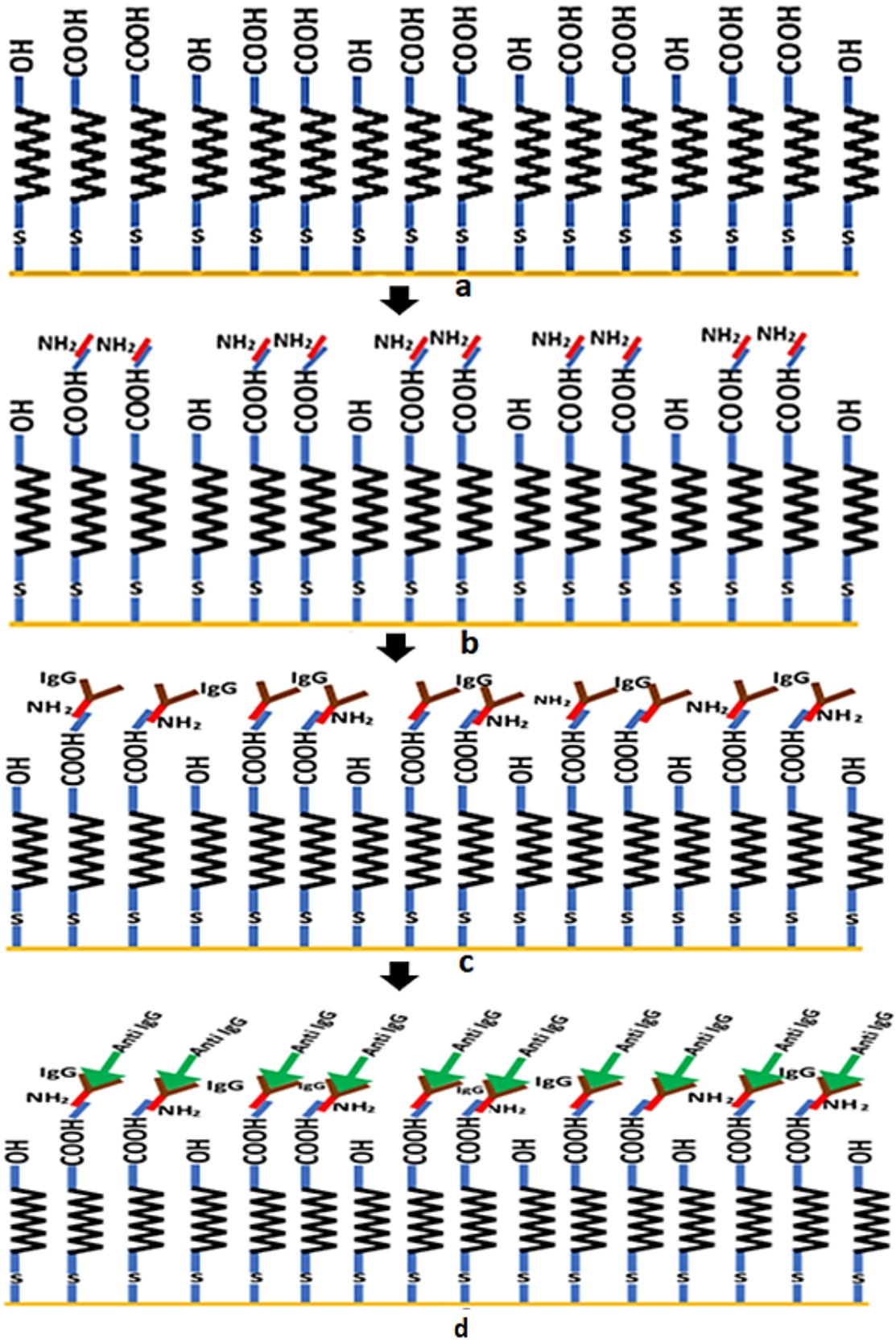

Figure 6. 3 The Functionalization of the measuring device, a) The carboxy and the Blocking reagents in 80:20 ratio on the gold surface, b) Amine attachment to the COOH group after NHS/EDC incubation, c) IgG bonding after NHS/EDC incubation, d) Bonded anti-Mouse I

6.3.2 MES Buffer Solution

The MES (4-morpholinoethanesulfonic acid) buffer solution was needed to make an amine coupling solution for the measuring devices. To begin the amine attachment to the SAM on the devices shown in figure 6.3b above, a 1-ethyl-3-(3-dimethylaminopropyl)carbodiimide hydrochloride (EDC) was used in conjunction with a N-hydroxysuccinimide (NHS), the NHS/EDC was used to prepare amine reactive esters of carboxylate groups (-COOH) which can react with primary amines (-NH2) to form a stable amide bond [124, 125]. EDC reacts with carboxylic acid groups to form an active O-acylisourea intermediate that is easily displaced by nucleophilic attack from primary amino groups in the reaction mixture[125]. The primary amine forms an amide bond with the original carboxyl group, and an EDC by-product is released as a soluble urea derivative. EDC crosslinking is most efficient in acidic (pH 4.5) conditions and must be performed in buffers devoid of extraneous carboxyls and amines[125, 126]. MES buffer is a suitable carbodiimide reaction buffer [127]. Phosphate buffers and neutral pH (up to 7.2) conditions are compatible with the reaction chemistry, although with lower efficiency; increasing the amount of EDC in a reaction solution can compensate for the reduced efficiency. EDC can be used alone but the addition of N-hydroxysuccinimide (NHS) enhances the coupling efficiency with the primary amines. The result of this coupling can be seen in figure 6.3b where NH_2 was attached before the IgG in figure 6.3c.

The NHS or its water-soluble analogue (Sulfo-NHS) is often included in EDC coupling protocols to improve efficiency or create dry-stable (amine-reactive) intermediates. EDC couples NHS to carboxyls, forming an NHS ester that is considerably more stable than the O-acylisourea intermediate while allowing for efficient conjugation to primary amines at physiologic pH. NHS esters have a half-life of 10 minutes at pH8.6, 1 hour at pH 8, and 4.5 hours at pH7 [124]. Proteins (antibodies) are deprotonated at physiological pH (The pH that normally prevails in the human body, it is approximately 7.4) so have a net negative charge. The NHS/EDC reaction is most efficient at pH 4.5-7.2 so the reaction of the -COOH reactive groups on the SAM surface will be carried out at low pH (0.1M MES pH 6) [125, 127, 128]. To prepare the MES buffer involves getting the required volume at the desired pH value. For this preparation, 1.952g of MES was dissolved in 70ml of water

(H_2O), an S20 model number Mettler Toledo (Mettler Toledo, UK) pH meter was calibrated and used to determine the pH of the solution used. The pH was adjusted by adding sodium hydroxide (NaOH) until a value of pH6 was reached, the final concentration of solution was 0.1M after which the volume of the resultant solution was poured in a plastic measuring cylinder and the final volume of 100ml was made up with water.

To prepare the EDC involves getting the required volume and concentration. For this preparation, 80.89mg of EDC was dissolved in 1.055ml of MES, a 1454 model number Jenway hotplate magnetic stirrer (Scientific Support, USA) was used to stir the solute-solution mixture until all the solutes was dissolved. The final concentration of solution was 400mM. In a similar vein, the NHS preparation involves dissolving 42.4mg NHS in 3.684ml of MES and using the same stirrer, the solute-solution mixture was stirred until all the solutes was dissolved, the final concentration of solution was 100mM.

6.3.3 The Mouse IgG

The Mouse IgG (Immunoglobulin G (IgG)) is a glycoprotein antibody that regulates immune responses such as phagocytosis and is also involved in the development of autoimmune diseases. The Mouse IgG was used to test the sensitivity and selectivity of the devices, and its implementation can be seen in figure 6.3c above. The quantity used for this work is of most importance in this section, it is important to state that, this part of the device functionalization is only done on the devices that are intended to be used for sensing of the biological sample. The concentration of the stock sample used here was high as such it was then diluted. The chemicals used for this functionalization stage were IgG (Sigma-Aldrich, UK) supplied as a stock solution of 1mg/ml and PBS. 5µl of IgG was mixed with 495µl of PBS at room temperature giving a final concentration of IgG of 10µg/ml this was done for a volume of 0.5ml solution (comprising the IgG and the PBS). 60µl of this solution was placed into the reservoir of the device for 30 minutes at a room temperature of 24^0C after which it was drained out and ready for the next step. The full details are given in section 6.6 below. It should be noted however that the IgG should be prepared only when it is about to be used, else it will lose it potency and may not give the desired response.

6.4 The sensing Procedure

The first step towards testing the devices for sensing application was to wash the device thoroughly to have a clean surface, first with ethanol and them oxygen plasma was used to further clean the surface of the devices. Afterwards the devices were separated into pairs of their various kind which were: the 5th and 7th order low pass filters, and the 5th and the 3rd order bandpass filters. Each of these filters have two devices, one to be used for sensing the target analyte, while the other was to control to see if the sensing ability of the devices was achieved. To achieve this testing technique one set of devices were coated with 100% OH (the control device) reagent and the other set was coated with the 80:20 OH: COOH (the sensing device) reagent. At this stage VNA measurement of the devices was taken before the addition of the mouse IgG (that is after SAM), these measurements were done for 2 separate occasion (with and without PBS). Another measurement was done after the addition of the analyte (the anti-mouse IgG) on them, all of these was to observe their response characteristics, the results were recorded as observed. Before this was done it was ensured that the VNA was calibrated prior to use for measurements on the day. The next step was to wash the devices with ethanol three times, and then the reagent prepared as stated above was introduced, using a pipette to fill the reservoir on the surface of the devices selected for each reagent type and then glass cover slips were used to cover the individual reservoirs. The devices used grouped as shown in table 6.1 below.

Table 6. 1 Devices group for different reagent

Control device (For 100% OH)	Measuring device (For 80% OH: 20% COOH)
3rd order bandpass filter device number 4	3rd order bandpass filter device number 6
5th order bandpass filter device number 1	5th order bandpass filter device number 2
7th order lowpass filter device number 1A	7th order lowpass filter device number 2A
5th order lowpass filter device number 1	5th order lowpass filter device number 5

These respective devices were enclosed in a plastic container to limit the evaporation of the reagent from the devices to the barest minimum, since the reagents were prepared with a mixture of ethanol. All the plastic containers were then store in a cold room for 24

hours, so that there was enough time for the active compound (OH and COOH) to stick to the surface of the device (to ensure that the active reagents firmly bind and form a layer on the devices it was kept topped up every hour with ethanol during the lab opening times of 9am to 5pm and left overnight in its sealed container). Upon, removing the devices from the cold room, they were allowed to cool down and then washed three time with ethanol and once with PBS after which their responses were measured both in air and in PBS using a VNA, these results were recorded as observed.

The next step was to wash once with MES and then make a mixture of the NHS/EDC in a ratio 1:1 (1ml:1ml) in a container, using pipette, fill the reservoir of the 4 COOH SAM devices with this mixture, allow for the COOH and the NHS/EDC to incubate at room temperature for 30 minutes to form a bond. While waiting, the Mouse IgG (5µl conc. IgG + 495µl of PBS (1XPBS)) was then produced as described in section6.5.3 above. After 30 minutes the mixture (COOH and NHS/EDC) was then sucked out of the devices and they were then rinsed once using the MES (0.1M, pH6). Now the reservoir on the devices was filled (with volume of 80µl) with the just produced Mouse IgG solution and allow to incubate for another 30 minutes. This was then sucked out after the incubation period. Then any unreacted NHS activated site was blocked with Tris (trisaminomethane of 50mM, pH 7.5) and allow it to incubate for another 15 minutes. The Tris solution contains large quantity of amine, its introduction to the surface ensured that every COOH group has got an amine group attached to it, this will prevent reaction of the COOH and ensure complete functionalisation. After 15 minutes the Tris was drained out and the devices was rinsed once with PBS, the result of the outlined steps above has yielded a functionalised surface with the anti-body (mouse IgG) of interest. After this step, the responses of the devices were measure in PBS, the observed results were recorded.

The next step of was to make the anti-mouse IgG in a similar way to how the Mouse IgG was made since they have the same concentration. This time the volume of the anti-mouse IgG was more than that of the mouse IgG since they (anti-mouse IgG) are made for all the devices (both the 100% OH and the 80%:20% COOH). This was done to check if the Pure OH laden devices change response with the introduction of the anti-mouse IgG. Now

the anti-mouse IgG was introduced to the surface of all the (8) devices and was incubate for 1 hour. After 1 hour the anti-mouse IgG on the devices were drained and washed with a wash buffer (PBS-Tween (100ml 1XPBS + 0.05ml 0.05% Tween)) three (3) times and once with PBS. Then VNA measurement of the response of the devices were taken in PBS and the results were recorded as observed. The results of each of the stages will indicate the sensing limit and capability of the biosensor. After the measurement, the modified surface was then rinsed in PBS, then water and stored at 4^0C in the cold room.

6.5 Presentation of Result for Measuring and Control Devices

The results of the observed recorded values for the Measurement and control devices for both the LPF and BPF are presented here to explain the level of sensitivity and selectivity of the devices. The measuring devices will try to highlight the sensitivity and selectivity of the devices while the control devices will try to only indicate the selectivity of the devices. Since VNA was used for measuring and testing of the devices, as such obtaining the observed results was achieved by exporting to external storage, this means there was a large data collected for all the devices. The results of all the data collected were then processed by curve fitting the data points in a manner as shown in figure 6.4 below, this was achieved by transferring the data to be treated to MATLAB for result processing using the correct approach, this was done to ease the determination of the peak frequency and gain of each measurement obtained. The importance of this is that any changes resulting from each step of the functionalization of the devices can be highlighted including changes in the peak frequency and change in gain from previous measurement due to the sensing of the target analyte.

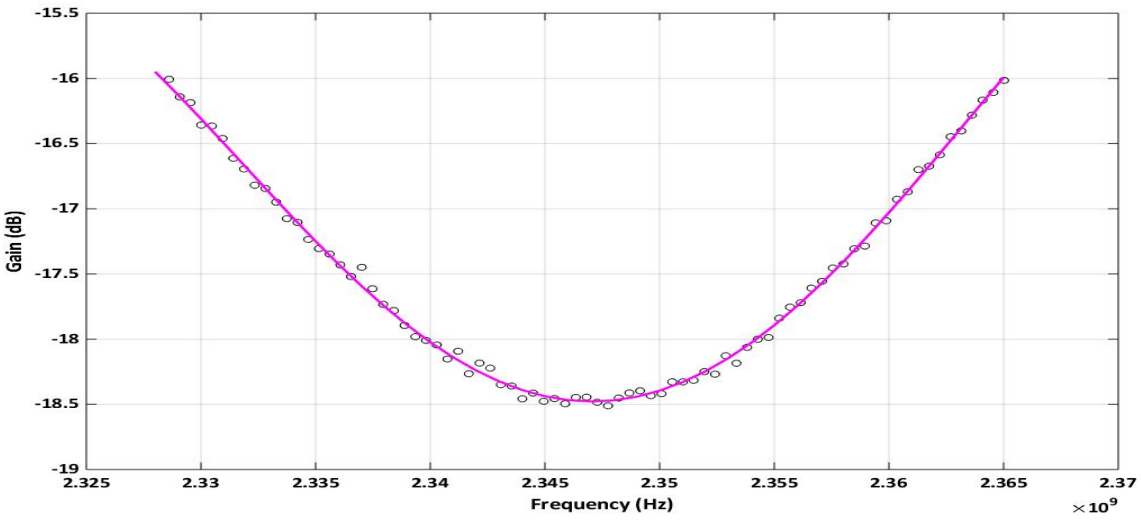

Figure 6. 4 A typical processed result for 3BPFD6 with Mouse IgG in PBS

6.5.1 The 3BPF Device

Figure 6.6 above shows a typical processed curve-fitted result of the measurement of device response obtained from a VNA. From these results the peak gain and frequency for the 3BPF devices were recorded for further data interpretation. Table 6.2 below shows the record of the frequency and change in gain obtained for the measure and control 3BPF devices. The recorded values of frequency and change in gain are for the S11 response of the filter type being discussed. M3BPFD6_F is an acronym for measuring device of 3rd order band pass filter for device 6 frequency value, M3BPFD6_G is an acronym for measuring device of 3rd order band pass filter for device 6 gain value, C3BPFD4_F is an acronym for control device of 3rd order band pass filter for device 4 frequency value, C3BPFD4_G is an acronym for control device of 3rd order band pass filter for device 4 gain value.

Table 6. 2 Recorded frequency and gain from the processed response of the measuring and control 3BPF devices

Test Layer	M3BPFD6_G(dB)	M3BPFD6_F (Hz)	C3BPFD4_G(dB)	C3BPFD4_F(Hz)
PD in PBS	-17.40	2.11E9	-18.43	2.38E9
SAM in PBS	-18.50	2.35E9	-18.15	2.39E9
Anti-Mouse IgG	-9.05	2.28E9	-6.38	2.00E9

From table 6.2 above the plot of the frequency and changes in gain against the functionalized layer was done and presented in figure 6.5 below.

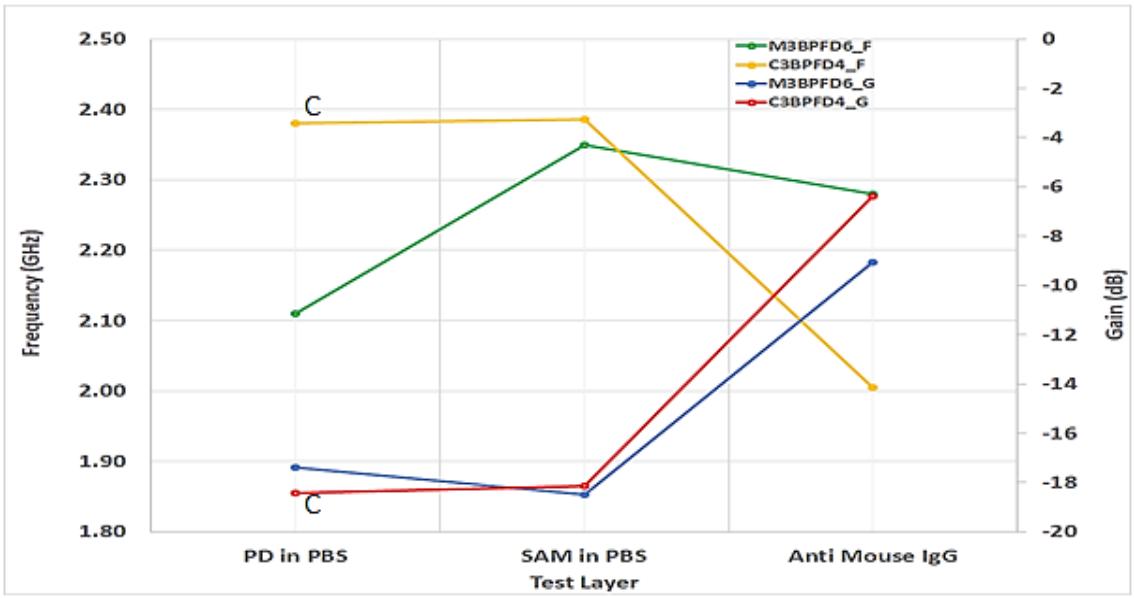

Figure 6. 5 The line plot of changes in frequency and gain due to surface modification of the 3BPF devices. 'PD means Plain Device, SAM means Self Assembly Monolayer, PBS means Phosphate Buffer Solution and IgG is Immunoglobulin G'

From figure 6.5 it can be observed that the frequency change for the measuring device shifted significantly to a higher frequency value when measurement was done between PD in PBS and SAM in PBS as compared to the changes in frequency observed for the control device which although initially indicated higher frequency value but remained fairly stable between the same change in test layers. With the introduction of the anti-mouse IgG (that is measurement between SAM in PBS and anti-mouse IgG), it was observed that the rate of change of the control device tends towards lower frequency values while that of the measuring device tend to slightly change from its previous value to remain at a frequency valued within the vicinity of the designed centre frequency of the BPF. In a similar vein, between PD in PBS and SAM in PBS the measuring device indicates significant loss due to ample change in gain value as compared to the control device whose change in gain to higher value was small between the same change in test layer. With the introduction of the anti-mouse IgG, it was observed that both devices follow similar trend but with the control device exhibiting higher gain value. Although the measuring and the control devices follows similar trend, the significant difference

between them was clearly notice when results were taken at PBS in air and when the anti-mouse IgG was introduced. Since the response of both devices tend to follow similar trend, the sensitivity to changes in functionalized layer cannot be fully understood when considering only the responses of their change in gain value.

6.5.2 The 5BPF Device

The same method used for extracting the peak frequency and gain for the curve-fitted result of figure 6.4 above was used for the 5BPF devices, the results obtained from this approach is presented in table 6.3 below. Similarly the recorded values of frequency and change in gain are for the S11 response of the 5BPF, where from table 6.3 M5BPFD2_F is an acronym for measuring device of 5th order band pass filter for device 2 frequency value, M5BPFD2_G is an acronym for measuring device of 5th order band pass filter for device 2 gain value, C5BPFD1_F is an acronym for control device of 5th order band pass filter for device 1 frequency value, C5BPFD1_G is an acronym for control device of 5th order band pass filter for device 1 gain value.

Table 6. 3 Recorded frequency and gain from the processed response of the measuring and control 5BPF devices

Test Layer	M5BPFD2_G(dB)	M5BPFD2_F (Hz)	C5BPFD1_G(dB)	C5BPFD1_F(Hz)
PD in PBS	-34.20	2.21E9	-22.95	2.22E9
SAM in PBS	-34.50	2.30E9	-24.89	2.31E9
Anti-Mouse IgG	-16.10	2.28E9	-23.19	2.31E9

From table 6.3 above the plot of the frequency and changes in gain against the functionalized layers was done and presented in figure 6.6 below.

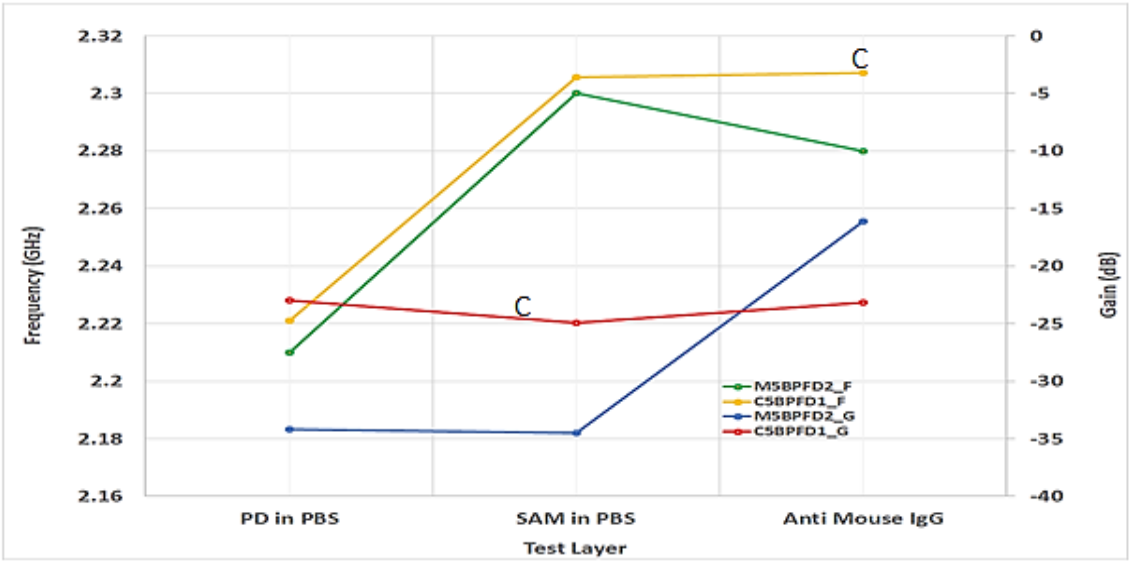

Figure 6. 6 The plot of changes in frequency and gain due to surface modification of the measuring and control 5BPF devices. . 'PD means Plain Device, SAM means Self Assembly Monolayer, PBS means Phosphate Buffer Solution and IgG is Immunoglobulin G'

From figures 6.6 it can be observed that the resonant or peak frequency of the measuring and control devices exhibit a steep change between PD in PBS and SAM in PBS, but with the starting peak frequency at PD in PBS for the control device being higher than that of the measuring device. However, between SAM in PBS and anti-mouse IgG the frequency response of the measuring device changes to a lower frequency while that of the control device remained stable, which is the expected response for this device. This observed response which indicates that the specific binding of the anti-mouse was measured, consequently the sensitivity of this device to the target analyte can be said to have been recorded. The change in gain for the measuring device between PD in PBS and SAM in PBS indicate a slight change to lower gain values, while that of the control device also indicating a change to lower gain values between the same change in test layer but has gain values higher than that of the measuring device. However, between SAM in PBS and anti-mouse IgG, the change in gain for the control device was observed to slightly increase, while that of the measuring device indicated a to significant increase when compared. This result also indicate that the measuring device is showing substantial sensitivity to the target analyte.

6.5.3 The 5LPF Device

Similarly, the approach for extracting the peak frequency and gain for the curve-fitted result of figure 6.4 above was used for the 5LPF devices, the obtained results from this method is shown in table 6.4 below. The recorded values of frequency and change in gain are for the S11 response of the 5LPF. From table 6.4 M5LPFD5_F is an acronym for measuring device of 5th order band pass filter for device 2 frequency value, M5LPFD5_G is an acronym for measuring device of 5th order band pass filter for device 2 gain value, C5LPFD1_F is an acronym for control device of 5th order band pass filter for device 1 frequency value, C5LPFD1_G is an acronym for control device of 5th order band pass filter for device 1 gain value.

Table 6. 4 Recorded frequency and gain from the processed response of the measuring and control 5LPF devices

Test Layer	M5LPFD5_G(dB)	M5LPFD5_F (Hz)	C5LPFD1_G(dB)	C5LPFD1_F(Hz)
PD in PBS	-24.9	1.14E9	-11.60	1.11E9
SAM in PBS	-24.6	1.13E9	-23.67	1.14E9
Anti-Mouse IgG	-12.7	1.14E9	-11.95	1.12E9

From table 6.4 above the plot of the frequency and changes in gain against the functionalized layers was done and presented in figure 6.7 below.

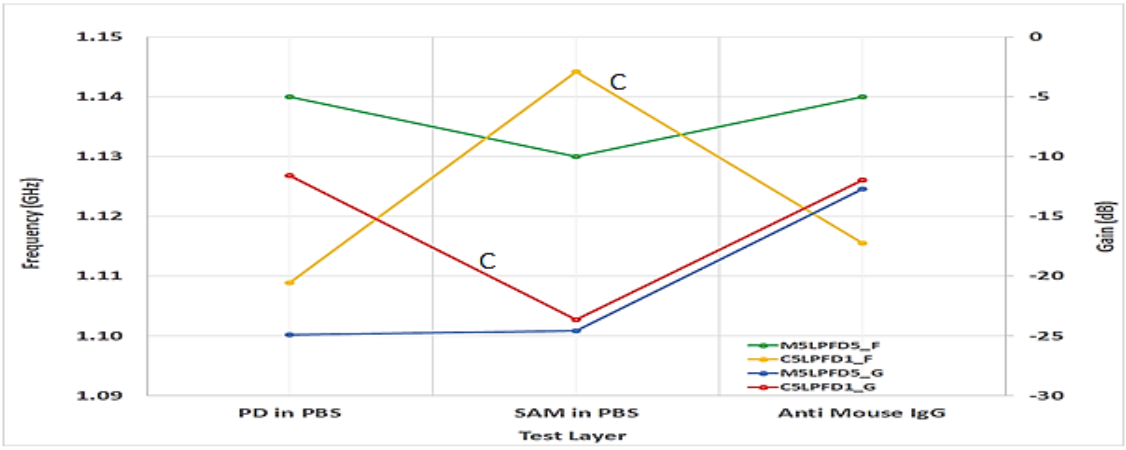

Figure 6. 7 The plot of changes in frequency and gain due to surface modification of the measuring and control 5LPF devices. . 'PD means Plain Device, SAM means Self Assembly Monolayer, PBS means Phosphate Buffer Solution and IgG is Immunoglobulin G'

From figures 6.7 it can be observed that between PD in PBS and SAM in PBS the peak frequency of the measuring device exhibits a change in frequency from an initially higher value to a lower value while that of the control device indicate contrasting response, from a lower frequency value to a higher value. Between SAM in PBS and anti-mouse IgG the frequency response of the measuring device changes back to a higher frequency while that of the control device in contrast dropped back to a lower value. This swing is not desirable for the frequency response of the control device. The change in gain for the measuring device between PD in PBS and SAM in PBS indicate a slight change to a higher gain value as compared to that of the control device whose change in gain was sharp, and from a higher to a lower gain value. Conversely, between SAM in PBS and anti-mouse IgG, the change in gain value for both devices increased simultaneously to about -12dB for the control device and approximately -13dB for the measuring device.

6.5.4 The 7LPF Device

To analyse the results of this device the same method used for extracting the peak frequency and gain for the curve-fitted result of figure 6.6 above was also used for the 7LPF devices, the results obtained from this approach is presented in table 6.5 below. Similarly the recorded values of frequency and change in gain are for the S11 response of the 7LPF, where from table 6.3 M7LPFD2A_F is an acronym for measuring device of 7th order band pass filter for device 2A frequency value, MLPPFD2A_G is an acronym for measuring device of 7th order band pass filter for device 2A gain value, CLPPFD1A_F is an acronym for control device of 7th order band pass filter for device 1A frequency value, CLPPFD1A_G is an acronym for control device of 7th order band pass filter for device 1A gain value.

Table 6. 5 Recorded frequency and gain from the processed response of the measuring and control 7LPF devices

Test Layer	M7LPFD2A_G(dB)	M7LPFD2A_F (Hz)	C7LPFD1A_G(dB)	C7LPFD1A_F(Hz)
PD in PBS	-32	9.43E8	-37	9.47E8
SAM in PBS	-31.1	9.47E8	-40.18	9.53E8
Anti-Mouse IgG	-28.7	1.79E9	-31.65	9.55E8

From table 6.5 above the plot of the frequency and changes in gain against the functionalized layers was done and presented in figure 6.8 below.

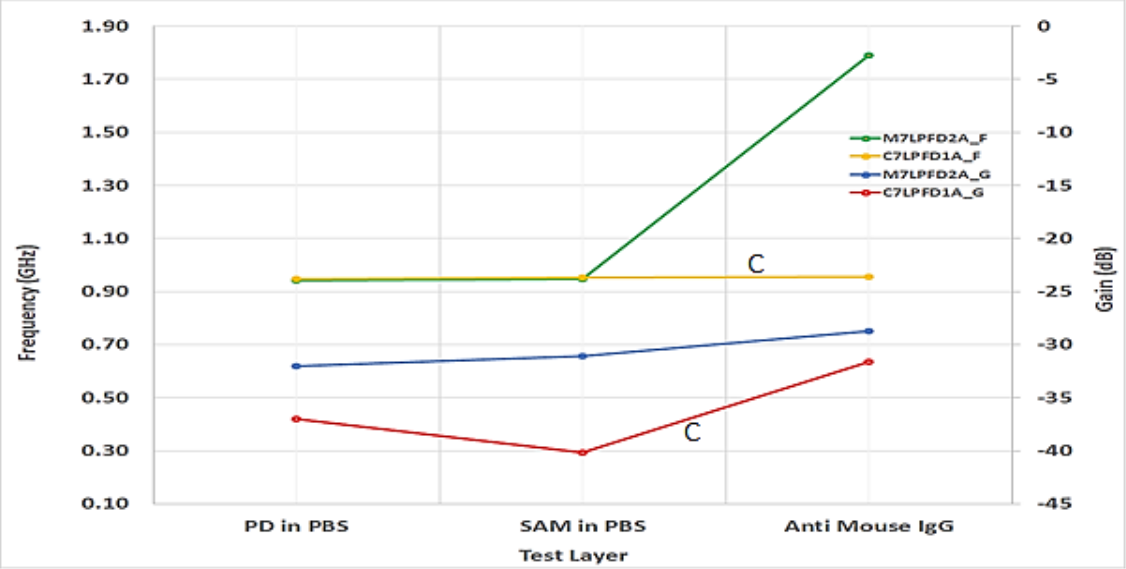

Figure 6. 8 The plot of changes in frequency and gain due to surface modification of the measuring and control 5LPF devices. . 'PD means Plain Device, SAM means Self Assembly Monolayer, PBS means Phosphate Buffer Solution and IgG is Immunoglobulin G'

From figures 6.8 it can be observed that the peak frequency of the measuring and control devices exhibits a steady value of 0.95GHz between PD in PBS and SAM in PBS, while between SAM in PBS and anti-mouse IgG the frequency response of the measuring device increased significantly to 1.79GHz, but with that of the control device remaining unchanged at 0.95GHz, which is the expected response for this device. This observed response indicates specific binding of the anti-mouse and consequently the sensitivity of this device to the target analyte can be said to have been recorded. The change in gain for the measuring device between PD in PBS and SAM in PBS indicate slight change in gain to a higher value, while that of control device was observed to change significantly to lower values. Between SAM in PBS and anti-mouse IgG, the change in gain for the control device then rose to -31.6dB, while that of the measuring device was observed to increase slightly when compared.

Form the above results presentation and analysis from the tables, charts and plots, the suitable device from the two filter types can be seen to be obvious, where for the LPF the

7th order filter appears to present better performance as compared to its 5th order counterpart. While for the BPF, the 5th order filter devices indicate better performance as compared to the 3rd order filter. The next section gives a brief insight to obtaining a result as to which devices can best serve as the sensing device for the proposed application, which also served as the basis for the fabrication of the second sets of devices.

6.6 Summary

In the beginning of this chapter the reservoir and device cleaning were discussed where it was stated that there are three methods by which the devices can be cleaned, but the Plasma Ashing (Oxygen plasma) was used. Then the Pre-functionalisation was discussed where it was done to make sure the first layer of the functionalisation scheme can be firmly bonded to the gold surface. The functionalisation protocol was then discussed, this being the preparation of the surface of the device from SAM to the application of the mouse IgG, so as to selectively respond and bind to the analyte of interest because of the specific binding action of the anti-body being tested for. Then the sensing procedure, where a VNA measurement of the devices was taken for the plain device in PBS, the SAM in BPS and when the anti-mouse IgG was introduced to both the measuring and control devices to observe their responses, these results were recorded as observed. Then finally, from the results and analysis, the suitable device was chosen based on their response characteristics, enabling more specific filter design and fabrication for biosensing application. To now determine the suitable device from each of the filter devices (BPF and LPF) that if used as the sensing device will exhibit the desired selectivity and sensitivity of the proposed sensor, results from table 6.2 to 6.5 were used. From these results, it can be observed that the suitable devices that can be used for biosensing application are the 7LPF and the 5BPF. Comparing these two devices, it was observed from the presented results above that the 5BPF device showed better response to biological changes and is the suitable device for the fabrication of the sensing element of a biosensor. Hence the second set of devices used for the sensing devices were fabricated as a 5BPF.

Chapter 7. Conclusion and Recommendation

7.1 Conclusion

The application of sensor technology has been studied and known to have significant impact in point-of-care (POC) applications, especially the biosensor. One of the basic aims of developing POC devices is to significantly cut down the diagnostic test result time, as well as making medical test devices easy to handle. Developing very sensitive, accurate, reliable, and rapid response biomedical analysis system is the basis for POC testing systems. Consequently, new rapid methods and technology are considered necessary to develop point-of-application sensors with better performance, considering selectivity, sensitivity, and cost. Therefore, a detection technique which is reliable, simple, sensitive, selective, and cost effective is a necessity in order to cut down the diagnostic turnaround time, which leads to quick and reliable diagnostic results that aids quick and precise medication. In addition, it should be able to detect very low concentrations levels of the samples and must be suitable for in situ real-time monitoring as well. Such a technique of detecting and sensing would offer a great commercial advantage to the biomedical sector.

The aim of this research is to develop an RF biosensor that is reliable, simple, sensitive, selective, and cost effective. To do this, three materials were used to implement the sensing element designed as a microstrip RF filter, these are LIG, rGO and Gold. The LIG material has two sets, the multiple strip material, which indicated a conductivity results of 0.28mS/mm and the single strip material with a conductivity result is 0.23mS/mm. The characterization results of the filter designed with the multiple strip material though better conductivity than the single strip material, does not appear favourable since its conductivity is very low as compared to a gold material that has traditionally been used. Simulation results however showed the conductivity levels that are needed for them to find application as a biosensing element. While the filter device fabricated from the rGO indicated better characterization results and conductivity value than that of the LIG material, however, its conductivity is very low as compared to its gold counterpart, which has conventionally been used, but simulation result on the material indicated how much the conductivity of this material need to be raised for it to be used to implement the

sensing element of a biosensor. As a backup, the gold material was used to implement the sensing element of the biosensor device in the form of an RF filter. Two sets of these devices were produced for biological measurement, the first sets comprise a combination of the 5^{th} and 7^{th} order for the LPF and the 3^{rd} and 5^{th} order for the BPF. The biological measurement involves the Pre-functionalisation and functionalisation protocols, to ensure the biosensor can selectively respond and bind to the analyte of interest because of the specific binding action of the anti-body being tested for. Then the sensing procedure, where a VNA measurement of the devices was taken for the plain device in PBS, the SAM in BPS and when the anti-mouse IgG was introduced to both the measuring and control devices.

From the results of the biological testing the following observations were made; For the 3BPF, frequency for both measuring and control devices showed less significant pattern, its change in gain appears to show a pattern but with a significant jump for anti-Mouse. Possible reason is that the SAM layer did not work, and one is getting non-specific binding in final stage hence both show similar effects. For the 5BPF, frequency seems to rise slightly per layer for both measuring and control devices this implies spike in control trace. The gain for measuring device shows similar pattern to 3BPF, and no significant change for control device. For the 5LPF, frequency does not show significant pattern for both devices. The gain for measuring device shows similar pattern to 3BPF, while that of the control device is inconsistent. For the 7LPF, frequency looks flat for both devices until after the addition of the anti-mouse then that of the measuring device rose significantly. While the gain for both measuring and control devices show same general pattern as 3 BPF, less so in the measuring device. In conclusion the frequency of the devices currently shows ample evidence of being sensitive enough. A general pattern of gain increase for anti-mouse on all samples for both measuring and control devices so, this indicates sensitivity but not selectivity. As the SAM stage shows small evidence, then this implies the SAM stage may not have performed its function and one is getting non-specific binding for the anti-mouse IgG indicating sensitivity but not selectivity. To come to a more useful conclusion better device functionalisation and more measurements are needed.

From these results however, the suitable device was chosen based on their response characteristics, enabling more specific filter design and fabrication for biosensing application. Suitable device from each of the filter devices (BPF and LPF) was determined, so that if used to implement the sensing device it would exhibit the desired selectivity and sensitivity of the proposed sensor. From these results, it can be observed that the suitable devices that can be used for biosensing application are the 7LPF and the 5BPF. Comparing these two devices, it was observed from the presented results above that the 5BPF device showed better response to biological changes and is the suitable device for the fabrication of the sensing element of the RF biosensor. This is because from the sets of the fabricated filters the BPF indicated better response that would make it suitable for the design of a sensing element and between the 3BPF and the 5BPF devices the 5BPF device indicate better performance based on the analysis of results. Hence, from the results of these first set of devices, the second set of devices were fabricated as a 5BPF. From the results presented and the analysis of results, the 5^{th} order BPF gold devices were taken forward for biological testing.

From this second fabrication run, a randomly selected sample was characterized, to enable the identification of the point on the device which produce the desired change in peak resonance frequency and gain. These points on the sensor that showed best repeatability in measurements were investigated. The addition of water at the midpoint of the filter demonstrated a repeatability of 2.4GHz peak resonance value and a +/- 0.19MHz standard deviation in the frequency measurement and a repeatability of -5.5dB gain value and +/-0.01dB standard deviation in change in gain measurement. This was identified as the most appropriate region to conduct future biological sensing.

7.2 Recommendation for Future Work

From the results and conclusion above it is important to enhance the output and performance of the sensor device. The first task is to improve on the device implementation material, for the LIG it is recommended that new approach of fabricating of the RF filter from a Kapton tape be devised, this may include optimising design and

fabrication parameters and probably the pre-treatment of the Kapton tape before the fabrication process. In order to obtain an electrically conductive reduced graphene oxide with enhanced conductivity the improved chemical reduction method is an option to explore, where thermal reduction at 450^0C and hydroiodic acid reduction could be used to directly reduce a graphene oxide film for 48 h. Alternatively the Lawesson's reagent could be used as a reducing reagent at moderate temperature of 300^0C to obtain an electrically conductive reduced graphene oxide elements for the implementation of the sensing element designed as microstrip RF filter.

Future work would include the miniaturisation of the microstrip Rf filter device and to explore how to incorporate them to other portable electronics. In the immediate future however, the biological testing of the characterized 5BPF sensing device would be done to determine their calibration curve and consequently the sensitivity and selectivity of the microstrip RF biosensor device.

Reference

1. Turner, A.P., *Biosensors: sense and sensibility.* Chem Soc Rev, 2013. **42**(8): p. 3184-96.
2. By Wan He, D.G., and Paul Kowal, *An Aging World: 2015*. 2016.
3. Nations, U., *World Population Ageing* 2015.
4. Guha, S., F.I. Jamal, and C. Wenger, *A Review on Passive and Integrated Near-Field Microwave Biosensors.* Biosensors (Basel), 2017. **7**(4).
5. Petryayeva, E. and W.R. Algar, *Toward point-of-care diagnostics with consumer electronic devices: the expanding role of nanoparticles.* RSC Advances, 2015. **5**(28): p. 22256-22282.
6. Chin, C.D., V. Linder, and S.K. Sia, *Commercialization of microfluidic point-of-care diagnostic devices.* Lab Chip, 2012. **12**(12): p. 2118-34.
7. Rogers, K.R., *Biosensors for environmental Applications.* Biosensors and Bioelectronics, 1995. **10**: p. 533-541.
8. Lowe, C.R., *Biosensors.* 1984.
9. Ronkainen, N.J., H.B. Halsall, and W.R. Heineman, *Electrochemical biosensors.* Chem Soc Rev, 2010. **39**(5): p. 1747-63.
10. Scarano, S., S. Mariani, and M. Minunni, *SPR-Based Affinity Biosensors as Innovative Analytical Devices.* Journal of Lightwave Technology, 2015. **33**(16): p. 3374-3384.
11. Shailaja, S.S.a., *Analysis, Design and Fabrication of Microwave Passive couplers.* International Journal of Computer Applications, 2015.
12. K.Rajasekaran, J.J., and T.Jayasankar, *Design and Analysis of Stepped Impedance Microstrip low pass filter using ADS simulation tools for wireless applications.* International Journal of Scientific and Research Publications, 2013. **3**.
13. M.Pozar, D., *Microwave Engineering*. Fourth Edition ed. 2012, Massachusetts, USA: JohnWiley & Sons, Inc.
14. Christopher Bowick, J.B.a.C.A., *RF Circuit Design*. Second ed. 2008,, United States of America: Elsevier.

15. Lancaster, J.-S.H.a.M.J., *Microstrip Filters for RF/Microwave Applications*. 2001, New York / Chichester / Weinheim / Brisbane / Singapore / Toronto: JOHN WILEY & SONS, INC.
16. Liao, S.Y., *Microwave Circuit Analysis and Amplifier Design*. 1987, New Jersey USA: Prentice-Hall International Inc.
17. K. C. Gupta, R.G., Inder Bahl and Prakash Bhartia, *Microstrip lines and Slotlines*. 1996, Massachusette USA: Artech House, Inc.
18. G.L. Matthaei, L.Y.a.E.M.T.J., *Design of Microwave Filters, Impedance-Matching Networks, and Coupling Structures*. 1963.
19. Brian-c-Wadell, *Transmission Line Design Handbook* 1991, Noorwood Masachusette: Artech House Inc.
20. Liew Hui Fang, S.I.S.H., Mohd Fareq Abd Malek, Yufridin Wahab and Lee Yeng Seng, *A Review of Technique To Convert Low Pass Filter Into Microstrip Line Circuit.* ARPN Journal of Engineering and Applied Sciences, 2015.
21. K. U-yen, D.C., and E.J. Wollack, *Planar Transmission Line Technologies.*
22. Zehentner, J., J. Machac, and J. Mrkvica, *Planar Transmission Lines in MW and MMW Circuits.* 2005. **1**: p. P-I-P-XI.
23. Bretchko, R.l.a.P., *RF Circuit Design Theory and Applications*. 2000, New Jersye USA: Tom Robins.
24. Islam Mansour, H.E., and Adly S. Tag El-dein, *Design of Stepped Impedance Microstrip Low Pass Filter with DGS.* International Journal of Engineering Research and Development, 2014. **10**(7): p. 58-67.
25. Jim Godwin R.S., V.V., S. Purushothaman, Dr. S. Raghavan, *Design of Parallel Coupled Microstrip Bandpass Filter for IRNSS Navigation system.* 2015.
26. A. Tirado-Mendez, H.J.-A., and R. Flores-Leal, *Improving Frequency Response Of Microstrip Filters Using Defected Ground And Defected Microstrip Structures.* Progress In Electromagnetics Research, 2010. **13**.
27. Kushwah, V.S.T., Geetam S. Bhadauria, Sarita Singh, *Designing Stepped Impedance Microstrip Low-Pass Filters Using Artificial Neural Network at 1.8 GHz.* IEEE, 2013: p. 11-16.
28. K. Rajasekaran, J.J.a.T.J., *Design and Analysis of Stepped Impedance Microstrip low pass filter using ADS simulation tools for wireless applications.* IJSRP, 2013.

29. Sudipta Das, D.S.K.C., *Design Simulation and Fabrication of Stepped Impedance microstrip LPF.* IJECT, 2012.
30. Tomar, N.S.V.a.P.S., *Design and Analysis of Stepped Impedance microstrip fractal LPF.* International Journal of Electronics and Communication Engineering, 2012. **5**(5): p. 603-607.
31. Garvansh, N.S.a.A.K., *Design and Synthesis of Stepped Impedance Microstrip Line Low Pass Filter.* International Journal of Scientific Research Engineering & Technology, 2014: p. 48-50.
32. Singh, A.S.a.P., *Design and analysis of Stepped impedence lowpass filter using microstrip line.* KIET IJCE, 2015. **3**.
33. Homayoon Oraizi, M.S.E.a.E.F., *Design of Stepped-Impedance Low Pass Filters with impedance matching by particle swamp optimization.* IEEE, 2009.
34. Wikipedia. *Radio frequency*. 2018 [cited 2018 16/04/2018]; Available from: https://en.wikipedia.org/wiki/Radio_frequency.
35. Mr. Daniel G. Swanson, J., *microstrip_filter_design_using_electromagnetics.*
36. Fan, S.S.H.X.C., *Potential diagnostic applications of biosensors current and future directions.* International Journal of Nanomedicine, 2006.
37. Gopinath, P.G., V.R. Anitha, and S.A. Mastani, *Microcantilever based Biosensor for Disease Detection Applications.* Journal of Medical and Bioengineering, 2015. **4**(4): p. 307-311.
38. .D.Malhotra, M.G.A.C.B., *Application of conducting polymers to biosensors.* Biosensors and Bioelectronics, 2002. **17**(5): p. 345-359.
39. HIMSS, W.s.N.W. *What is the role of biosensors in next generation health care? The Role of Biosensors in Routine Practice*. 2014; Available from: http://www.himss.org/what-role-biosensors-next-generation-health-care-0.
40. Wu, W., et al., *Wafer-scale synthesis of graphene by chemical vapor deposition and its application in hydrogen sensing.* Sensors and Actuators B: Chemical, 2010. **150**(1): p. 296-300.
41. Vaddiraju, S., et al., *Emerging synergy between nanotechnology and implantable biosensors: a review.* Biosens Bioelectron, 2010. **25**(7): p. 1553-65.
42. Haun, J.B., et al., *Magnetic nanoparticle biosensors.* Wiley Interdiscip Rev Nanomed Nanobiotechnol, 2010. **2**(3): p. 291-304.

43. Kim, Y.I., et al., *Biosensors for label free detection based on RF and MEMS technology.* Sensors and Actuators B: Chemical, 2006. **119**(2): p. 592-599.
44. Xu Chen, S.D., *Sol-gel-derived titanium oxide copolymer composite based glucose biosensor.* Biosensors and Bioelectronics 2003.
45. Lee, H.-J., et al., *An RF Circuit Model for Interdigital Capacitors-Based Carbon Nanotube Biosensors.* IEEE Transactions on Nanotechnology, 2010. **9**(6): p. 682-686.
46. Lee, H.J. and J.G. Yook, *Recent research trends of radio-frequency biosensors for biomolecular detection.* Biosens Bioelectron, 2014. **61**: p. 448-59.
47. Sun, N., et al., *CMOS RF Biosensor Utilizing Nuclear Magnetic Resonance.* IEEE Journal of Solid-State Circuits, 2009. **44**(5): p. 1629-1643.
48. Mamishev, A.V., et al., *Interdigital sensors and transducers.* Proceedings of the IEEE, 2004. **92**(5): p. 808-845.
49. Barry Friedman, M.A.G., Sergey Kalachikov, Kiejin Lee, Rastislav Levicky, and a.H.Y. Gang Shen, *Sensitive, Label-Free DNA Diagnostics Based on Near-Field Microwave imaging.* communications, 2006.
50. Lee, H.-J., et al., *Asymmetric split-ring resonator-based biosensor for detection of label-free stress biomarkers.* Applied Physics Letters, 2013. **103**(5): p. 053702.
51. Chithra, P. S, and A.A. Prince, *RF MEMS-Based Biosensor for Pathogenic Bacteria Detection.* BioNanoScience, 2013. **3**(3): p. 321-328.
52. Chen, Y.F., et al., *40 GHz RF biosensor based on microwave coplanar waveguide transmission line for cancer cells (HepG2) dielectric characterization.* Biosens Bioelectron, 2014. **61**: p. 417-21.
53. *Coplanar Waveguide* 2016 [cited 2016 11/11/2016]; Available from: https://www.microwaves101.com/encyclopedias/327-coplanar-waveguide-microwave-encyclopedia-microwaves101-com.
54. Baur, J., et al., *Immobilization of biotinylated biomolecules onto electropolymerized poly(pyrrole-nitrilotriacetic acid)–Cu2+ film.* Electrochemistry Communications, 2010. **12**(10): p. 1287-1290.
55. Taleat, Z., A. Khoshroo, and M. Mazloum-Ardakani, *Screen-printed electrodes for biosensing: a review (2008–2013).* Microchimica Acta, 2014. **181**(9-10): p. 865-891.

56. McCreery, R.L. and M.T. McDermott, *Comment on electrochemical kinetics at ordered graphite electrodes.* Anal Chem, 2012. **84**(5): p. 2602-5.

57. J. Lin, et al., *Laser-induced porous graphene films from commercial polymers.* Nat Commun, 2014. **5**: p. 5714.

58. Wen, F., et al., *Enhanced laser scribed flexible graphene-based micro-supercapacitor performance with reduction of carbon nanotubes diameter.* Carbon, 2014. **75**: p. 236-243.

59. Maher F. El-Kady, V.S., Sergey Dubin, Richard B. Kaner, *Laser Scribing of High-Performance and Flexible Graphene-Based Electrochemical Capacitors*. 2012.

60. H. Tian, et al., *Scalable fabrication of high-performance and flexible graphene strain sensors.* Nanoscale, 2014. **6**(2): p. 699-705.

61. K. Griffiths, J.H. C. Dale, and R.B.K. M. D. Kowal, N. Keegan, , *Laser-scribed graphene presents an opportunity to print a new generation of disposable electrochemical sensors.* Nanoscale, 2014. **6**(22): p. 13613-22.

62. Yang, W., et al., *Carbon nanomaterials in biosensors: should you use nanotubes or graphene?* Angew Chem Int Ed Engl, 2010. **49**(12): p. 2114-38.

63. S. Zhang , G.W., Y. Yang, *Materials and techniques for electrochemical biosensor design and construction.* 2000.

64. Farré, M., et al., *Sensors and biosensors in support of EU Directives.* TrAC Trends in Analytical Chemistry, 2009. **28**(2): p. 170-185.

65. Walcarius A, E.M., Herzog G, Urbanova V, Vila N. , *Electrode materials (bulk materials and modification).* , in *Environmental Analysis by Electrochemical Sensors and Biosensors.*, K.K. Moretto LM, Editor. 2014, Springer: New York:. p. p. 403-495.

66. Wilson's, W., *New materials for biosensors, biochips and molecular bioelectronics*, in *BIOSENSORS AND MODERN BIOSPECIFIC ANALYTICAL TECHNIQUES*, L. GORTON, Editor. 2005, ELSEVIER: AMSTERDAM - BOSTON - HEIDELBERG - LONDON - NEW YORK - OXFORD - PARIS SAN DIEGO - SAN FRANCISCO - SINGAPORE - SYDNEY-TOKYO. p. 285.

67. Sandulescu, R., et al., *New Materials for the Construction of Electrochemical Biosensors.* Biosensors - Micro and Nanoscale Applications, 2015.

68. Nambiar, S. and J.T. Yeow, *Conductive polymer-based sensors for biomedical applications.* Biosens Bioelectron, 2011. **26**(5): p. 1825-32.

69. Zhou, Y., C.W. Chiu, and H. Liang, *Interfacial structures and properties of organic materials for biosensors: an overview.* Sensors (Basel), 2012. **12**(11): p. 15036-62.

70. O. Ouerghi, A.S., N. Jaffrezic-Renault, C. Martelet, H. Ben Ouada, S. Cosnier, *Gold electrode functionalized by electropolymerization of a cyano N substituted pyrrole Application to an impedimetric immunosensor.* Journal of Electroanalytical Chemistry, 2001.

71. B. Wang, J.Z., S. Dong *Silica sol gel composite film as an encapsulation matrix for the construction of an amperometric tyrosinase-based biosensor.* Biosensors & Bioelectronics, 2000.

72. Abdulbari, H.A. and E.A.M. Basheer, *Electrochemical Biosensors: Electrode Development, Materials, Design, and Fabrication.* ChemBioEng Reviews, 2017. **4**(2): p. 92-105.

73. Miloslav Pravda , C.P., Yvette Mlchotte , Jean-Michel Kauffmann, Karel Vyffas, *Study of a new solid carbon paste tyrosinase-modified amperometric biosensor for the determination of catecholamines by high-performance liquid chromatography* Journal of Chromatography, 1996.

74. Carralero Sanz, V., et al., *Development of a tyrosinase biosensor based on gold nanoparticles-modified glassy carbon electrodes.* Analytica Chimica Acta, 2005. **528**(1): p. 1-8.

75. Zhou, M., et al., *Highly ordered mesoporous carbons as electrode material for the construction of electrochemical dehydrogenase- and oxidase-based biosensors.* Biosens Bioelectron, 2008. **24**(3): p. 442-7.

76. Justino, C.I.L., et al., *Review of analytical figures of merit of sensors and biosensors in clinical applications.* TrAC Trends in Analytical Chemistry, 2010. **29**(10): p. 1172-1183.

77. Shao, Y., et al., *Graphene Based Electrochemical Sensors and Biosensors: A Review.* Electroanalysis, 2010. **22**(10): p. 1027-1036.

78. Zhang, B., Q. Li, and T. Cui, *Ultra-sensitive suspended graphene nanocomposite cancer sensors with strong suppression of electrical noise.* Biosens Bioelectron, 2012. **31**(1): p. 105-9.

79. Browne, J., *Materials Form Foundations for RFMicrowave Circuits*. 2015.

80. Murthy VRK, S.S.a.V., Balasubramanian, *Microwave materials*. 1994: Springer.

81. Atta, N.F., A. Galal, and E.H. El-Ads, *Graphene — A Platform for Sensor and Biosensor Applications.* 2015.

82. Chen, L., et al., *Direct electrodeposition of reduced graphene oxide on glassy carbon electrode and its electrochemical application.* Electrochemistry Communications, 2011. **13**(2): p. 133-137.

83. Jeremy T. Robinson, F.K.P., Eric S. Snow, and a.P.E.S. Zhongqing Wei, *Reduced Graphene Oxide Molecular sensor.* **8**: p. 3137-3140.

84. Hill, E.W., A. Vijayaragahvan, and K. Novoselov, *Graphene Sensors.* IEEE Sensors Journal, 2011. **11**(12): p. 3161-3170.

85. Kahana, D. *What is the Dirac point in graphene*. [web] 2014 24/02/2014 [cited 2016 20/12/2016]; Available from: https://www.quora.com/What-is-the-Dirac-point-in-graphene.

86. Yang, S., et al., *A facile method for preparation of graphene film electrodes with tailor-made dimensions with Vaseline as the insulating binder.* Electrochemistry Communications, 2009. **11**(10): p. 1912-1915.

87. Ming Zhou, Y.Z., and Shaojun Dong, *Electrochemical Sensing and Biosensing Platform based on chemically reduced graphene oxide.pdf.* Analytical Chemistry, 2009. **Vol. 81,**: p. 11.

88. Lin, W.-J., et al., *Graphene modified basal and edge plane pyrolytic graphite electrodes for electrocatalytic oxidation of hydrogen peroxide and β-nicotinamide adenine dinucleotide.* Electrochemistry Communications, 2009. **11**(11): p. 2153-2156.

89. Hannes C. Schniepp, J.-L.L., Michael J. McAllister, Hiroaki Sai, Margarita Herrera-Alonso, Douglas H. Adamson, Robert K. Prud'homme, Roberto Car, Dudley A. Saville, and Ilhan A. Aksay, *Functionalized Single Graphene Sheets Derived from Splitting Graphite Oxide.* Journal of Physical Chemistry, 2006: p. 5.

90. Park, S. and R.S. Ruoff, *Chemical methods for the production of graphenes.* Nat Nanotechnol, 2009. **4**(4): p. 217-24.

91. Stankovich, S., et al., *Synthesis of graphene-based nanosheets via chemical reduction of exfoliated graphite oxide.* Carbon, 2007. **45**(7): p. 1558-1565.

92. Banks, C.E., et al., *Electrocatalysis at graphite and carbon nanotube modified electrodes: edge-plane sites and tube ends are the reactive sites.* Chem Commun (Camb), 2005(7): p. 829-41.

93. Khatayevich, D., et al., *Selective detection of target proteins by peptide-enabled graphene biosensor.* Small, 2014. **10**(8): p. 1505-13, 1504.

94. *Delocalization of Electrons*. 2016, LibreTexts.

95. Bai, J. and Y. Huang, *Fabrication and electrical properties of graphene nanoribbons.* Materials Science and Engineering: R: Reports, 2010. **70**(3-6): p. 341-353.

96. Terrones, M., et al., *Graphene and graphite nanoribbons: Morphology, properties, synthesis, defects and applications.* Nano Today, 2010. **5**(4): p. 351-372.

97. NOVOSELOV, A.K.G.A.K.S., *The rise of graphene*.

98. Wisitsoraat, A.M., J. P. Karuwan, C. Sriprachuabwong, C. Jaruwongrungsee, K. Phokharatkul, D. and T.M.L. Daniels, C. Tuantranont, A., *Printed organo-functionalized graphene for biosensing applications.* Biosens Bioelectron, 2017. **87**: p. 7-17.

99. Huang, Y., et al., *Graphene-based biosensors for detection of bacteria and their metabolic activities.* Journal of Materials Chemistry, 2011. **21**(33): p. 12358.

100. Yoon, J., et al., *Highly Sensitive Biosensors Based on Biomolecules and Functional Nanomaterials Depending on the Types of Nanomaterials: A Perspective Review.* Materials (Basel), 2020. **13**(2).

101. L. Wu, H.S.C., W. S. Koh, and E. P. Li, *Highly sensitive graphene biosensors based on.*

102. Kuila, T., et al., *Recent advances in graphene-based biosensors.* Biosens Bioelectron, 2011. **26**(12): p. 4637-48.

103. Liu, K., et al., *Direct electrochemistry and electrocatalysis of hemoglobin based on poly(diallyldimethylammonium chloride) functionalized graphene sheets/room temperature ionic liquid composite film.* Electrochemistry Communications, 2010. **12**(3): p. 402-405.

104. Chakraborty, S. and C.R. Raj, *Mediated electrocatalytic oxidation of bioanalytes and biosensing of glutamate using functionalized multiwall carbon nanotubes-biopolymer nanocomposite.* Journal of Electroanalytical Chemistry, 2007. **609**(2): p. 155-162.

105. Lacanette, K., *A Basic Introduction to Filters - Active, Passive, and Switched-Capacitor*, in *National Semiconductor*

Application Note. 1991.

106. ORCHARD, H.J., *Methods of Filter Design.* IEEE, 1964.

107. Kuo, F.F., *Network Analysis Synthesis*. 1962, John Wiley & Sons, Inc: Singapore.

108. Karki, J., *Active Low-Pass Filter Design*. 2002, Texas Instruments Texas

109. Hank Zumbahlen, a.A.D., Inc., *LowPass to BandPass Filter transformation*. 2012.

110. Behagi, A., *RF and Microwave Circuit Design*. 2015, California USA.

111. Smyth, J.R., *Quartz.*

112. King, H.M., *Quartz A ubiquitous mineral with an enormous number of uses*. 2020.

113. Microwave, F., *SMA Female Bulkhead PCB Connector*. 2017.

114. Laser, H., *Laserscript*. 2019.

115. Tesa, *Flame retardant polyimide high grade masking tape*. 2013.

116. Aliyev, E., et al., *Structural Characterization of Graphene Oxide: Surface Functional Groups and Fractionated Oxidative Debris.* Nanomaterials (Basel), 2019. **9**(8).

117. Perrozzi, F., S. Prezioso, and L. Ottaviano, *Graphene oxide: from fundamentals to applications.* J Phys Condens Matter, 2015. **27**(1): p. 013002.

118. Heaney, M.B., *Electrical-Conductivity-and-Resistivity*. 2003, Palo Alto Research Center.

119. Calvert, P., *Inkjet Printing for Materials and Devices.* Chemistry of Materials, 2001. **13**(10): p. 3299-3305.

120. Lee, D.H., et al., *Highly selective organic transistor biosensor with inkjet printed graphene oxide support system.* J Mater Chem B, 2017. **5**(19): p. 3580-3585.

121. Rao, S.U., Jahnavee Polychronopoulou, Kyriaki Umer, Rehan Das, Raj, *Reduced Graphene Oxide: Effect of Reduction on Electrical Conductivity.* Journal of Composites Science, 2018. **2**(2).

122. Chen, J.L., H. Zhang, L. Du, C. Fang, T. Hu, J., *Direct Reduction of Graphene Oxide/Nanofibrillated Cellulose Composite Film and its Electrical Conductivity Research.* Sci Rep, 2020. **10**(1): p. 3124.

123. Liu, H.Z., Lei. Guo, Yunlong. Cheng, Cheng. Yang, Lianjiang. Jiang, Lang. Yu, Gui. Hu, Wenping. Liu, Yunqi. Zhu, Daoben, *Reduction of graphene oxide to highly*

conductive graphene by Lawesson's reagent and its electrical applications. Journal of Materials Chemistry C, 2013. **1**(18).

124. scientific, t., *NHS and Sulfo-NHS*. 2011.
125. Inc., T.F.S. *EDC carbodiimide crosslinker: EDC reaction chemistry*. 2011; Available from: https://www.thermofisher.com/uk/en/home/life-science/protein-biology/protein-biology-learning-center/protein-biology-resource-library/pierce-protein-methods/carbodiimide-crosslinker-chemistry.html.
126. Inc, T.F.S., *EDC*. 2017: USA.
127. Cammarata, C.R., M.E. Hughes, and C.M. Ofner, 3rd, *Carbodiimide induced cross-linking, ligand addition, and degradation in gelatin.* Mol Pharm, 2015. **12**(3): p. 783-93.
128. NanoSciences, E., *PI-for-Immunodox®-Amine-PEGylated*. 2018: USA.

Appendix A

This appendix details the coefficient values for the parallel coupled bandpass filter as summarized in section 3.6 above.

$$\frac{J_{0,1}}{Y_0} = J_{0,1} = \sqrt{\frac{\pi FBW}{2g_0g_1}} = 0.3773$$

$$J_{1,2} = \frac{\pi FBW}{2}\sqrt{\frac{1}{g_1g_2}} = 0.1991$$

$$J_{2,3} = \frac{\pi FBW}{2}\sqrt{\frac{1}{g_2g_3}} = 0.1679$$

$$J_{3,4} = \frac{\pi FBW}{2}\sqrt{\frac{1}{g_3g_4}} = 0.1679$$

$$J_{4,5} = \frac{\pi FBW}{2}\sqrt{\frac{1}{g_4g_5}} = 0.1991$$

$$J_{5,6} = J_{0,1} = 0.3773$$

To determine the EVEN mode characteristic Impedance of the BPF was done using equation below:

$$(Z_{oe})_{j,j+1} = \frac{1}{Y_0}\left[1 + \frac{J_{j,j+1}}{Y_0} + \left(\frac{J_{j,j+1}}{Y_0}\right)^2\right] \quad (3.40)$$

$(Z_{oe})_{j,j+1}$ is the characteristic impedance of the even mode for the $J_{j,j+1}$ element.

$$(Z_{oe})_{0,1} = \frac{1}{Y_0}\left[1 + \frac{J_{0,1}}{Y_0} + \left(\frac{J_{0,1}}{Y_0}\right)^2\right] = 75.9818$$

$$(Z_{oe})_{1,2} = \frac{1}{Y_0}\left[1 + \frac{J_{1,2}}{Y_0} + \left(\frac{J_{1,2}}{Y_0}\right)^2\right] = 61.9378$$

$$(Z_{oe})_{2,3} = \frac{1}{Y_0}\left[1 + \frac{J_{2,3}}{Y_0} + \left(\frac{J_{2,3}}{Y_0}\right)^2\right] = 59.8059$$

$$(Z_{oe})_{3,4} = \frac{1}{Y_0}\left[1 + \frac{J_{3,4}}{Y_0} + \left(\frac{J_{3,4}}{Y_0}\right)^2\right] = 59.8059$$

$$(Z_{oe})_{4,5} = \frac{1}{Y_0}\left[1 + \frac{J_{4,5}}{Y_0} + \left(\frac{J_{4,5}}{Y_0}\right)^2\right] = 61.9378$$

$$(Z_{oe})_{5,6} = (Z_{oe})_{0,1} = 75.9818$$

While the ODD mode characteristic Impedance of the BPF was determined as:

$$(Z_{oo})_{j,j+1} = \frac{1}{Y_0}\left[1 + \frac{J_{j,j+1}}{Y_0} + \left(\frac{J_{j,j+1}}{Y_0}\right)^2\right] \quad (3.4)$$

$(Z_{oo})_{j,j+1}$ is the characteristic impedance of the odd mode for the $J_{j,j+1}$ element.

$$(Z_{oo})_{0,1} = \frac{1}{Y_0}\left[1 - \frac{J_{0,1}}{Y_0} + \left(\frac{J_{0,1}}{Y_0}\right)^2\right] = 38.2529$$

$$(Z_{oo})_{1,2} = \frac{1}{Y_0}\left[1 - \frac{J_{1,2}}{Y_0} + \left(\frac{J_{1,2}}{Y_0}\right)^2\right] = 42.0267$$

$$(Z_{oo})_{2,3} = \frac{1}{Y_0}\left[1 - \frac{J_{2,3}}{Y_0} + \left(\frac{J_{2,3}}{Y_0}\right)^2\right] = 43.0138$$

$$(Z_{oo})_{3,4} = \frac{1}{Y_0}\left[1 - \frac{J_{3,4}}{Y_0} + \left(\frac{J_{3,4}}{Y_0}\right)^2\right] = 43.0138$$

$$(Z_{oo})_{4,5} = \frac{1}{Y_0}\left[1 - \frac{J_{4,5}}{Y_0} + \left(\frac{J_{4,5}}{Y_0}\right)^2\right] = 42.0267$$

$$(Z_{oo})_{5,6} = (Z_{oo})_{0,1} = 38.2529$$

The single Microstrip line EVEN and ODD characteristic Impedance were determined as shown below:

$$(Z_{ose})_{0,1} = \frac{(Z_{oe})_{0,1}}{2} = 37.9909$$

$$(Z_{ose})_{1,2} = \frac{(Z_{oe})_{1,2}}{2} = 30.9689$$

$$(Z_{ose})_{2,3} = \frac{(Z_{oe})_{2,3}}{2} = 29.9030$$

$$(Z_{ose})_{3,4} = \frac{(Z_{oe})_{3,4}}{2} = 29.9030$$

$$(Z_{ose})_{4,5} = \frac{(Z_{oe})_{4,5}}{2} = 30.9689$$

$$(Z_{ose})_{5,6} = (Z_{ose})_{0,1} = 37.9909$$

While for the ODD single Microstrip line it is as follows:

$$(Z_{oso})_{0,1} = \frac{(Z_{oo})_{0,1}}{2} = 19.1265$$

$$(Z_{oso})_{1,2} = \frac{(Z_{oo})_{1,2}}{2} = 21.0134$$

$$(Z_{oso})_{2,3} = \frac{(Z_{oo})_{2,3}}{2} = 21.5069$$

$$(Z_{oso})_{3,4} = \frac{(Z_{oo})_{3,4}}{2} = 21.5069$$

$$(Z_{oso})_{4,5} = \frac{(Z_{oo})_{4,5}}{2} = 21.0134$$

$$(Z_{oso})_{5,6} = (Z_{oso})_{0,1} = 19.1265$$

To determine the single line shape ratio of Width and Thickness for the EVEN mode the following approach was used.

$$(A_e)_{0,1} = \frac{(Z_{ose})_{0,1}}{60}\left(\frac{\varepsilon_r + 1}{2}\right)^{0.5} + \frac{\varepsilon_r - 1}{\varepsilon_r + 1}\left(0.23 + \frac{0.11}{\varepsilon_r}\right) = 1.1320$$

$$(w/h)_{se0,1} = \frac{8Exp(A_e)_{0,1}}{Exp\left(2(A_e)_{0,1}\right) - 2} = 3.2560$$

$$(A_e)_{1,2} = \frac{(Z_{ose})_{1,2}}{60}\left(\frac{\varepsilon_r + 1}{2}\right)^{0.5} + \frac{\varepsilon_r - 1}{\varepsilon_r + 1}\left(0.23 + \frac{0.11}{\varepsilon_r}\right) = 0.9507$$

$$(w/h)_{se1,2} = \frac{8Exp(A_e)_{1,2}}{Exp(\left(2(A_e)_{1,2}\right) - 2} = 4.4090$$

$$(A_e)_{2,3} = \frac{(Z_{ose})_{2,3}}{60}\left(\frac{\varepsilon_r + 1}{2}\right)^{0.5} + \frac{\varepsilon_r - 1}{\varepsilon_r + 1}\left(0.23 + \frac{0.11}{\varepsilon_r}\right) = 0.9231$$

$$(w/h)_{se2,3} = \frac{8Exp(A_e)_{2,3}}{Exp\left(2(A_e)_{2,3}\right) - 2} = 4.6440$$

$$(A_e)_{3,4} = \frac{(Z_{ose})_{3,4}}{60}\left(\frac{\varepsilon_r + 1}{2}\right)^{0.5} + \frac{\varepsilon_r - 1}{\varepsilon_r + 1}\left(0.23 + \frac{0.11}{\varepsilon_r}\right) = 0.9231$$

$$(w/h)_{se3,4} = \frac{8Exp(A_e)_{3,4}}{Exp\left(2(A_e)_{3,4}\right) - 2} = 4.6440$$

$$(A_e)_{4,5} = \frac{(Z_{ose})_{4,5}}{60}\left(\frac{\varepsilon_r + 1}{2}\right)^{0.5} + \frac{\varepsilon_r - 1}{\varepsilon_r + 1}\left(0.23 + \frac{0.11}{\varepsilon_r}\right) = 0.9507$$

$$(w/h)_{se4,5} = \frac{8Exp(A_e)_{4,5}}{Exp\left(2(A_e)_{4,5}\right) - 2} = 4.4090$$

$$(A_e)_{5,6} = (A_e)_{0,1} = 1.1320$$

$$(w/h)_{se5,6} = (w/h)_{se0,1} = 3.2560$$

While to determine the single line shape ratio of Width and Thickness for the ODD mode is done below:

$$(A_o)_{0,1} = \frac{(Z_{oso})_{0,1}}{60}\left(\frac{\varepsilon_r + 1}{2}\right)^{0.5} + \frac{\varepsilon_r - 1}{\varepsilon_r + 1}\left(0.23 + \frac{0.11}{\varepsilon_r}\right) = 0.6449$$

$$(w/h)_{so0,1} = \frac{8Exp(A_o)_{0,1}}{Exp\left(2(A_o)_{0,1}\right) - 2} = 9.3419$$

$$(A_o)_{1,2} = \frac{(Z_{oso})_{1,2}}{60}\left(\frac{\varepsilon_r + 1}{2}\right)^{0.5} + \frac{\varepsilon_r - 1}{\varepsilon_r + 1}\left(0.23 + \frac{0.11}{\varepsilon_r}\right) = 0.6936$$

$$(w/h)_{so1,2} = \frac{8Exp(A_o)_{1,2}}{Exp(\left(2(A_o)_{1,2}\right) - 2} = 7.9888$$

$$(A_o)_{2,3} = \frac{(Z_{ose})_{2,3}}{60}\left(\frac{\varepsilon_r + 1}{2}\right)^{0.5} + \frac{\varepsilon_r - 1}{\varepsilon_r + 1}\left(0.23 + \frac{0.11}{\varepsilon_r}\right) = 0.7064$$

$$(w/h)_{so2,3} = \frac{8Exp(A_o)_{2,3}}{Exp\left(2(A_o)_{2,3}\right) - 2} = 7.6944$$

$$(A_o)_{3,4} = \frac{(Z_{oso})_{3,4}}{60}\left(\frac{\varepsilon_r + 1}{2}\right)^{0.5} + \frac{\varepsilon_r - 1}{\varepsilon_r + 1}\left(0.23 + \frac{0.11}{\varepsilon_r}\right) = 0.7064$$

$$(w/h)_{so3,4} = \frac{8Exp(A_o)_{3,4}}{Exp\left(2(A_o)_{3,4}\right) - 2} = 7.6944$$

$$(A_o)_{4,5} = \frac{(Z_{oso})_{4,5}}{60}\left(\frac{\varepsilon_r + 1}{2}\right)^{0.5} + \frac{\varepsilon_r - 1}{\varepsilon_r + 1}\left(0.23 + \frac{0.11}{\varepsilon_r}\right) = 0.6936$$

$$(w/h)_{so4,5} = \frac{8Exp(A_o)_{4,5}}{Exp\left(2(A_o)_{4,5}\right) - 2} = 7.9888$$

$$(A_o)_{5,6} = (A_o)_{0,1} = 0.6449$$

$$(w/h)_{so5,6} = (w/h)_{so0,1,} = 9.3419$$

Then to determine the single line shape ratio of space and Thickness the approach is as done below

$$(A)_{0,1} = \cosh\left(\left(\frac{\pi}{2}\right)(w/h)_{se0,1}\right) = 83.2172$$

$$(B)_{0,1} = \cosh\left(\left(\frac{\pi}{2}\right)(w/h)_{so0,1}\right) = 1.1801 \times 10^{6}$$

$$(s/h)_{0,1} = \left(\frac{\pi}{2}\right)\cosh^{-1}\left(\frac{\left((A)_{0,1} + (B)_{0,1}\right) - 2}{(B)_{0,1} - (A)_{0,1}}\right) = 0.0106$$

$$(A)_{1,2} = \cosh\left(\left(\frac{\pi}{2}\right)(w/h)_{se1,2}\right) = 509.0348$$

$$(B)_{1,2} = \cosh\left(\left(\frac{\pi}{2}\right)(w/h)_{so1,2}\right) = 1.4087 \times 10^{5}$$

$$(s/h)_{1,2} = \left(\frac{\pi}{2}\right)\cosh^{-1}\left(\frac{\left((A)_{1,2} + (B)_{1,2}\right) - 2}{(B)_{1,2} - (A)_{1,2}}\right) = 0.0766$$

$$(A)_{2,3} = \cosh\left(\left(\frac{\pi}{2}\right)(w/h)_{se2,3}\right) = 736.2903$$

$$(B)_{2,3} = \cosh\left(\left(\frac{\pi}{2}\right)(w/h)_{so2,3}\right) = 8.8709 \times 10^{4}$$

$$(s/h)_{2,3} = \left(\frac{\pi}{2}\right)\cosh^{-1}\left(\frac{\left((A)_{2,3} + (B)_{2,3}\right) - 2}{(B)_{2,3} - (A)_{2,3}}\right) = 0.1162$$

$$(A)_{3,4} = \cosh\left(\left(\frac{\pi}{2}\right)(w/h)_{se3,4}\right) = 736.2903$$

$$(B)_{3,4} = \cosh\left(\left(\frac{\pi}{2}\right)(w/h)_{so3,4}\right) = 8.8709 \times 10^4$$

$$(s/h)_{3,4} = \left(\frac{\pi}{2}\right)\cosh^{-1}\left(\frac{\left((A)_{3,4} + (B)_{3,4}\right) - 2}{(B)_{3,4} - (A)_{3,4}}\right) = 0.1162$$

$$(A)_{4,5} = \cosh\left(\left(\frac{\pi}{2}\right)(w/h)_{se4,5}\right) = 509.0348$$

$$(B)_{4,5} = \cosh\left(\left(\frac{\pi}{2}\right)(w/h)_{so4,5}\right) = 1.4087 \times 10^5$$

$$(s/h)_{4,5} = \left(\frac{\pi}{2}\right)\cosh^{-1}\left(\frac{\left((A)_{4,5} + (B)_{4,5}\right) - 2}{(B)_{4,5} - (A)_{4,5}}\right) = 0.0766$$

$$(A)_{5,6} = (A)_{0,1} = 83.2172$$
$$(B)_{5,6} = (B)_{0,1} = 1.1801 \times 10^6$$
$$(s/h)_{5,6} = (s/h)_{0,1} = 0.0106$$

To determine the single line shape ratio of width by Thickness of the element the approach is as done below

$$(C)_{0,1} = \left(\frac{\pi}{2}\right)(s/h)_{0,1} = 0.0167$$

$$(D)_{0,1} = \left(\frac{\pi}{2}\right)(w/h)_{se0,1} = 5.1146$$

$$(E)_{0,1} = \cosh(C)_{0,1} = 1.0001$$

$$(F)_{0,1} = \cosh(D)_{0,1} = 83.2172$$

$$(w/h)_{0,1} = \frac{1}{\pi}\cosh^{-1}\left(\frac{1}{2}\left((C)_{0,1} - 1\right)\right) + \left(\left(\left(\cosh(C)_{0,1} + 1\right)\left(\cosh(D)_{0,1}\right)\right) - (C)_{0,1}\right)$$
$$= 1.5418$$

$$(C)_{1,2} = \left(\frac{\pi}{2}\right)(s/h)_{1,2} = 0.1203$$

$$(D)_{1,2} = \left(\frac{\pi}{2}\right)(w/h)_{se1,2} = 6.9257$$

$$(E)_{1,2} = \cosh(C)_{1,2} = 1.0072$$

$$(F)_{1,2} = \cosh(D)_{1,2} = 509.0348$$

$$(w/h)_{1,2} = \frac{1}{\pi}\cosh^{-1}\left(\frac{1}{2}\left((C)_{1,2} - 1\right)\right) + \left(\left(\left(\cosh(C)_{1,2} + 1\right)\left(\cosh(D)_{1,2}\right)\right) - (C)_{1,2}\right)$$
$$= 2.1134$$

$$(C)_{2,3} = \left(\frac{\pi}{2}\right)(s/h)_{2,3} = 0.1826$$

$$(D)_{2,3} = \left(\frac{\pi}{2}\right)(w/h)_{se2,3} = 7.2948$$

$$(E)_{2,3} = \cosh(C)_{2,3} = 1.0167$$

$$(F)_{2,3} = \cosh(D)_{2,3} = 736.2903$$

$$(w/h)_{2,3} = \frac{1}{\pi}\cosh^{-1}\left(\frac{1}{2}\left((C)_{2,3} - 1\right)\right) + \left(\left(\left(\cosh(C)_{2,3} + 1\right)\left(\cosh(D)_{2,3}\right)\right) - (C)_{2,3}\right)$$
$$= 2.2274$$

$$(C)_{3,4} = \left(\frac{\pi}{2}\right)(s/h)_{3,4} = 0.1826$$

$$(D)_{3,4} = \left(\frac{\pi}{2}\right)(w/h)_{se3,4} = 7.2948$$

$$(E)_{3,4} = \cosh(C)_{3,4} = 1.0167$$

$$(F)_{3,4} = \cosh(D)_{3,4} = 736.2903$$

$$(w/h)_{3,4} = \frac{1}{\pi}\cosh^{-1}\left(\frac{1}{2}\left((C)_{3,4} - 1\right)\right) + \left(\left(\left(\cosh(C)_{3,4} + 1\right)\left(\cosh(D)_{3,4}\right)\right) - (C)_{3,4}\right)$$
$$= 2.2274$$

$$(C)_{4,5} = \left(\frac{\pi}{2}\right)(s/h)_{4,5} = 0.1203$$

$$(D)_{4,5} = \left(\frac{\pi}{2}\right)(w/h)_{se4,5} = 6.9257$$

$$(E)_{4,5} = \cosh(C)_{4,5} = 1.0072$$

$$(F)_{4,5} = \cosh(D)_{4,5} = 509.0348$$

$$(w/h)_{4,5} = \frac{1}{\pi}\cosh^{-1}\left(\frac{1}{2}\left((C)_{4,5} - 1\right)\right) + \left(\left(\left(\cosh(C)_{4,5} + 1\right)\left(\cosh(D)_{4,5}\right)\right) - (C)_{4,5}\right)$$
$$= 2.1134$$

$$(w/h)_{5,6} = (w/h)_{0,1} = 1.5418$$

From the above results the Effective dielectric constants of each elements was determined as below.

$$(G)_{0,1} = 12\left(\frac{1}{(w/h)_{0,1}}\right) = 7.7832$$

$$(H)_{0,1} = \sqrt{1 + (G)_{0,1}} = 2.9636$$

$$(I)_{0,1} = \frac{1}{(H)_{0,1}} = 0.3374$$

$$\varepsilon_{r0,1} = \left(\frac{\varepsilon_r + 1}{2}\right) + \left(\frac{\varepsilon_r - 1}{2}\right)(I)_{0,1} = 2.8724$$

While the wavelength is given by

$$\lambda_{g0,1} = \frac{300}{F_c\sqrt{\varepsilon_{r0,1}}} = 70.8043$$

The length of the element is a quarter of a wavelength given by:

$$Length_{0,1} = \frac{\lambda_{g0,1}}{4} = 17.7011$$

$$(G)_{1,2} = 12\left(\frac{1}{(w/h)_{1,2}}\right) = 5.6780$$

$$(H)_{1,2} = \sqrt{1 + (G)_{1,2}} = 2.5842$$

$$(I)_{1,2} = \frac{1}{(H)_{1,2}} = 0.3870$$

$$\varepsilon_{r1,2} = \left(\frac{\varepsilon_r + 1}{2}\right) + \left(\frac{\varepsilon_r - 1}{2}\right)(I)_{1,2} = 2.9418$$

While the wavelength is given by

$$\lambda_{g1,2} = \frac{300}{F_c\sqrt{\varepsilon_{r1,2}}} = 69.9645$$

The length of the element is a quarter of a wavelength given by:

$$Length_{1,2} = \frac{\lambda_{g1,2}}{4} = 17.4911$$

$$(G)_{2,3} = 12\left(\frac{1}{(w/h)_{2,3}}\right) = 5.3874$$

$$(H)_{2,3} = \sqrt{1 + (G)_{2,3}} = 2.5273$$

$$(I)_{2,3} = \frac{1}{(H)_{2,3}} = 0.3957$$

$$\varepsilon_{r2,3} = \left(\frac{\varepsilon_r + 1}{2}\right) + \left(\frac{\varepsilon_r - 1}{2}\right)(I)_{2,3} = 2.9539$$

While the wavelength is given by

$$\lambda_{g2,3} = \frac{300}{F_c\sqrt{\varepsilon_{r2,3}}} = 69.8200$$

The length of the element is a quarter of a wavelength given by:

$Length_{2,3} = \frac{\lambda_{g2,3}}{4}$ =17.4550

$$(G)_{3,4} = 12\left(\frac{1}{(w/h)_{3,4}}\right) = 5.3874$$

$$(H)_{3,4} = \sqrt{1 + (G)_{3,4}} = 2.5273$$

$$(I)_{3,4} = \frac{1}{(H)_{3,4}} = 0.3957$$

$$\varepsilon_{r3,4} = \left(\frac{\varepsilon_r + 1}{2}\right) + \left(\frac{\varepsilon_r - 1}{2}\right)(I)_{3,4} = 2.9539$$

While the wavelength is given by

$$\lambda_{g3,4} = \frac{300}{F_c\sqrt{\varepsilon_{r3,4}}} = 69.8200$$

The length of the element is a quarter of a wavelength given by:

$Length_{3,4} = \frac{\lambda_{g3,4}}{4} = 17.4550$

$(G)_{4,5} = 12\left(\frac{1}{(w/h)_{4,5}}\right) = 5.6780$

$(H)_{4,5} = \sqrt{1 + (G)_{4,5}} = \ 2.5842$

$(I)_{4,5} = \frac{1}{(H)_{4,5}} =$

$\varepsilon_{r4,5} = \left(\frac{\varepsilon_r + 1}{2}\right) + \left(\frac{\varepsilon_r - 1}{2}\right)(I)_{4,5} = 2.9418$

While the wavelength is given by

$\lambda_{g4,5} = \frac{300}{F_c\sqrt{\varepsilon_{r4,5}}} = 69.9645$

The length of the element is a quarter of a wavelength given by:

$Length_{4,5} = \frac{\lambda_{g4,5}}{4} = 17.4911$

$\lambda_{g5,6} = \lambda_{g0,1} = 70.8043$

The length of the element is a quarter of a wavelength given by:

$Length_{5,6} = Length_{0,1} = 17.7011$